

**SYNTHESIS AND CHARACTERIZATION OF COPPER ARSENIC
SULFIDE FOR SOLUTION-PROCESSED PHOTOVOLTAICS**

by

Scott Andrew McClary

A Dissertation

Submitted to the Faculty of Purdue University

In Partial Fulfillment of the Requirements for the degree of

Doctor of Philosophy



Davidson School of Chemical Engineering

West Lafayette, Indiana

August 2019

**THE PURDUE UNIVERSITY GRADUATE SCHOOL
STATEMENT OF COMMITTEE APPROVAL**

Dr. Rakesh Agrawal, Chair

Davidson School of Chemical Engineering

Dr. Bryan W. Boudouris

Davidson School of Chemical Engineering

Dr. Carol A. Handwerker

School of Materials Engineering

Dr. Michael T. Harris

Davidson School of Chemical Engineering

Approved by:

Dr. John A. Morgan

Head of the Graduate Program

To my family, friends, and society

ACKNOWLEDGMENTS

The journey to getting a Ph.D. has undoubtedly been the absolute most challenging and rewarding experience of my life. It would not have been possible for me to achieve the pinnacle of higher education without the support of many individuals who were always willing to lend a hand or discuss issues I faced in my research. I will acknowledge as many people as I can here.

I would first like to thank my research advisor, Prof. Rakesh Agrawal, for mentoring me these past five years. Through his careful guidance, I have learned how to ask the critical questions and design the key experiments needed to become an independent researcher capable of succeeding in the professional world. I also learned a valuable thing or two about prioritization, time management, and flexibility through our interactions in my time here! I would also like to thank Prof. Carol Handwerker, who served on my prelim and dissertation committees, reminded me to consider the fundamental aspects of materials science, and always had insightful questions to guide the next steps of my research. I acknowledge Prof. Bryan Boudouris for his technical and big-picture comments, as well as his meticulous attention to the details in every aspect of written and oral presentations. I'd also like to thank Prof. Michael Harris for his service on my prelim and dissertation committees and for useful questions regarding nanoparticles and heat treatments.

I have been fortunate to work with the best research group that anyone could ever ask for. I joined the Agrawal group in late 2014 as the fifteenth active group member, giving me the opportunity to learn from many graduate students and pass my knowledge on to the nine graduate students who joined the group after me. Special thanks are owed to Dr. Bobby Balow, who taught me everything he knew about the copper arsenic sulfide system, how to “think like a chemist”, and how to maximize the information I could get out of any experiment I designed. He and I would frequently discuss current research directions and coauthored a paper several years after he graduated. I'd also like to acknowledge Joseph Andler for diving headfirst into the copper arsenic sulfide system with me and emerging relatively unscathed. Joe has always been willing to listen to my crazy ideas, challenging them where appropriate, and helping me brainstorm and design the next experiment to improve our emerging material system. The rest of the group members have also contributed in a very positive manner to my research, but there is not enough space to acknowledge their contributions individually. I instead leave this extensive list of graduate students who I have shared the laboratory experience with: Kevin Brew, Nathan Carter, Chuck Hages, Erik

Sheets, David Yang, Ruihong Zhang, Brian Graeser, Steven McLeod, Caleb Miskin, Mark Koeper, Xin Zhao, Robert Boyne, Xianyi Hu, Essam AlRuqobah, Swapnil Deshmukh, Ryan Ellis, David Rokke, Kyle Weideman, Anna Murray, Apurva Pradhan, and Jonathan Turnley.

My research endeavors would not have been possible without the dedication and experience of a great number of collaborators. First and foremost, I'd like to thank Prof. Yanfa Yan and his research team at the University of Toledo for our computational and experimental collaborations, with special recognition to Xinxing Yin, Weiwei Meng, and Canglang Yao for their contributions. I thank Darius Kuciauskas and Patricia Dippo of the National Renewable Energy Laboratory for their assistance with photoluminescence measurements and helping me write a successful abstract for the 46th PVSC conference. I am deeply indebted to Siming Li, Mohammad Taheri, and Prof. Jason Baxter of Drexel University for their terahertz spectroscopy measurements. I acknowledge Daria Blach and Prof. Libai Huang (Purdue Chemistry) for their assistance with time-resolved photoluminescence, and Yining Feng and Prof. Luna Lu (Purdue Civil Engineering) for their Hall effect measurements. I am grateful to Dr. Christopher Gilpin for his discussions regarding microscopy and EDX and for his, Bob Seiler's, and Laurie Mueller's wonderful support at the Life Sciences Microscopy Facility. I thank Glenn Teeter of NREL and Dmitry Zemlyanov of Purdue for preliminary XPS and UPS measurements on my copper arsenic sulfide thin films.

I have also had the fortune to mentor three hard-working undergraduate students throughout my time at Purdue and would like to thank them for their efforts. Trey Sanfrey studied the processing of copper antimony sulfide from aqueous molecular precursors. Louie Schroeder worked on copper arsenic sulfide films from aqueous molecular precursors and was instrumental in getting the ligand exchange project off the ground and running. Deepa Korani researched nanoparticle synthesis using alternative ligands.

Teaching has been a consistent passion of mine, and graduate school provided me with an excellent opportunity to improve my skills. I would like to thank Prof. Bryan Boudouris, Prof. Stephen Beaudoin, and Prof. David Corti for their advice when I served as a teaching assistant for their classes. I acknowledge Prof. Phil Wankat and Prof. Matthew Ohland for their constructive criticism of my teaching skills in the ENE685 course. I also must, of course, recognize Prof. Matthew Liberatore and Prof. Charles Vestal for giving me the chance to be a teaching assistant at Colorado School of Mines, which partially inspired my decision to attend graduate school.

I thank the organizers of the 44th and 46th IEEE Photovoltaics Specialists Conference (PVSC) and the 2018 AIChE Annual Meeting for providing me with forums to disseminate my research to an international audience and make lasting connections that will prove useful in the years to come. I am also indebted to Sarah Kurtz, Adele Tamboli, and others for their efforts in organizing the Hands-On Photovoltaics (HOPE) Workshop that I attended at NREL in July of 2016.

Outside of the laboratory setting, I was able to spend time with many inspiring individuals who were always there when I needed a break from the rigors of academia. Specifically, I'd like to acknowledge Jason Bates, Phil Kester, Robert Warburton, and Adam Wingate for our Tuesday nights at Professor Joe's and other general shenanigans. The trivia and softball teams provided a source of weekly entertainment and at least something resembling physical activity. I would also like to thank all the individuals who shared living arrangements with me throughout my time at Purdue: Andrew Cook, Leonid Miroshnik, Jamie Harris, Elizabeth Sahagun, and Aidan Coffey.

And last, but certainly not least, I would like to thank my parents, my brother, and my grandparents for their unconditional love and support throughout my Ph.D. journey. Their ability to inspire and motivate me from over 1500 miles away has never ceased to amaze me, and I look forward to spending more time with them in the coming years.

TABLE OF CONTENTS

LIST OF TABLES	13
LIST OF FIGURES	15
ABSTRACT	25
1. INTRODUCTION	27
1.1 A Need for Sustainable Energy.....	27
1.2 A Brief Overview of Photovoltaic Cells.....	27
1.3 The Promise of the Copper-Arsenic-Sulfur System for Solar Cells	29
1.4 Objectives and Structure of This Thesis	30
1.5 References.....	33
2. SOLUTION-PROCESSED COPPER ARSENIC SULFIDE (Cu_3AsS_4) THIN FILMS FOR PHOTOVOLTAIC APPLICATIONS	36
2.1 Introduction.....	36
2.2 Experimental Methods	37
2.2.1 Materials	37
2.2.2 Cu_3AsS_4 Nanoparticle Synthesis	38
2.2.3 Film Fabrication.....	38
2.2.4 Ampoule Preparation	38
2.2.5 Annealing Treatments and Device Fabrication	39
2.2.6 Ligand Exchange	39
2.2.7 Treatments with Ligand Exchanged Particles	40
2.2.8 Characterization.....	40
2.3 Results and Discussion	40
2.3.1 Thermal Analysis of As-synthesized Luzonite (Cu_3AsS_4) Nanoparticles	40
2.3.2 Process Design for Cu_3AsS_4 Grain Growth.....	42
2.3.3 Materials Characterization of Large-Grained Cu_3AsS_4 Thin Films	43
2.3.4 Effects of Various Annealing Atmospheres on Grain Structure	48
2.3.5 Preliminary Solar Cells Using Cu_3AsS_4 Absorber Layer	50
2.4 Conclusions.....	52
2.5 Acknowledgements.....	53

2.6	References.....	53
3.	INSIGHTS INTO THE GROWTH OF ENARGITE FILMS FROM NANOPARTICLE PRECURSORS.....	56
3.1	Introduction.....	56
3.2	Experimental Methods.....	56
3.2.1	Materials.....	56
3.2.2	Heat Treatments.....	57
3.2.3	Deposition of Arsenic(III) Sulfide Thin Films.....	57
3.2.4	Characterization.....	57
3.3	Results and Discussion.....	58
3.3.1	Vacuum Annealing of Luzonite Nanoparticle Films.....	58
3.3.2	Sulfurization of Luzonite Nanoparticle Films.....	59
3.3.3	Deposition and Annealing of Stacked Arsenic(III) Sulfide-Luzonite Films.....	62
3.3.4	Optimization of Arsenic(V) Sulfide Heat Treatments.....	67
3.3.5	Pre-Annealing of Luzonite Nanoparticle Films.....	73
3.3.6	Impacts of Substrate on Enargite Film Orientation.....	74
3.4	Conclusions.....	76
3.5	Acknowledgements.....	77
3.6	References.....	77
4.	POST-HEAT TREATMENT PROCESSING OF ENARGITE THIN FILMS.....	79
4.1	Introduction.....	79
4.2	Experimental Methods.....	80
4.2.1	Chemicals.....	80
4.2.2	Post-Processing Techniques.....	80
4.2.3	Monte Carlo Simulations.....	80
4.2.4	Characterization.....	80
4.3	Results and Discussion.....	81
4.3.1	Surface Etches of Enargite Thin Films.....	81
4.3.2	Post-Heat Treatment Annealing of Enargite Thin Films.....	85
4.3.3	Hot Pressing of Enargite Thin Films.....	88
4.3.4	Electrochemical Etching of Enargite Thin Films.....	89

4.4	Conclusions.....	90
4.5	Acknowledgements.....	91
4.6	References.....	91
5.	LIGAND EXCHANGE OF LUZONITE AND COPPER SULFIDE NANOPARTICLES TOWARDS CARBON-FREE ENARGITE THIN FILMS.....	93
5.1	Introduction.....	93
5.2	Experimental Methods.....	95
5.2.1	Materials.....	95
5.2.2	Nanoparticle Synthesis.....	96
5.2.3	Ligand Exchange and Coating.....	96
5.2.4	Heat Treatments.....	97
5.2.5	Characterization.....	98
5.3	Results and Discussion.....	98
5.3.1	Identifying Candidate Ligands for Luzonite Nanoparticles.....	98
5.3.2	Optimizing Ligand Exchange with AsS_3^{3-} Ligands.....	101
5.3.3	Ligand Exchange of AsS_3^{3-} with Copper(I) Sulfide Nanoparticles.....	104
5.3.4	Heat Treatments of Ligand Exchanged Luzonite Nanoparticles.....	105
5.3.5	Heat Treatments of Ligand Exchanged Copper Sulfide Nanoparticles.....	107
5.4	Conclusions.....	109
5.5	Acknowledgements.....	109
5.6	References.....	110
6.	OPTOELECTRONIC CHARACTERIZATION OF ENARGITE THIN FILMS AND DEVICES.....	113
6.1	Introduction.....	113
6.2	Experimental Methods.....	114
6.2.1	Materials.....	114
6.2.2	Characterization Methods.....	114
6.2.3	Simulation Methods.....	115
6.3	Results and Discussion.....	115
6.3.1	Photoluminescence.....	115
6.3.2	Hall Effect Measurements.....	118

6.3.3	Time-Resolved Terahertz Spectroscopy	119
6.3.4	Time-Resolved Photoluminescence Spectroscopy	125
6.3.5	On the Origins of Poor Enargite Device Performance	129
6.4	Conclusions.....	135
6.5	Acknowledgements.....	136
6.6	References.....	136
7.	ROLE OF ANNEALING ATMOSPHERE ON THE CRYSTAL STRUCTURE AND COMPOSITION OF TETRAHEDRITE-TENNANTITE ALLOY NANOPARTICLES ...	140
7.1	Introduction.....	140
7.2	Experimental Methods.....	142
7.2.1	Materials	142
7.2.2	Nanoparticle Alloy Synthesis and Washing Procedure	142
7.2.3	Heat Treatments.....	143
7.2.4	Characterization.....	145
7.3	Results and Discussion	145
7.3.1	Characterization of Synthesized $\text{Cu}_{12}(\text{As}_{1-x}\text{Sb}_x)_4\text{S}_{13}$ Nanoparticles	145
7.3.2	Characterization of Nanoparticles Annealed in Sulfur.....	148
7.3.3	Characterization of Nanoparticles Annealed in H_2S	151
7.3.4	Characterization of Nanoparticles Annealed in Nitrogen.....	155
7.3.5	Grain Growth for All Three Heat Treatments	158
7.3.6	Discussion.....	160
7.4	Conclusions.....	165
7.5	Acknowledgements.....	165
7.6	Statement of Data Access	165
7.7	References.....	166
8.	SYNTHESIS AND CHARACTERIZATION OF SEMICONDUCTING SINNERITE ($\text{Cu}_6\text{As}_4\text{S}_9$) THIN FILMS	172
8.1	Introduction.....	172
8.2	Experimental Methods.....	173
8.2.1	Materials	173
8.2.2	Nanoparticle Synthesis and Coating.....	174

8.2.3	Ampoule Preparation and Heat Treatment	174
8.2.4	Ligand Exchange	175
8.2.5	Characterization.....	176
8.3	Results and Discussion	176
8.4	Conclusions.....	188
8.5	Acknowledgements.....	188
8.6	Statement of Data Access	188
8.7	References.....	188
9.	MOLECULAR PRECURSOR ROUTES TO THIN FILMS OF COPPER ARSENIC SULFIDE	193
9.1	Introduction.....	193
9.2	Experimental Methods	194
9.2.1	Materials	194
9.2.2	Low-Temperature Baking.....	194
9.2.3	High-Temperature Annealing.....	195
9.2.4	Characterization.....	195
9.3	Results and Discussion	195
9.3.1	Precursor Solubility	195
9.3.2	Low-Temperature Baking.....	197
9.3.3	High-Temperature Annealing.....	199
9.4	Conclusions.....	204
9.5	Acknowledgements.....	205
9.6	References.....	205
10.	MOLECULAR PRECURSOR ROUTES TO THIN FILMS OF COPPER ANTIMONY SULFIDE	207
10.1	Introduction	207
10.2	Experimental Methods.....	208
10.2.1	Materials.....	208
10.2.2	Low-Temperature Baking	209
10.2.3	High-Temperature Annealing	209
10.2.4	Characterization	210

10.3	Results and Discussion	210
10.3.1	Precursor Solubility	210
10.3.2	Low-Temperature Baking	211
10.3.3	High-Temperature Annealing	216
10.4	Conclusions	221
10.5	Acknowledgements	222
10.6	References	222
11.	CONCLUSIONS AND FUTURE WORK	226
11.1	Conclusions	226
11.2	Future Work.....	227
11.3	References	229
APPENDIX A.	STUDIES ON THE COATING AND WASHING OF LUZONITE NANOPARTICLES.....	230
APPENDIX B.	PRELIMINARY STUDIES TOWARDS SYNTHESIS OF ALLOYED COPPER ARSENIC SULFIDE THIN FILMS.....	235
APPENDIX C.	EXPLORATION OF ALTERNATIVE SYNTHESIS METHODS FOR Cu_3AsS_4 NANOPARTICLES.....	242
APPENDIX D.	PRELIMINARY SYNTHESIS OF ZINC SULFIDE THIN FILMS USING THE SILAR METHOD.....	246
APPENDIX E.	SUPPLEMENTARY CHARACTERIZATION FOR TETRAHEDRITE- TENNANTITE AND COPPER ARSENIC ANTIMONY SELENIDE NANOPARTICLES	249
APPENDIX F.	ON THE USE OF EDX TO DETERMINE NANOPARTICLE COMPOSITIONS	253
VITA.....		255
PUBLICATIONS.....		256

LIST OF TABLES

Table 1.1. Ternary phases in the Cu-As-S system.	29
Table 2.1. EDX compositions measured for NP samples treated at 375 °C, 425 °C, and 500 °C with As ₂ S ₅ for 1 h. The measured ratios indicate that arsenic and sulfur have incorporated into the film beyond the target 3:1 Cu:As and 0.75 Cu:S ratios.	46
Table 2.2. Device statistics (n = 10) for solar cells based on a common ENG absorber layer (cell area = 0.1 cm ²). Out of the ten devices, one had a fill factor and efficiency of 0%. The second set of columns represents the device statistics without this particular device included (n = 9).	52
Table 4.1. Summary of interactions between ampoule residues and candidate etchants.	83
Table 4.2. Low-voltage EDX-determined elemental ratios before and after etches in the given solution. Standard deviations are based on multiple measurements at different spots on the sample.	84
Table 4.3. XRF-determined compositions of ENG films etched in DAS for 1 min. Sample 1 is on Mo-coated soda-lime glass, Sample 2 is on Mo-coated borosilicate glass, and Sample 3 is was made from ligand exchanged NPs on Mo-coated soda-lime glass. Standard deviations are computed from three repeated measurements on 3-4 different spots on the sample.	84
Table 5.1. Detailed information for chemicals used in Chapter 5. A * signifies an air-sensitive chemical.	95
Table 5.2. Qualitative summary of two-phase ligand exchange screening experiments.	99
Table 5.3. Dissolution of AsS ₃ ³⁻ -based ligands in various polar solvents at ~20 mg/mL.	101
Table 6.1. ENG carrier concentration, conductivity, and mobility derived from Hall measurements.	119
Table 6.2. TRPL-derived time constants and relative weights for ENG samples fabricated on various substrates. Excitation wavelength was 447 nm.	126
Table 6.3. Parameters used for simulation of J-V curves in SCAPS.	132
Table 7.1. Calculated elemental ratios of as-synthesized Cu ₁₂ (As _{1-x} Sb _x) ₄ S ₁₃ NPs from SEM-EDS data. The standard deviations are based on three measurements from random areas of each sample. Note that the stoichiometric ratios for Cu/(Sb+As) and (Cu+Sb+As)/S are 3.00 and 1.23, respectively.	148
Table 7.2. Rietveld refinement-determined weight percent of resulting phases after Cu ₁₂ (As _{1-x} Sb _x) ₄ S ₁₃ NPs were annealed in sulfur for 1 h at 450 °C. The more As-rich phases partially formed a mixture of the orthorhombic enargite and tetragonal famatinite/luzonite crystal structures. The tendency to form the orthorhombic phase was suppressed with increasing Sb concentration. ..	149
Table 7.3. SEM-EDS calculated elemental ratios of Cu ₁₂ (As _{1-x} Sb _x) ₄ S ₁₃ nanoparticles treated in a sulfur atmosphere at 450 °C for 1 h. The standard deviations are based on three measurements from random areas of the samples.	150

Table 7.4. Rietveld refinement-determined weight percent of resulting phases after $\text{Cu}_{12}(\text{As}_{1-x}\text{Sb}_x)_4\text{S}_{13}$ NPs were annealed in H_2S for 1 h at 450 °C. Significant decomposition is observed in the purely Sb- and As-samples, while the mixed alloy compositions displayed significantly higher resistance to decomposition into crystalline secondary phases.	154
Table 7.5. SEM-EDS calculated elemental ratios of $\text{Cu}_{12}(\text{As}_{1-x}\text{Sb}_x)_4\text{S}_{13}$ nanoparticles treated in an H_2S atmosphere at 450 °C for 1 h. The standard deviations are based on three measurements from random areas of the samples.	155
Table 7.6. Rietveld refinement-determined weight percent of resulting phases after $\text{Cu}_{12}(\text{As}_{1-x}\text{Sb}_x)_4\text{S}_{13}$ NPs were annealed in nitrogen for 1 h at 450 °C. Significant decomposition is observed in the purely Sb- and As-samples, while the mixed alloy compositions displayed significantly higher resistance to decomposition into crystalline secondary phases.	157
Table 7.7. SEM-EDS calculated elemental ratios of $\text{Cu}_{12}(\text{As}_{1-x}\text{Sb}_x)_4\text{S}_{13}$ nanoparticles heat treated in a nitrogen atmosphere at 450 °C for 1 h. The standard deviations are based on three measurements from random areas of the samples.	157
Table 7.8. Cu/(Sb+As) ratios for the various 450 °C heat treatments. SEM-EDS data is reproduced from Tables 7.1, 7.3, 7.5, and 7.7, and the XRD-calculated results are computed using weight fractions estimated by Rietveld refinement (Tables 7.4 and 7.6). GIXRD-calculated results were not determined for the starting NPs or sulfur due to the lack of binary phases appearing in the GIXRD spectra.....	161
Table 8.1. Detailed information for chemicals used in this chapter.	173
Table 9.1. Qualitative solubility results for Cu, As, and S precursors in amine-thiol mixtures (9:1 v:v amine:thiol). A green box indicates complete solubility at 0.1 M, a yellow box indicates either partial solubility or a color change in the solvent, a red box indicates no dissolution and no interaction with the solvent, and a black box indicates that the combination was not tested.	196

LIST OF FIGURES

- Figure 2.1. Crystal structures and compositions of three copper-arsenic-sulfur structures encountered in this chapter. 37
- Figure 2.2. a) TGA curve of dried LUZ NPs during a 10 °C/min ramp to 600 °C under a 100 mL/min He flow. b) EDX-measured As:Cu and S:Cu ratios as a function of temperature, acquired by heating samples to the indicated temperatures in a nitrogen-filled glovebox, holding for 15 min, and then removing from heat. Error bars correspond to 95% confidence intervals with standard deviations obtained from multiple measurements in different spots on the same sample. The initial EDX ratios for this particular set of NPs were 0.40 (As:Cu) and 1.43 (S:Cu). 41
- Figure 2.3. Raman spectra of luzonite NP films heated to the indicated temperature. A clear phase transition from luzonite to tennantite is noted between 315 °C and 370 °C. The nanoparticle and 315 °C spectra are noticeably shifted from the Cu_3AsS_4 LUZ reference (RRUFF ID R060390) due to antimony in the reference spectrum. ($\text{Cu}_{12}\text{As}_4\text{S}_{13}$ reference: RRUFF ID R050474). 42
- Figure 2.4. Ternary isothermal sections of the Cu-As-S system at 400 °C and 500 °C, adapted from Maske and Skinner. Diagrams copyright ASM International (2006) and reprinted with permission. 44
- Figure 2.5. SEM Images of LUZ NP films heated with As_2S_5 in a sealed ampoule at given temperatures and times: a) 500 °C for 10 min, b) 500 °C for 20 min, c) 500 °C for 1 h, d) 375 °C for 1 h, e) 425 °C for 1 h, and f) 500 °C for 1 h. 45
- Figure 2.6. a) XRD and b) Raman spectra of luzonite NP films treated in As_2S_5 at 375, 425, and 500 °C for 1 h. In the XRD spectra, the peak locations match well with those of an ENG reference mineral (JCPDS 01-082-1464) with overly dominant intensities attributed to oriented growth. The peak at 40° is indexed to the Mo substrate and the peak at 36.5° (*) is attributed to incomplete filtering of the k-beta radiation from the Mo peak. In the Raman spectra, the stretches also match well with an enargite reference (RRUFF ID: R050373) with an additional peak at 494 cm^{-1} , the origins of which are discussed later in this chapter. 45
- Figure 2.7. XRD and Raman of LUZ NPs treated at 425 °C for 1 h with added As_2S_5 . a) The XRD pattern agrees with ENG mineral reference (JCPDS 01-082-1464). The peak at 40° is from the Mo substrate, with the peak at 36.5° (*) a k-beta peak from the Mo. b) The Raman spectrum agrees with a reference ENG mineral (RRUFF ID R050373), with additional modes at 360, 494, and 560 cm^{-1} 47
- Figure 2.8. Raman spectra of ligand-exchanged luzonite Cu_3AsS_4 NPs. The NPs were treated first in As_2S_5 at 425 °C for 1 h, showing no trace of the peak at 494 cm^{-1} seen in materials with OLA-capped particles. Then, OLA was drop-cast on the surface of the treated film, which was treated in sulfur at 425 °C for 60 minutes, resulting in the Raman spectrum with peaks at 360, 494, and 560 cm^{-1} that may be attributed to the impurity phase; the peak around 380 cm^{-1} may be attributed to tennantite $\text{Cu}_{12}\text{As}_4\text{S}_{13}$ or also to the impurity phase. 48
- Figure 2.9. SEM images of LUZ NPs treated at 425 °C for 1 h in varying atmospheres: a) S, b) As, and c) As and S in a 2:5 molar ratio. 49

Figure 2.10. a) XRD and b) Raman spectra of LUZ NPs treated in separate sulfur and arsenic atmospheres. In the XRD spectrum, the sulfur-treated film matches well with a tetragonal luzonite reference (JCPDS 01-074-1125), with shifts due to antimony in the reference spectrum. The arsenic-treated film, however, matches with the cubic tennantite $\text{Cu}_{12}\text{As}_4\text{S}_{13}$ reference (JCPDS 42-560). In both, the peaks at 40° are indexed to the Mo substrate and the peaks at 36.5° (*) are attributed to incomplete filtering of the k-beta radiation from the Mo peaks..... 50

Figure 2.11. Side-view SEM image of LUZ NP film treated in a sealed ampoule with As_2S_5 powder for 1 h at 425°C . A thin fine-grain layer and some contrast in the molybdenum are noted. 51

Figure 2.12. J-V curve of the champion solar cell based on a Cu_3AsS_4 absorber layer. The inset table provides performance parameters of the device..... 51

Figure 2.13. a) External quantum efficiency (EQE) measurements of the device shown in Figure 2.12. When integrated, a J_{sc} of 3.4 mA/cm^2 is obtained, which agrees well with the value (3.3 mA/cm^2) obtained from J-V measurements. 2.2 mA/cm^2 of this current occurs at wavelengths greater than 510 nm (or below 2.43 eV , the approximate band gap of CdS) and is therefore attributed to carrier generation in the Cu_3AsS_4 absorber layer only. b) Extrapolation of band gap energy through a plot of $[\ln(1-\text{EQE})]^2$ vs photon energy. A band gap of 1.4 eV is obtained in agreement with a previous experimental result [14]..... 52

Figure 3.1. XRD spectra, Raman spectra, and plan-view SEM images of LUZ NP films heated in a sealed ampoule at 300 , 400 , and 500°C for 1 h. The peak at $40^\circ 2\theta$ is attributed to the Mo substrate. 59

Figure 3.2. XRD and Raman spectra of LUZ NP films annealed in sulfur flow environments at the given temperatures for 1 h. In the XRD spectra, the (*) signify peaks corresponding to covellite CuS , and the (*) in the 400°C Raman spectra signify signal from room light that was inadvertently included during the sample's measurement. 60

Figure 3.3. XRD spectra, Raman spectra, and plan view SEM images of LUZ NP films heated in a sealed glass ampoule with added sulfur flakes. The peak at $40^\circ 2\theta$ is attributed to the Mo substrate. 62

Figure 3.4. XRD spectra, Raman spectra, and plan-view SEM images of stacks of As_2S_3 on top of LUZ NPs heated for 30 min at 425°C in the indicated atmosphere. In the argon XRD spectrum, the (*) is attributed to the molybdenum substrate..... 64

Figure 3.5. XRD spectra, Raman spectra, and plan-view SEM images of stacks of As_2S_3 on LUZ NPs heated in sulfur for 30 min at the indicated temperature. In the XRD spectra, the (*) symbolizes a (210) shoulder of enargite Cu_3AsS_4 , and the (+) indicates the (222) peak of tennantite $\text{Cu}_{12}\text{As}_4\text{S}_{13}$ 65

Figure 3.6. XRD and Raman spectra, and plan view and cross-sectional SEM images of stacks of LUZ NPs on top of As_2S_3 annealed at 425°C for 30 min in the indicated atmosphere. The (*) in the argon XRD spectra is attributed to the Mo substrate. 67

Figure 3.7. Raman spectra and plan-view SEM images of LUZ NPs heated at 425°C for 30 min with reduced amounts of As_2S_5 added to the ampoule. 69

- Figure 3.8. XRD spectrum, Raman spectra, and plan view SEM image of a LUZ NP film that was annealed at 325 °C for 30 min while face down in As₂S₅ powder. 70
- Figure 3.9. SEM images (plan-view and cross-sectional) and J-V curves of double-treated enargite-based devices. 71
- Figure 3.10. J-V and EQE analysis of the champion NP-based ENG device achieved in this thesis. The left panel shows a MgF₂-coated device with $J_{sc} = 5.1 \text{ mA/cm}^2$, $V_{oc} = 0.23 \text{ V}$, $FF = 29.8\%$, and efficiency = 0.35%. The middle panel gives the EQE as a function of wavelength and the current densities above and below the bandgap of CdS, and the right panel shows the extraction of the band gap from EQE data. 72
- Figure 3.11. Raman spectra of LUZ NP films that were (left panel) pretreated in argon or H₂S at the given time and temperature and then (right panel) annealed in an ampoule with As₂S₅ for 1 h at 425 °C. 73
- Figure 3.12. Plan view SEM images of one film that was pre-annealed in argon at 250 °C for 1 h, and five films that were pre-annealed at the given conditions and then heat treated in As₂S₅ at 425 °C for 1 h. 74
- Figure 3.13. Relative intensity of three XRD peaks in BB mode acquired from five different substrates: a standard Mo-soda lime glass substrate, a Mo-SLG substrate with a thinner absorber layer, a Mo-SLG substrate with NaF added to the surface, a quartz substrate, and a Mo-coated borosilicate glass substrate. 75
- Figure 3.14. XRD and Raman spectra of LUZ NPs on FTO heated in As₂S₅ at 425 °C for 1 h. In the XRD spectra, the (*) stand symbolize tetragonal Cu₂SnS₃ (ICSD collection code 29-570), with an additional peak at 31° 2θ tentatively attributed to covellite CuS. The Raman spectrum matches with a previous report [13]. 76
- Figure 4.1. XPS narrow-scan spectra for a luzonite nanoparticle film treated in As₂S₅ for 1 h at 425 °C. 82
- Figure 4.2. Winxray-simulated trajectory of electrons at a 5 kV accelerating voltage into a thick film of Cu₃AsS₄. 83
- Figure 4.3. Plan view SEM images of an ENG thin film before and after etching in ammonium sulfide. 85
- Figure 4.4. Thermogravimetric analysis (TGA) of an ENG film ramped to 600 °C at 10 °C/min in a 100 mL/min helium flow. 86
- Figure 4.5. XRD and Raman spectra of ENG films that were annealed in argon at the indicated temperatures and times. SEM plan-view images of the film that was annealed at 500 °C for 1 h. 87
- Figure 4.6. XRD and Raman spectra of ENG films that were annealed in sulfur and H₂S atmospheres at 425 °C. 88
- Figure 4.7. Raman spectra and plan-view SEM images of ENG films that were pressed (one with heat applied) at 1000 psi for 10 min. 89

Figure 4.8. Raman spectra of an ENG thin film subjected to electrochemical etching in 0.1 M HCl.	90
Figure 5.1. FTIR spectra on LUZ NPs exchanged with a variety of ligands.....	100
Figure 5.2. FTIR spectra of OLA-capped LUZ NPs exchanged with $(\text{NH}_4)_3\text{AsS}_3$ in various solvent combinations.	102
Figure 5.3. NMR spectra in deuterated chloroform of LUZ NPs after successive washes in chloroform-ethanol mixtures. The regions for OLA and EtOH are magnified for clarity.	103
Figure 5.4. FTIR spectra of copper(I) sulfide NPs ligand exchanged with $(\text{NH}_4)_3\text{AsS}_3$ and Na_3AsS_3 ligands.	105
Figure 5.5. (a) GIXRD spectrum, (b) Raman spectrum, (c) Plan-view SEM image, and (d) cross-sectional SEM image of a ligand exchanged LUZ NP film heat treated in a sealed ampoule with As_2S_5 powder for 30 min at 425 °C.	106
Figure 5.6. (a) GIXRD spectrum, (b) Raman spectrum, and (c) plan-view SEM image of ligand exchanged LUZ NPs heat treated in an ampoule with no added powders at 350 °C for 1 h.....	107
Figure 5.7. GIXRD spectra, Raman spectra, and plan-view SEM images of ligand exchanged Cu_2S NPs heat treated in various atmospheres at 400 °C for 30 min. In the GIXRD spectra, a * indicates a peak attributable to copper sulfide Cu_{2-x}S	108
Figure 6.1. Room-temperature photoluminescence spectra of ENG thin films using a 633 nm laser excitation. Solid lines indicate raw data, while dashed lines indicate the best fit Voigt curves.	116
Figure 6.2. (a) Cryogenic (4.25 K) photoluminescence spectra of an ENG thin film at various laser powers. [© 2019, IEEE] (b) Estimated peak position from Voigt-fit peaks as a function of incident laser power.	117
Figure 6.3. Change in electric field from TRTS measurements as a function of delay time (excitation wavelength is 740 nm). Solid lines are the global fits of the diffusion-recombination model assuming third-order recombination kinetics with $\alpha = 3 \cdot 10^4 \text{ cm}^{-1}$, $D = 0 \text{ cm}^2/\text{s}$, and $k_{\text{Aug}} = 3.4 \cdot 10^{-27} \text{ cm}^6/\text{s}$. [© 2019, IEEE].....	120
Figure 6.4. Change in electric field from TRTS reflection mode measurements. All spectra were taken with an 800 nm excitation source. (a) ENG response on quartz for both reflection and transmission mode. (b) ENG response for a soda-lime glass (no Mo) substrate at a variety of fluences. (c) – (e) ENG response on Mo-coated soda-lime glass substrate at the indicated fluence.	122
Figure 6.5. Change in electric field from TRTS reflection mode measurements on the indicated substrates and laser fluences at 400 and 800 nm.	123
Figure 6.6. Change in electric field from short-time TRTS measurements on ENG films fabricated on quartz and Mo-SLG. Pump wavelength is 800 nm.....	124
Figure 6.7. TRPL response of an ENG film on quartz at 447 nm excitation wavelength. The curve is well fit by a biexponential decay with $\tau_1 = 0.42 \text{ ns}$ and $\tau_2 = 2.08 \text{ ns}$, with relative weights for each curve as 24% and 76%, respectively.	126

- Figure 6.8. TRPL for ENG films fabricated on Mo-SLG substrates, time-shifted such that the initial carrier densities match. 127
- Figure 6.9. TRPL response from an ENG sample fabricated on Mo-SLG at 447 and 600 nm excitation wavelengths..... 128
- Figure 6.10. Cyclic voltammetry of an ENG thin film in 0.1 M tetrabutylammonium hexafluorophosphate in acetonitrile. The inset shows the CV response of a ferrocene internal standard. [© 2019, IEEE]..... 130
- Figure 6.11. (a) ADEPT-simulated band diagram for the ENG-CdS interface. (b) SCAPS-simulated J-V curve for an ENG-CdS solar cell assuming 100 ns lifetime and no interfacial recombination. [© 2019, IEEE] 131
- Figure 6.12. Admittance spectroscopy measurements at zero bias on ENG-based solar cells with a CdS buffer layer..... 133
- Figure 6.13. Simulations of ENG-ZnS solar cell. (a) ADEPT-simulated band diagram for the ZnS-ENG interface, assuming a ZnS conduction band minimum of -3.5 eV. [© 2019, IEEE] (b) SCAPS-simulated J-V curve assuming no interfacial recombination and 100 ns ENG lifetime. [© 2019, IEEE] (c) SCAPS-simulated efficiencies as a function of ZnS electron affinity and carrier lifetime (0.01 ns to 100 ns). 134
- Figure 7.1. Grazing incidence X-ray diffraction (GIXRD) and Raman spectra of as-synthesized (A) $\text{Cu}_{12}\text{Sb}_4\text{S}_{13}$, (B) $\text{Cu}_{12}(\text{As}_{0.25}\text{Sb}_{0.75})_4\text{S}_{13}$, (C) $\text{Cu}_{12}(\text{As}_{0.50}\text{Sb}_{0.50})_4\text{S}_{13}$, (D) $\text{Cu}_{12}(\text{As}_{0.75}\text{Sb}_{0.25})_4\text{S}_{13}$, and (E) $\text{Cu}_{12}\text{As}_4\text{S}_{13}$ NPs. No secondary peaks were detected, suggesting the formation of impurity-free NPs..... 146
- Figure 7.2. Calculated lattice parameter for as-synthesized TET-TEN NPs using Rietveld refinement. A linear shift in lattice parameter is observed with increasing Sb content, consistent with Vegard's law for alloy materials..... 146
- Figure 7.3. SEM micrographs of (A) $\text{Cu}_{12}\text{Sb}_4\text{S}_{13}$, (B) $\text{Cu}_{12}(\text{As}_{0.25}\text{Sb}_{0.75})_4\text{S}_{13}$ (C) $\text{Cu}_{12}(\text{As}_{0.50}\text{Sb}_{0.50})_4\text{S}_{13}$, (D) $\text{Cu}_{12}(\text{As}_{0.75}\text{Sb}_{0.25})_4\text{S}_{13}$, and (E) $\text{Cu}_{12}\text{As}_4\text{S}_{13}$ nanoparticles. Scale bars are 300 nm. 147
- Figure 7.4. GIXRD and Raman spectra of nanoparticles treated in a sulfur atmosphere at 450 °C for 1h. (A) $\text{Cu}_{12}\text{Sb}_4\text{S}_{13}$, (B) $\text{Cu}_{12}(\text{As}_{0.25}\text{Sb}_{0.75})_4\text{S}_{13}$, (C) $\text{Cu}_{12}(\text{As}_{0.50}\text{Sb}_{0.50})_4\text{S}_{13}$, (D) $\text{Cu}_{12}(\text{As}_{0.75}\text{Sb}_{0.25})_4\text{S}_{13}$, and (E) $\text{Cu}_{12}\text{As}_4\text{S}_{13}$. Peaks marked with a * correspond to the (210) plane in orthorhombic enargite Cu_3AsS_4 (JCPDS 01-082-1464)..... 149
- Figure 7.5. GIXRD and Raman spectra of nanoparticles treated in a sulfur atmosphere at 350 °C for 1 h. (A) $\text{Cu}_{12}\text{Sb}_4\text{S}_{13}$, (B) $\text{Cu}_{12}(\text{As}_{0.25}\text{Sb}_{0.75})_4\text{S}_{13}$, (C) $\text{Cu}_{12}(\text{As}_{0.50}\text{Sb}_{0.50})_4\text{S}_{13}$, (D) $\text{Cu}_{12}(\text{As}_{0.75}\text{Sb}_{0.25})_4\text{S}_{13}$, and (E) $\text{Cu}_{12}\text{As}_4\text{S}_{13}$. Peaks marked with a * correspond to the (210) plane in enargite Cu_3AsS_4 (JCPDS 01-082-1464). In the GIXRD and Raman spectra, slight deviations of the purely arsenic endmember from the reference spectra are attributed to Sb impurities in the reference spectra themselves. The Raman peaks near 490 cm^{-1} are likely due to surface condensed elemental sulfur [49]–[51]. 151

Figure 7.6. GIXRD and Raman spectra of nanoparticles treated in an H₂S atmosphere at 450 °C for 1 h. (A) Cu₁₂Sb₄S₁₃, (B) Cu₁₂(As_{0.25}Sb_{0.75})₄S₁₃, (C) Cu₁₂(As_{0.50}Sb_{0.50})₄S₁₃, (D) Cu₁₂(As_{0.75}Sb_{0.25})₄S₁₃, and (E) Cu₁₂As₄S₁₃. The peak marked with (*) in GIXRD spectrum A is attributable to the (222) stretch of tetrahedrite Cu₁₂Sb₄S₁₃ (JCPDS #42-560), and the peaks marked with (+) in spectrum E are attributable to digenite Cu_{1.8}S (JCPDS 01-088-2045). 153

Figure 7.7. GIXRD and Raman spectra of nanoparticles treated in H₂S at 350 °C for 1 h. (A) Cu₁₂Sb₄S₁₃, (B) Cu₁₂(As_{0.25}Sb_{0.75})₄S₁₃, (C) Cu₁₂(As_{0.50}Sb_{0.50})₄S₁₃, (D) Cu₁₂(As_{0.75}Sb_{0.25})₄S₁₃, and (E) Cu₁₂As₄S₁₃. In the Raman spectrum, deviations of the antimony endmember from the reference spectrum are attributed to Zn impurities in the reference spectrum itself. 153

Figure 7.8. GIXRD and Raman spectra of Cu₁₂As₄S₁₃ nanoparticles treated in an H₂S atmosphere for 1 h at 350 °C with H₂S flow maintained during the cool down procedure. The Cu₁₂As₄S₁₃ phase is maintained both here and in the case where H₂S flow is stopped during the cool down procedure (Figure 7.6, spectrum E). This result eliminates the possibility of a phase change during the cool down procedure, further confirming that H₂S promotes the formation of the cubic Cu₁₂As₄S₁₃ phase. 154

Figure 7.9. Raman spectra of two different spots on the Cu₁₂Sb₄S₁₃ NP film treated in H₂S for 1 h at 450 °C. Peaks corresponding to tetrahedrite Cu₁₂Sb₄S₁₃, chalcostibite CuSbS₂, and skinnerite Cu₃SbS₃ (denoted with *) are observed, suggesting an inhomogeneous film after heat treatment. 155

Figure 7.10. GIXRD and Raman spectra of nanoparticles treated in a nitrogen atmosphere at 450 °C for 1 h. (A) Cu₁₂Sb₄S₁₃, (B) Cu₁₂(As_{0.25}Sb_{0.75})₄S₁₃, (C) Cu₁₂(As_{0.50}Sb_{0.50})₄S₁₃, (D) Cu₁₂(As_{0.75}Sb_{0.25})₄S₁₃, and (E) Cu₁₂As₄S₁₃. The (+) in GIXRD spectrum (A) denotes a skinnerite Cu₃SbS₃ (JCPDS 01-083-0563) impurity phase, and the (*) in GIXRD spectrum (E) denotes a digenite Cu_{1.8}S impurity phase (JCPDS-01-088-2045). 156

Figure 7.11. GIXRD and Raman spectra of nanoparticles treated in a nitrogen atmosphere at 350 °C for 1 h. (A) Cu₁₂Sb₄S₁₃, (B) Cu₁₂(As_{0.25}Sb_{0.75})₄S₁₃, (C) Cu₁₂(As_{0.50}Sb_{0.50})₄S₁₃, (D) Cu₁₂(As_{0.75}Sb_{0.25})₄S₁₃, and (E) Cu₁₂As₄S₁₃. In the Raman spectrum, slight deviations of the purely antimony endmember from the reference spectrum are attributed to Zn impurities in the reference spectrum itself. 157

Figure 7.12. SEM micrographs of (A) Cu₁₂Sb₄S₁₃, (B) Cu₁₂(As_{0.25}Sb_{0.75})₄S₁₃ (C) Cu₁₂(As_{0.50}Sb_{0.50})₄S₁₃, (D) Cu₁₂(As_{0.75}Sb_{0.25})₄S₁₃, and (E) Cu₁₂As₄S₁₃ nanoparticles heat treated in a flowing 1% H₂S (balance argon) atmosphere at 450 °C for 1 h. Scale bars are 5 μm. 158

Figure 7.13. SEM micrographs of (A) Cu₁₂Sb₄S₁₃, (B) Cu₁₂(As_{0.25}Sb_{0.75})₄S₁₃ (C) Cu₁₂(As_{0.50}Sb_{0.50})₄S₁₃, (D) Cu₁₂(As_{0.75}Sb_{0.25})₄S₁₃, and (E) Cu₁₂As₄S₁₃ nanoparticles heat treated in a flowing nitrogen atmosphere at 450 °C for 1 h. Scale bars are 5 μm. 159

Figure 7.14. SEM micrographs of (A) Cu₁₂Sb₄S₁₃, (B) Cu₁₂(As_{0.25}Sb_{0.75})₄S₁₃ (C) Cu₁₂(As_{0.50}Sb_{0.50})₄S₁₃, (D) Cu₁₂(As_{0.75}Sb_{0.25})₄S₁₃, and (E) Cu₁₂As₄S₁₃ nanoparticles heat treated in a flowing sulfur/argon atmosphere at 450 °C for 1 h. Scale bars are 5 μm. 159

Figure 7.15. Calculated lattice parameters of $\text{Cu}_{12}(\text{As}_{1-x}\text{Sb}_x)_4\text{S}_{13}$ NP films after heat treatment at 450 °C for 1 h in the indicated atmospheres. A nearly linear trend is observed as expected from Vegard's law, implying that the crystalline portion of the material retained its original Sb/(Sb+As) ratio. 162

Figure 7.16. GIXRD and Raman spectra of nanoparticles treated in an elemental sulfur atmosphere at 450 °C for 1 h. (A) Cu_3SbS_4 , (B) $\text{Cu}_3\text{As}_{0.25}\text{Sb}_{0.75}\text{S}_4$, (C) $\text{Cu}_3\text{As}_{0.50}\text{Sb}_{0.50}\text{S}_4$, (D) $\text{Cu}_3\text{As}_{0.75}\text{Sb}_{0.25}\text{S}_4$, and (E) Cu_3AsS_4 . Peaks marked with a * correspond to orthorhombic enargite Cu_3AsS_4 (JCPDS 01-082-1464). In the GIXRD and Raman spectra, slight deviations of the purely arsenic endmember from the reference spectra are attributed to Sb impurities in the reference spectra themselves. The Raman peaks around 490 cm^{-1} are attributed to excess sulfur on the surface. [49]–[51]..... 163

Figure 7.17. GIXRD and Raman spectra of nanoparticles treated in an H_2S atmosphere at 450 °C for 1 h. (A) Cu_3SbS_4 , (B) $\text{Cu}_3\text{As}_{0.25}\text{Sb}_{0.75}\text{S}_4$, (C) $\text{Cu}_3\text{As}_{0.50}\text{Sb}_{0.50}\text{S}_4$, (D) $\text{Cu}_3\text{As}_{0.75}\text{Sb}_{0.25}\text{S}_4$, and (E) Cu_3AsS_4 . In the GIXRD spectra, the peak marked with (*) in A is attributable to the (222) stretch of tetrahedrite $\text{Cu}_{12}\text{Sb}_4\text{S}_{13}$ (JCPDS #42-560), and the peaks marked with (+) in spectra C-E are attributable to digenite $\text{Cu}_{1.8}\text{S}$ (JCPDS 01-088-2045). In the Raman spectra, slight deviations of the purely antimony endmember from the reference spectrum are attributed to Zn impurities in the reference spectrum itself. Severe reductions in the $\text{Cu}_{12}\text{As}_4\text{S}_{13}$ ν_1 stretch relative to the $\text{Cu}_{12}\text{Sb}_4\text{S}_{13}$ ν_1 stretch imply more significant decomposition in the arsenic-rich compositions relative to the antimony-rich compositions. Cu_3SbS_3 was not detected by Raman in these films; the reader is referred elsewhere for a reference spectrum [54]. 164

Figure 7.18. GIXRD and Raman spectra of nanoparticles treated in a nitrogen atmosphere at 450 °C for 1 h. (A) Cu_3SbS_4 , (B) $\text{Cu}_3\text{As}_{0.25}\text{Sb}_{0.75}\text{S}_4$, (C) $\text{Cu}_3\text{As}_{0.50}\text{Sb}_{0.50}\text{S}_4$, (D) $\text{Cu}_3\text{As}_{0.75}\text{Sb}_{0.25}\text{S}_4$, and (E) Cu_3AsS_4 . In GIXRD spectra D and E, the (*) correspond to a digenite $\text{Cu}_{1.8}\text{S}$ impurity phase (JCPDS 01-088-2045). In the Raman spectrum, slight deviations of the purely antimony endmember from the reference spectrum are attributed to Zn impurities in the reference spectrum itself. Additionally, severe reductions in the $\text{Cu}_{12}\text{As}_4\text{S}_{13}$ ν_1 stretch relative to the $\text{Cu}_{12}\text{Sb}_4\text{S}_{13}$ ν_1 stretch imply more significant decomposition in the arsenic-rich compositions relative to the antimony-rich compositions..... 164

Figure 8.1. (a) GIXRD spectrum of a luzonite Cu_3AsS_4 NP film that was treated in an As_2S_2 atmosphere at 400 °C for 10 min. The pattern agrees with a reference standard for sinnerite $\text{Cu}_6\text{As}_4\text{S}_9$ (ICSD collection code 236895) and is free of detectable impurity phases [27]. The peak marked with (*) is attributed to the Mo substrate. (b) The same GIXRD spectrum with an enlarged reference showing spectrum, showing that other visible minor peaks (e.g. 20.8°) exist but are obscured by the sphalerite subcell reflections. 177

Figure 8.2. Raman spectrum of a LUZ NP film heat treated in an ampoule with As_2S_2 for 10 min at 400 °C. As discussed in the main text, there is not a reference spectrum available for sinnerite $\text{Cu}_6\text{As}_4\text{S}_9$, but the obtained spectrum is significantly different than that of a mineral for Cu_3AsS_4 (RRUFF ID R060390), ruling out the possibility of luzonite formation. 179

- Figure 8.3. GIXRD and Raman spectra of 300 nm evaporated Cu films treated in As_2S_2 at 400 °C for 10 min or As_2S_5 at 425 °C for 30 min. The GIXRD spectrum for the As_2S_2 treatment matches well with a reference $\text{Cu}_6\text{As}_4\text{S}_9$ spectrum (ICSD collection code 236895), and the Raman spectrum matches closely with that obtained in Figure 8.2. The GIXRD and Raman spectra for the As_2S_5 treatment match well with enargite Cu_3AsS_4 references (JCPDS 01-082-1464 and RRUFF ID R050373, respectively). 180
- Figure 8.4. Plan-view SEM images of LUZ NPs heat treated in As_2S_2 at the indicated temperature for 30 min. The 350 °C and 400 °C treatments resulted in micron-sized grains with relatively high packing density, whereas the 450 °C and 500 °C treatments gave isolated groups of grains with significant portions of the substrate exposed. 181
- Figure 8.5. GIXRD and Raman spectra of LUZ NPs heat treated in As_2S_2 at the indicated temperature for 30 min. GIXRD spectra match with reference spectrum #236895 on the ICSD, and the Raman spectra match well with the spectrum depicted in Figure 8.2. In the 500 °C GIXRD spectrum, the peak marked with an asterisk (*) matches with the (222) plane of tennantite $\text{Cu}_{12}\text{As}_4\text{S}_{13}$ (reference spectrum JCPDS #01-073-3934). The Cu/As ratios (as determined by XRF) were 1.17, 1.19, 1.22, and 1.09 for the un-etched 350 °C, 400 °C, 450 °C, and 500 °C treatments, respectively. 181
- Figure 8.6. Plan-view SEM images of LUZ NP films heated with As_2S_2 at 400 °C for 5, 10, 15, 30, and 60 min..... 182
- Figure 8.7. GIXRD and Raman spectra of LUZ NPs heat treated in As_2S_2 at 400 °C for the indicated time. GIXRD spectra match with reference spectrum #236895 on the ICSD, and the Raman spectra match well with the spectrum depicted in Figure 8.2. The Cu/As ratios (as measured by XRF) were 1.33, 1.30, 1.29, 1.22, and 1.21 for the 5, 10, 15, 30, and 60 min treatments, respectively. 182
- Figure 8.8. Cross-sectional SEM image of LUZ NPs heat treated in As_2S_2 for 10 min at 400 °C. The film demonstrates a bilayer morphology, with micron-thick grains on top of a thinner “fine-grain” layer..... 183
- Figure 8.9. GIXRD spectrum, Raman spectrum, and plan-view SEM image of a SIN film heat treated in a sulfur-containing ampoule at 425 °C for 1 h..... 183
- Figure 8.10. GIXRD spectrum, Raman spectrum, and plan-view SEM images of a LUZ NP film that was first heated in a sulfur-containing ampoule for 1 h at 425 °C, and then heated in an As_2S_2 -containing ampoule for 1 h at 425 °C. 185
- Figure 8.11. Fourier transform infrared spectroscopy (FTIR) spectra of as-synthesized LUZ NPs and ligand exchanged LUZ NPs. The removal of characteristic oleylamine C-H stretches demonstrates the effectiveness of the ligand exchange protocol. 185

Figure 8.12. Optoelectronic characterization of sinnerite $\text{Cu}_6\text{As}_4\text{S}_9$ thin films. A) Diffuse reflectance spectroscopy data and Tauc plot of the Kubelka-Munk function. Linear extrapolation gives a direct band gap of 1.16 eV. B) Cyclic voltammetry in 0.1 M tetrabutylammonium hexafluorophosphate in acetonitrile electrolyte. The current onset occurs at 0.39 V vs Ag^+/AgCl . C) Photoelectrochemical current generation in aqueous EuCl_3 electrolyte under chopped AM1.5G illumination. D) Time-resolved photoluminescence decay and biexponential fit to the measured data..... 186

Figure 8.13. Cyclic voltammetry (scan rate = 50 mV/s) on ferrocene dissolved in 0.1 M tetrabutylammonium hexafluorophosphate/acetonitrile solution. The onset current occurs at 0.33 V vs. Ag^+/AgCl 187

Figure 9.1. XRD and Raman spectra of a 0.1 M solution of CuCl , As_2S_5 , and S (2.6:1:6 Cu:As:S ratio) drop cast on a microscope glass slide and annealed for 3 h at 150 °C in air. 197

Figure 9.2. Raman spectrum of a 0.1 M solution of CuCl , As_2S_5 , and S (2.6:1:4 Cu:As:S ratio) drop cast on a microscope glass slide and annealed for 2 h at 150 °C in a nitrogen-filled glovebox. 198

Figure 9.3. XRD and Raman spectra of a 0.1 M solution of CuCl , As_2S_5 , and S (2.8:1:4 and 2.8:1:6 Cu:As:S ratios) drop cast on a microscope glass slide and annealed for 2 h at 150 °C in a nitrogen-filled glovebox. The (*) peak is attributed to incomplete filtering of tungsten $L\alpha$ radiation from the X-ray source..... 199

Figure 9.4. XRD and Raman spectra of Cu-As-S molecular precursor films baked in a glovebox at 75 °C and then annealed in an argon atmosphere for 1 h at the given temperature. A (*) indicates a peak attributable to copper sulfide Cu_{2-x}S 200

Figure 9.5. XRD and Raman spectra of Cu-As-S molecular precursor films baked in a glovebox at 75 °C and then annealed in an elemental sulfur/argon atmosphere for 1 h at the given temperature. In the XRD spectra, the (+) symbols are attributed to covellite CuS and the (*) to enargite Cu_3AsS_4 . In the Raman spectra, the (*) are attributed to covellite CuS or potential contamination from Cu-Sb-S films that were heat treated concurrently with the Cu-As-S films..... 201

Figure 9.6. XRD and Raman spectra of Cu-As-S molecular precursor films baked in a glovebox at 75 °C and then annealed in 1% H_2S (balance argon) at the given temperature for 1 h. The (+) peak signifies a Cu_2S phase, and the (*) represent incomplete filtering of the tungsten $L\alpha$ peak from the X-ray source..... 202

Figure 9.7. Plan-view SEM images of Cu-As-S molecular precursor films that were spin coated in a glovebox and then heated in a flowing S atmosphere at 400 °C or an As_2S_5 -filled ampoule at 425 °C for 1 h..... 203

Figure 9.8. XRD and Raman spectra of a spin coated Cu-As-S molecular precursor film that was baked in the glovebox at 75 °C and heat treated in a sealed ampoule with As_2S_5 for 1 h at 425 °C. The (*) peak is attributed to incomplete filtering of the copper $K\beta$ peak from the X-ray source. 204

Figure 10.1. XRD and Raman spectra of a 0.1 M solution of CuCl , SbCl_3 , and S (2.8:1:4 ratio) drop cast on a microscope slide and annealed for 3 h at 150 °C in air. 211

- Figure 10.2. XRD spectra of a 0.1 M solution of CuCl, SbCl₃, and S (1:1:3 ratio) drop cast on a microscope slide and annealed for 2 h at 175 °C in air. 212
- Figure 10.3. Time course of XRD and Raman spectra of 2.8:1:4 Cu:Sb:S films dropcast from a BA/ET mixture and annealed for 2 h at 175 °C..... 213
- Figure 10.4. XRD and Raman spectra of CuCl/SbCl₃/S precursor solutions (2.8:1 Cu:Sb ratio) annealed at 200 °C for 2 h in a nitrogen-filled glovebox..... 214
- Figure 10.5. XRD spectra of CuCl, SbCl₃, and S solutions (BA/ET solvent) drop cast individually (5 min apart) and annealed at 150 °C for 2 h after the final solution was cast. 215
- Figure 10.6. Thermogravimetric analysis (TGA) of a Cu-Sb-S molecular precursor film. The initial sample mass was 3.02 mg, and exotherms are indicated by downward spikes in the heat flow curve. 217
- Figure 10.7. XRD and Raman spectra of Cu-Sb-S molecular precursor films soft baked in a glovebox at 75 °C (2.8:1 CuCl:SbCl₃ ratio in 9:1 v:v BA:ET) and then annealed in a sulfur/argon atmosphere for 1 h at the given temperature..... 218
- Figure 10.8. XRD and Raman spectra of Cu-Sb-S molecular precursor films annealed in H₂S for 1 h at the given temperatures and initial sulfur contents. In the “300 °C no S” spectra, additional peaks correspond to digenite Cu_{1.8}S and chalcocite Cu₂S. In the “150 °C no S” and “450 °C S” films, the stretches in the 280-340 cm⁻¹ do not correspond to a known mineral in the RRUFF database; the peaks are instead attributed to skinnerite Cu₃SbS₃ as described in Chapter 7. 219
- Figure 10.9. Plan view SEM images of Cu-Sb-S molecular precursor films treated in sulfur or Sb₂S₃ for 1 h at 450 °C..... 220
- Figure 10.10. XRD and Raman spectra of a Cu-Sb-S molecular precursor film annealed in an ampoule containing Sb₂S₃ for 1 h at the given temperature. The XRD peaks at 40° 2θ correspond to the molybdenum substrate. 221

ABSTRACT

Author: McClary, Scott A. PhD

Institution: Purdue University

Degree Received: August 2019

Title: Synthesis and Characterization of Copper Arsenic Sulfide for Solution-Processed Photovoltaics

Committee Chair: Dr. Rakesh Agrawal

Global warming poses an existential threat to humanity and is inevitable unless significant efforts are made to eliminate its root causes. The need to replace fossil fuels with renewable sources has been obvious for many years, yet the world still receives the vast majority of its energy from non-renewable reservoirs. Harnessing solar radiation is the most promising route to ensure a carbon-free energy future, as the sun is the sole source of energy that can meet humankind's energy demands for generations to come.

The most widely recognized technology associated with the sun is a photovoltaic (PV) cell, which converts electromagnetic radiation directly into electricity that can either be used immediately or stored for later use. Silicon-based solar cells currently dominate (>90% market share) the global PV market, driven in part due to parallel research in the microelectronics industry. However, silicon is an indirect bandgap material, resulting in inflexible solar modules, and it requires high capital expenditures and high energy inputs for terawatt scale manufacturing.

The remainder of the commercial PV market consists of thin-film technologies based on Cu(In,Ga)Se_2 (CIGSe) and CdTe. These materials have a direct bandgap, so they can be used in flexible applications, and they are readily scalable due to their amenability to low-cost, roll-to-roll manufacturing. The power conversion efficiencies of CIGSe and CdTe cells have exceeded 20% and are nearing those of silicon cells, but concerns over the long-term supply of indium and tellurium cast doubt on whether these materials can be deployed at large scales. Alternative materials, such as $\text{Cu}_2\text{ZnSnS}_{4-x}\text{Se}_x$ (CZTSSe), have been researched for many years; the allure of a material with earth abundant elements and properties similar to CIGSe and CdTe was quite enticing. However, recent work suggests that CZTSSe is fundamentally limited by the formation of defects and band tails in the bulk material, and the efficiencies of CZTSSe-based devices have been saturated since 2013.

New materials for the PV market must meet several criteria, including constituent earth abundant elements, outstanding optoelectronic properties, and low propensity for defect formation. In this regard, the copper-arsenic-sulfur family of materials is an attractive candidate for PV applications. Cu, As, and S are all earth abundant elements with sufficiently different ionic radii, suggesting high defect formation energies. In addition, previous computational work has suggested that several ternary phases, most notably enargite Cu_3AsS_4 , have appropriate bandgaps, high absorption coefficients, and high predicted efficiencies in a thin-film PV device. The system must be investigated experimentally, with attention not only paid to synthesis and device performance, but also to characteristics that give clues as to whether high efficiencies are achievable.

This dissertation studies the Cu-As-S system in the context of thin-film photovoltaics, with an emphasis on Cu_3AsS_4 and detours to related materials discussed when appropriate. The first synthesis of Cu_3AsS_4 thin-films is reported using solution-processed nanoparticles as precursors. Initial device efficiencies reach 0.18%, which are further boosted to 0.35% through optimization of the annealing procedure. Several limitations to the initial approach are identified (most notably the presence of a carbonaceous secondary phase) and addressed through post-processing treatments and ligand exchange. Cu_3AsS_4 is also rigorously characterized using a suite of optoelectronic techniques which demonstrate favorable defect characteristics that motivate continued research. The current limitations to Cu_3AsS_4 performance stem from improper device architecture rather than material properties. Further development of Cu-As-S thin films must focus on identifying and fabricating ideal device architectures in parallel with continued improvements to film fabrication.

This dissertation ultimately demonstrates high promise for Cu_3AsS_4 as a thin-film PV material. It also may serve as an example for other researchers studying new materials, as the examination of fundamental optoelectronic properties early in the material's development phase is key to ensure that limited scientific resources are invested into the compounds with the highest potential impact on society

1. INTRODUCTION

1.1 A Need for Sustainable Energy

The world's energy demand is projected to increase by ~25% between now and 2040 [1]; such an increase will require the construction of significant amounts of energy generation capacity. Fossil fuels remain one of the most well-developed, readily accessible, and energy-dense sources to produce electrical and thermal energy, and they will likely comprise at least three-fourths of the world's energy consumption over the next 20 years. However, the harmful properties of fossil fuels greatly outweigh their convenience. The burning of fossil fuels releases greenhouse gases such as carbon dioxide to the upper atmosphere, where they become trapped and contribute to global warming processes that, if left unchecked, will cause irreversible damage to Earth's rich biodiversity and alter the course of humankind for eternity.

One encouraging sign is that nearly half of all new installed energy capacity between now and 2040 will be renewable [1]. Of the various renewable energy technologies, solar stands out as the one with the most potential impact. The solar energy resource is vast, with roughly 10^5 TW solar radiation incident on Earth's surface as compared to ~27 TW predicted consumption in 2040 [2], [3]. The sun is the only source of energy that can singlehandedly meet all of humankind's energy demands for the foreseeable future. However, the energy density of sunlight is dilute, so technologies must be developed to concentrate solar radiation into a useful form. Numerous technologies have been developed to harness the power of the sun; this thesis will focus on the photovoltaic (PV) cell.

1.2 A Brief Overview of Photovoltaic Cells

A photovoltaic cell converts electromagnetic radiation directly into electricity. The PV cell operates based on the photovoltaic effect – when photons with sufficiently high energy strike a semiconductor, electrons are excited from the valence band to the conduction band, creating a voltage from which useful electrical work can be extracted. Excited electrons will eventually relax back to the valence band; a PV cell uses a built-in electric field to extract the electron to an external circuit before it loses its voltage. The electric field is established by a p-n junction, in which a p-type (electron-poor or hole-rich) material is brought in contact with an n-type (electron-rich)

material. Electrons from the n-type material diffuse to the p-type material, leaving behind positively charged sites which establish an electric field. When light is shined on a semiconductor, the electric field sweeps charge carriers across the junction. A p-n junction is sandwiched between other layers that facilitate the extraction of charge carriers to an external circuit for immediate use or storage.

The majority of the PV market (>90%) is dominated by silicon solar cell technology. The first solar cell based on silicon was demonstrated in 1954 at Bell Labs, and continuous improvements to wafer synthesis and efficiency have been made, in part spurred by parallel technological developments in the transistor industry. The record efficiency for a lab-scale crystalline-silicon based solar cell is 26.7%, and commercial modules with efficiencies nearing 20% constitute the industry standard [4]. Silicon has high abundance in the earth's crust, so it has the potential for deployment at terawatt scales. However, silicon has several drawbacks. One is that it has an indirect bandgap, meaning that it requires relatively thick wafers to ensure complete absorption of light; this limits its flexibility and scope of application. Another is that it requires high-vacuum and high capital expenditures, making scalability a challenge. Progress has been made towards both issues, but alternatives must be considered.

The remainder of the PV market consists of thin-film technologies, including copper indium gallium diselenide (Cu(In,Ga)Se_2 , CIGSe) and cadmium telluride (CdTe). These materials have an advantage over silicon because they have direct bandgaps, meaning that they can be used in flexible thin film architectures. Solar Frontier (now a subsidiary of Showa Shell Sekiyu) recently announced a record CIGSe cell efficiency of 23.35% [5], and the record cell efficiency for CdTe is 21.0% by First Solar [4], with efficiency increases expected soon due to recent progress in increasing the carrier concentration. However, both materials consist of elements (indium and tellurium) whose abundance in the earth's crust is low, so there is significant market uncertainty and doubt on whether these materials can ever be deployed at the terawatt scale [6], [7].

Researchers have studied several alternative materials consisting of earth abundant elements for use in thin-film solar cells, the most prominent of these being copper zinc tin sulfoselenide ($\text{Cu}_2\text{ZnSn}(\text{Se}_x\text{S}_{1-x})_4$, CZTSSe), a derivative of CIGSe in which the indium and gallium atoms are replaced by zinc and tin. CZTSSe was first recognized as a photovoltaic material in 1988 [8], and over the next 25 years, significant research into CZTSSe was conducted using vacuum- and solution-based processes [9]–[13]. The record CZTSSe-based solar cell was

fabricated by IBM in 2013, with a 12.6% efficiency achieved using a hydrazine-based deposition procedure [14]. However, the record efficiency has saturated since then, primarily due to open-circuit voltages far below the Shockley-Queisser limit [15]. There are several possible causes of this deficit, including a low antisite defect formation energy due to similar crystal radii of Cu and Zn and potential fluctuations due to local compositional variations [16]–[19]. These properties were not studied early in the development phase of CZTSSe, and the full implications are just coming to light after ~30 years of research. Alternatives to CZTSSe may be required for high-efficiency earth abundant thin film solar cells.

1.3 The Promise of the Copper-Arsenic-Sulfur System for Solar Cells

The number of candidates for semiconducting and photovoltaic applications is immense, so methods must be devised to select a manageable number of promising compounds for investigation. Among other criteria, the compounds should consist of earth abundant elements for eventual scale up to terawatt-level manufacturing, and these elements should have dissimilar ionic radii so that the formation of harmful antisite defects is avoided. Compounds meeting these criteria may then be subjected to rapid computational screening to estimate properties such as bandgap, stability, and absorption coefficient. This narrows the list of compounds significantly, but further screening must be conducted experimentally.

One promising and relatively unexplored system for photovoltaic applications is the copper-arsenic-sulfur (Cu-As-S) set of compounds. Copper, arsenic, and sulfur are all relatively earth abundant elements, their cation sizes are significantly dissimilar (91 pm for Cu^+ and 60 pm for As^{5+}), and many exist as stable minerals in nature. There are six ternary Cu-As-S phases, as detailed in Table 1.1 [20].

Table 1.1. Ternary phases in the Cu-As-S system.

Phase Name	Abbreviation	Ideal Formula	Crystal Structure
Luzonite	LUZ	Cu_3AsS_4	Tetragonal
Enargite	ENG	Cu_3AsS_4	Orthorhombic
Tennantite	TEN	$\text{Cu}_{12}\text{As}_4\text{S}_{13}$	Cubic
Sinnerite	SIN	$\text{Cu}_6\text{As}_4\text{S}_9$	Triclinic
Lautite	n/a	CuAsS	Orthorhombic
“Compound A”	n/a	$\text{Cu}_{24}\text{As}_{12}\text{S}_{31}$	unknown

Of the six compounds, four may be relevant for PV applications: LUZ, ENG, TEN, and SIN. Several works have used density functional theory (DFT) to determine electronic properties of Cu-As-S materials. Yu et al. proposed a metric to evaluate novel PV absorbers known as spectroscopic limited maximum efficiency (SLME); it identified ENG and SIN as materials capable of achieving high efficiencies in thin films [21], [22]. Wallace et al. calculated the band structure, carrier effective masses, and the dielectric constant for ENG and suggested that it possesses ferroelectric properties that may be exploited in very thin absorber layers [23]; they later used computational routines to suggest appropriate n-type layers to pair with ENG [24]. Shi et al. calculated the band structures for LUZ and ENG, suggesting that they have proper bandgaps and stability for PV applications [25].

While there is an extensive body of work on the properties of naturally occurring Cu-As-S minerals, the number of experimental studies related to the optoelectronic properties of the Cu-As-S system is limited. Pauporte and Lincot measured the semiconducting properties of a naturally occurring ENG mineral, showing a p-type material with carrier concentrations nearing 10^{17} cm^{-3} and a mobility of $9 \text{ cm}^2/\text{Vs}$ [26]. Our research group synthesized nanoparticles (NPs) of LUZ and TEN, demonstrating stable photocurrent generation in an electrochemical solution and bandgaps of 1.25 eV and 1.75 eV, respectively [27], [28]. Das et al. synthesized ENG NPs using arsenic silylamide as a precursor [29]. However, there has not yet been a report related to crystalline thin films of Cu-As-S phases or their application in solar cells.

1.4 Objectives and Structure of This Thesis

In light of the need to synthesize and evaluate novel semiconductors for photovoltaic and other semiconducting applications, this thesis focuses on solution-based routes to films of enargite copper arsenic sulfide (Cu_3AsS_4) and closely related materials where appropriate. The following objectives were used to guide the work presented here:

- Develop solution-based methods to fabricate continuous films of copper arsenic sulfides suitable for application in thin-film photovoltaic devices.
- Characterize the thin films and solar cells fabricated from copper arsenic sulfides and use the results to make systematic modifications to improve the overall system performance.
- Evaluate the technical feasibility of the Cu-As-S system for high-performance semiconducting applications.

This thesis consists of eleven chapters and six appendices. Of these, Chapters 2 and 7 have already been published as journal articles, and Chapters 5, 6, and 8 will be published soon. A brief synopsis of each chapter is presented below.

Chapter 2 details the synthesis of enargite Cu_3AsS_4 thin films using luzonite Cu_3AsS_4 nanoparticles as precursors. A scheme that exploits liquid-assisted grain growth is used to grow thin films with micron-sized dense grains. These films are applied as the absorber layer in the first Cu-As-S-based thin-film solar cells; preliminary device efficiencies of 0.18% are obtained. Several issues related to device performance, particularly a secondary phase from the reaction of carbonaceous ligands with sulfur, are identified; they are addressed later in this work.

Chapter 3 describes the optimization of the heat treatment procedure used to make ENG thin films, with a focus on tailoring the grain growth and reducing the presence and impacts of the secondary phase. The annealing times, temperatures, and atmospheres are adjusted, and the effects of growing thin films directly from a liquid phase are investigated. With several modifications to the original procedure, the record efficiency of ENG-based solar cells doubles to 0.35%.

Chapter 4 outlines several post-processing treatments for ENG thin films, including surface etching using diammonium sulfide $(\text{NH}_4)_2\text{S}$, low-temperature anneals in an inert environment, hot pressing, and electrochemical etching. The post-processing techniques are successful in removing an arsenic- and sulfur-rich species from the surface of the ENG thin film, but the secondary phase persists after the treatments used here.

Chapter 5 details a ligand exchange protocol aimed at eliminating carbonaceous ligands from the initial film altogether. A number of ligands are trialed, and the one ultimately selected for use is derived from arsenic(III) sulfide. The impacts of various processing parameters on the ligand exchange procedure and the surface chemistry of the LUZ NPs are explored. Preliminary thin films are formed from ligand exchanged LUZ NPs, though obtaining a uniform coating is an ongoing challenge. Heat treatments of ligand exchanged LUZ and copper(I) sulfide NPs are then conducted, demonstrating the ability to grow micron-sized grains for eventual application in solar cells and other electronic devices.

Chapter 6 presents the results of extensive optoelectronic characterization on thin films of enargite with the aim of determining its long-term viability in photovoltaic applications. A combination of photoluminescence and time-resolved terahertz spectroscopy is used to study the defect characteristics of ENG, and time-resolved photoluminescence spectroscopy is used to

provide more information about the carrier dynamics in enargite. The measured properties indicate that ENG's solar cell performance should be much higher than the current record of 0.35%. A combination of simulations and experimental measurements of the band edges show that ENG devices are currently severely restricted by device architecture, rather than film properties.

Chapter 7 describes a synthetic protocol for the tetrahedrite-tennantite $\text{Cu}_{12}\text{As}_{4-x}\text{Sb}_x\text{S}_{13}$ alloy NP system; these materials are closely related to LUZ and ENG and are formed during some heat treatments conducted throughout the course of this work. Anneals in nitrogen, sulfur, and hydrogen sulfide are conducted to determine the role of the oxidation state of the sulfur in controlling the final phase of the film. Additionally, elemental losses are noted and must be controlled in future work in the Cu-As-S and Cu-Sb-S systems.

Chapter 8 discusses the first synthesis and properties of crystalline sinnerite $\text{Cu}_6\text{As}_4\text{S}_9$ that make it attractive for photovoltaic applications. It is fabricated from LUZ NP precursors, but by adjusting the annealing atmosphere, the selectivity between SIN and ENG is controllable. SIN films display an appropriate band gap (~ 1.16 eV) and stable photocurrent generation, motivating further research into this understudied material system.

Chapters 9 and 10 discuss work performed early in my Ph.D. career related to the molecular precursor-based synthesis of Cu-As-S and Cu-Sb-S materials. The dissolution of various compounds in the amine-thiol solvent system is explored, and various film deposition and heat treatment conditions are studied to elucidate phase selectivity in the ternary systems. These experiments represent a potential route to carbon-free thin films with micron-sized dense grains without the need for NP synthesis and purification as an intermediate step.

Chapter 11 summarizes the major findings of this thesis and describes critical experiments and information needed to fabricate enargite-based thin-film solar cells for high-efficiency applications. The initial results presented in this work suggest that enargite is a material worthy of significant further research and development efforts, with the ultimate vision of terawatt scale deployment for a fossil-fuel-free future.

1.5 References

- [1] L. Capuano, “International Energy Outlook 2018 (IEO2018),” 2018.
- [2] R. Agrawal and D. S. Mallapragada, “Chemical engineering in a solar energy-driven sustainable future,” *AIChE J.*, vol. 56, no. 11, pp. 2762–2768, Nov. 2010.
- [3] C. A. Wolden *et al.*, “Photovoltaic manufacturing: Present status, future prospects, and research needs,” *J. Vac. Sci. Technol. A Vacuum, Surfaces, Film.*, vol. 29, no. 3, p. 030801, May 2011.
- [4] M. A. Green *et al.*, “Solar cell efficiency tables (Version 53),” *Prog. Photovoltaics Res. Appl.*, vol. 27, no. 1, pp. 3–12, 2019.
- [5] M. Nakamura, K. Yamaguchi, Y. Kimoto, Y. Yasaki, and T. Kato, “Cd-free Cu(In,Ga)(Se,S)₂ thin-film solar cell with a new world record efficacy of 23.35%,” *46th IEEE Photovoltaics Spec. Conf.*, pp. 2–4, 2019.
- [6] C. Wadia, a. P. Alivisatos, and D. M. Kammen, “Materials Availability Expands the Opportunity for Large-Scale Photovoltaics Deployment,” *Environ. Sci. Technol.*, vol. 43, no. 6, pp. 2072–2077, Mar. 2009.
- [7] C. Candelise, M. Winkler, and R. Gross, “Implications for CdTe and CIGS technologies production costs of indium and tellurium scarcity,” *Prog. Photovoltaics Res. Appl.*, vol. 20, no. 6, pp. 816–831, Sep. 2012.
- [8] K. Ito and T. Nakazawa, “Electrical and Optical Properties of Stannite-Type Quaternary Semiconductor Thin Films,” *Jpn. J. Appl. Phys.*, vol. 27, no. 11, pp. 2094–2097, Nov. 1988.
- [9] H. Katagiri *et al.*, “Development of CZTS-based thin film solar cells,” *Thin Solid Films*, vol. 517, no. 7, pp. 2455–2460, 2009.
- [10] Q. Guo, H. W. Hillhouse, and R. Agrawal, “Synthesis of Cu₂ZnSnS₄ Nanocrystal Ink and Its Use for Solar Cells,” *J. Am. Chem. Soc.*, vol. 131, no. 33, pp. 11672–11673, Aug. 2009.
- [11] C. Steinhagen, M. G. Panthani, V. Akhavan, B. Goodfellow, B. Koo, and B. A. Korgel, “Synthesis of Cu₂ZnSnS₄ Nanocrystals for Use in Low-Cost Photovoltaics,” *J. Am. Chem. Soc.*, vol. 131, no. 35, pp. 12554–12555, Sep. 2009.
- [12] S. K. Wallace, D. B. Mitzi, and A. Walsh, “The Steady Rise of Kesterite Solar Cells,” *ACS Energy Lett.*, vol. 2, no. 4, pp. 776–779, 2017.

- [13] S. Giraldo, Z. Jehl, M. Placidi, V. Izquierdo-Roca, A. Pérez-Rodríguez, and E. Saucedo, “Progress and Perspectives of Thin Film Kesterite Photovoltaic Technology: A Critical Review,” *Adv. Mater.*, vol. 31, no. 16, p. 1806692, Apr. 2019.
- [14] W. Wang *et al.*, “Device Characteristics of CZTSSe Thin-Film Solar Cells with 12.6% Efficiency,” *Adv. Energy Mater.*, vol. 4, no. 7, p. 1301465, May 2014.
- [15] W. Shockley and H. J. Queisser, “Detailed Balance Limit of Efficiency of p-n Junction Solar Cells,” *J. Appl. Phys.*, vol. 32, no. 3, pp. 510–519, Mar. 1961.
- [16] S. Chen, X. G. Gong, A. Walsh, and S.-H. Wei, “Crystal and electronic band structure of $\text{Cu}_2\text{ZnSnX}_4$ (X=S and Se) photovoltaic absorbers: First-principles insights,” *Appl. Phys. Lett.*, vol. 94, no. 4, p. 041903, Jan. 2009.
- [17] T. Gokmen, O. Gunawan, T. K. Todorov, and D. B. Mitzi, “Band tailing and efficiency limitation in kesterite solar cells,” *Appl. Phys. Lett.*, vol. 103, no. 10, p. 103506, Sep. 2013.
- [18] M. Kumar, A. Dubey, N. Adhikari, S. Venkatesan, and Q. Qiao, “Strategic review of secondary phases, defects and defect-complexes in kesterite CZTS–Se solar cells,” *Energy Environ. Sci.*, vol. 8, no. 11, pp. 3134–3159, 2015.
- [19] C. J. Hages, N. J. Carter, and R. Agrawal, “Generalized quantum efficiency analysis for non-ideal solar cells: Case of $\text{Cu}_2\text{ZnSnSe}_4$,” *J. Appl. Phys.*, vol. 119, no. 1, p. 014505, Jan. 2016.
- [20] S. Maske and B. J. Skinner, “Studies of the sulfosalts of copper I. Phases and phase relations in the system Cu-As-S,” *Econ. Geol.*, vol. 66, no. 6, pp. 901–918, Oct. 1971.
- [21] L. Yu and A. Zunger, “Identification of Potential Photovoltaic Absorbers Based on First-Principles Spectroscopic Screening of Materials,” *Phys. Rev. Lett.*, vol. 108, no. 6, p. 068701, Feb. 2012.
- [22] L. Yu, R. S. Kokenyesi, D. A. Keszler, and A. Zunger, “Inverse Design of High Absorption Thin-Film Photovoltaic Materials,” *Adv. Energy Mater.*, vol. 3, no. 1, pp. 43–48, Jan. 2013.
- [23] S. K. Wallace *et al.*, “Candidate photoferroic absorber materials for thin-film solar cells from naturally occurring minerals: enargite, stephanite, and bournonite,” *Sustain. Energy Fuels*, vol. 1, no. 6, pp. 1339–1350, 2017.
- [24] S. K. Wallace, K. T. Butler, Y. Hinuma, and A. Walsh, “Finding a junction partner for candidate solar cell absorbers enargite and bournonite from electronic band and lattice matching,” *J. Appl. Phys.*, vol. 125, no. 5, p. 055703, Feb. 2019.

- [25] T. Shi, W.-J. Yin, M. Al-Jassim, and Y. Yan, "Structural, electronic, and optical properties of $\text{Cu}_3\text{-V-VI}_4$ compound semiconductors," *Appl. Phys. Lett.*, vol. 103, no. 15, p. 152105, Oct. 2013.
- [26] T. Pauporté and D. Lincot, "Electrical, optical and photoelectrochemical properties of natural enargite, Cu_3AsS_4 ," *Adv. Mater. Opt. Electron.*, vol. 5, no. 6, pp. 289–298, Nov. 1995.
- [27] R. B. Balow, E. J. Sheets, M. M. Abu-Omar, and R. Agrawal, "Synthesis and Characterization of Copper Arsenic Sulfide Nanocrystals from Earth Abundant Elements for Solar Energy Conversion," *Chem. Mater.*, vol. 27, no. 7, pp. 2290–2293, Apr. 2015.
- [28] R. B. Balow, C. K. Miskin, M. M. Abu-Omar, and R. Agrawal, "Synthesis and Characterization of $\text{Cu}_3(\text{Sb}_{1-x}\text{As}_x)\text{S}_4$ Semiconducting Nanocrystal Alloys with Tunable Properties for Optoelectronic Device Applications," *Chem. Mater.*, vol. 29, no. 2, pp. 573–578, Jan. 2017.
- [29] A. Das, A. Shamirian, and P. T. Snee, "Arsenic Silylamide: An Effective Precursor for Arsenide Semiconductor Nanocrystal Synthesis," *Chem. Mater.*, vol. 28, no. 11, pp. 4058–4064, Jun. 2016.

2. SOLUTION-PROCESSED COPPER ARSENIC SULFIDE (Cu_3AsS_4) THIN FILMS FOR PHOTOVOLTAIC APPLICATIONS

A version of this chapter has been previously published as a journal article: Scott A. McClary, Joseph Andler, Carol A. Handwerker, and Rakesh Agrawal, “Solution-processed copper arsenic sulfide thin films for photovoltaic applications,” *Journal of Materials Chemistry C*, vol. 5, no. 28, pp. 6913-6916, 2017. It is reproduced here with permission from the Royal Society of Chemistry. The main journal article and supporting information have been merged, and the text and figures have been modified where appropriate.

2.1 Introduction

Thin-film solar cells represent a promising avenue to sustainably meet the world’s growing energy demand. Fabrication of such devices from colloidal nanoparticle (NP) inks or homogeneous molecular solutions is of great interest due to potential scalability to high-volume manufacturing levels and avoidance of costly vacuum-based processes. Efficient devices utilizing solution-processed CdTe [1], [2] and Cu(In,Ga)Se₂ [3]–[5] (CIGSe) absorber layers have been reported, but elemental scarcity (In, Te) may limit these materials’ ability to significantly penetrate future energy markets [6]. Earth abundant Cu₂ZnSn(S,Se)₄ (CZTSSe) has emerged as an alternative material [7], [8], but its ultimate performance in solar cells is limited primarily due to a V_{oc} deficit resulting from band tails in the material [9], [10].

In the continuous search for novel earth abundant materials to apply in photovoltaic devices, computational studies have predicted optimal absorption properties, ideal bandgaps, and high efficiencies for semiconducting copper-pnictogen-chalcogen (e.g. Cu₃PSe₄, CuSbS₂) compounds [11], [12]. Such material systems have multiple phases with different optoelectronic properties, allowing for device tailoring and optimization. There are at least six distinct ternary crystal structures in the copper-arsenic-sulfur system, three of which are depicted in Figure 2.1 [13]. The tetragonal luzonite phase (Cu₃AsS₄, LUZ) and the orthorhombic enargite phase (Cu₃AsS₄, ENG) both have direct bandgaps (1.2 eV – 1.4 eV) suitable for application in single junction solar cells [14]. Both LUZ [15] and ENG [16] have recently been synthesized as NPs, but to the best of our knowledge, complete solar cells have not been reported, likely due to complications in obtaining

dense films that prevent electrical shunting. Herein we describe a method in which LUZ NPs are converted to ENG thin films with micron-sized dense grains through a scheme exploiting specific phase relations within the Cu-As-S system. These films were also applied as the absorber layer in single junction solar cells; these devices are the first to utilize any combination of Cu, As, and S.

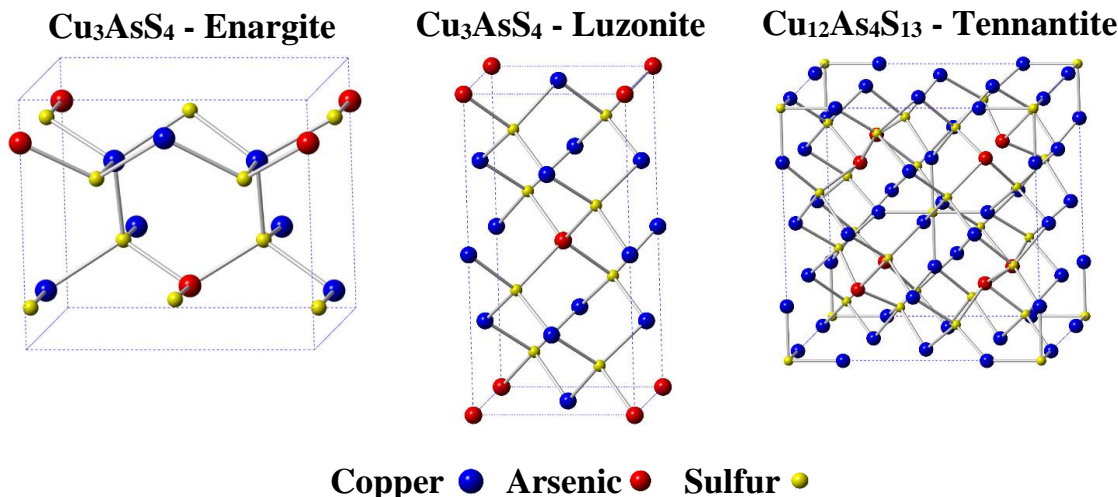


Figure 2.1. Crystal structures and compositions of three copper-arsenic-sulfur structures encountered in this chapter.

2.2 Experimental Methods

Caution: Arsenic compounds are highly toxic and must be handled with extreme caution and appropriate personal protective equipment after consulting the safety data sheets (SDSs) for each material. In particular, arsenic trichloride (AsCl₃) MUST always be handled under an inert environment. Specific data on the toxicity of Cu₃AsS₄ is not available, so it should also be handled with the utmost care.

2.2.1 Materials

All raw materials were used as received with standard air-free techniques unless otherwise noted. Sulfur flakes (S, 99.99%), arsenic (III) chloride (AsCl₃, 99.99%), arsenic (As, 99.997%), arsenic (III) sulfide (As₂S₃, 99.99%), oleylamine (OLA, >98% primary amine), 1-hexanethiol (HT, 95%), and ammonium sulfide ((NH₄)₂S, 40-48 wt% in water) were obtained from Sigma-Aldrich. OLA was degassed using three freeze-pump-thaw (FPT) cycles and stored under nitrogen prior to use in synthesis. Arsenic (V) sulfide (As₂S₅, >98%) was obtained from Santa Cruz Biotechnology. Copper (I) chloride (CuCl, 99.99%) was obtained from Strem. Ammonium hydroxide (NH₄OH,

28-30 wt% in water) was obtained from J.T. Baker. Hexanes (98.5%) were obtained from Fisher. Ethanol (200 proof) was obtained from Koptec. Acetone (99.5%) was obtained from EM Science.

2.2.2 Cu₃AsS₄ Nanoparticle Synthesis

Nanoparticles (NPs) were synthesized according to the recipe of Balow et al. scaled up 50% with a modified washing procedure [15]. Briefly, solutions of 1 M S in FPT OLA and 0.2 M CuCl/AsCl₃ in FPT OLA (2.8:1 Cu:As ratio, concentration refers to Cu only) were prepared by heating to 65 °C and stirring for 2 h under nitrogen before use. A three-neck flask consisting of 10.5 mL non-FPT OLA was refluxed at 120 °C for 1 h to remove dissolved gases and then heated to 175 °C. Then, 1.2 mL of S-OLA solution was injected, followed by 3.0 mL of CuCl/AsCl₃-OLA solution 20 s later. The reaction proceeded for 10 min and was then cooled via natural convection to room temperature. The mixture was then extracted into a centrifuge tube, topped with ethanol, and centrifuged at 14 krpm for 5 min. The supernatant was discarded, and two more washes were performed with a ~1:3 v:v mixture of hexane and ethanol. After washing, particles were dried under nitrogen flow and stored for later use. The as-synthesized NPs are slightly copper poor (2.6-3.0 Cu:As ratio) and sulfur rich (3.9-4.5 S:As ratio) and are expected to average between 7-8 nm in diameter in agreement with previous reports [15], [17].

2.2.3 Film Fabrication

NP films were cast by dispersing NPs in HT at 250 mg/mL and then doctor blading the resulting NP “ink” onto a 2” by 1” molybdenum-coated soda-lime glass (Mo-SLG) substrate. One coat of 15 µL ink was applied and dried at room temperature for five minutes. Then, another coat of 10 µL was applied followed by overnight drying before use.

2.2.4 Ampoule Preparation

NP samples (cut to ¼” by 1”) and powders (by experiment: As₂S₅ – 37 mg, S – 10.8 mg, As – 9.9 mg, S and As – 19.7 and 18.4 mg, respectively) were placed in a ChemGlass 10 mL borosilicate glass type 1 ampoule, which was then attached to a Schlenk line. The ampoule was evacuated and refilled with argon three times. It was then evacuated again to a pressure below 100 mtorr, and the neck was slowly rotated through a butane flame to collapse the glass walls and form a seal. *For safety reasons, the amounts of added powders were chosen such that the total pressure inside the ampoule would not exceed 0.8 atm, assuming that all solid vaporized into an ideal gas.*

2.2.5 Annealing Treatments and Device Fabrication

Sealed ampoules were heated individually in a horizontal tube furnace under 10 sccm argon flow. Each ampoule was pushed into the furnace after the temperature had reached the desired setpoint; once the treatment was completed, the furnace was opened and cooled by natural convection. Afterwards, ampoules were broken in the ambient atmosphere by scribing around the neck with a diamond-tip pen and snapping them forcefully. At this point, samples were either characterized or processed into full devices. Additional solar cell device layers were applied using chemical bath deposition of ~50 nm CdS, RF-sputtering of ~80 nm i-ZnO, RF-sputtering of ~220 nm ITO, and electron beam evaporation of patterned Ni/Al grids. The grids resulted in separate cells that had an area of 0.1 cm²; these cells were electrically isolated from each other by mechanical scribing.

2.2.6 Ligand Exchange

In order to investigate the effects of ligands on the formation of the 494 cm⁻¹ and other peaks in the Raman spectrum of treated NPs (as discussed later in this chapter), carbonaceous OLA ligands were replaced with an As₂S₃-based molecular metal chalcogenide complex using a ligand exchange procedure adapted from the method of Kovalenko et al [18]. To synthesize (NH₄)₃AsS₃, 246 mg (1 mmol) As₂S₃ was vigorously stirred with 0.43 mL (NH₄)₂S and 5 mL ultrapure water until complete dissolution occurred (~24 h). The mixture was then mechanically filtered using a 10 μm PTFE filter. To conduct the ligand exchange, a newly-synthesized batch of luzonite (LUZ) Cu₃AsS₄ NPs was diluted to 25 mg/mL in toluene. 1 mL of this toluene suspension was vortexed with 6 mL hexane in a centrifuge tube, along with a Teflon-coated stir bar. The mixture was taken into a nitrogen-filled glovebox, where 6 mL of NH₄OH and 1 mL of the (NH₄)₃AsS₃ solution were added. The mixture was vigorously stirred on a magnetic stir plate for 90 min, at which point the NPs had transferred from the nonpolar organic phase to the polar aqueous phase, indicating that a successful ligand exchange had occurred. The clear nonpolar supernatant was drawn off, 7 mL hexane was added, and the mixture was stirred again for 1 h to remove any residual OLA from the nanoparticles. The hexane mixture was drawn off again, and the particles were centrifuged at 14 krpm for 5 min in the presence of 10 mL water and 10 mL acetone mixtures.

2.2.7 Treatments with Ligand Exchanged Particles

The ligand-exchanged nanoparticles were diluted to 10 mg/mL with water and spray coated onto a 1" by 1" Mo-SLG substrate held at a temperature of 150 °C. The substrate was then cut to ¼" by 1" and sealed in an ampoule with added As₂S₅, as described in Section 2.2.4. The ampoule was heated at 425 °C for 1 h and cooled in accordance with other treatments. The substrate was then characterized. 50 µL OLA was then drop-cast on the surface and allowed to dry overnight. This sample was sealed in an ampoule with sulfur and treated again for 1 h at 425 °C.

2.2.8 Characterization

X-ray diffraction (XRD) data were collected on a Rigaku SmartLab diffractometer using a copper K α X-ray source in Bragg-Brentano mode. Raman spectra were taken using a Horiba/Jobin-Yvon LabRAM HR800 confocal microscope system with a 17 mW 633 nm He:Ne laser. Scanning electron microscopy (SEM) and energy-dispersive X-ray spectroscopy (EDX) were conducted on an FEI Quanta electron microscope equipped with a silicon drift EDX detector, and elemental compositions were obtained with AzTEC software using a standardless quantitative analysis based on the Cliff-Lorimer method. SEM images and EDX measurements were taken at accelerating voltages of 7 kV and 20 kV, respectively. Thermogravimetric analysis (TGA) was conducted using a TA Instruments SDT Q600 system in a 100 mL/min helium flow at a ramp rate of 10°C/min. The current-voltage (J-V) measurements were acquired with an Oriel Sol3A solar simulator with the AM1.5G spectrum calibrated to 100 mW/cm² using a certified silicon reference cell. External quantum efficiency (EQE) measurements were performed at 160 Hz and zero bias using a lock-in amplifier and preamplifier for signal processing.

2.3 Results and Discussion

2.3.1 Thermal Analysis of As-synthesized Luzonite (Cu₃AsS₄) Nanoparticles

LUZ NPs were synthesized according to Balow et al. [15], [17]. TGA was performed to determine appropriate temperatures for grain growth. Persistent mass loss occurred above ~250 °C (Figure 2.2a), indicating that significant material besides the nanoparticle surface ligands was lost. To monitor compositional changes as a function of temperature, EDX was performed on films heated to temperatures corresponding to inflection points on the TGA curve. Steady decreases in

the As:Cu and S:Cu ratios (Figure 2.2b) indicate a loss of As and S relative to the starting NPs. Losses up to 315°C were primarily sulfur, with arsenic losses beginning and accelerating at higher temperatures. The high vapor pressure of sulfur at these temperatures is well-established [19], and the propensity of various arsenic species, including the sulfides, to volatilize has been reported [20], [21]. Raman spectra (Figure 2.3) reveal a phase transition to S-deficient tennantite ($\text{Cu}_{12}\text{As}_4\text{S}_{13}$, TEN) between 315°C and 370°C, further confirming the loss of sulfur.

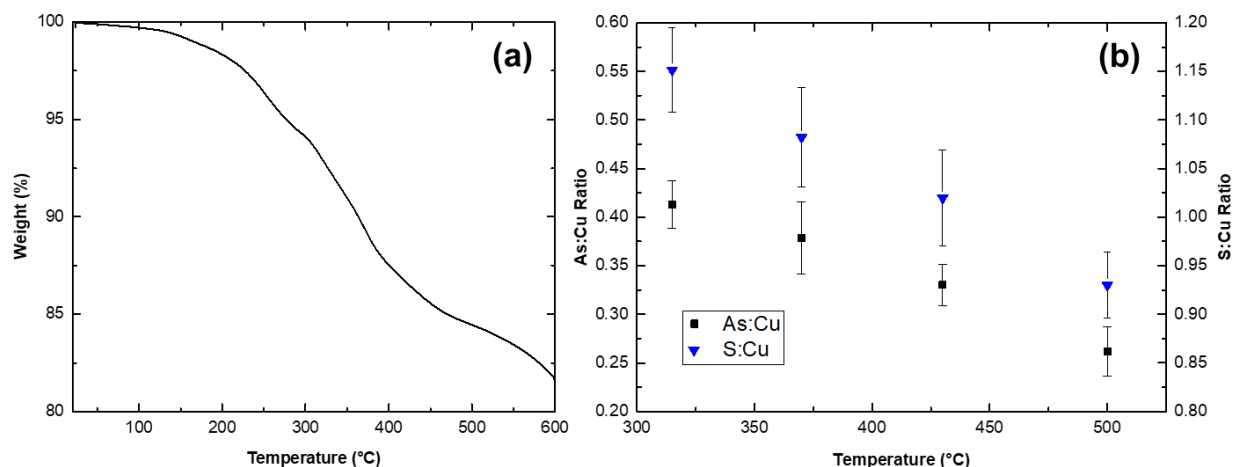


Figure 2.2. a) TGA curve of dried LUZ NPs during a 10 °C/min ramp to 600 °C under a 100 mL/min He flow. b) EDX-measured As:Cu and S:Cu ratios as a function of temperature, acquired by heating samples to the indicated temperatures in a nitrogen-filled glovebox, holding for 15 min, and then removing from heat. Error bars correspond to 95% confidence intervals with standard deviations obtained from multiple measurements in different spots on the same sample. The initial EDX ratios for this particular set of NPs were 0.40 (As:Cu) and 1.43 (S:Cu).

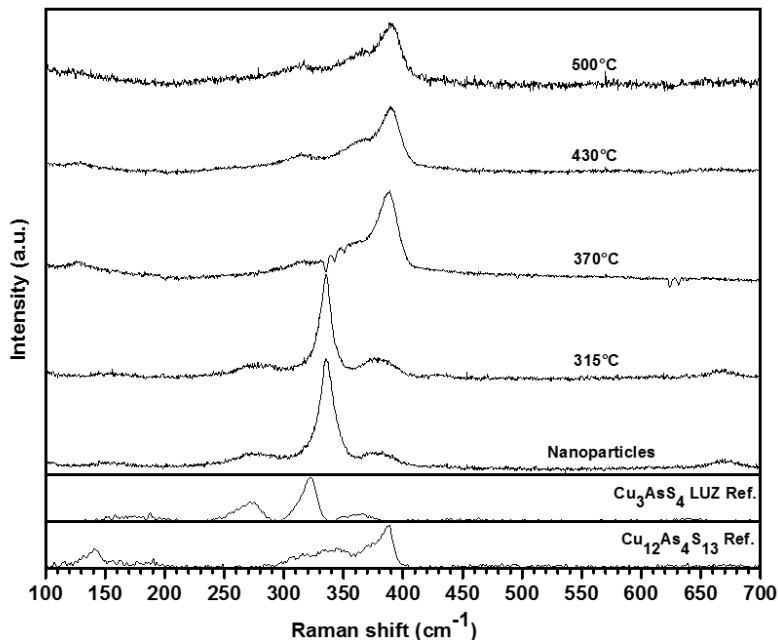


Figure 2.3. Raman spectra of luzonite NP films heated to the indicated temperature. A clear phase transition from luzonite to tennantite is noted between 315 °C and 370 °C. The nanoparticle and 315 °C spectra are noticeably shifted from the Cu_3AsS_4 LUZ reference (RRUFF ID R060390) due to antimony in the reference spectrum. ($\text{Cu}_{12}\text{As}_4\text{S}_{13}$ reference: RRUFF ID R050474)

2.3.2 Process Design for Cu_3AsS_4 Grain Growth

To mitigate elemental losses associated with heating, a NP-coated substrate was sealed in an evacuated ampoule with excess As- and S-containing compounds; these species may saturate the vapor space and prevent evaporation from the film. Furthermore, at the temperatures necessary for grain growth and sintering, sulfur and arsenic sulfides are liquids, so vapor may condense at high curvature particle-particle contacts. This liquid may accelerate grain growth through a liquid-assisted mechanism similar to one previously proposed for device-quality CZTSe NP-based absorbers [22].

Binary As-S phases (i.e. As_4S_4 , As_2S_3 , and As_2S_5), are expected to promote grain growth because they melt by 320 °C and dissolve small amounts of copper between 300 °C and 500 °C [13]. These liquids are in equilibrium with Cu_3AsS_4 when the sulfur composition is above ~55 at. %, as seen in the Cu-As-S isothermal sections in Figure 2.4. An As-S liquid may dissolve copper species from decomposing NPs, establishing a ternary liquid from which solid Cu_3AsS_4 can

nucleate. As the film cools, the copper solubility decreases, and additional solid Cu_3AsS_4 can precipitate from the now-supersaturated liquid.

2.3.3 Materials Characterization of Large-Grained Cu_3AsS_4 Thin Films

As_2S_5 was chosen as the specific As-S annealing atmosphere because it has the closest As:S molar ratio (0.4) necessary to offset the elemental losses observed from TGA at 500 °C (0.27). Figures 2.5a-2.5c show SEM micrographs of the time-dependent grain structure when LUZ NPs were heated in an ampoule with added As_2S_5 at 500 °C. After 10 min, individual grains had formed on top of the NP layer. After 20 min, the average grain size increased while the number density of grains decreased, and the film became less porous, indicating continuing grain growth and coarsening in the film, likely aided by an As-S liquid. After 1 h, the grains continued to grow slightly at the expense of the initial NP material and smaller grains, thus creating a more porous film than after 20 min annealing. The grain size distribution also became bimodal, as seen in Figures 2.5c and 2.5f.

The rapid growth and coarsening behavior seen at 500 °C with an apparent maximum in the film density with time suggests that lower temperatures are required to increase the rate of nucleation of new grains to their rate of coarsening. Figures 2.5d-2.5f show SEM images of grains formed after 1 h treatments at 375 °C, 425 °C, and 500 °C. Under all three conditions, heterogeneous crystal growth occurred on the top surface. At 375 °C, a porous film of small, anisotropic grains formed with plate- and rod-like morphologies, suggesting that grain densification is not favored. As noted earlier, after 1 h at 500 °C, large, isolated, faceted grains formed on the surface. These porous films and isolated grains make these films unsuitable for semiconducting applications due to the likelihood of electrical shunting. In contrast, the treatment at 425 °C resulted in densely-packed, equiaxed, micron-sized grains with minimal void space. The grains have fairly rounded edges, suggesting the possibility of diffusion-controlled growth after 1 h, in contrast to the anisotropic, faceted surfaces at lower and higher temperatures [23]. XRD patterns and Raman spectra (Figure 2.6) support the formation of highly crystalline ENG grains as the majority phase at all three temperatures. EDX measurements (Table 2.1) show that the grain compositions are not deficient in S or As, thus confirming that an As_2S_5 atmosphere is effective in both suppressing elemental losses from the film and providing conditions favorable for growth of Cu-As-S films.

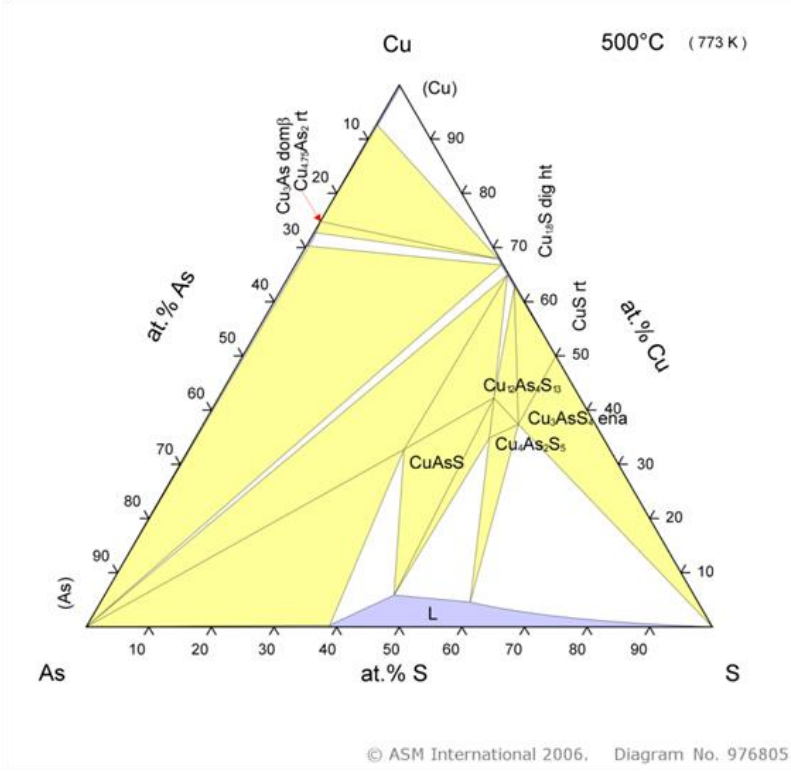
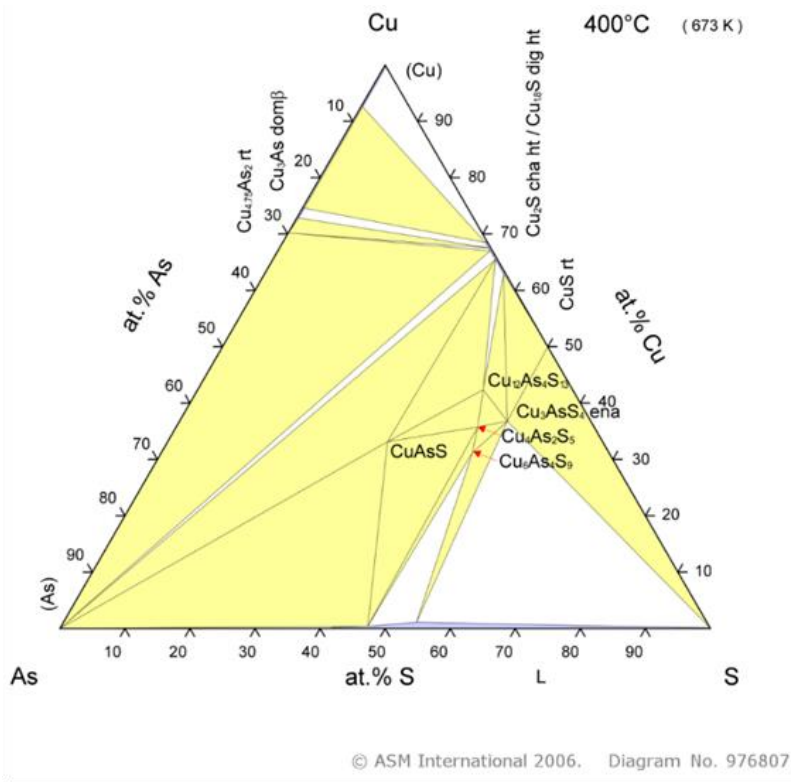


Figure 2.4. Ternary isothermal sections of the Cu-As-S system at 400 °C and 500 °C, adapted from Maske and Skinner. Diagrams copyright ASM International (2006) and reprinted with permission.

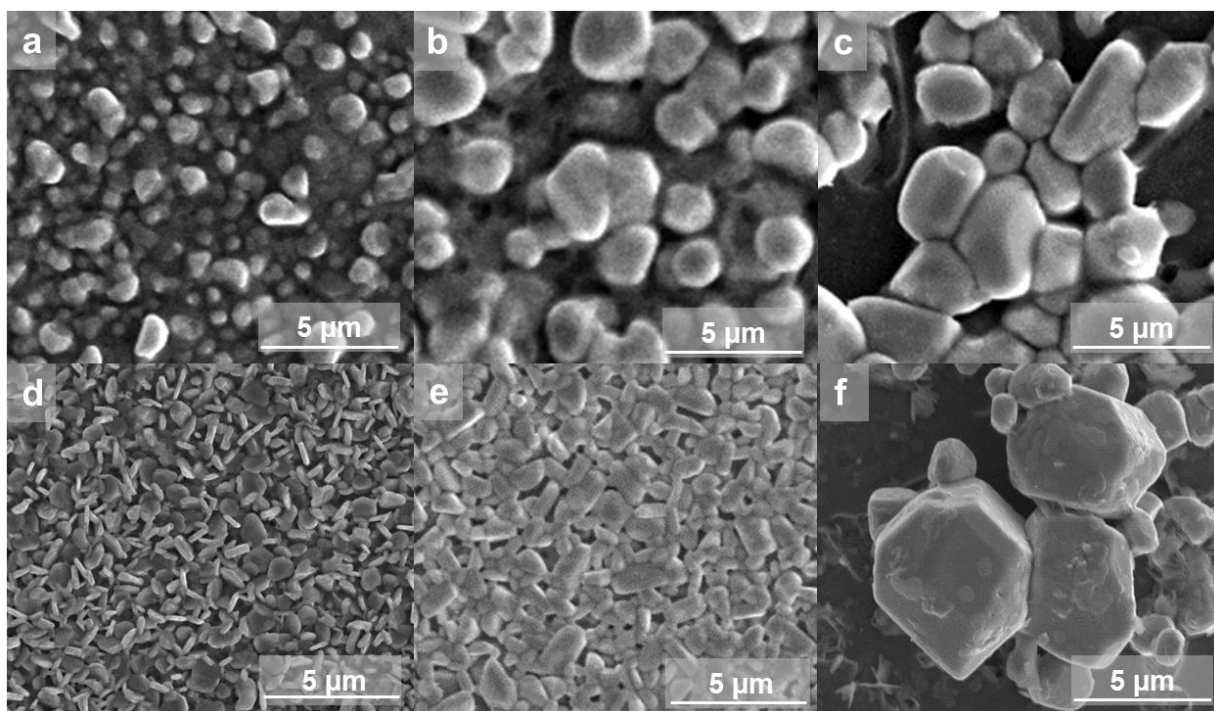


Figure 2.5. SEM Images of LUZ NP films heated with As_2S_5 in a sealed ampoule at given temperatures and times: a) 500 °C for 10 min, b) 500 °C for 20 min, c) 500 °C for 1 h, d) 375 °C for 1 h, e) 425 °C for 1 h, and f) 500 °C for 1 h.

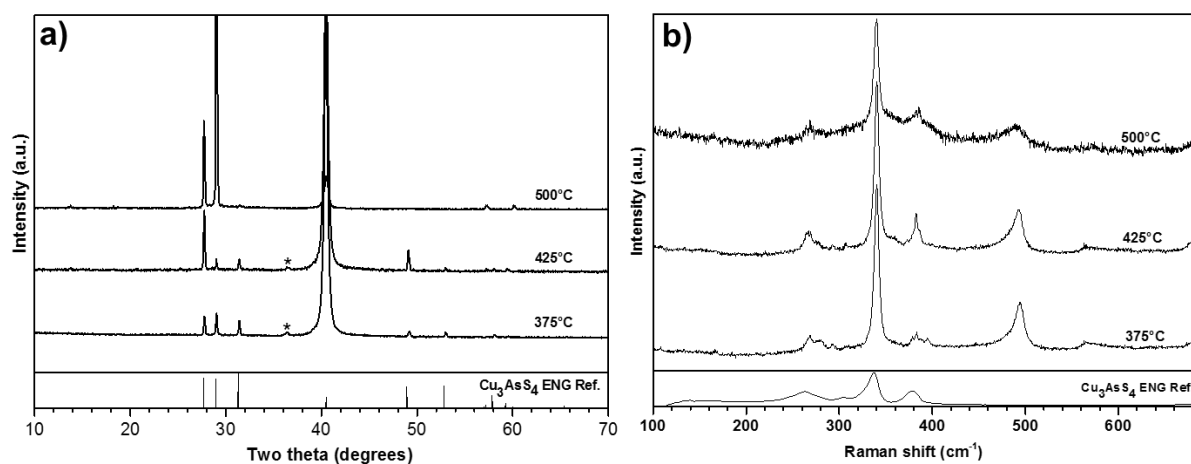


Figure 2.6. a) XRD and b) Raman spectra of luzonite NP films treated in As_2S_5 at 375, 425, and 500 °C for 1 h. In the XRD spectra, the peak locations match well with those of an ENG reference mineral (JCPDS 01-082-1464) with overly dominant intensities attributed to oriented growth. The peak at 40° is indexed to the Mo substrate and the peak at 36.5° (*) is attributed to incomplete filtering of the k-beta radiation from the Mo peak. In the Raman spectra, the stretches also match well with an enargite reference (RRUFF ID: R050373) with an additional peak at 494 cm^{-1} , the origins of which are discussed later in this chapter.

Table 2.1. EDX compositions measured for NP samples treated at 375 °C, 425 °C, and 500 °C with As₂S₅ for 1 h. The measured ratios indicate that arsenic and sulfur have incorporated into the film beyond the target 3:1 Cu:As and 0.75 Cu:S ratios.

	375 °C	425 °C	500 °C
Cu:As	1.83	2.04	2.29
S:As	4.41	3.94	4.15
Cu:S	0.42	0.52	0.55

Figure 2.7a displays the XRD pattern after LUZ NPs were treated at 425 °C for 1 h with added As₂S₅ (i.e. the film shown in Figure 2.5e). The peak positions match those of Pmn2₁ ENG (JCPDS 01-082-1464) Cu₃AsS₄; the intense peak near 40° results from the Mo substrate. Note that this agrees with the observation that the formation of ENG over LUZ is thermodynamically favored at temperatures higher than 320 °C [13]. Oriented growth along the (210) and (230) planes may explain the differences in the relative intensities between the measured pattern and JCPDS 01-082-1464; instances of preferential orientation have been reported for liquid-assisted growth in the CIGSe and CZTSe systems [22], [24]. A mean crystallite size of 65 nm is estimated by applying the Scherrer equation to the (210) peak, which may suggest that the grains seen in Fig. 2.5 are composed of smaller domains, possibly due to the presence of stacking faults seen previously in natural ENG crystals [25]. The Scherrer equation may also not be adequate here due to the large grain sizes.

The Raman spectrum of the treated LUZ NPs is given in Figure 2.7b. The major Raman modes closely match the reference spectrum of a mineral ENG sample. However, the prominent stretch at 494 cm⁻¹, as well as shoulders around 360 cm⁻¹ and 560 cm⁻¹, cannot be assigned to any reported binary or ternary phase in the Cu-As-S system. These Raman modes may result from S-S bonds which are likely present on NP and grain surfaces [26]–[28]. EDX data suggest a highly As- and S-rich film with Cu:As:S molar ratios of 2.0:1:3.9 and without significant lateral deviations. ENG is not expected to deviate significantly from stoichiometry [13], so it is likely that the observed second phase (and measured off-stoichiometric composition) is related to a condensation of S and As species formed either during annealing or during cooling. If one assumes all the copper is incorporated into the ENG grains, the remaining material is approximately 20 at. % As and 80 at. % S, which is more S-rich than any of the reported stable As-S binary phases [13]. It is expected that the composition will approach the stoichiometric value by developing a procedure to selectively etch excess As and S from the film surface after ampoule treatments.

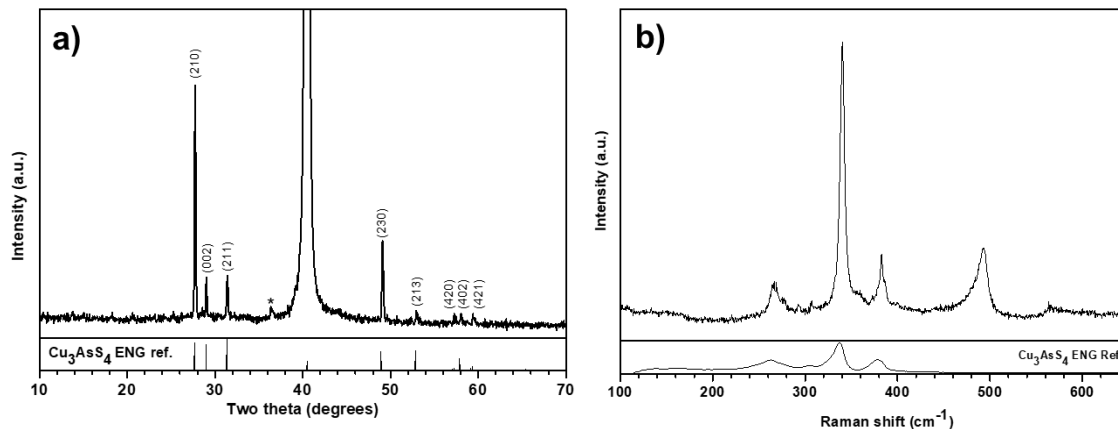


Figure 2.7. XRD and Raman of LUZ NPs treated at 425 °C for 1 h with added As_2S_5 . a) The XRD pattern agrees with ENG mineral reference (JCPDS 01-082-1464). The peak at 40° is from the Mo substrate, with the peak at 36.5° (*) a k-beta peak from the Mo. b) The Raman spectrum agrees with a reference ENG mineral (RRUFF ID R050373), with additional modes at 360, 494, and 560 cm^{-1} .

Although Raman indicates the presence of S-S bonds, a purely sulfur impurity is unlikely to be responsible for the mode at 494 cm^{-1} , as reported modes deviate from this value by 15 cm^{-1} or more [19]. The NP ligands have so far been neglected; however, it is possible that residual carbon species react with other elements, including S, to form a structure with a primary Raman signal at 494 cm^{-1} . To test this hypothesis, ligand exchange was performed on a freshly synthesized batch of LUZ NPs, replacing oleylamine (OLA) ligands with an As_2S_3 -based carbon-free molecular metal chalcogenide complex [18], [29]. These NPs were treated at 425 °C for 1h with added As_2S_5 . The Raman spectrum (Figure 2.8) shows no trace of the stretches at 360, 494, or 560 cm^{-1} . The peaks were then “recovered” by drop-casting OLA on the surface of this film and heating in sulfur for 1 h at 425 °C. The resulting Raman spectrum is dominated by a peak at 494 cm^{-1} (Figure 2.8); additionally, EDX measurements on the top surface of the film detected only C and S. Therefore, we suggest that carbonaceous ligands promote the formation of an unwanted secondary phase in Cu-As-S films.

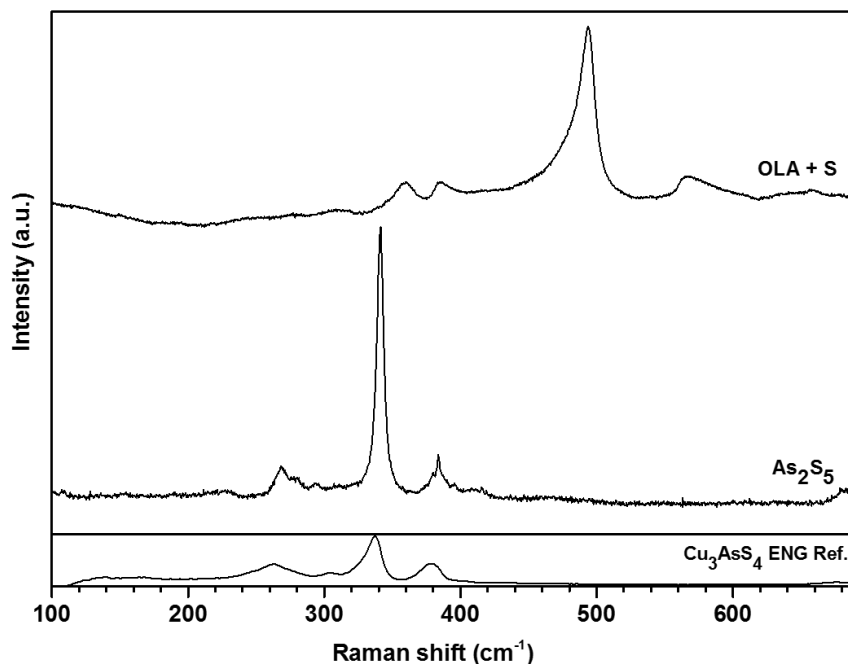


Figure 2.8. Raman spectra of ligand-exchanged luzonite Cu_3AsS_4 NPs. The NPs were treated first in As_2S_5 at 425°C for 1 h, showing no trace of the peak at 494 cm^{-1} seen in materials with OLA-capped particles. Then, OLA was drop-cast on the surface of the treated film, which was treated in sulfur at 425°C for 60 minutes, resulting in the Raman spectrum with peaks at 360 , 494 , and 560 cm^{-1} that may be attributed to the impurity phase; the peak around 380 cm^{-1} may be attributed to tennantite $\text{Cu}_{12}\text{As}_4\text{S}_{13}$ or also to the impurity phase.

2.3.4 Effects of Various Annealing Atmospheres on Grain Structure

Elemental sulfur and arsenic were compared with As_2S_5 as vapor sources for LUZ NP films at 425°C for 1 h. Under such conditions, different growth mechanisms are expected because there is no pathway to a Cu-containing ternary liquid phase (Figure 2.4). A sulfur atmosphere facilitated heterogeneous grain formation (Figure 2.9a) of the tetragonal LUZ crystal structure (Figure 2.10). This is a surprising result, as LUZ was previously reported to convert to ENG by 320°C [13]. In contrast, arsenic alone resulted in a few isolated grains and a highly cracked film (Figure 2.9b). Under these conditions, the film converted to the sulfur-deficient TEN structure (Figure 2.10) as expected. For both elemental treatments, the large size of the grains made it possible to take Raman data on both the grains and the background “floor” layer. Both sulfur-treated spectra match well with enargite Cu_3AsS_4 (RRUFF ID: R050373) or luzonite Cu_3AsS_4 (RRUFF ID R060390, not shown) references, though there are additional impurity peaks only seen in the floor grains. The arsenic-treated “floor” layer matches with a reference tennantite $\text{Cu}_{12}\text{As}_4\text{S}_{13}$ mineral (RRUFF ID:

R050474); the grains, however, do not match with a recorded spectrum of binary or ternary Cu-As-S phases. Due to EDX measurements, we suspect that the grains are the lautite CuAsS phase, which, to the best of our knowledge, does not have a reported Raman spectrum.

In a separate experiment, both elemental As and S were added in a 2:5 molar ratio for comparison with the As_2S_5 additive. When LUZ NPs were treated at $425\text{ }^\circ\text{C}$ for 1 h, the grain size distribution was quite different – isolated, large grains formed on the surface with a dense network of smaller grains filling the remaining space (Figure 2.9c). This phenomenon may be explained by different annealing environments seen with different ampoule additives. For instance, elemental sulfur will fill the vapor space more quickly than a binary compound will due to its higher vapor pressure, thereby introducing a more sulfur-rich environment at the early stages of grain development. Further investigation is needed to determine the precise environments seen by the NPs and to understand their effects on grain growth. When the As_2S_5 and elemental atmosphere experiments are considered jointly, it is evident that a binary As-S compound must be externally supplied to facilitate the growth of unimodal micron-sized dense grains.

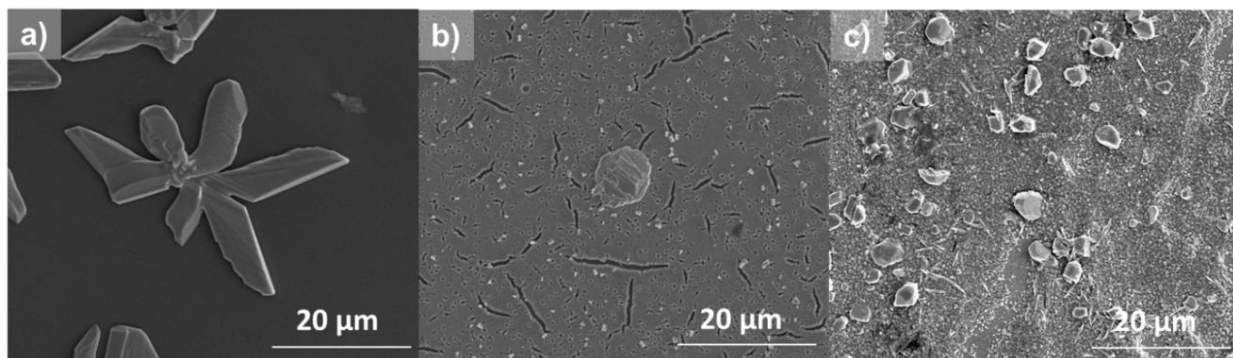


Figure 2.9. SEM images of LUZ NPs treated at $425\text{ }^\circ\text{C}$ for 1 h in varying atmospheres: a) S, b) As, and c) As and S in a 2:5 molar ratio.

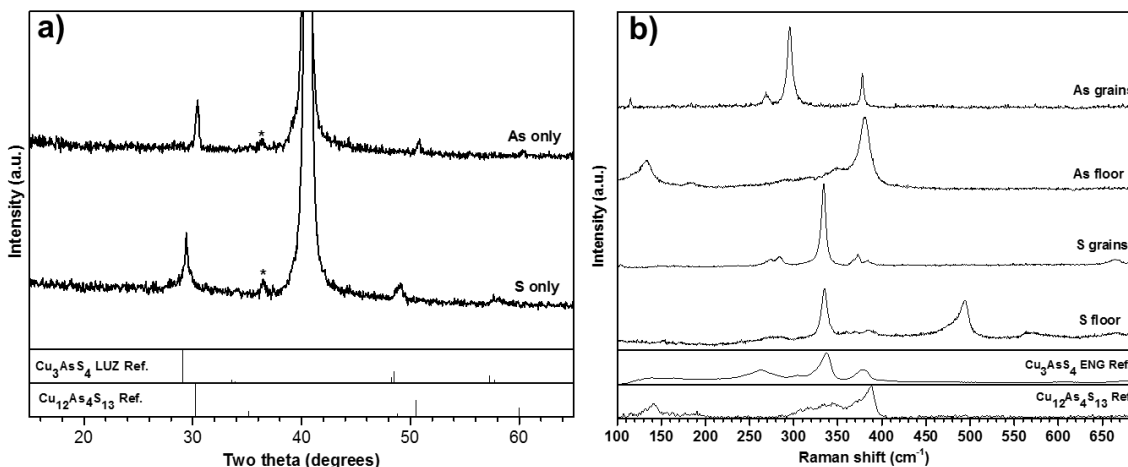


Figure 2.10. a) XRD and b) Raman spectra of LUZ NPs treated in separate sulfur and arsenic atmospheres. In the XRD spectrum, the sulfur-treated film matches well with a tetragonal luzonite reference (JCPDS 01-074-1125), with shifts due to antimony in the reference spectrum. The arsenic-treated film, however, matches with the cubic tennantite $\text{Cu}_{12}\text{As}_4\text{S}_{13}$ reference (JCPDS 42-560). In both, the peaks at 40° are indexed to the Mo substrate and the peaks at 36.5° (*) are attributed to incomplete filtering of the k-beta radiation from the Mo peaks.

2.3.5 Preliminary Solar Cells Using Cu_3AsS_4 Absorber Layer

To demonstrate the utility of the micron-thick ENG films (Figure 2.11) a solar cell was fabricated by first doctor blading the LUZ NPs onto molybdenum coated soda-lime glass and treating at 425°C as previously described. Device fabrication was completed by adding CdS, ZnO, and ITO layers, followed by Ni-Al grids, as previously reported by Graeser et al [30]. The champion cell (0.1 cm^2 area) had an open circuit voltage of 0.17 V, a short-circuit photocurrent density of 3.3 mA cm^{-2} , and a fill factor of 32.3%, with an overall efficiency of 0.18% (Figure 2.12). Table 2.2 gives the average performance parameters for the ten individual cells fabricated on a substrate. Two indicators of poor performance are low shunt resistance ($< 1000\ \Omega\text{-cm}^2$) and low V_{oc} , possibly due to the slight porosity of the film and misalignment between the conduction bands of ENG and CdS, respectively. External quantum efficiency (EQE) measurements (Figure 2.13) revealed poor carrier collection overall but a significant photocurrent from the Cu_3AsS_4 layer. Additionally, a band gap of 1.4 eV was extracted, consistent with a previous report [14]. Further research is needed to fully understand the impacts of various processing parameters and device architectures on device performance.

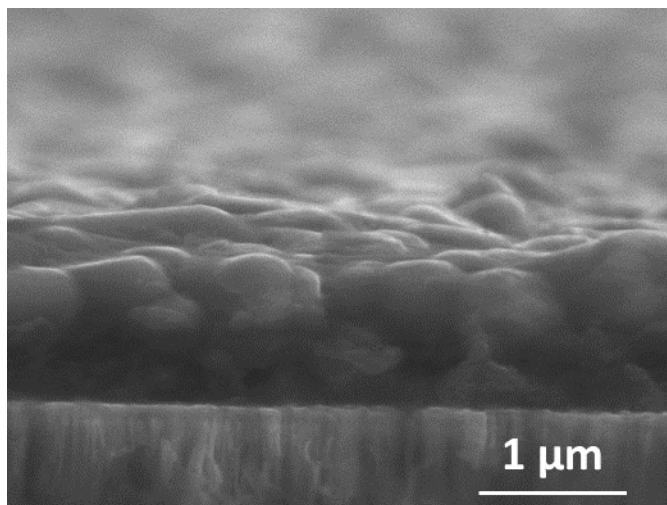


Figure 2.11. Side-view SEM image of LUZ NP film treated in a sealed ampoule with As_2S_5 powder for 1 h at 425°C . A thin fine-grain layer and some contrast in the molybdenum are noted.

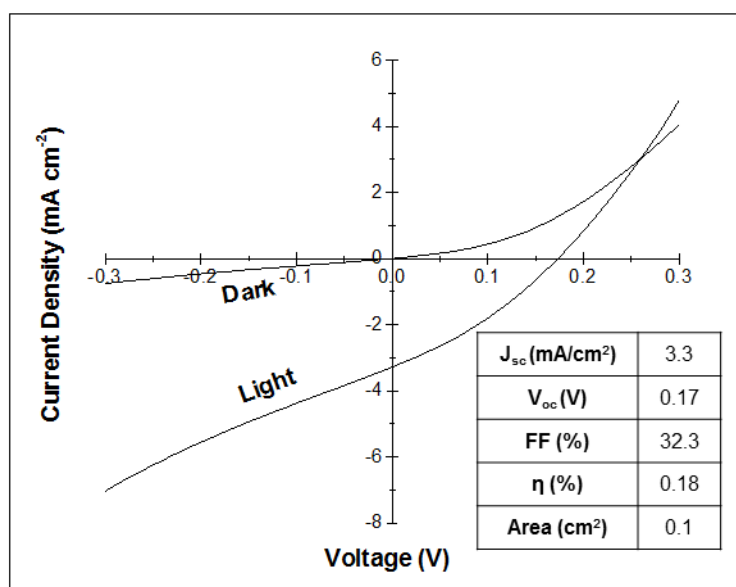


Figure 2.12. J-V curve of the champion solar cell based on a Cu_3AsS_4 absorber layer. The inset table provides performance parameters of the device.

Table 2.2. Device statistics ($n = 10$) for solar cells based on a common ENG absorber layer (cell area = 0.1 cm^2). Out of the ten devices, one had a fill factor and efficiency of 0%. The second set of columns represents the device statistics without this particular device included ($n = 9$).

	n = 10		n = 9	
	Average	St. Dev.	Average	St. Dev.
V_{oc} (V)	0.12	0.07	0.13	0.07
J_{sc} (mA cm^{-2})	2.3	1.2	2.5	1.1
FF (%)	24.0	8.3	26.7	2.4
Efficiency (%)	0.08	0.06	0.09	0.06

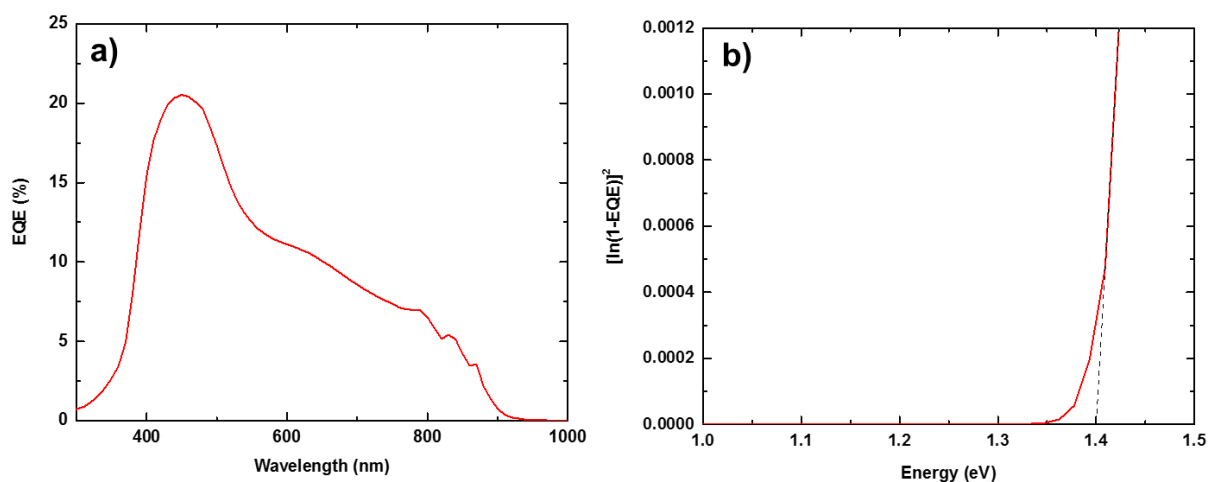


Figure 2.13. a) External quantum efficiency (EQE) measurements of the device shown in Figure 2.12. When integrated, a J_{sc} of 3.4 mA/cm^2 is obtained, which agrees well with the value (3.3 mA/cm^2) obtained from J-V measurements. 2.2 mA/cm^2 of this current occurs at wavelengths greater than 510 nm (or below 2.43 eV , the approximate band gap of CdS) and is therefore attributed to carrier generation in the Cu_3AsS_4 absorber layer only. b) Extrapolation of band gap energy through a plot of $[\ln(1-\text{EQE})]^2$ vs photon energy. A band gap of 1.4 eV is obtained in agreement with a previous experimental result [14].

2.4 Conclusions

We have fabricated the first thin films and solar cells based on Cu-As-S materials through careful selection of an annealing atmosphere and processing conditions to facilitate grain growth and mitigate elemental losses during heating. Treatment of LUZ nanoparticles in As_2S_5 results in the formation of ENG grains and an amorphous secondary phase on the surface. Elimination of the secondary phase will be critical for improving the quality of ENG films; following that, detailed characterization will be necessary to determine the parameters that most significantly govern device performance. These preliminary results establish a foundation for Cu-As-S-based solar cells and justify further research into this family of compounds.

2.5 Acknowledgements

S.A.M. and R.A. acknowledge support from the NSF under grant #1534691-DMR (DMREF: Rapid Design of Earth Abundant Inorganic Materials for Future PVs). J.A. and C.A.H. acknowledge support from the IGERT Program under grant #1144843 (IGERT: Global Traineeship in Sustainable Electronics). The authors would like to thank Mr. Robert Boyne, Dr. Brian Graeser, and Ms. Xianyi Hu for their expertise in preparing molybdenum-coated soda-lime glass, and Dr. Christopher Gilpin, Dr. Brian Graeser, Dr. Charles Hages, Ms. Joanne Lax, and Dr. Robert Balow for their helpful discussions and feedback about the project and manuscript. The authors declare no competing financial interests.

2.6 References

- [1] M. G. Panthani *et al.*, “High Efficiency Solution Processed Sintered CdTe Nanocrystal Solar Cells: The Role of Interfaces,” *Nano Lett.*, vol. 14, no. 2, pp. 670–675, Feb. 2014.
- [2] C. K. Miskin, A. Dubois-Camacho, M. O. Reese, and R. Agrawal, “A direct solution deposition approach to CdTe thin films,” *J. Mater. Chem. C*, vol. 4, no. 39, pp. 9167–9171, 2016.
- [3] S. M. McLeod, C. J. Hages, N. J. Carter, and R. Agrawal, “Synthesis and characterization of 15% efficient CIGSSe solar cells from nanoparticle inks,” *Prog. Photovoltaics Res. Appl.*, vol. 23, no. 11, pp. 1550–1556, Nov. 2015.
- [4] X. Zhao, M. Lu, M. J. Koeper, and R. Agrawal, “Solution-processed sulfur depleted Cu(In,Ga)Se₂ solar cells synthesized from a monoamine–dithiol solvent mixture,” *J. Mater. Chem. A*, vol. 4, no. 19, pp. 7390–7397, 2016.
- [5] T. Zhang *et al.*, “High efficiency solution-processed thin-film Cu(In,Ga)(Se,S)₂ solar cells,” *Energy Environ. Sci.*, vol. 9, no. 12, pp. 3674–3681, 2016.
- [6] C. Wadia, a. P. Alivisatos, and D. M. Kammen, “Materials Availability Expands the Opportunity for Large-Scale Photovoltaics Deployment,” *Environ. Sci. Technol.*, vol. 43, no. 6, pp. 2072–2077, Mar. 2009.
- [7] W. Wang *et al.*, “Device Characteristics of CZTSSe Thin-Film Solar Cells with 12.6% Efficiency,” *Adv. Energy Mater.*, vol. 4, no. 7, p. 1301465, May 2014.

- [8] C. K. Miskin *et al.*, “9.0% efficient $\text{Cu}_2\text{ZnSn}(\text{S},\text{Se})_4$ solar cells from selenized nanoparticle inks,” *Prog. Photovoltaics Res. Appl.*, vol. 23, no. 5, pp. 654–659, May 2015.
- [9] T. Gokmen, O. Gunawan, T. K. Todorov, and D. B. Mitzi, “Band tailing and efficiency limitation in kesterite solar cells,” *Appl. Phys. Lett.*, vol. 103, no. 10, p. 103506, Sep. 2013.
- [10] C. J. Hages, N. J. Carter, and R. Agrawal, “Generalized quantum efficiency analysis for non-ideal solar cells: Case of $\text{Cu}_2\text{ZnSnSe}_4$,” *J. Appl. Phys.*, vol. 119, no. 1, p. 014505, Jan. 2016.
- [11] L. Yu, R. S. Kokenyesi, D. A. Keszler, and A. Zunger, “Inverse Design of High Absorption Thin-Film Photovoltaic Materials,” *Adv. Energy Mater.*, vol. 3, no. 1, pp. 43–48, Jan. 2013.
- [12] T. Shi, W.-J. Yin, M. Al-Jassim, and Y. Yan, “Structural, electronic, and optical properties of $\text{Cu}_3\text{-V-VI}_4$ compound semiconductors,” *Appl. Phys. Lett.*, vol. 103, no. 15, p. 152105, Oct. 2013.
- [13] S. Maske and B. J. Skinner, “Studies of the sulfosalts of copper I. Phases and phase relations in the system Cu-As-S ,” *Econ. Geol.*, vol. 66, no. 6, pp. 901–918, Oct. 1971.
- [14] T. Pauporté and D. Lincot, “Electrical, optical and photoelectrochemical properties of natural enargite, Cu_3AsS_4 ,” *Adv. Mater. Opt. Electron.*, vol. 5, no. 6, pp. 289–298, Nov. 1995.
- [15] R. B. Balow, E. J. Sheets, M. M. Abu-Omar, and R. Agrawal, “Synthesis and Characterization of Copper Arsenic Sulfide Nanocrystals from Earth Abundant Elements for Solar Energy Conversion,” *Chem. Mater.*, vol. 27, no. 7, pp. 2290–2293, Apr. 2015.
- [16] A. Das, A. Shamirian, and P. T. Snee, “Arsenic Silylamide: An Effective Precursor for Arsenide Semiconductor Nanocrystal Synthesis,” *Chem. Mater.*, vol. 28, no. 11, pp. 4058–4064, Jun. 2016.
- [17] R. B. Balow, C. K. Miskin, M. M. Abu-Omar, and R. Agrawal, “Synthesis and Characterization of $\text{Cu}_3(\text{Sb}_{1-x}\text{As}_x)\text{S}_4$ Semiconducting Nanocrystal Alloys with Tunable Properties for Optoelectronic Device Applications,” *Chem. Mater.*, vol. 29, no. 2, pp. 573–578, Jan. 2017.
- [18] M. V. Kovalenko, M. I. Bodnarchuk, J. Zaumseil, J.-S. Lee, and D. V. Talapin, “Expanding the Chemical Versatility of Colloidal Nanocrystals Capped with Molecular Metal Chalcogenide Ligands,” *J. Am. Chem. Soc.*, vol. 132, no. 29, pp. 10085–10092, Jul. 2010.

- [19] B. Meyer, "Elemental sulfur," *Chem. Rev.*, vol. 76, no. 3, pp. 367–388, Jun. 1976.
- [20] R. Padilla, Y. Fan, and I. Wilkomirsky, "Decomposition of Enargite in Nitrogen Atmosphere," *Can. Metall. Q.*, vol. 40, no. 3, pp. 335–342, Jan. 2001.
- [21] D. H. Webber and R. L. Brutchey, "Alkahest for V_2VI_3 Chalcogenides: Dissolution of Nine Bulk Semiconductors in a Diamine-Dithiol Solvent Mixture," *J. Am. Chem. Soc.*, vol. 135, no. 42, pp. 15722–15725, Oct. 2013.
- [22] C. J. Hages, M. J. Koeper, C. K. Miskin, K. W. Brew, and R. Agrawal, "Controlled Grain Growth for High Performance Nanoparticle-Based Kesterite Solar Cells," *Chem. Mater.*, vol. 28, no. 21, pp. 7703–7714, Nov. 2016.
- [23] R. M. German, P. Suri, and S. J. Park, "Review: liquid phase sintering," *J. Mater. Sci.*, vol. 44, no. 1, pp. 1–39, Jan. 2009.
- [24] J. R. Tuttle *et al.*, "Structure, chemistry, and growth mechanisms of photovoltaic quality thin-film $Cu(In,Ga)Se_2$ grown from a mixed-phase precursor," *J. Appl. Phys.*, vol. 77, no. 1, pp. 153–161, Jan. 1995.
- [25] M. Posfai and M. Sundberg, "Stacking disorder and polytypism in enargite and luzonite," *Am. Mineral.*, vol. 83, no. 3–4, pp. 365–372, Apr. 1998.
- [26] A. Stronski, M. Vlcek, and A. Sklena, "Photoinduced structural changes in $As_{100-x}S_x$ layers," *Semicond. Physics, Quantum Electron. Optoelectron.*, vol. 3, no. 3, pp. 394–399, 2000.
- [27] R. M. Holomb and V. M. Mitsa, "Simulation of Raman Spectra of As_xS_{100-x} Glasses by the Results of Ab Initio Calculations of As_nS_m Clusters Vibrations," *J. Optoelectron. Adv. Mater.*, vol. 6, no. 4, pp. 1177–1184, 2004.
- [28] B. D. Chernomordik, A. E. Béland, D. D. Deng, L. F. Francis, and E. S. Aydil, "Microstructure Evolution and Crystal Growth in Cu_2ZnSnS_4 Thin Films Formed By Annealing Colloidal Nanocrystal Coatings," *Chem. Mater.*, vol. 26, no. 10, pp. 3191–3201, May 2014.
- [29] Z. Xia *et al.*, "Generalized Water-Processed Metal Chalcogenide Complexes: Synthesis and Applications," *Chem. Mater.*, vol. 27, no. 23, pp. 8048–8057, Dec. 2015.
- [30] B. K. Graeser *et al.*, "Synthesis of $(CuInS_2)_{0.5}(ZnS)_{0.5}$ Alloy Nanocrystals and Their Use for the Fabrication of Solar Cells via Selenization," *Chem. Mater.*, vol. 26, no. 14, pp. 4060–4063, Jul. 2014.

3. INSIGHTS INTO THE GROWTH OF ENARGITE FILMS FROM NANOPARTICLE PRECURSORS

3.1 Introduction

The previous chapter outlined the fabrication of enargite (ENG) Cu_3AsS_4 thin films by annealing luzonite (LUZ) Cu_3AsS_4 nanoparticles (NPs) in an atmosphere containing As and S, with an arsenic(V) sulfide (As_2S_5) atmosphere at 425 °C proving most ideal for solar cell applications. Preliminary device efficiencies reached 0.18%, but an increase of two orders of magnitude is required for ENG-based solar cells to be commercially viable. Two shortcomings were identified with this original approach: the films contained pores that contribute to electrical shunting, and the carbonaceous ligands reacted with sulfur vapor, leading to a secondary phase and fine grain layer that impede device performance.

In this chapter, selected experiments aimed towards understanding the growth of LUZ NP precursors into ENG thin films are presented. The phase transformation and coarsening behavior of LUZ NPs in vacuum and sulfur atmospheres are first explored; the incomplete conversion to ENG and the lack of densification illustrate the need for an external supply of arsenic. Then, the effects of annealing LUZ- As_2S_3 stacks are presented. Modifications to the As_2S_5 annealing procedure are explored, and several treatment conditions are found that nearly double the 0.18% champion efficiency presented in Chapter 2. Finally, the effects of pre-annealing NP films for carbon removal are discussed; the formation of the secondary phase is greatly reduced or even eliminated, but device performance is not improved due to the formation of widespread cracks in the film. The work in this chapter is a strong indication that using oleylamine (OLA)-capped LUZ NPs as precursors for ENG thin films may not be a feasible route for high efficiency solar cells; alternative methods must be developed.

3.2 Experimental Methods

3.2.1 Materials

The chemicals used in this chapter (besides those used in NP synthesis, which was described in Chapter 2) were arsenic(V) sulfide (As_2S_5 , Santa Cruz Biotechnology and Sigma-Aldrich), arsenic(III) sulfide (As_2S_3 , Strem chemicals), sulfur (S, flakes, Sigma-Aldrich), n-

butylamine (BA, Sigma-Aldrich), argon (Indiana Oxygen), and hydrogen sulfide (H_2S , 0.97%, balance argon, Airgas). The non-gases were stored and used under an inert nitrogen atmosphere unless otherwise indicated.

3.2.2 Heat Treatments

LUZ NP anneals were conducted in 10 mL borosilicate glass ampoules (Chemglass). The LUZ NP films and any desired powders were placed into the ampoule, which was then attached to a Schlenk line and purged three times before sealing with a butane torch under vacuum. The ampoules were then inserted into a preheated three-zone tube furnace for a set time; the furnace was then opened and cooled naturally to room temperature. Pre-annealing treatments in argon (10 sccm) or H_2S (40 sccm) were done in a vertical three-zone tube furnace with samples secured in a custom graphite holder attached to a manual push-pull rod. Sulfur anneals occurred in a horizontal three-zone tube furnace, with the samples of interest in the center zone and sulfur vapors produced by effusion from a graphite box in a separate zone set at 200 °C. Full details of the furnaces may be found in Chapter 7.

3.2.3 Deposition of Arsenic(III) Sulfide Thin Films

As_2S_3 films were deposited onto Mo-coated soda-lime glass or directly onto LUZ NP films using a procedure adapted from the literature [1], [2]. Briefly, As_2S_3 was dissolved in high concentrations (~0.5 - 1 M) in BA in a nitrogen-filled glovebox. The solution was then drop-cast on a pre-cleaned substrate or one coated with LUZ NPs; it was spun at 2000 rpm for 45 seconds and then annealed for 10 min at 70 °C and for 30 min at 100 °C to break BA- As_2S_3 complexes and remove them from the film. Afterwards, the substrates were either used immediately or dried in a vacuum oven at 100 °C to ensure complete removal of carbon from the As_2S_3 film.

3.2.4 Characterization

X-ray diffraction (XRD) data were collected in parallel beam mode with a 0.5° incidence angle on a Rigaku Smartlab diffractometer with a copper $K\alpha$ source. Raman spectroscopy was conducted using a 633 nm He:Ne laser mounted in a custom Horiba/Jobin-Yvon LabRAM HR800 system through a 100x objective lens. Scanning electron microscopy (SEM) images and energy-dispersive X-ray spectroscopy (EDX) data were acquired using an FEI Quanta SEM equipped with a silicon drift EDX detector and AzTEC software; EDX data was collected at 20 kV. The current-

voltage (J-V) measurements were acquired using a calibrated Oriel Sol3A solar simulator. External quantum efficiency (EQE) measurements were performed 160 Hz and 0 V bias; the system was equipped with a preamplifier and lock-in amplifier for signal processing.

3.3 Results and Discussion

3.3.1 Vacuum Annealing of Luzonite Nanoparticle Films

To investigate coarsening behavior and phase transformations of LUZ NPs without the influence of an external atmosphere, samples were sealed in ampoules without any powders (base argon pressure ~150 mtorr) and heated to elevated temperatures for 1 h. As noted in Chapter 2, sulfur and arsenic losses are lost from LUZ NPs at elevated temperatures; a phase transformation from LUZ to tennantite (TEN, $\text{Cu}_{12}\text{As}_4\text{S}_{13}$) also occurs. Figure 3.1 gives the XRD and Raman spectra of these films, confirming the formation of TEN at 300, 400, and 500 °C. The relatively sharp peaks in the XRD spectra indicate that the mean crystallite size increased, suggesting that LUZ NPs coarsen upon heating even without As_2S_5 . Plan-view SEM images of the films are also shown in Figure 3.1. At lower temperatures, the films developed significant cracks, likely caused by detachment and evaporation of OLA ligands. At 500 °C, isolated faceted grains formed throughout the film, though it is unclear if they resulted from direct coarsening of LUZ NPs or from the decomposition and re-reaction of various binary species. The average EDX-determined Cu/As ratio of several grains is 3.28, while the S/As ratio is 2.99, suggesting the formation of a Cu-rich TEN phase. While this deviates from the ideal TEN stoichiometry, secondary phases are not necessarily present, as TEN has been reported to have a wide composition range [3], [4]; these films are also on molybdenum, whose L peak overlaps with the sulfur K peak. The background (i.e. not the grains) of the 500 °C film, by contrast, shows Cu/As and S/As ratios of 8.39 and 7.96, respectively, suggesting that most of the arsenic was either incorporated into the grains or vaporized and condensed on the walls of the ampoule.

Overall, the vacuum anneals demonstrate that LUZ NP films containing OLA ligands have a natural tendency to crack upon heating, which must be considered in any atmosphere. Additionally, the NPs phase transition to TEN as seen previously, reiterating the need to externally supply sulfur to the film for maintenance of the LUZ/ENG phase.

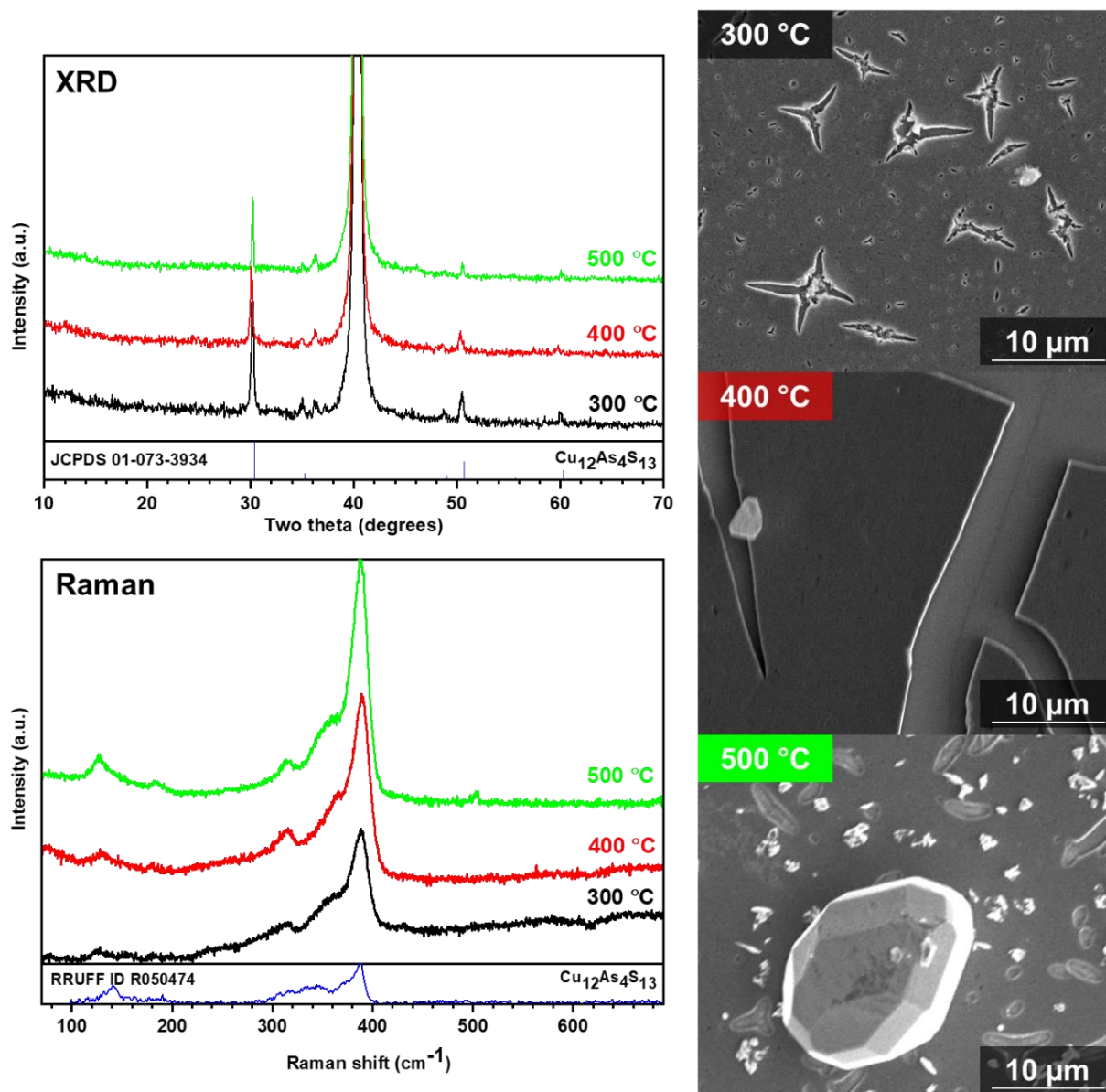


Figure 3.1. XRD spectra, Raman spectra, and plan-view SEM images of LUZ NP films heated in a sealed ampoule at 300, 400, and 500 °C for 1 h. The peak at 40° 2 θ is attributed to the Mo substrate.

3.3.2 Sulfurization of Luzonite Nanoparticle Films

In Chapter 2, LUZ NPs were sealed in an ampoule with sulfur and heated for 1 h at 425 °C; surprisingly, the LUZ phase was maintained, and very large isolated grains were formed. To further explore the impacts that sulfur has on the behavior of LUZ NPs, an additional suite of experiments was conducted. Figure 3.2 gives the XRD and Raman spectra of LUZ NP films that

were heated in a horizontal tube furnace with an argon flow that continuously purged the sulfur and any evaporating species. For the spectra labeled “300 °C,” “350 °C,” and “400 °C,” the sulfur vapor was produced at 200 °C and carried to the samples in a hotter zone; such conditions are representative of an undersaturated atmosphere. For the “425 °C graphite box” sample, the sample and a vast excess of sulfur were placed together in a covered graphite box. While the sulfur completely leaks out of the graphite box prior to the end of the treatment, there is likely a short period of time in which the atmosphere is saturated, leading to the possibility of a liquid existing in the film. The XRD spectra indicate that the LUZ structure was maintained except when using an undersaturated atmosphere at 400 °C, which converted the film completely to ENG. In the other three spectra, the shoulder peak around $28^\circ 2\theta$ may correspond to ENG, but the conversion is certainly not complete. The Raman spectra also indicate maintenance of the LUZ phase in the three samples, as the A1 peak occurs at 335 cm^{-1} rather than 340 cm^{-1} that is expected for ENG [5]. Note that the 490 cm^{-1} impurity peak is weaker in samples treated at undersaturated conditions; therefore, it is plausible that excess sulfur reacts with carbon and suppresses its removal from the film during annealing.

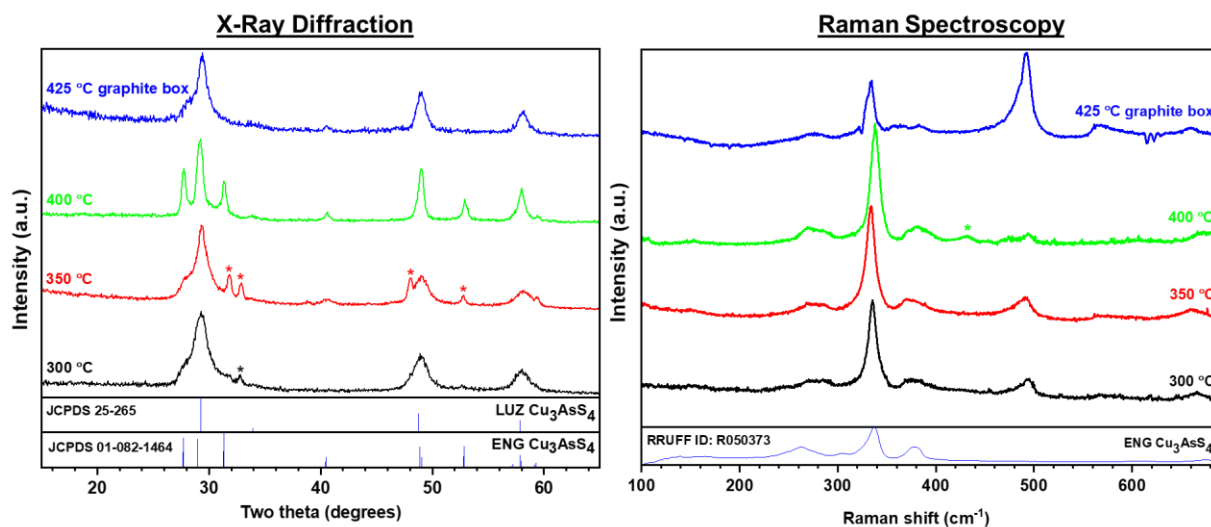


Figure 3.2. XRD and Raman spectra of LUZ NP films annealed in sulfur flow environments at the given temperatures for 1 h. In the XRD spectra, the (*) signify peaks corresponding to covellite CuS, and the (*) in the 400 °C Raman spectra signify signal from room light that was inadvertently included during the sample’s measurement.

Heat treatments in an open atmosphere, such as those just described, are not likely to suppress the escape of arsenic species from the film, which was observed in thermogravimetric analysis in Chapter 2. Therefore, a glass ampoule was used to mitigate arsenic losses and to produce a higher partial pressure of sulfur than what was used in Chapter 2. The XRD spectra (Figure 3.3) show that the LUZ phase was maintained during the heat treatments at 350 and 425 °C. The Raman spectra generally support this conclusion, though there was some nonuniformity in the 425 °C 60 min film, with areas of both LUZ and ENG noted. An impurity peak at 490 cm^{-1} is present in most cases (excluding the one where the laser beam was focused directly on a grain) and has a higher intensity than seen in the open atmosphere sulfurization experiments. The plan-view SEM images show formation of large faceted island grains that are not suitable for device applications.

The vacuum and sulfurization experiments suggest that added arsenic is necessary for growth of thin films with micron-sized dense grains. While the formation of island grains can occur without arsenic, the lack of densification renders such films ill-suited for device applications. One unexplored area here is adding more sulfur so that the atmosphere is saturated for the entirety of the heat treatment; however, this will likely lead to the formation of additional C-S secondary phases seen in Raman and impede device performance. One other note is that the transformation of LUZ to ENG is suppressed (at least partially) in high-temperature sulfur environments. Further exploration of sulfurization conditions and elucidation of grain growth mechanisms may lead to densified films of LUZ, though it may also require a different precursor film with less carbon for a single-phase material.

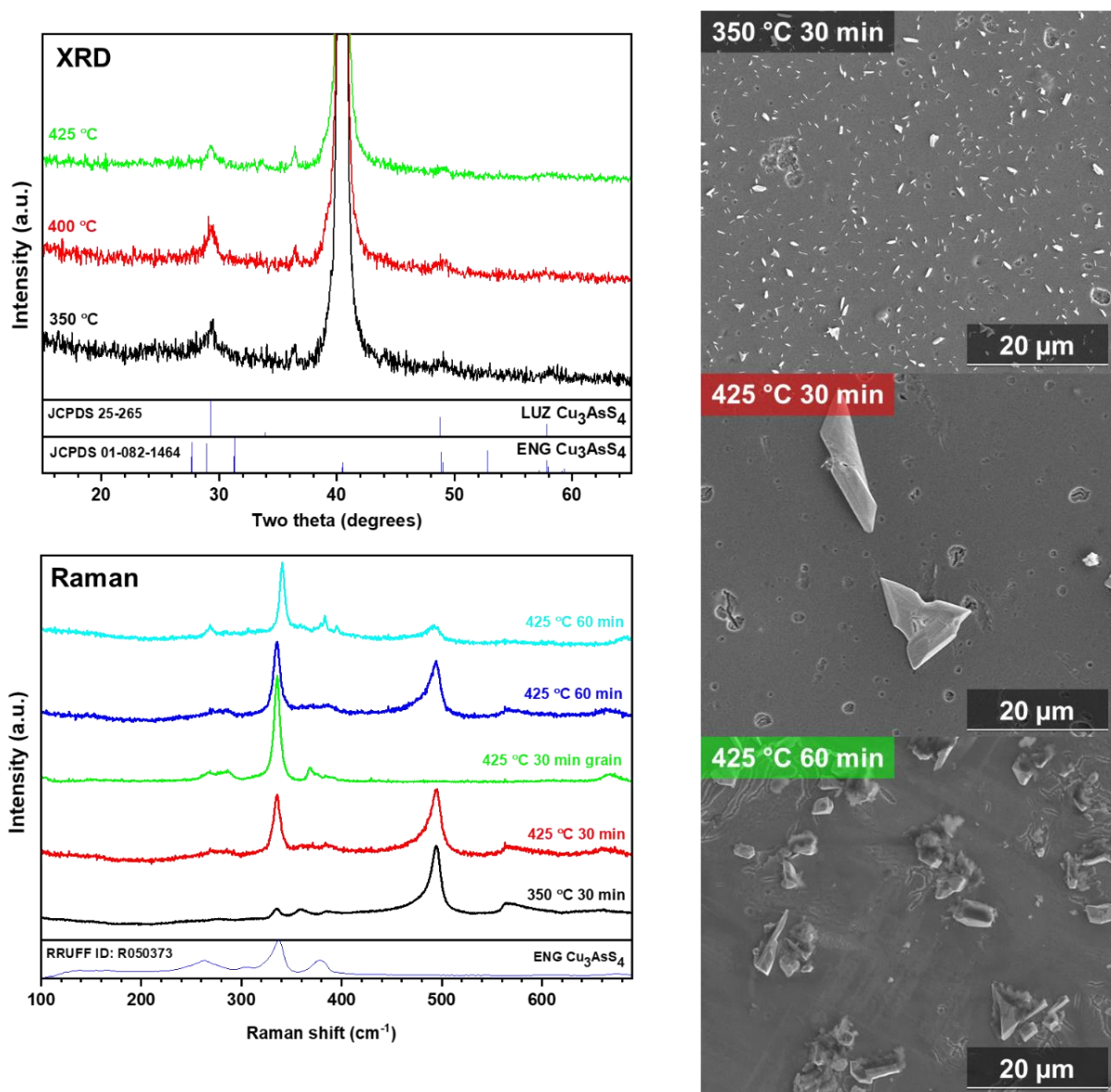


Figure 3.3. XRD spectra, Raman spectra, and plan view SEM images of LUZ NP films heated in a sealed glass ampoule with added sulfur flakes. The peak at $40^\circ 2\theta$ is attributed to the Mo substrate.

3.3.3 Deposition and Annealing of Stacked Arsenic(III) Sulfide-Luzonite Films

The previous two sections have shown that arsenic must be supplied to OLA-capped LUZ NPs for growth of densified thin films with large grains. However, in the scheme outlined in Chapter 2, the condensation of As-S species from the atmosphere may not occur uniformly due to porosity and roughness of the film. Amorphous thin films of As_2S_3 from short-chained amine solvents have been deposited previously via spin coating [1], [6]. As_2S_3 melts starting at 300°C ,

forming a liquid that may aid in growth of LUZ NPs. Furthermore, placing As_2S_3 above or below the LUZ NPs may provide opportunities to direct the initial nucleation of Cu_3AsS_4 grains, as has been demonstrated with evaporated selenium in CIGS and CZTS NP systems [7], [8].

As_2S_3 films were deposited on top of LUZ NP films and annealed in a furnace with flowing argon, a graphite box with sulfur, and a glass ampoule with As_2S_5 for 30 min at 425 °C. The XRD and Raman spectra in Figure 3.4 indicate that the film converted to TEN in an argon atmosphere and to ENG when heated in either sulfur or As_2S_5 . Because the sulfurization treatment resulted in complete (rather than partial, as seen previously) conversion to ENG, it is likely that the As_2S_3 layer was significantly involved in the film growth. However, the As_2S_3 was not enough to prevent the decomposition of LUZ NPs into TEN in an argon atmosphere; a reduction in the anneal time may keep the film as LUZ or ENG. Additionally, a Raman peak at 490 cm^{-1} was present in all three treatments; this may result from the reaction of sulfur with either OLA ligands or residual amine complexes from the As_2S_3 deposition.

Plan-view SEM images (Figure 3.4) indicate that the As_2S_5 and sulfur treatments result in grains with relatively similar densities and sizes, along with some extra material between the grains. In contrast, large dense grains were not formed during the argon treatment; instead, spherical grains of roughly $\sim 100\text{ nm}$ diameter were formed. It is possible that As_2S_3 melted and evaporated more quickly than it reacted with the LUZ NPs; further experiments should aim to suppress this evaporation through methods such as an evaporated SiO_2 layer.

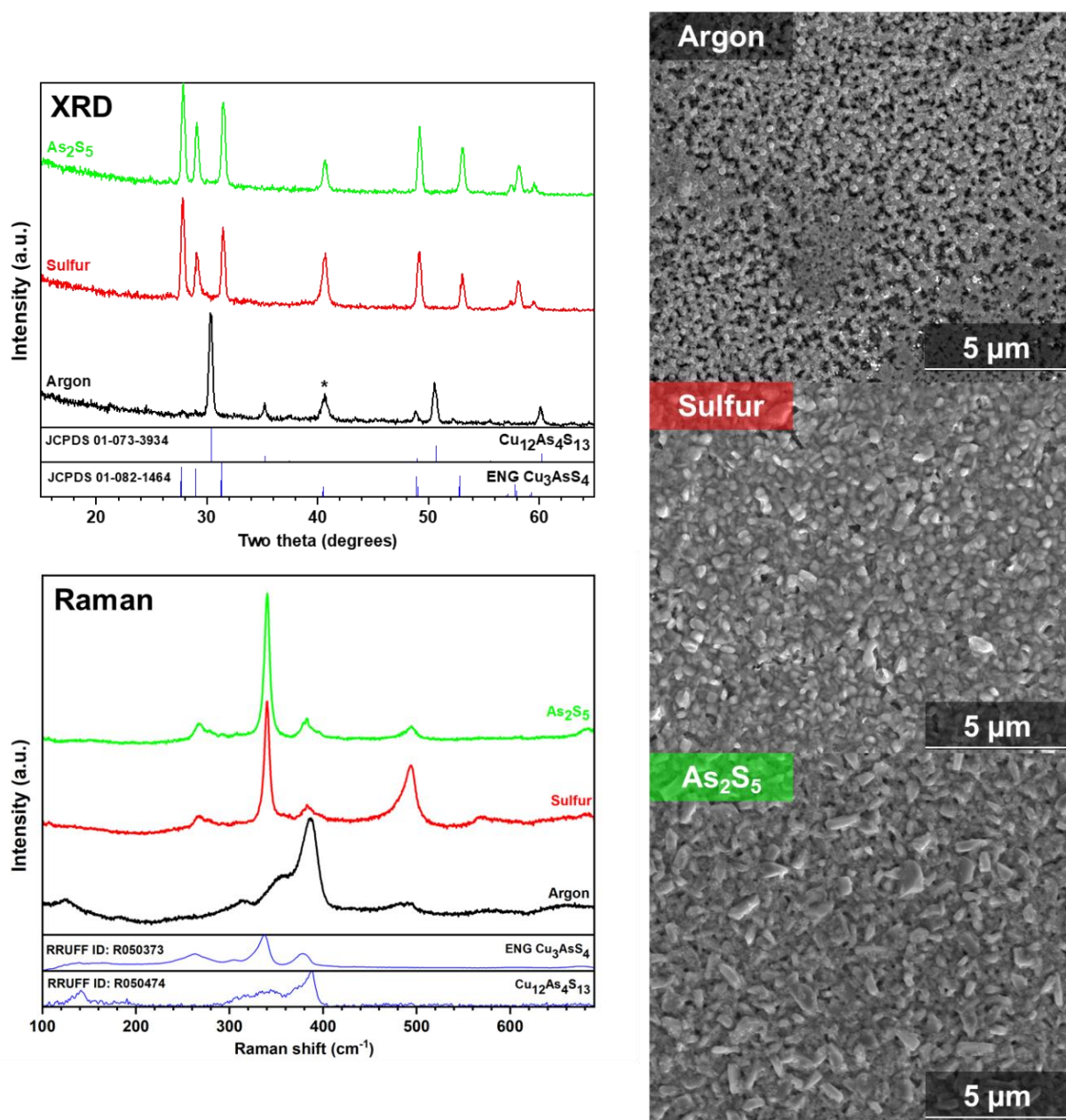


Figure 3.4. XRD spectra, Raman spectra, and plan-view SEM images of stacks of As_2S_3 on top of LUZ NPs heated for 30 min at 425°C in the indicated atmosphere. In the argon XRD spectrum, the (*) is attributed to the molybdenum substrate.

The plan-view SEM images in Figure 3.4 indicate that a sulfur atmosphere can grow large, dense grains when paired with an As_2S_3 thin film deposited on the surface of LUZ NPs. Such a system is advantageous over the currently used ampoule method because it allows for larger substrates and simplifies the number of processing steps. As_2S_3 -above-LUZ films were sulfurized in a graphite box at 350 , 425 , and 500°C . The XRD and Raman spectra (Figure 3.5) indicate that

LUZ NPs converted to ENG at 425 and 500 °C, while remaining as LUZ (with a small XRD shoulder attributed to the start of ENG growth) at 350 °C. At all three temperatures, plan view SEM images show a relatively dense packing of grains, in contrast to the island grains seen at 500 °C in previous anneals. Further optimization of the sulfurization conditions and the ratio of As_2S_3 to LUZ NPs may result in routes to tuning the grain size.

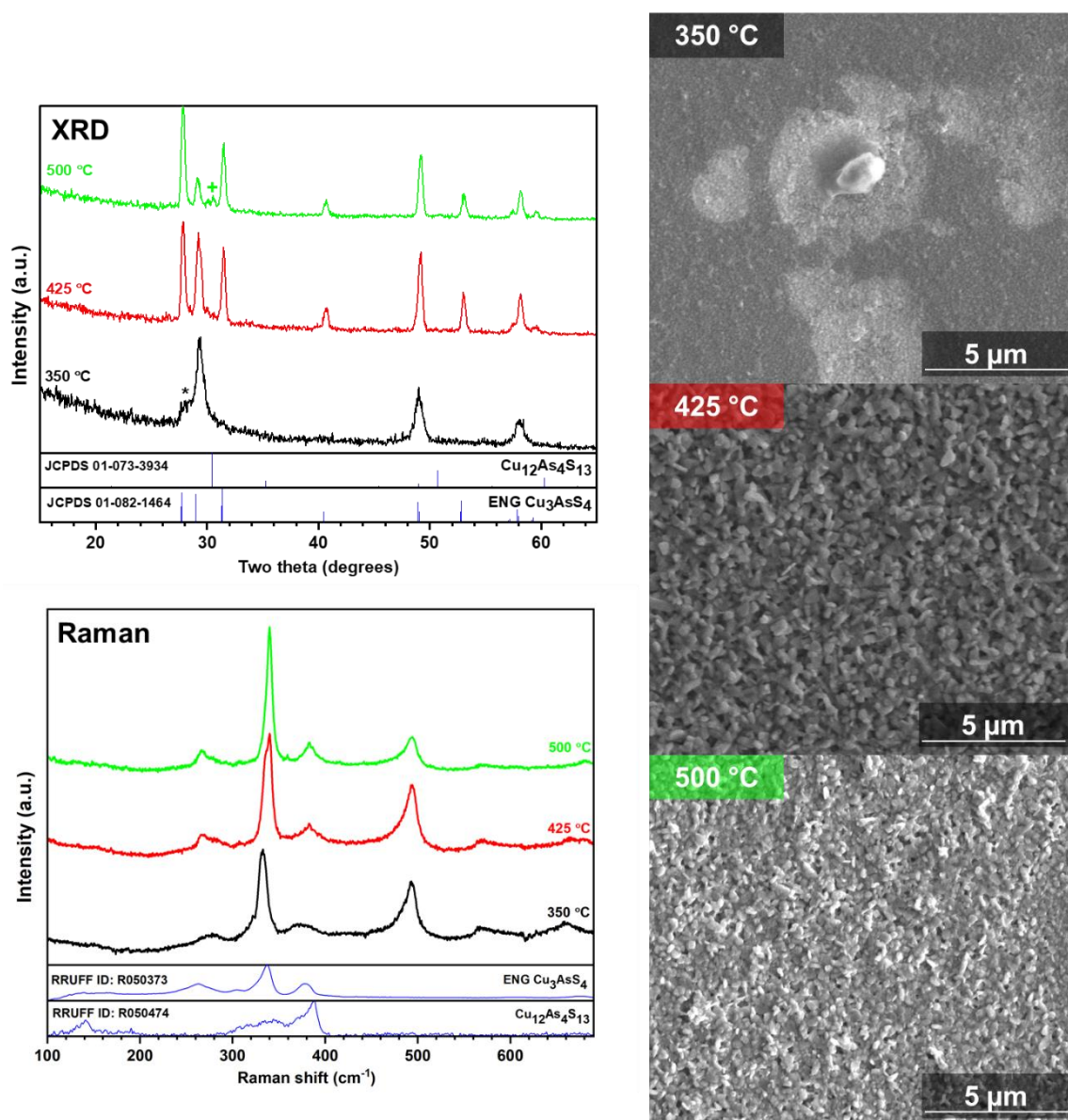


Figure 3.5. XRD spectra, Raman spectra, and plan-view SEM images of stacks of As_2S_3 on LUZ NPs heated in sulfur for 30 min at the indicated temperature. In the XRD spectra, the (*) symbolizes a (210) shoulder of enargite Cu_3AsS_4 , and the (+) indicates the (222) peak of tennantite $\text{Cu}_{12}\text{As}_4\text{S}_{13}$.

The effects of coating As_2S_3 directly onto molybdenum and then depositing LUZ NPs on top were also investigated. Such a scenario may result in bottom-up growth of grains and the rejection of carbonaceous ligands and excess As-S species to the surface of the film, where they can be removed using chemical or mechanical etching. Consistent with previous results, the XRD and Raman spectra (Figure 3.6) of $425\text{ }^\circ\text{C}$ treated films indicate conversion to TEN in argon and conversion to ENG in sulfur and As_2S_5 . Plan view SEM images indicate grain growth in all atmospheres, though the grains are significantly larger in an As_2S_5 atmosphere than the other two. Cracks are apparent in the argon and sulfur samples and are also seen in optical microscope images of As_2S_3 films, suggesting a need to refine the spin coating deposition of BA- As_2S_3 . Side view SEM images suggest that bottom-up growth has occurred in all three, with one $\sim 100\text{ nm}$ thick layer of grains in the sulfur and As_2S_5 cases and a stack of $\sim 100\text{ nm}$ grains in the argon sample. The argon-treated sample has one amorphous layer on top of its grains, likely consisting of rejected material from the film. The sulfur and As_2S_5 samples, however, have two additional layers – one without significant grain growth, and the other with grains formed because of interactions with the annealing atmosphere. The top layer of grains will likely be more difficult to selectively etch due to the general insolubility of ternary phases.

The deposition of As_2S_3 films on top of or below LUZ NPs represent an improvement to ENG film processing, particularly because sulfur treatments can occur on larger substrates compared to the current As_2S_5 heat treatments. Optimization of the amount of As_2S_3 added, as well as tuning the composition (S can also dissolve in BA as discussed in Chapter 9 and 10) and adjusting the heating profile, may ultimately result in the fabrication of films containing micron-sized dense grains throughout. However, the carbonaceous secondary phase persists in this scheme, and methods to eliminate it must be developed.

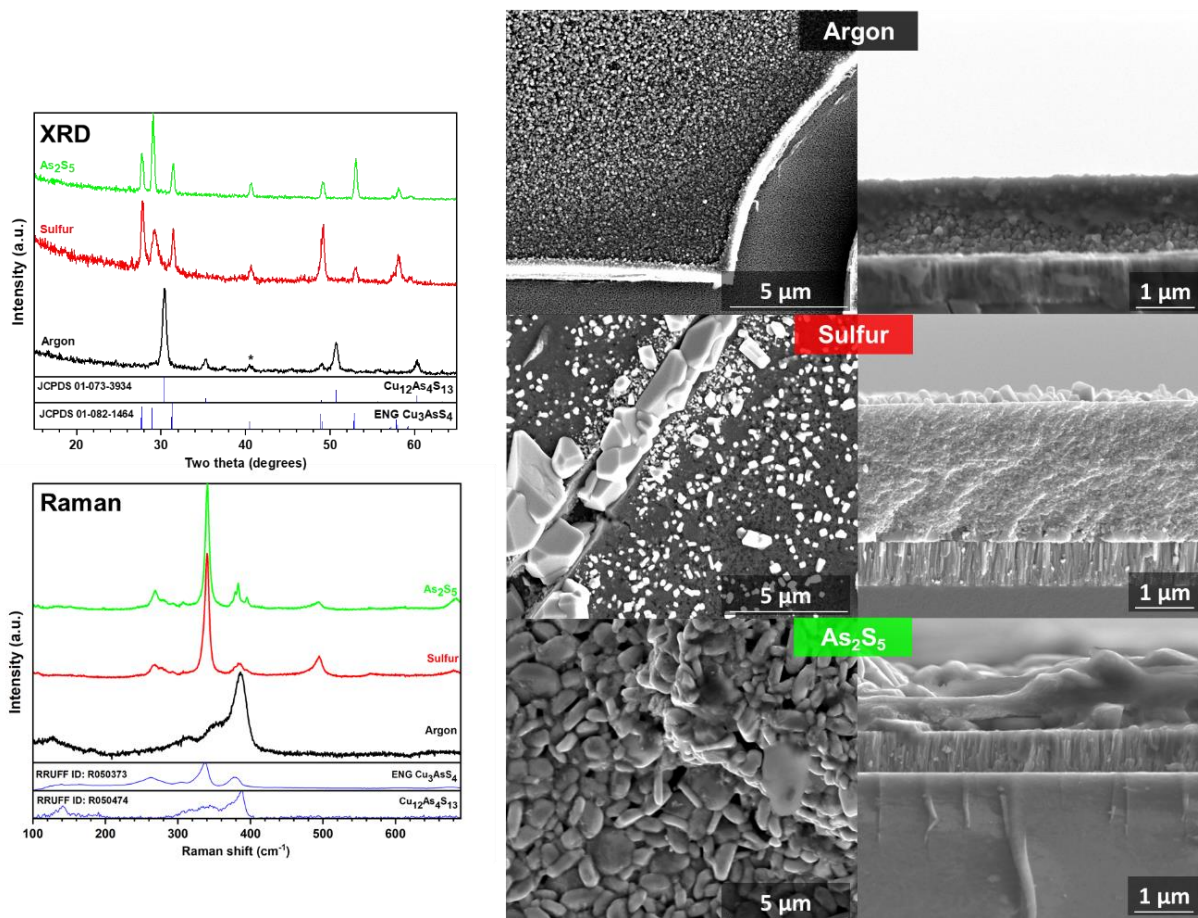


Figure 3.6. XRD and Raman spectra, and plan view and cross-sectional SEM images of stacks of LUZ NPs on top of As₂S₃ annealed at 425 °C for 30 min in the indicated atmosphere. The (*) in the argon XRD spectra is attributed to the Mo substrate.

3.3.4 Optimization of Arsenic(V) Sulfide Heat Treatments

The As₂S₅-based annealing procedure outlined in Chapter 2 focused on the effects of temperature on the growth of ENG films from LUZ NP precursors. Other variables, such as the amount of As₂S₅ added to the ampoule, the thickness of the final ENG film, and the time of annealing were not considered there; this section outlines selected experiments related to these parameters using 425 °C as the annealing temperature unless otherwise noted.

3.3.4.1 Reduction of Arsenic(V) Sulfide Charged to the Ampoule

In Chapter 2, ~37 mg of As₂S₅ was added to the ampoule before sealing in an ampoule and heating at 425 °C. Assuming (to the zeroth order) that all As₂S₅ vaporizes congruently into an ideal

gas, the pressure established in the ampoule is roughly 520 torr. In reality, As_2S_5 decomposes at low temperatures and then evaporates as S_x and As_2S_y compounds, which both contribute to the pressure inside of the ampoule [9]. Vapor pressures of arsenic sulfide at ENG processing conditions are not available, but due to the high boiling point ($\sim 707^\circ\text{C}$ for As_2S_3), it is highly likely that 37 mg of As_2S_5 at 425°C corresponds to saturation of the atmosphere with arsenic species. Conversely, the atmosphere is undersaturated with sulfur, as its vapor pressure is ~ 0.9 atm (~ 680 torr) at 425°C [10]. Therefore, any liquid phase is likely due to the condensation of As-S species on the surface. Smaller amounts of As_2S_5 charged to the ampoule may minimize the reaction of carbonaceous ligands with sulfur and the amount of excess species that may condense on the surface of the sample during cool down.

Figure 3.7 gives the Raman spectra and plan view SEM images of LUZ NP films that were treated in the presence of 1.7, 5.2, and 10.1 mg of As_2S_5 ; these masses correspond to zeroth-order vapor pressures of 24, 73, and 140 torr, respectively. Conversion to the ENG phase is noted, with the presence of the 490 cm^{-1} impurity in all three spectra. However, the SEM images reveal a difference in grain size – the 1.7 mg sample showed grains that are much smaller than either of the other two samples. This result suggests that ~ 5 mg of As_2S_5 is the minimum to ensure growth of micron sized grains at 425°C . Many experiments discussed in the remainder of this thesis were conducted with ~ 10 mg of As_2S_5 to reduce the excess material in the ampoule.

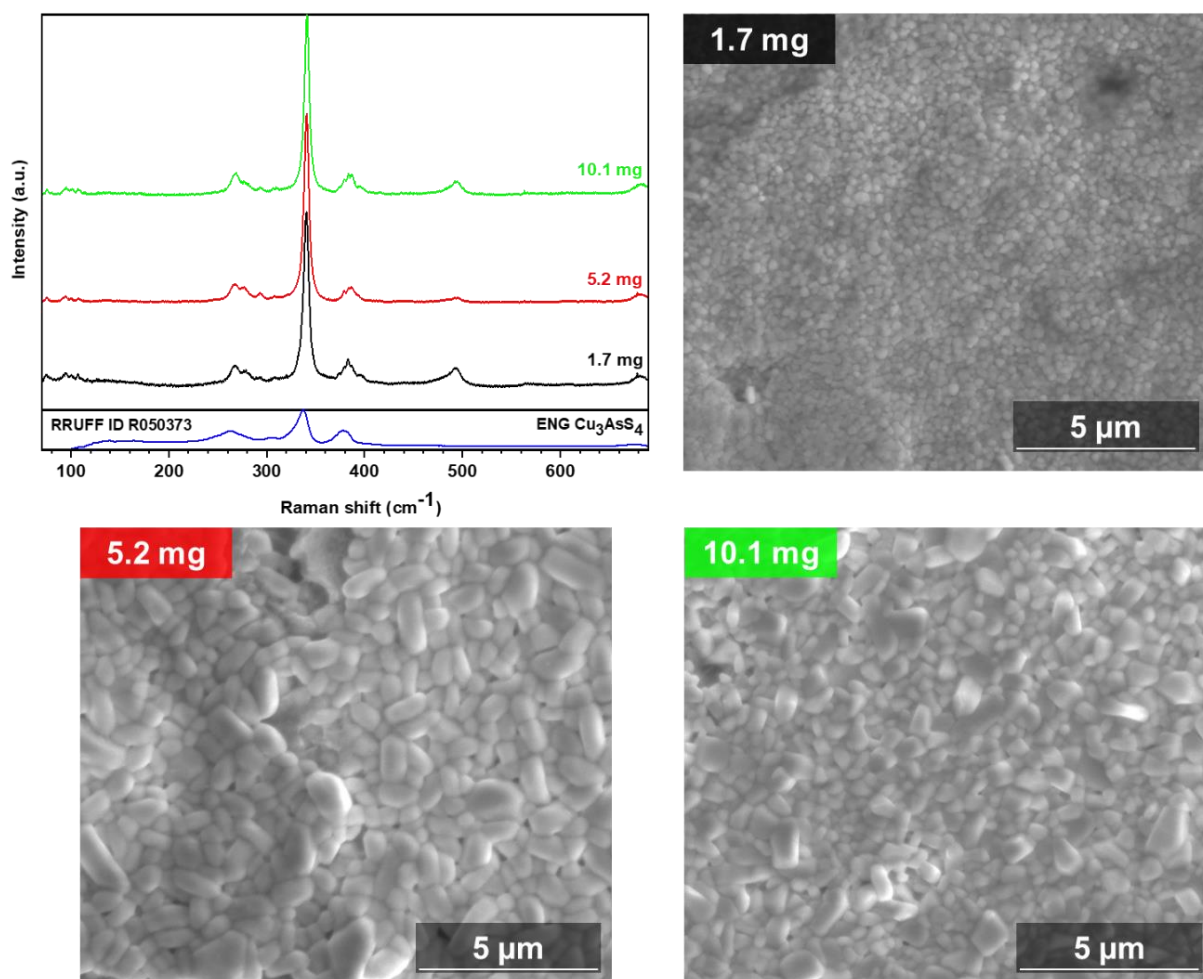


Figure 3.7. Raman spectra and plan-view SEM images of LUZ NPs heated at 425 °C for 30 min with reduced amounts of As_2S_5 added to the ampoule.

3.3.4.2 Effects of Direct Reaction with As-S Liquid at Low Temperature

The hypothesized mechanism of grain growth for ENG thin films from LUZ NPs involves the formation of a liquid phase consisting of arsenic and sulfur. Previous experiments have assumed condensation of the liquid from a supersaturated atmosphere, but differences in film roughness and uneven distribution of As_2S_5 powder can result in nonuniformities throughout the film. One approach to fabricating more uniform films is to immerse the film directly in a liquid phase. As a proof-of-concept experiment, a LUZ NP film was sealed in an ampoule and placed face down in a pile of ~ 200 mg As_2S_5 powder. The ampoule was heated to 325 °C (just exceeding the melting point of all As-S binaries) for 30 min. Figure 3.8 gives the XRD, Raman, and SEM

characterization of the material. Conversion to ENG is noted even at 325 °C, which was not observed with the sulfur anneals discussed earlier in this chapter and further suggests the need for added arsenic to facilitate the LUZ-to-ENG phase transformation. Additionally, a thin orange material was noted on some areas of the sample; the Raman spectrum indicates that this is likely As_4S_4 in the monoclinic bonazzite crystal structure (RRUFF ID: R061028). The SEM image shows growth of elongated grains with lengths on the order of several hundred nm, though there is significant porosity noted. Further experiments must focus on optimizing the temperature and annealing time to grow larger grains, though the importance of safety in working with large amounts of arsenic at high temperatures must be stressed.

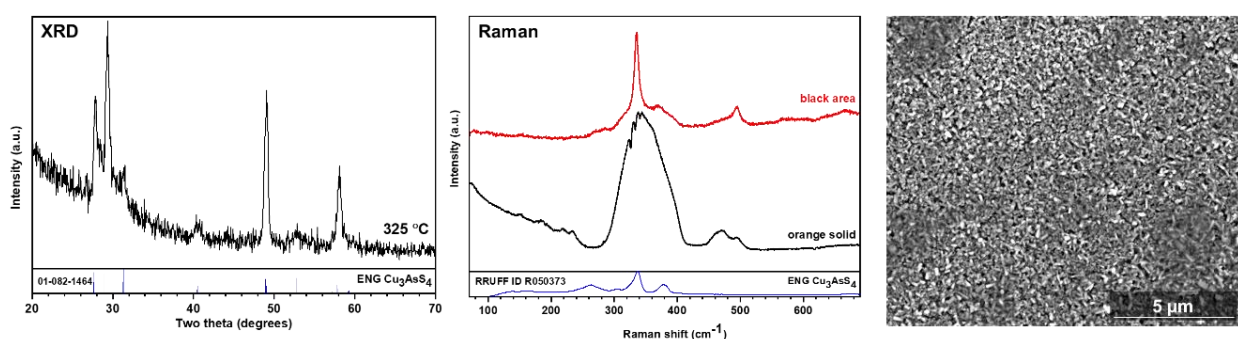


Figure 3.8. XRD spectrum, Raman spectra, and plan view SEM image of a LUZ NP film that was annealed at 325 °C for 30 min while face down in As_2S_5 powder.

3.3.4.3 Effects of Doubling the Active Layer Thickness on Device Performance

In the initial iterations of Cu_3AsS_4 device fabrication, two layers of NPs were coated, followed by ampoule sealing and As_2S_5 annealing. This treatment did not fully densify the film, resulting in pores by which n-type cadmium sulfide can infiltrate ENG films and directly contact the Mo substrate, reducing the shunt resistance and degrading device performance significantly. To minimize the effect of pores, a two-treatment procedure was tested – LUZ NPs were coated and heated in As_2S_5 as normal, but after the first treatment, two more layers of LUZ NPs were coated on top, and the film was heated again for 1 h in As_2S_5 . The hypothesis was that the second layer of NPs may either infiltrate the pores or that the growing grains would block shunt pathway formation.

The plan-view SEM image in Figure 3.9 shows that micron-sized grains are formed in this heat treatment scheme (though it appears that the roughness of the film has increased), and that discontinuities between grains appear to be filled by a solid material, as opposed to nothing. A representative cross-section of the completed device shows two distinct layers of grains, with a “fine-grain” layer below each; the top layer of ~ 400 nm consists of cadmium sulfide and transparent conductive oxides that were deposited to finish the device. The J-V curves of the champion cell are also given in Figure 3.9; indicating that the efficiency (0.33%) nearly doubled over the base case (0.18%) presented in Chapter 2. The device benefitted primarily from a significant increase in short-circuit current density (from 3.3 to 5.4 mA/cm²), with only modest increases in the open-circuit voltage (0.17 to 0.19 V) and fill factor (32.3 to 32.8%). (Note that the J-V data in Figure 3.9 is noisy; during measurements, the compliance current was set too high (0.3 A). For devices with low current density, a setting of 0.1 A is recommended.)

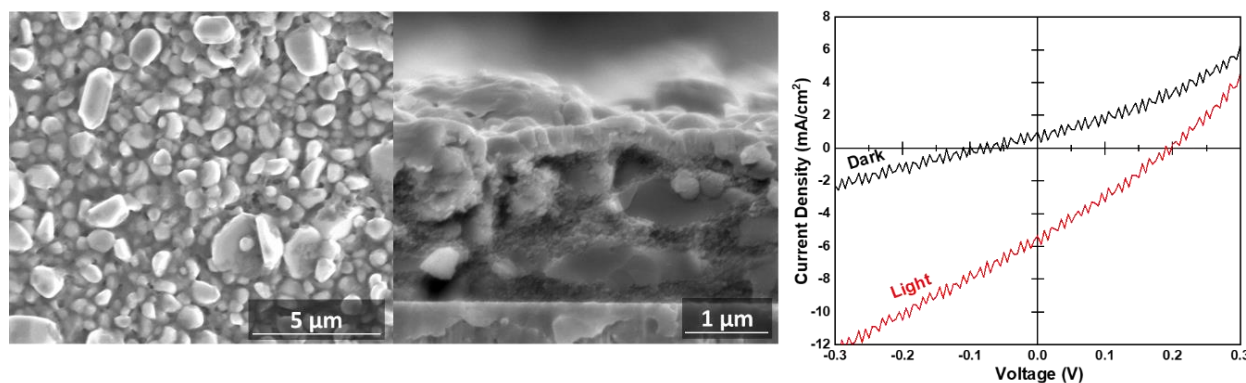


Figure 3.9. SEM images (plan-view and cross-sectional) and J-V curves of double-treated enargite-based devices.

Devices were also fabricated with films using several different combinations of variables, including thicker NP precursor layers, two treatments at different temperatures, etc. However, none of them achieved the same performance improvements that were just discussed. Further investigation into the double coating scheme may prove worthwhile for device efficiencies, though the effects of carrier mobility and lifetime (see Chapter 6) must also be considered to avoid an excessively thick film.

3.3.4.4 Procedural Modifications for a 0.35% Efficient Enargite Device

As suggested in Section 3.3.4.1, using less As_2S_5 for heat treatments may reduce the amount of species that condense on the surface during cooling. When ~ 10 mg As_2S_5 was used with an optimized coating procedure (see Appendix A), a 30 min anneal at 425 °C, and treatment of two ampoules in the tube furnace at once, a champion device efficiency for a single heat treatment process was achieved. Figure 3.10 gives the J-V and EQE characterization of this device with a magnesium fluoride (MgF_2) antireflective coating added on top of the grids. The original device (MgF_2 coated device) had performance characteristics of $J_{\text{sc}} = 3.8$ (5.1) mA/cm^2 , $V_{\text{oc}} = 0.22$ (0.23) V, $\text{FF} = 27.7$ (29.8) %, and efficiency = 0.23 (0.35) %. This 0.35% efficiency is the highest achieved from a NP-based device to date, though application of MgF_2 to the double-treated device described in the previous section would have almost certainly resulted in a higher efficiency. Integration of the EQE curve gives a zero-bias current density of 5.5 mA/cm^2 , in close agreement with the value obtained from J-V measurements. The current density below 510 nm (~ 2.43 eV, or the band gap of CdS) was 3.8 mA/cm^2 , indicating that a significant amount of current was obtained from the ENG absorber layer. A band gap of 1.4 eV was also extracted by extrapolating a plot of $[\ln(1-\text{EQE})]^2$ to zero [11].

The achievement of a 0.35% device is an important step towards the development of high-efficiency ENG-based devices. However, despite many other iterations on the parameters here, better performance was not achieved. It is likely that the carbonaceous secondary phase and the band alignment at the pn junction limit device efficiencies; both topics are explored later in this thesis.

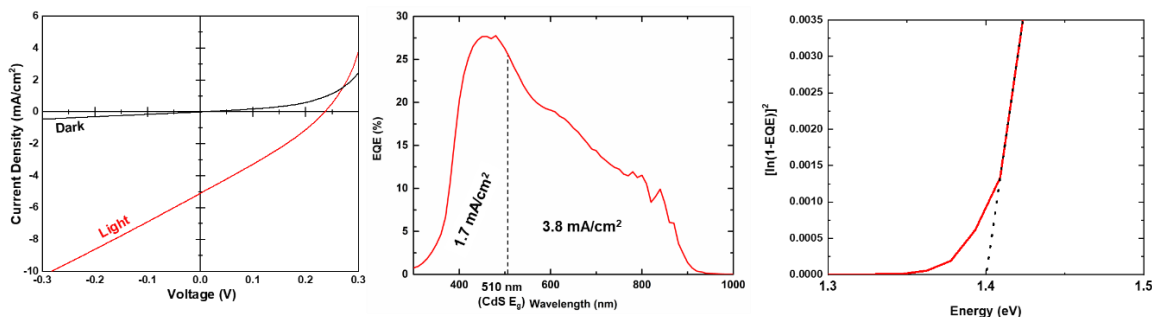


Figure 3.10. J-V and EQE analysis of the champion NP-based ENG device achieved in this thesis. The left panel shows a MgF_2 -coated device with $J_{\text{sc}} = 5.1$ mA/cm^2 , $V_{\text{oc}} = 0.23$ V, $\text{FF} = 29.8\%$, and efficiency = 0.35%. The middle panel gives the EQE as a function of wavelength and the current densities above and below the bandgap of CdS, and the right panel shows the extraction of the band gap from EQE data.

3.3.5 Pre-Annealing of Luzonite Nanoparticle Films

The OLA ligands present on LUZ NPs ensure colloidal stability for solution deposition and size and shape control during hot-injection synthesis. However, their effects on device performance are likely detrimental, as they form a secondary phase with a signature Raman peak near 490 cm^{-1} . Additionally, a recent study showed that a solid sphere with very high resistivity results from the reaction of OLA and sulfur at elevated temperatures [12]. Removal of carbon from the film is therefore key in ensuring devices with appropriate conductivity throughout.

One potential method to remove carbonaceous ligands from the film is to anneal them at a relatively low temperature; TGA results in Chapter 2 showed several mass loss events prior to the loss of arsenic sulfide species (i.e. $< 300\text{ }^\circ\text{C}$) from the film. Figure 3.11 gives the Raman characterization of LUZ NP films that were indicated at the time and temperature indicated in argon (or 1% H_2S). When the temperature was below $250\text{ }^\circ\text{C}$, the film remained as LUZ, but conversion to TEN was observed at $250\text{ }^\circ\text{C}$ (though only partially when exposed to H_2S). When such films were heated in As_2S_5 at $425\text{ }^\circ\text{C}$ for 1 h, the intensity of the secondary phase peak was greatly reduced (or even eliminated for the sample treated at $250\text{ }^\circ\text{C}$ for 1 h in argon) suggesting that the pre-anneals removed some of the original carbon from the film.

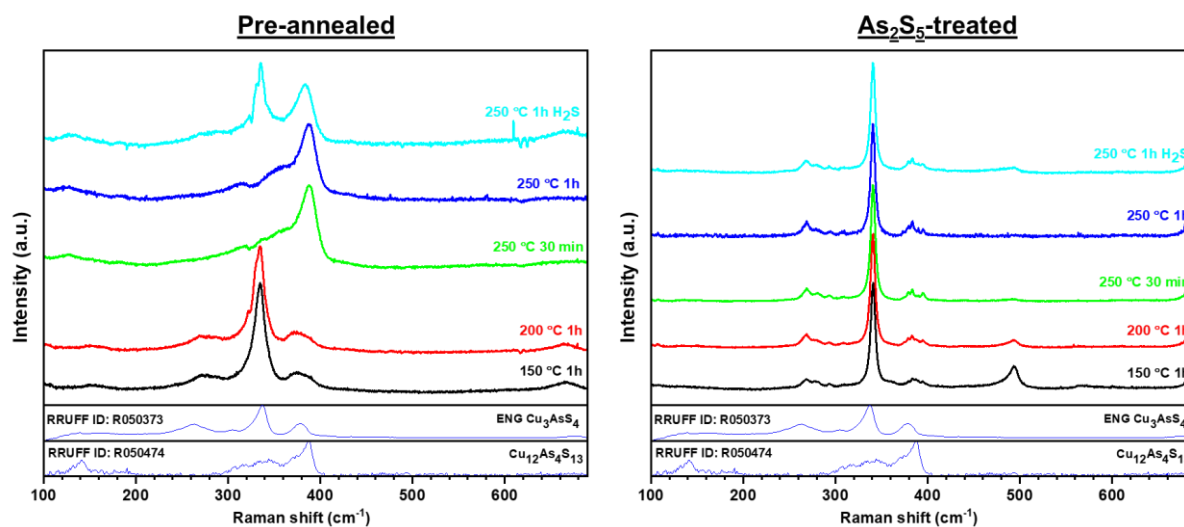


Figure 3.11. Raman spectra of LUZ NP films that were (left panel) pretreated in argon or H_2S at the given time and temperature and then (right panel) annealed in an ampoule with As_2S_5 for 1 h at $425\text{ }^\circ\text{C}$.

Devices were made from films depicted in Figure 3.11, but high efficiencies were not achieved. In fact, the best efficiency achieved was only 0.07%, and many cells were short-circuited. Figure 3.12 gives the SEM images of one pre-treated film and all five post-treated films. Significant cracking occurred throughout the film, resulting in short-circuit pathways that decreased the shunt resistance and ultimately degraded device performance. While it is interesting that some grains grew in the cracks, they did not completely fill them. The preliminary experiments here indicate that simple annealing is not a suitable route to remove carbon from the film; alternative routes such as ligand exchange (Chapter 5) may be necessary to eliminate secondary phases in NP-based ENG devices.

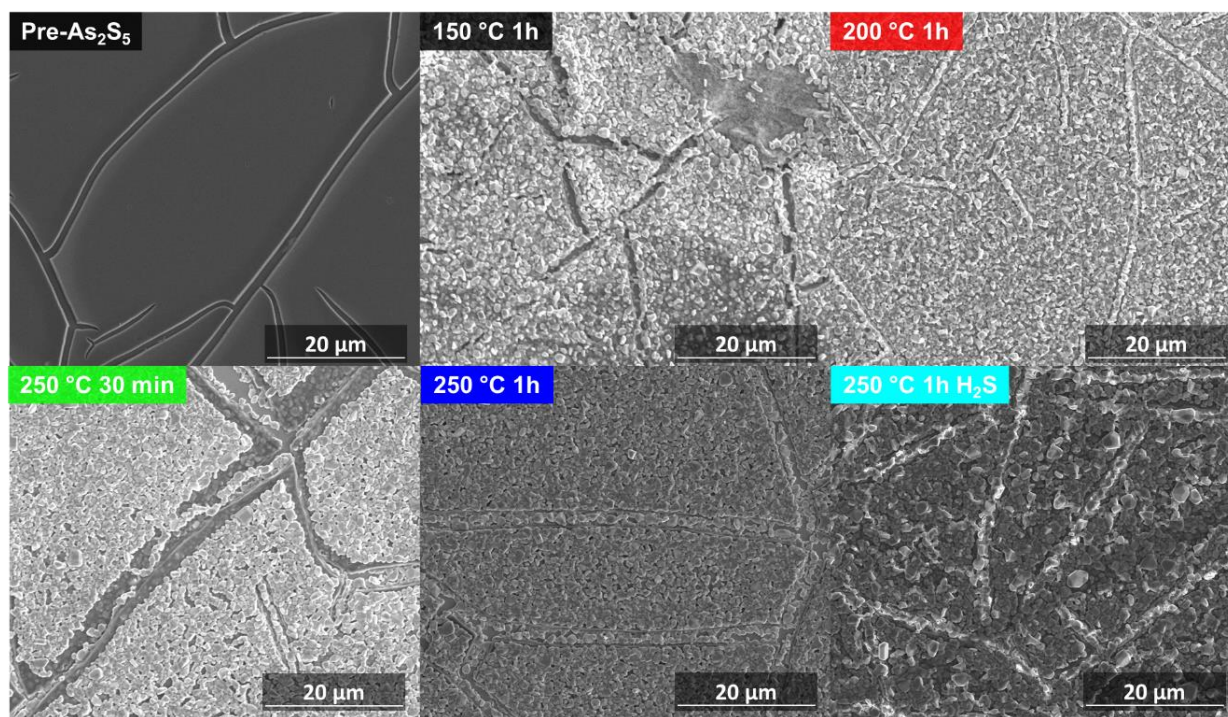


Figure 3.12. Plan view SEM images of one film that was pre-annealed in argon at 250 °C for 1 h, and five films that were pre-annealed at the given conditions and then heat treated in As_2S_5 at 425 °C for 1 h.

3.3.6 Impacts of Substrate on Enargite Film Orientation

In later chapters of this thesis, the results of several characterization techniques on ENG films are presented; many required substrates besides molybdenum-coated soda lime glass. For example, time-resolved terahertz spectroscopy (Chapter 6) requires a quartz substrate. Heat

treatments at 425 °C were conducted, and the impacts on the XRD patterns were studied. Figure 3.13 gives the relative intensity ratios of the (210), (002), and (211) peaks (the trio appearing between 28 and 32° 2 θ) of the ENG films taken in PB mode. The results suggest that the substrate may play a significant role in determining preferred orientation of ENG films, with the preliminary data suggesting that substrates with higher levels of sodium may result in preferred texturing along the (002) plane. This observation is a first step towards controlling the orientation of ENG films, though a more rigorous study is needed, as other factors such as As₂S₅ quantity, carbonaceous residue, small variations in film thickness, etc. may contribute to the variations in orientation seen here.

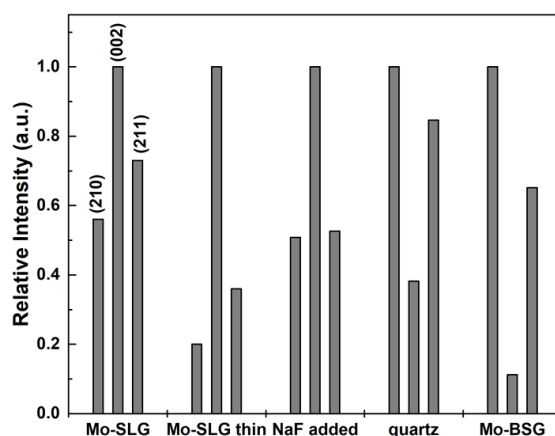


Figure 3.13. Relative intensity of three XRD peaks in BB mode acquired from five different substrates: a standard Mo-soda lime glass substrate, a Mo-SLG substrate with a thinner absorber layer, a Mo-SLG substrate with NaF added to the surface, a quartz substrate, and a Mo-coated borosilicate glass substrate.

Fluorine-doped tin oxide (FTO) was also tested as a substrate for LUZ NP heat treatments; such a material is often used in inverted device configurations. However, tin is NOT inert to the combination of LUZ NPs and the As₂S₅ annealing atmosphere, as copper tin sulfide (Cu₂SnS₃) was formed upon heating at 425 °C for 1 h (Figure 3.14).

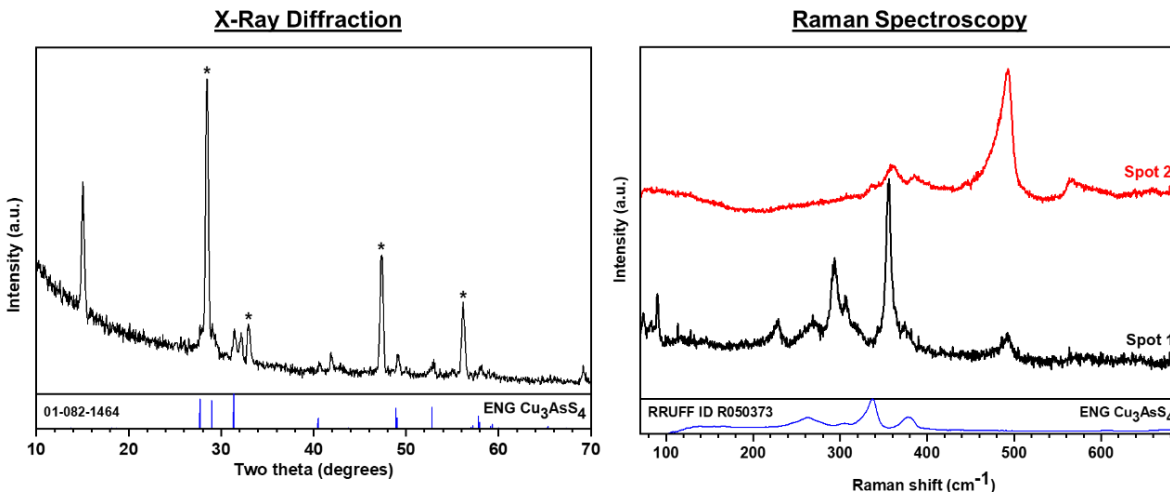


Figure 3.14. XRD and Raman spectra of LUZ NPs on FTO heated in As_2S_5 at $425\text{ }^\circ\text{C}$ for 1 h. In the XRD spectra, the (*) stand symbolize tetragonal Cu_2SnS_3 (ICSD collection code 29-570), with an additional peak at $31^\circ 2\theta$ tentatively attributed to covellite CuS . The Raman spectrum matches with a previous report [13].

3.4 Conclusions

In this chapter, a variety of methods aimed at engineering growth of enargite Cu_3AsS_4 thin films and their ultimate impact on grain structure and device performance were explored. Anneals in vacuum and sulfur indicated that LUZ NPs naturally coalesce into large, isolated grains, suggesting that an external supply of an arsenic sulfide is necessary for densified film growth. The deposition of thin As_2S_3 films onto or beneath LUZ NPs was used to grow grains on larger substrates, and the minimum amount of As_2S_5 required for significant grain growth was determined. Routes to improving solar cell performance were also presented – by either optimizing the precursor film depositions and heat treatment times, or by conducting two separate heat treatments on the same film, device efficiencies exceeded 0.3%. However, in all cases, the secondary carbonaceous phase persisted, restricting efficiencies to low values. The secondary phase was reduced by pre-annealing in argon, but cracks in the film outweighed any benefits from reducing the secondary phase. A more dramatic change to processing conditions is clearly needed to produce high quality ENG thin films for device applications. This may be recognized through ligand exchange (Chapter 5) or the use of molecular precursors (Chapter 9), which eliminate carbon from the film prior to As_2S_5 treatments and hence avoid secondary phase formation altogether.

3.5 Acknowledgements

S.A.M. acknowledges the National Science Foundation (grant #DMR-1534691) and Purdue University (Bilsland Dissertation Fellowship) for financial support, and thanks Brian Graeser, Robert Boyne, Xianyi Hu, Joe Andler, and Essam AlRuqobah for their expertise in preparing molybdenum-coated soda lime glass. He declares no competing financial interests.

3.6 References

- [1] G. C. Chern and I. Lauks, "Spin-coated amorphous chalcogenide films," *J. Appl. Phys.*, vol. 53, no. 10, pp. 6979–6982, 1982.
- [2] G. C. Chern and I. Lauks, "Spin coated amorphous chalcogenide films: Structural characterization," *J. Appl. Phys.*, vol. 54, no. 5, pp. 2701–2705, May 1983.
- [3] S. Maske and B. J. Skinner, "Studies of the sulfosalts of copper I. Phases and phase relations in the system Cu-As-S," *Econ. Geol.*, vol. 66, no. 6, pp. 901–918, Oct. 1971.
- [4] E. Makovicky and B. J. Skinner, "Studies of the sulfosalts of copper. VI. Low-temperature exsolution in synthetic tetrahedrite solid solution, $\text{Cu}_{12+x}\text{Sb}_{4+y}\text{S}_{13}$," *Can. Mineral.*, vol. 16, pp. 611–623, 1978.
- [5] R. B. Balow, E. J. Sheets, M. M. Abu-Omar, and R. Agrawal, "Synthesis and Characterization of Copper Arsenic Sulfide Nanocrystals from Earth Abundant Elements for Solar Energy Conversion," *Chem. Mater.*, vol. 27, no. 7, pp. 2290–2293, Apr. 2015.
- [6] G. C. Chern, I. Lauks, and A. R. McGhie, "Spin coated amorphous chalcogenide films: Thermal properties," *J. Appl. Phys.*, vol. 54, no. 8, pp. 4596–4601, 1983.
- [7] C. J. Hages, M. J. Koeper, C. K. Miskin, K. W. Brew, and R. Agrawal, "Controlled Grain Growth for High Performance Nanoparticle-Based Kesterite Solar Cells," *Chem. Mater.*, vol. 28, no. 21, pp. 7703–7714, Nov. 2016.
- [8] S. McLeod, E. Alruqobah, and R. Agrawal, "Liquid assisted grain growth in solution processed $\text{Cu}(\text{In,Ga})(\text{S,Se})_2$," *Sol. Energy Mater. Sol. Cells*, vol. 195, no. February, pp. 12–23, 2019.
- [9] A. F. Holleman, E. Wiberg, and N. Wiberg, *Inorganic Chemistry*. San Diego, CA: Academic Press, 2001.
- [10] B. Meyer, "Elemental sulfur," *Chem. Rev.*, vol. 76, no. 3, pp. 367–388, Jun. 1976.

- [11] C. J. Hages, N. J. Carter, and R. Agrawal, “Generalized quantum efficiency analysis for non-ideal solar cells: Case of $\text{Cu}_2\text{ZnSnSe}_4$,” *J. Appl. Phys.*, vol. 119, no. 1, p. 014505, Jan. 2016.
- [12] T. J. Huang, X. Yin, C. Tang, G. Qi, and H. Gong, “Influence of Ligands on the Formation of Kesterite Thin Films for Solar Cells: A Comparative Study,” *ChemSusChem*, vol. 9, no. 9, pp. 1032–1041, May 2016.
- [13] D. M. Berg *et al.*, “Raman analysis of monoclinic Cu_2SnS_3 thin films,” *Appl. Phys. Lett.*, vol. 100, no. 19, 2012.

4. POST-HEAT TREATMENT PROCESSING OF ENARGITE THIN FILMS

4.1 Introduction

Chapter 2 outlined a scheme for the fabrication of (ENG) Cu_3AsS_4 thin films from luzonite (LUZ) Cu_3AsS_4 nanoparticle (NP) precursors. The process resulted in a thin film with micron-sized dense grains but had two major shortcomings: a secondary phase formed from the reaction of carbonaceous ligands with sulfur species in the atmosphere, and the off-stoichiometric composition resulting from condensation of arsenic and sulfur species on the film's surface during cool down. Efforts to remove the secondary phase by modifying the annealing conditions during film synthesis were generally unsuccessful, as discussed in Chapter 3, and the composition of the ENG film surface has not yet been addressed.

Etching of chalcogenide thin films has been studied widely in the literature. Many use highly hazardous materials – for example, potassium cyanide (KCN) and bromine have been used to remove copper selenide phases from the surface of $\text{Cu}(\text{In,Ga})\text{Se}_2$ films [1]. However, the scheme used for the fabrication of ENG films results in surfaces that are almost certainly As- and S-rich, so materials that etch copper should be avoided. For arsenic-based compounds, diammonium sulfide ($(\text{NH}_4)_2\text{S}$, DAS) and amine-thiol mixtures can dissolve As_2S_3 compounds, though certain combinations of amine and thiol also dissolve copper species [2]–[4]. Additionally, a paper on CuSbS_2 -based solar cells reports selective etching of Sb_2S_3 by potassium hydroxide (KOH) [5]. Because arsenic and antimony occupy the same column of the periodic table, it is worth exploring techniques developed for the etching of antimony-based materials.

In this chapter, post-processing experiments aimed at cleaning the surface of ENG thin films and removing the secondary phase are presented. First, the surface chemistry is explored with X-ray photoelectron spectroscopy (XPS). The effects of liquid-based etching procedures on ENG's composition and the secondary phase are discussed. Then, heat treatments of ENG films in various atmospheres are explored with the goal of removing the secondary phase through evaporation. Finally, experiments related to hot pressing and electrochemically etching ENG films are discussed. The results presented in this chapter reveal a straightforward route for etching of the surface of ENG thin films but suggest that removing the secondary phase via post-processing methods is not feasible.

4.2 Experimental Methods

4.2.1 Chemicals

All chemicals were used as received unless otherwise noted. Ammonium sulfide ((NH₄)₂S, 40 – 48 wt% in water), hydrochloric acid (HCl, 37%), n-butylamine (BA, >99.5%), ethanethiol (ET, >97%) and potassium cyanide (KCN, >85%) were obtained from Sigma-Aldrich. Ammonium hydroxide (NH₄OH, 28-30 wt% in water) was obtained from J. T. Baker. Potassium hydroxide (KOH, ACS Reagent) and sodium hydroxide (NaOH, ACS Reagent) were obtained from Macron. Argon gas (>99.997%) was obtained from Indiana Oxygen, and hydrogen sulfide (H₂S, 0.97%, balance argon) was obtained from Airgas.

4.2.2 Post-Processing Techniques

All liquid etches were conducted by placing an ENG film into a 4 mL vial and adding the liquid via pipet. Post-annealing heat treatments occurred in furnaces described in more detail in Chapter 7 of this thesis. Briefly, argon and H₂S anneals took place in a vertical tube furnace with samples secured in place using a manual push-pull rod and a custom graphite sample holder, and the sulfur anneal took place in a horizontal tube furnace with the sulfur at 200 °C and the samples at 425 °C. Hot pressing experiments were conducted on a Carver hot press (Model 3851-00). Electrochemical etches were conducted in a home-built quartz cell with an ENG film as the working electrode, molybdenum as the counter electrode, and Ag⁺/AgCl as the reference electrode. The electrodes were connected to a Digi-Ivy D2011 potentiostat, and the applied bias was swept between -1 and 1 V cyclically at 50 mV/s, starting at 0 V and going in the positive direction.

4.2.3 Monte Carlo Simulations

Monte Carlo simulations of a 5 kV electron beam impinging on the top surface of a 1 μm Cu₃AsS₄-800 nm Mo film stack were conducted using Winxray, a free software program developed in Prof. Raynald Gauvin's group at McGill University (Canada) [6].

4.2.4 Characterization

X-ray diffraction (XRD) spectra were collected using a Rigaku Smartlab diffractometer in parallel beam mode with a 0.5° incident angle (Cu Kα radiation source, λ = 1.5406 Å). Raman spectra were acquired using a 633 He:Ne laser on a confocal microscope system (Horiba/Jobin-

Yvon LabRAM HR800). Scanning electron microscopy (SEM) and energy-dispersive X-ray spectroscopy (EDX) were conducted on an FEI Quanta 3D FEG dual-beam field emission SEM at 5 kV (EDX surface), 7 kV (SEM imaging), or 20 kV (EDX bulk). X-ray photoelectron spectroscopy (XPS) was conducted on a Kratos AXIS Nova system at the National Renewable Energy Laboratory (NREL). X-ray fluorescence (XRF) was conducted on a Fisherscope X-Ray XAN 250 with He flow at 50 kV using a 10 μm thick Ni filter.

4.3 Results and Discussion

4.3.1 Surface Etches of Enargite Thin Films

To determine the surface chemistry of as-treated ENG films, XPS was conducted on a LUZ NP sample that was heat treated at 425 °C for 1 h in As_2S_5 . XPS probes only the top ~5 nm of a sample, so it is very sensitive to oxygen and moisture. Therefore, the sample was shipped to the XPS at NREL in an ampoule taken directly from the furnace, and it was broken open in the glovebox, thereby avoiding air exposure after heat treatment. Figure 4.1 gives the detailed XPS spectra of an unetched ENG film, indicating the presence of not only copper, arsenic, and sulfur as expected, but also carbon, oxygen, and sodium. The presence of carbon and oxygen is expected in all XPS samples. The sodium may have diffused from the glass substrate. A compositional analysis gives a Cu:As:S ratio of 1:3.3:16.9, or a vast excess of arsenic and sulfur, demonstrating condensation from the atmosphere.

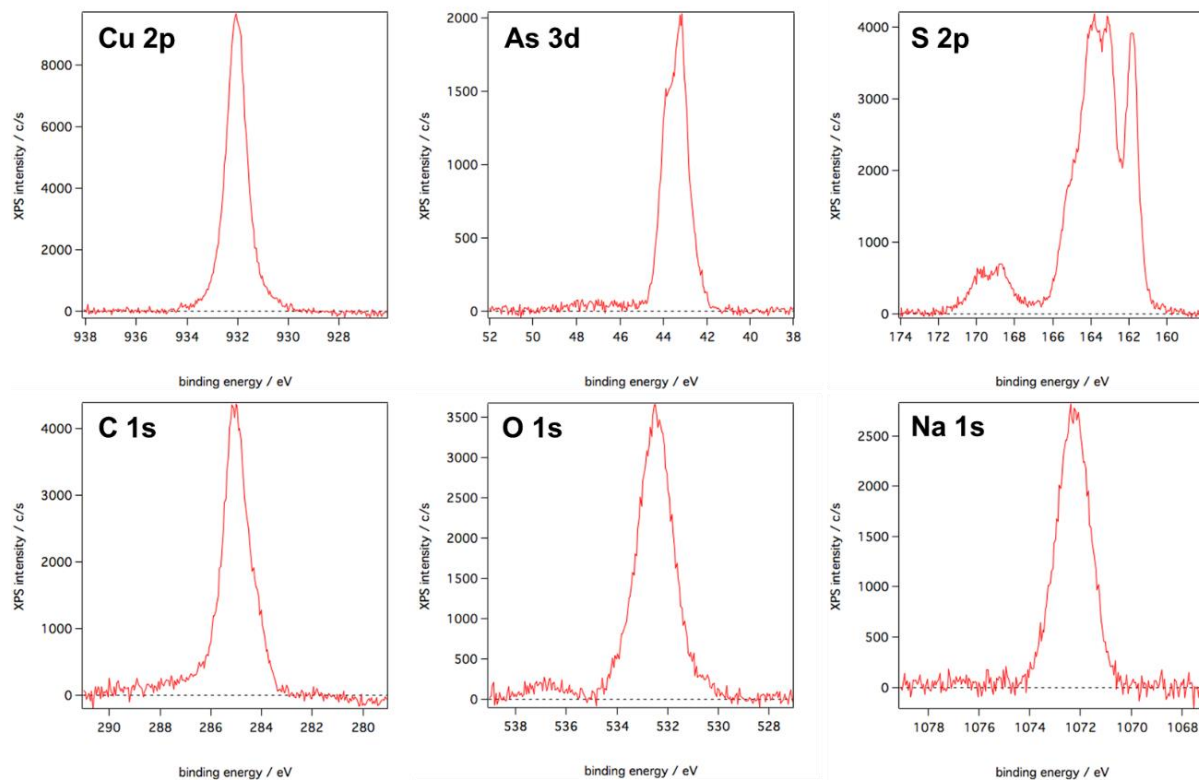


Figure 4.1. XPS narrow-scan spectra for a luzonite nanoparticle film treated in As_2S_5 for 1 h at $425\text{ }^\circ\text{C}$.

XPS is a powerful technique for analyzing the surfaces of samples, but instrument accessibility was an issue for these experiments. Another technique used to analyze composition is EDX, which is typically used for bulk analysis of thin films. In EDX, a sample is bombarded with an electron beam that ejects core electrons from a sample, which are then filled by relaxation of outer shell electrons that emit X-rays of characteristic energy, which are then analyzed. Typically, EDX is performed in an SEM at a high accelerating voltage ($\sim 20\text{ kV}$), ensuring that electrons penetrate deep ($\sim 1\text{ }\mu\text{m}$) into the sample. However, by using lower accelerating voltages and a different set of calibration standards, EDX can be used to roughly approximate changes in the surface composition. Figure 4.2 shows a Monte Carlo simulation of the trajectory of electrons impinging on a stoichiometric ENG film at an accelerating voltage of 5 kV , conditions that can be achieved using an SEM. Most electrons penetrate less than 100 nm into the material. While not as accurate or sensitive as XPS, any statistically significant changes in 5 kV EDX compositions will indicate significant etching of surface material.

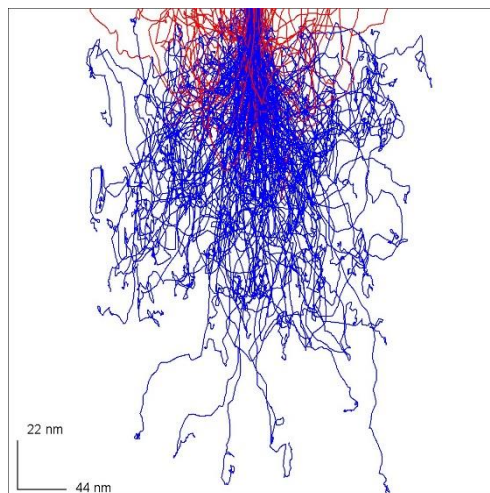


Figure 4.2. Winxray-simulated trajectory of electrons at a 5 kV accelerating voltage into a thick film of Cu_3AsS_4 .

The dissolution properties of arsenic compounds in liquids is not well known besides DAS. After As_2S_5 heat treatments are conducted, a significant amount of yellow-orange residue condenses on the internal walls of the ampoule; this residue was used to qualitatively screen the ability of various liquids to etch the surfaces of ENG thin films. Table 4.1 summarizes the interactions between various solutions and the condensed As-S residues. Aside from DAS, it appears that an amine-thiol mixture and two hydroxides may be effective for surface etching.

Table 4.1. Summary of interactions between ampoule residues and candidate etchants.

Etchant	Interaction with Residue
DAS	Near-instantaneous dissolution of residue
0.1 M NH_4OH	Slow dissolution of orange material with black particles remaining
0.1 M HCl	Dislodged residue from wall but no other interaction
0.1 M NaOH	Slow dissolution of orange material with black particles remaining
0.1 M KOH	Dislodged residue from wall but no other interaction
BA-ET (9:1 v:v)	Residue dissolved within 30 seconds
0.1 M KCN	Dislodged residue from wall but no other interaction

To quantify the effectiveness of the etchants, low-voltage EDX was conducted on ENG samples before and after immersion in the etching solution for 30 s. The results are summarized in Table 4.2. For many of the samples, the standard deviation is too large to make a statistically significant conclusion. However, a DAS solution clearly etches arsenic species preferentially, and

it also seems (less strongly) that KCN etches copper species preferentially. More precise quantification of the etching procedures should be done using XPS.

Table 4.2. Low-voltage EDX-determined elemental ratios before and after etches in the given solution. Standard deviations are based on multiple measurements at different spots on the sample.

Solution	Cu/As before	Cu/As after	S/As before	S/As after
DAS	2.53 ± 0.05	3.15 ± 0.05	5.26 ± 0.34	5.49 ± 0.11
0.1 M NH ₄ OH	2.69 ± 0.19	2.71 ± 0.03	5.30 ± 0.46	5.01 ± 0.12
0.1 M HCl	2.63 ± 0.01	2.52 ± 0.11	5.20 ± 0.10	4.73 ± 0.12
0.1 M NaOH	2.54 ± 0.06	2.52 ± 0.11	5.63 ± 0.06	5.83 ± 0.05
0.1 M KOH	2.75 ± 0.11	2.89 ± 0.07	4.69 ± 0.21	4.69 ± 0.14
BA-ET (9:1 v:v)	2.42 ± 0.08	2.69 ± 0.17	6.02 ± 0.33	6.40 ± 0.27
0.1 M KCN	2.45 ± 0.08	2.15 ± 0.11	5.73 ± 0.15	6.44 ± 0.39

DAS etching was further explored using XRF, which can determine the bulk composition and thickness, and unlike EDX, it can model a multi-layered film (including the Mo substrate). Table 4.3 shows the average elemental ratios before and after an etch in DAS, demonstrating a return to near-stoichiometric values. Additionally, the film thickness decreased, but the standard deviation was larger, suggesting that the As-S residues may not be distributed uniformly over the film. The effects on bulk morphology were explored using SEM (Figure 4.3); no noticeable changes were observed. While further optimization on etching times and re-measurement of the surface composition using XPS is still needed, it is clear that DAS is effective at removing As-S residues from ENG films and should be implemented in future device fabrication protocols.

Table 4.3. XRF-determined compositions of ENG films etched in DAS for 1 min. Sample 1 is on Mo-coated soda-lime glass, Sample 2 is on Mo-coated borosilicate glass, and Sample 3 is was made from ligand exchanged NPs on Mo-coated soda-lime glass. Standard deviations are computed from three repeated measurements on 3-4 different spots on the sample.

Sample	Thickness before	Thickness after	Cu/As before	Cu/As after
1	962 ± 57 nm	767 ± 81 nm	2.24 ± 0.03	3.00 ± 0.02
2	905 ± 36 nm	848 ± 73 nm	2.30 ± 0.02	3.01 ± 0.03
3	267 ± 13 nm	252 ± 18 nm	2.55 ± 0.08	2.90 ± 0.09

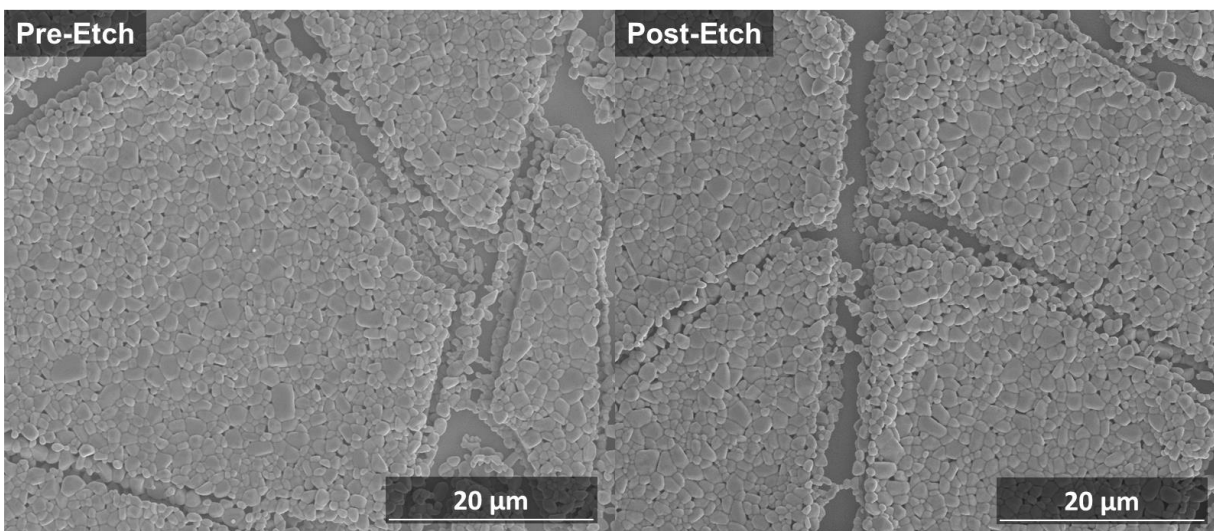


Figure 4.3. Plan view SEM images of an ENG thin film before and after etching in ammonium sulfide.

There are two other notes about the etching experiments presented in this section. One is that DAS etches on non-molybdenum substrates (e.g. quartz, bare soda-lime glass, etc.) resulted in delamination of the film; the role of the molybdenum-ENG interface must be explored in a future study. The other is that Raman spectra were taken before and after all etches; the etching had no effect on the carbonaceous secondary phase (stretch located near 490 cm^{-1}). A separate post-processing procedure may be required to eliminate this secondary phase, provided that OLA-based NPs are used extensively in future experiments.

4.3.2 Post-Heat Treatment Annealing of Enargite Thin Films

Annealing ENG films may remove As-S species from the surface (due to binary As-S species melting by $320\text{ }^{\circ}\text{C}$), may lead to evaporation of the carbonaceous secondary phase, and may lead to phase transformations while maintaining the micron-sized dense grain structure. To determine the thermal behavior of ENG thin films, TGA (Figure 4.4) was conducted on an ENG film that was scraped into an alumina sample pan and ramped to high temperatures under a flowing helium atmosphere. The film lost roughly 5% of its mass between 250 and $450\text{ }^{\circ}\text{C}$, with two additional mass loss events peaking near 480 and $540\text{ }^{\circ}\text{C}$. The lower-temperature losses may correspond to evaporation of material from the surface or the loss of some carbonaceous ligands, while the higher-temperature losses may correspond to more significant losses of material from the film bulk.

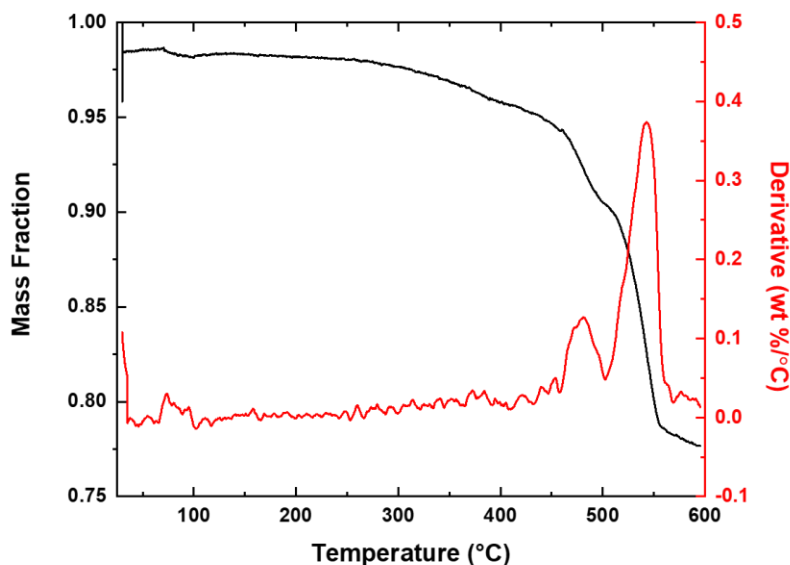


Figure 4.4. Thermogravimetric analysis (TGA) of an ENG film ramped to 600 °C at 10 °C/min in a 100 mL/min helium flow.

To investigate phase transformations of as-fabricated ENG films, three anneals were conducted: 160 °C for 21 h in argon flow, 400 °C for 1 h in an evacuated ampoule, and 500 °C for 1 h in argon flow. Characterization of all three samples is given in Figure 4.5. At lower temperatures (<450 °C), the film remained as ENG with no noticeable change in the XRD and Raman. There was no transformation to LUZ even though LUZ is more stable than ENG at low temperatures, suggesting a large activation energy for the ENG \rightarrow LUZ phase transition [7]. At 500 °C, the grain structure was severely degraded, resulting in a film without any discernable XRD peaks (besides the Mo substrate) and a Raman spectrum displaying peaks characteristic of the carbonaceous secondary phase only. EDX measurements also showed a near-complete loss of arsenic from this film. This suggests that micron-sized ENG grains are less stable than their mineral counterparts, which do not decompose until 550 °C [8], and confirms that the carbonaceous secondary phase has a very high melting or sublimation point as noted in a previous TGA study on oleylamine and sulfur [9].

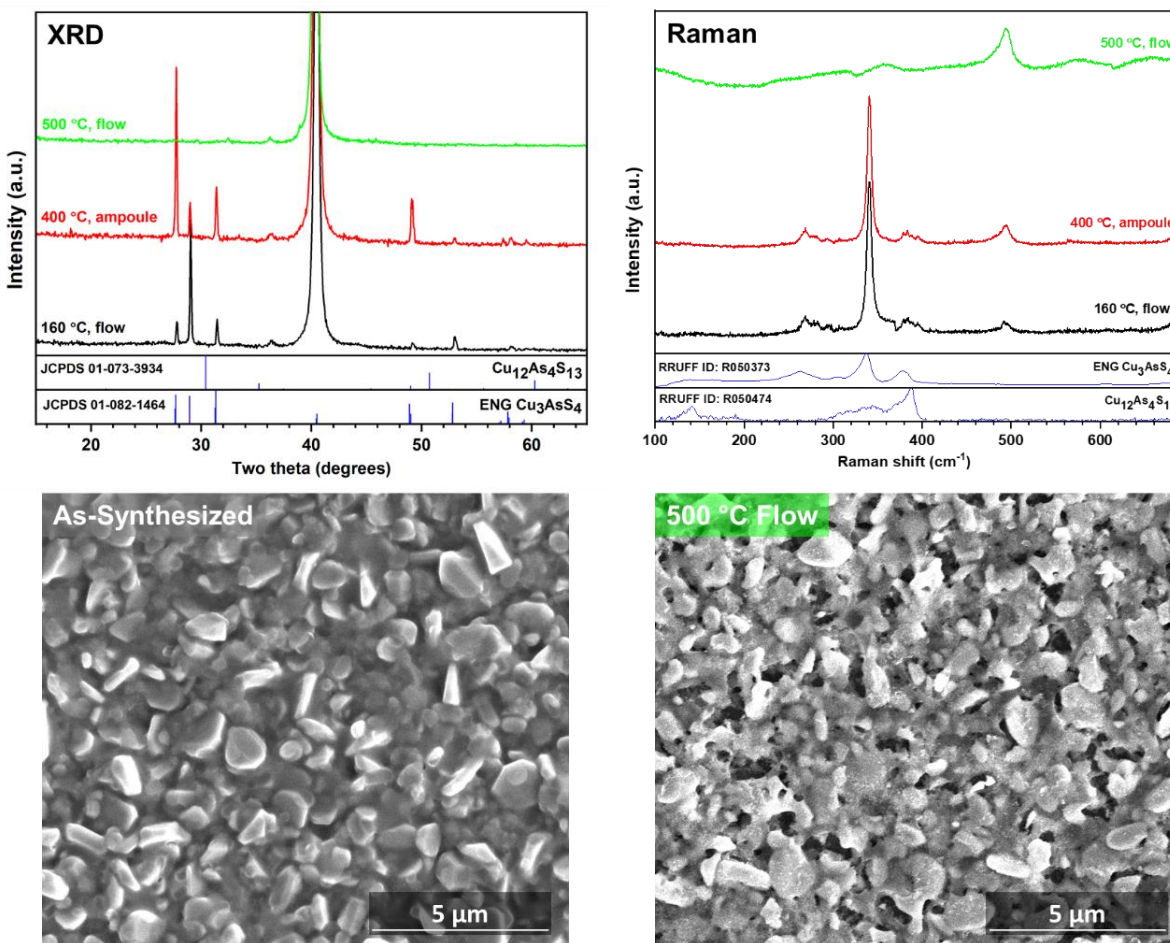


Figure 4.5. XRD and Raman spectra of ENG films that were annealed in argon at the indicated temperatures and times. SEM plan-view images of the film that was annealed at 500 °C for 1 h.

Anneals in sulfur-containing atmospheres were also explored. Figure 4.6 gives the XRD and Raman characterization of ENG films annealed in sulfur and H₂S at 425 °C. The ENG structure is maintained in sulfur, contrasting with the maintenance of LUZ structure when LUZ NP films are used as the starting point; this again suggests a high activation energy for the ENG → LUZ transition. By contrast, the film annealed in H₂S demonstrates near-complete conversion to tennantite Cu₁₂As₄S₁₃, with traces of ENG remaining in the XRD spectra. This confirms the tendency of H₂S to reduce arsenic from the nominal +5 to the nominal +3 oxidation state in Cu-As-S materials.

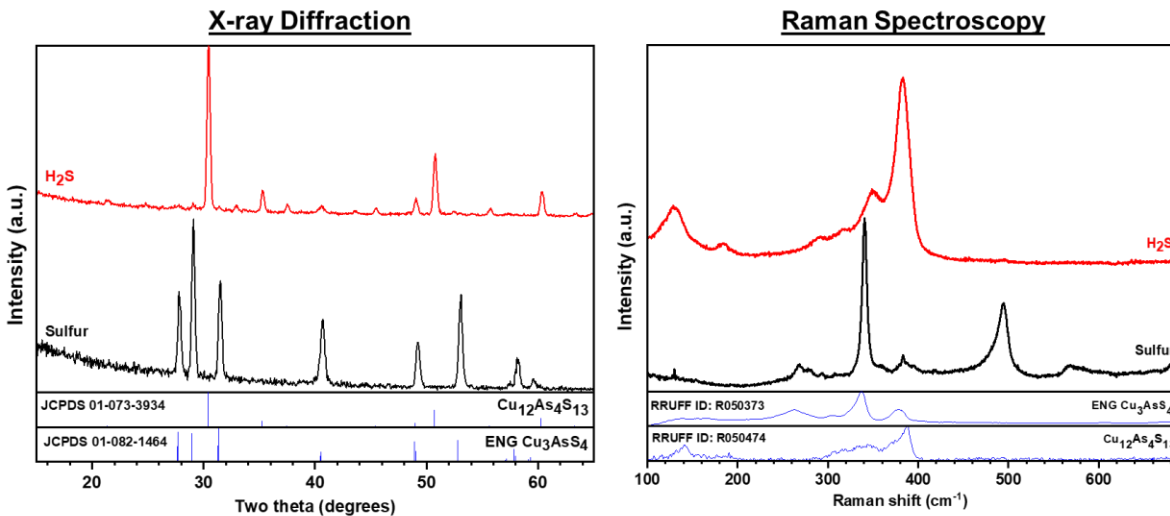


Figure 4.6. XRD and Raman spectra of ENG films that were annealed in sulfur and H₂S atmospheres at 425 °C.

The experiments in this section demonstrate that post-heat treatment anneals are not effective at removing the secondary phase from ENG films formed from OLA-capped LUZ NPs, nor do they transform ENG into LUZ. Post-anneals may have other beneficial effects on the film, such as improving cation ordering in the absorber layer [10], but should not be relied on to remove impurity phases in ENG thin films.

4.3.3 Hot Pressing of Enargite Thin Films

The secondary phase resists a suite of chemical etches and heat treatments aimed at removing it from ENG thin films. One potential factor that complicates its removal is that it is present in a “fine grain” layer below ENG grains and may also be distributed throughout the film. Moving it to the top surface may make it easier to remove. A hot press was used to apply a uniform high pressure to ENG films; such a scheme may also facilitate transformation of ENG grains back to LUZ, as LUZ is more stable at high pressures [7]. Figure 4.7 gives the Raman spectra and plan view SEM images of ENG films that were pressed at 1000 psi for 10 min, with one of the two films also being heated to ~175 °C (350 °F) during the procedure. While conversion to LUZ is not observed in either case, SEM images show that a solid material has migrated to the surface in patches. EDX indicates that these regions are significantly sulfur rich, suggesting that they are, in fact, the secondary phase. It may now be easier to remove because it interacts with a free surface

instead of ENG grains on all sides. Further pressing experiments must consider the grain structure in the film and the mechanical integrity of the substrate.

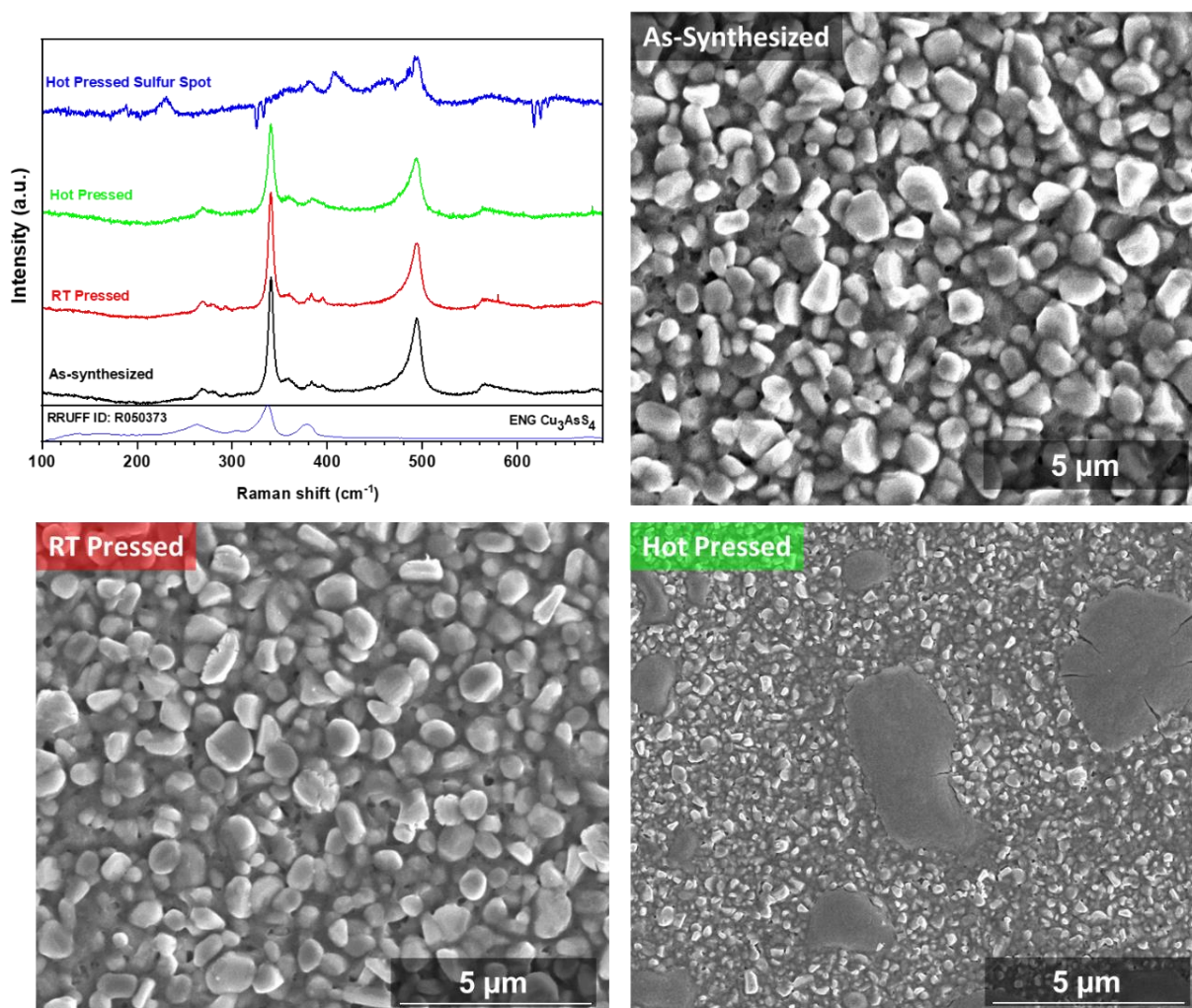


Figure 4.7. Raman spectra and plan-view SEM images of ENG films that were pressed (one with heat applied) at 1000 psi for 10 min.

4.3.4 Electrochemical Etching of Enargite Thin Films

One additional noteworthy finding that falls under the “post-processing” topic is presented here. Cyclic voltammetry on an ENG film was conducted using 0.1 M HCl as the electrolyte, and much of the film (including molybdenum) was etched, leaving behind regions of bare glass and a patchy blue and gray film. Raman spectroscopy (Figure 4.8) before and after the etch demonstrates significant reduction of the carbonaceous secondary phase. Interestingly, without any bias applied,

the Raman peak intensity was invariant. This finding warrants further research into the electrochemical properties of ENG thin films fabricated from OLA-capped NP precursors, as optimization of the electrolyte concentration and applied bias may selectively dissolve the secondary phase while leaving the Mo back contact intact. Aqueous solutions of Na_2S and NaOH were also tested but did not appear to have the same effect as HCl .

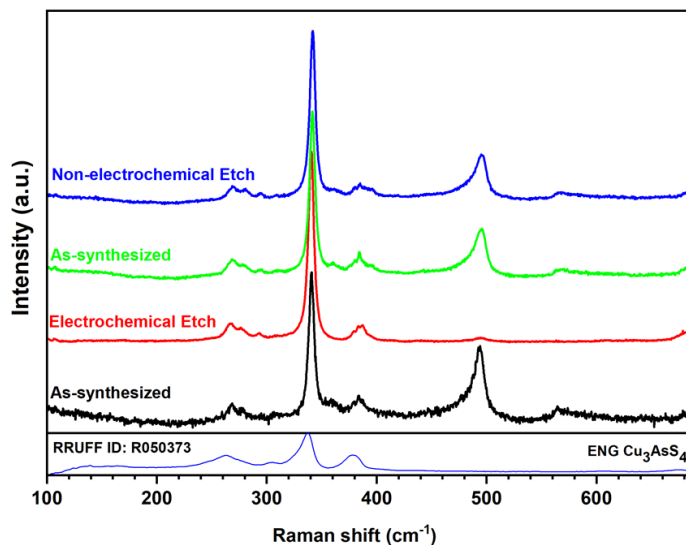


Figure 4.8. Raman spectra of an ENG thin film subjected to electrochemical etching in 0.1 M HCl .

4.4 Conclusions

In this chapter, post-processing treatments on ENG thin films were conducted to etch As-S species from the surface and remove the persistent carbonaceous secondary phase. XPS measurements showed a very arsenic- and sulfur-rich surface, which was subsequently etched by diammonium sulfide. The DAS etching procedure must become a staple in future protocols to form a high-quality pn junction for device applications. Annealing of ENG films in various atmospheres demonstrated the resistance of the secondary phase to evaporation and of enargite from transforming into its polymorph, luzonite. Hot pressing ENG films revealed some promise in controlling the location of the secondary phase, and electrochemical etching in acid may serve as a route for removing it completely from the film. However, the difficulty in removing the secondary phase from the film suggests that a more technically sound approach is to prevent it from forming in the first place, a topic that will be discussed in Chapters 5 and 9 of this thesis.

4.5 Acknowledgements

S.A.M. acknowledges funding support from the National Science Foundation under grant #DMR-1534691 and Purdue University under a Bilsland Dissertation Fellowship. He thanks Brian Graeser, Robert Boyne, Xianyi Hu, Joseph Andler, and Essam AlRaqobah for preparing molybdenum-coated soda-lime glass, Adam Wingate and Dr. Bryan Boudouris for training and access to the hot press, Juan Carlos Vega-Vila and Dr. Rajamani Gounder for training and access to the TGA unit, and Chris Gilpin for helpful discussions regarding EDX and the Winxray program. He also declares no competing financial interests.

4.6 References

- [1] Q. Guo, G. M. Ford, H. W. Hillhouse, and R. Agrawal, "Sulfide Nanocrystal Inks for Dense $\text{Cu}(\text{In}_{1-x}\text{Ga}_x)(\text{S}_{1-y}\text{Se}_y)_2$ Absorber Films and Their Photovoltaic Performance," *Nano Lett.*, vol. 9, no. 8, pp. 3060–3065, 2009.
- [2] M. V. Kovalenko, M. I. Bodnarchuk, J. Zaumseil, J.-S. Lee, and D. V. Talapin, "Expanding the Chemical Versatility of Colloidal Nanocrystals Capped with Molecular Metal Chalcogenide Ligands," *J. Am. Chem. Soc.*, vol. 132, no. 29, pp. 10085–10092, Jul. 2010.
- [3] D. H. Webber and R. L. Brutchey, "Alkahest for V_2VI_3 Chalcogenides: Dissolution of Nine Bulk Semiconductors in a Diamine-Dithiol Solvent Mixture," *J. Am. Chem. Soc.*, vol. 135, no. 42, pp. 15722–15725, Oct. 2013.
- [4] Z. Xia *et al.*, "Generalized Water-Processed Metal Chalcogenide Complexes: Synthesis and Applications," *Chem. Mater.*, vol. 27, no. 23, pp. 8048–8057, 2015.
- [5] F. W. de Souza Lucas *et al.*, "Effects of Thermochemical Treatment on CuSbS_2 Photovoltaic Absorber Quality and Solar Cell Reproducibility," *J. Phys. Chem. C*, vol. 120, no. 33, pp. 18377–18385, Aug. 2016.
- [6] H. Demers, P. Horny, R. Gauvin, and E. Lifshin, "Winxray." [Online]. Available: <http://montecarlomodeling.mcgill.ca/software/winxray/winxray.html>.
- [7] S. Maske and B. J. Skinner, "Studies of the sulfosalts of copper I. Phases and phase relations in the system Cu-As-S," *Econ. Geol.*, vol. 66, no. 6, pp. 901–918, Oct. 1971.
- [8] R. Padilla, Y. Fan, and I. Wilkomirsky, "Decomposition of Enargite in Nitrogen Atmosphere," *Can. Metall. Q.*, vol. 40, no. 3, pp. 335–342, Jan. 2001.

- [9] T. J. Huang, X. Yin, C. Tang, G. Qi, and H. Gong, "Influence of Ligands on the Formation of Kesterite Thin Films for Solar Cells: A Comparative Study," *ChemSusChem*, vol. 9, no. 9, pp. 1032–1041, May 2016.
- [10] M. Neuschitzer *et al.*, "Complex Surface Chemistry of Kesterites: Cu/Zn Reordering after Low Temperature Postdeposition Annealing and Its Role in High Performance Devices," *Chem. Mater.*, vol. 27, no. 15, pp. 5279–5287, 2015.

5. LIGAND EXCHANGE OF LUZONITE AND COPPER SULFIDE NANOPARTICLES TOWARDS CARBON-FREE ENARGITE THIN FILMS

5.1 Introduction

The previous three chapters in this thesis detailed the fabrication, optimization, and post-processing of enargite (ENG) Cu_3AsS_4 thin films from luzonite (LUZ) Cu_3AsS_4 nanoparticle (NP) precursors. As-synthesized LUZ NPs are capped with bulky oleylamine (OLA) ligands, which react with sulfur species in the atmosphere during heat treatment, forming an amorphous secondary phase with a characteristic Raman peak near 490 cm^{-1} . This secondary phase is highly detrimental to solar cell performance, as it has a very high resistance and may serve as a recombination center for charge carriers in thin-film devices [1]. So far, the secondary phase has proven resistant to several pre- and post-treatments aimed at eliminating it from the film. An alternative to etching the secondary phase is to prevent its formation in the first place; such an approach would simplify the processing of ENG thin films and may promote better grain growth and densification due to the lack of carbonaceous ligands that may occupy space between the grains.

Nanoparticles, however, are still useful precursors for thin film fabrication due to their controlled shapes, sizes, and compositions and amenability to solution deposition [2]. Ligand exchange is one strategy often employed to retain the beneficial properties of the NPs while eliminating carbon from the final film. In a typical ligand exchange procedure, native capping ligands (typically bulky, organic species) are replaced by ligands tailored to suit a specific need, such as colloidal stability in benign solvents, increased photoluminescence yield of quantum dots, or improved crystallization during post-exchange annealing. A wide variety of compounds can be used to displace native ligands on NPs, including small organic molecules (e.g. pyridine and thiourea) [3], [4], inorganic ions (e.g. S^{2-} and AsS_3^{3-}) [5], [6], and simple inorganic salts (e.g. CdCl_2 and SbCl_3) [7], [8], depending on the desired application. The Talapin group, in particular, has developed a large suite of inorganic “molecular metal chalcogenide” complexes in which chalcogenide compounds (such as SnS_2 and As_2S_3) are dissolved in hydrazine or ammonium sulfide and can serve as ligands for NPs by forming a stabilizing charged double layer at the surface [9]–[13].

The design of an effective ligand exchange procedure requires careful attention to the NP surface chemistry, as only the outer shell directly interacts with the ligands and surrounding liquid medium [14]. Surface chemistries may differ significantly from the bulk; for example, cadmium selenide (CdSe) NPs are typically terminated by a layer of Cd^{2+} ions which bind to carboxylic acids, rendering the overall NP Cd-rich [15], [16]. The affinity of surface atoms to various ligands can be qualitatively understood using Pearson's hard-soft acid-base theory, in which "harder" (i.e. weakly polarizable and highly charged) Lewis acids tend to react with "harder" bases, and vice versa [14]. Ligands must be chosen rationally such that they are likely to react with surface atoms of the target NP. The choice of a ligand exchange technique is often dictated by surface chemistry. If the native and replacement ligand bind similarly to a surface, a single-phase exchange in which an excess of the replacement ligand is dissolved and refluxed with the NPs may be used; equilibrium would favor adsorption of the new ligand and desorption of the old one [3]. If the two ligands do not bind similarly or are soluble in immiscible media, a two-phase exchange may be required to drive the exchange to completion [10]. Nuclear magnetic resonance (NMR) techniques have been developed for quantifying surface ligands, and by extension monitoring the progression of ligand exchange [17], [18].

In this chapter, a ligand exchange protocol for LUZ and copper(I) sulfide (Cu_2S) NPs is presented, with the aim of fabricating carbon-free films of ENG. Several ligands are screened for their ability to displace OLA from LUZ NPs, and the most promising candidates are identified. The conditions that resulted in complete ligand exchange are then discussed, and the procedure is extended to Cu_2S NPs. Several challenges plaguing the deposition of uniform thin films of these NPs are recognized and discussed. Finally, high-temperature heat treatments in various atmospheres are presented, demonstrating grain growth and the formation of ternary phases without a carbonaceous secondary phase. The results in this chapter suggest a route towards fabricating phase-pure ENG films for use in photovoltaic applications.

5.2 Experimental Methods

5.2.1 Materials

All chemicals were used as received unless otherwise noted. Table 5.1 lists the chemical information and abbreviations for all chemicals used in this chapter; those marked with a * were handled and stored using standard air-free techniques.

Table 5.1. Detailed information for chemicals used in Chapter 5. A * signifies an air-sensitive chemical.

Chemical	Abbreviation	Purity	Supplier
Acetone	--	>99.5% (ACS)	Fisher
Acetonitrile*	MeCN	>99.8% anhydrous	Sigma-Aldrich
Ammonium diethyldithiocarbamate*	NH ₄ -dedtc	--	Sigma-Aldrich
Ammonium hydroxide	NH ₄ OH	28-30 wt% in water	VWR
Ammonium sulfide*	DAS, (NH ₄) ₂ S	40-48 wt% in water	Sigma-Aldrich
Ammonium thioglycolate	ATG	60% in water	Sigma-Aldrich
Argon	Ar	>99.997%	Indiana Oxygen
Arsenic(III) chloride*	AsCl ₃	>99.99%	Sigma-Aldrich
Arsenic(III) sulfide*	As ₂ S ₃	>99.9%	Strem Chemicals
Arsenic(V) sulfide*	As ₂ S ₅	>99.99%	Sigma-Aldrich
n-Butylamine*	BA	>99.5%	Sigma-Aldrich
Chloroform	CHCl ₃	>99.8% (ACS)	Fisher
Copper(I) chloride*	CuCl	>99.99%	Strem Chemicals
Copper(II) acetylacetonate*	Cu(acac) ₂	>99.9%	Sigma-Aldrich
Dimethylsulfoxide*	DMSO	>99.9% anhydrous	Sigma-Aldrich
1-dodecanethiol*	DDT	>98%	Sigma-Aldrich
Ethanol	EtOH	200 proof	Fisher
Ethylene Glycol*	EG	>99.8% anhydrous	Sigma-Aldrich
Formamide*	FA	>99.5%	Sigma-Aldrich
Glycerol*	--	>99.5%	Alfa Aesar
Hexane	--	>99%, isomer mix	Fisher/Acros
Hydrogen sulfide	H ₂ S	1%, balance Ar	Airgas
Isopropanol	IPA	HPLC grade	Fisher
N-methylformamide*	NMF	>99%	Sigma-Aldrich
N,N-dimethylformamide*	DMF	>99.8%, anhydrous	Sigma-Aldrich
Oleic Acid	OA	>90% (tech. grade)	Sigma-Aldrich
Oleylamine	OLA	>70% (tech. grade)	Sigma-Aldrich
Sodium Sulfide*	Na ₂ S	--	Sigma-Aldrich
Sulfur	S	>99.99%, flakes	Sigma-Aldrich
Thiourea	TU	>99% (ACS)	Sigma-Aldrich
Toluene	--	ACS grade	Fisher

5.2.2 Nanoparticle Synthesis

Luzonite (LUZ) nanoparticles (NPs) were synthesized according to methods published previously and described in Chapter 2 of this thesis [19], [20], except that CHCl_3 and EtOH were used for washing. NPs were not typically dried prior to ligand exchange due to colloidal stability issues discussed later in this chapter. Several independent experiments demonstrated a ~50% mass loss when particles were dried under argon; this was used to estimate true particle mass for other experiments.

Copper(I) sulfide (Cu_2S) NPs were synthesized using a method adapted from Wu et al [21]. A precursor solution consisting of 1.33 mmol $\text{Cu}(\text{acac})_2$ was mixed with 4 mL OA and stirred at room temperature until a uniform suspension was formed. In a 100 mL 3-neck flask, 1.25 mmol $\text{NH}_4\text{-dedtc}$ was mixed with 10 mL DDT, 17 mL OA, and a Teflon stir bar. The solution was heated to 110 °C under argon; the ammonium salt dissolved around 80 °C. At 110 °C, 3 mL of the $\text{Cu}(\text{acac})_2$ -OA mixture was injected, and the temperature of the flask was increased to 180 °C. The reaction mixture turned a dark brown and reacted for 15 minutes at 180 °C before it was cooled naturally to room temperature and taken into a nitrogen-filled glovebox. The contents were extracted and centrifuged at 8 krpm for 10 min, and the gold supernatant was discarded. Then, three suspension/precipitation cycles using 5 mL toluene and 20 mL IPA occurred with centrifugation again at 8 krpm for 10 min each. The resulting pellet was then taken into the glovebox for ligand exchange.

5.2.3 Ligand Exchange and Coating

Most ligand exchange experiments were conducted by rapidly stirring two immiscible phases, with the OLA-capped (or DDT/OA, in the case of Cu_2S) NPs suspended in a nonpolar phase and the replacement ligands dissolved in a polar phase. As an example, the optimized procedure for LUZ NPs involved preparation of 25 mg/mL LUZ NPs in CHCl_3 and 0.15 M ammonium thioarsenite $[(\text{NH}_4)_3\text{AsS}_3]$ in FA. Equal volumes were added to a centrifuge tube (typically ~2 mL of each) and the mixture was stirred with a Teflon stir bar for ~36 h at 1600 rpm. Complete phase transfer was noted after ~16 h. When the exchange was complete, the nonpolar phase was removed and replaced with the same volume of chloroform; the mixture was stirred for another 1 h to remove residual OLA from the exchanged NPs. Then, the chloroform was withdrawn, and 6 mL acetonitrile was added. The tube was centrifuged at 14 krpm for 5 min, and

the yellow supernatant was discarded. The pellet was resuspended in 2 mL DMSO, 8 mL MeCN was added, and the tube was centrifuged at 14 krpm for 5 min. The supernatant was discarded, and the resulting pellet was used for further characterization and coatings.

The only ligands that were not purchased directly were ammonium thioarsenite and sodium thioarsenite. To prepare $(\text{NH}_4)_3\text{AsS}_3$ (Na_3AsS_3), 1 mmol of As_2S_3 was dissolved in 3 mmol (~470 μL , depending on the specific batch) DAS (Na_2S) in water, diluted with an additional 5 mL ultrapure water [10]. After ~24 h, the resulting mixture was filtered. In early experiments, this ligand/water mixture was used directly for ligand exchange; it was either injected directly into FA or diluted with NH_4OH . For later experiments, solid powder was isolated using a method adapted from Yakunin et al [6]. After filtering, the mixture was placed in a centrifuge tube, acetone was added, and the mixture was centrifuged at 14 krpm for 5 min. The bottom phase was kept, diluted with 1 mL ultrapure water, and centrifuged again with acetone at 14 krpm for 5 min. The pellet was dried under nitrogen for ~3 h before use.

Inks for coating were typically prepared at 200 mg/mL in DMSO, though DMF was successfully used in several early experiments. NPs were not dried after washing due to colloidal stability issues; the 200 mg/mL concentration assumes that drying ligand exchanged NPs results in a ~70% mass loss. Several independent experiments were conducted to arrive at this number, but it must continuously be monitored as the washing procedure and coating solvents are changed. Ideally, drying would occur for maximum experimental reproducibility.

Coatings of ligand exchanged NPs in DMSO were conducted using a heated manual blade coating setup. The hot plate and substrate (usually Mo-coated soda-lime glass) were preheated to 85 °C. Coatings of 20 μL , 15 μL , 15 μL (if desired), and 10 μL (if desired) were then applied using a glass rod, with 5 minute bakes in between each step. The film was then baked at 130 °C for 5 min and 200 °C for 5 min were then conducted to drive off the DMSO solvent. This procedure was conducted in both air and the glovebox; coatings in air typically required more layers for the same thickness and resulted in more matte and rough films than the coatings performed in the glovebox did.

5.2.4 Heat Treatments

Heat treatments of ligand exchanged LUZ and Cu_2S NPs occurred in an identical manner to the heat treatments described in detail elsewhere in this thesis (particularly Chapters 2 and 7).

For ampoule heat treatments, the sample and any desired powder (i.e. As_2S_5) were added to an ampoule, which was then attached to a Schlenk line and purged three times before sealing under vacuum using a butane torch. Ampoules were treated in a horizontal three-zone tube furnace and were inserted once the set point had been reached. Sulfur treatments also occurred in a horizontal tube furnace with argon flow; the sample and ~ 1 g sulfur were placed in the same graphite box, which was pushed into the middle of the furnace when the setpoint temperature was reached. Hydrogen sulfide and argon treatments occurred in a vertical tube furnace; samples were held in place using a custom graphite sample holder attached to a manual push-pull rod. All samples were annealed for the desired amount of time, and they were cooled naturally to < 40 °C before exposure to the ambient environment.

5.2.5 Characterization

Fourier Transform Infrared Spectroscopy (FTIR) data were collected using a Nicolet Nexus 670 FTIR; the chamber was purged with nitrogen for 10 min before data collection. Sodium chloride cards were used as the substrate; they were pre-annealed at 200 °C in a glovebox, and then samples were drop cast and annealed at 200 °C before evaluation to eliminate residual solvent signals. Nuclear magnetic resonance (NMR) data were collected on a Bruker AV-III-400-HD instrument at 400 MHz with a relaxation time of 6 seconds. X-ray fluorescence (XRF) data was collected using a Fisherscope X-Ray XAN 250 instrument at 50 kV using a 10 μm thick Ni filter; the chamber was purged with helium during measurements. Grazing incidence X-ray diffraction (GIXRD) data was collected using a Rigaku Smartlab diffractometer in parallel beam mode with a 0.5° incident angle and a copper $\text{K}\alpha$ wavelength source ($\lambda = 1.5406$ Å). Raman spectra were collected using a custom Horiba/Jobin-Yvon LABRAM 800 system with a Si detector and 633 nm He:Ne laser excitation source. Scanning electron microscopy (SEM) images and energy-dispersive x-ray spectroscopy (EDX) data were taken on an FEI Quanta scanning electron microscope at accelerating voltages of 7 kV and 20 kV, respectively.

5.3 Results and Discussion

5.3.1 Identifying Candidate Ligands for Luzonite Nanoparticles

The surface chemistry of LUZ NPs is not known explicitly, nor is the mechanism by which OLA binds to the surface. OLA may bind to undercoordinated surface sites by donating the lone

pair on its nitrogen atom (i.e. L-type binding), but technical grade OLA used here may also contain impurities that bind through sharing electrons from both atoms (i.e. X-type binding) [22]. Measurements of LUZ NPs using EDX and XRF generally reveal compositions that are slightly arsenic-rich. Pearson's HSAB theory suggests that a "hard" ligand should be used to target a presumed As-rich surface, but the binding of "softer" OLA suggests that As may not be the only surface atom.

Because of the uncertainty regarding binding mechanisms of ligands to LUZ NP surfaces, a variety of compounds with "hard" and "soft" character were tested for propensity to ligand exchange. Most of them dissolved in polar solvents, so a two-phase exchange was conducted in which a nonpolar solvent containing OLA-capped NPs was stirred with an immiscible polar solvent containing the ligand of interest. In such a scheme, NPs are transported to the interface by convection. Ligands may adsorb and desorb there; once enough of the ligands on a particle have been replaced, the NP becomes more stable in the polar solvent and transfers across the interface.

Table 5.2 summarizes selected ligand exchange screening experiments. The effectiveness of the exchange was determined by whether or not the LUZ NPs transferred from the nonpolar to the polar phase after ~24 h of stirring, with some manual vortexing and ultrasonication during that time.

Table 5.2. Qualitative summary of two-phase ligand exchange screening experiments.

Ligand	Toluene-FA	Hexane-NMF
(NH ₄) ₂ S	No phase transfer	Phase transfer
NH ₄ OH	Partial phase transfer	Phase transfer
ATG	No phase transfer	n/a
TU	No phase transfer	No phase transfer
AsS ₃ ³⁻ /H ₂ O	No phase transfer	Partial phase transfer

Aside from the ligands shown in Table 5.2, two others were tested. One was a combination of water/AsS₃³⁻ diluted with NH₄OH as the polar phase, discussed in Chapter 2 and initially used by the Talapin group [10], [11]; the combination resulted in complete phase transfer within several hours. The other ligand tested was n-butylamine (BA), which may be removed from LUZ NP films through low-temperature annealing due to its low boiling point (77 °C). To attempt a ligand exchange with BA, LUZ NPs were vortexed and sonicated in the presence of excess BA, with the

hypothesis that mass action would favor the adsorption of BA to the surface of LUZ and the desorption of OLA to the bulk liquid.

Phase transfer is not a perfect indicator of a complete ligand exchange; it does not guarantee that every OLA ligand was removed from a NP, but rather that the new ligand had displaced enough OLA to dominate the solubility characteristics of the NP. Fourier-transform infrared spectroscopy (FTIR) was used to probe NPs for the presence of OLA ligands after exchange (Figure 5.1); solvent signals were avoided by baking the NPs at 200 °C in the glovebox prior to analysis. Note that the spectra in Figure 5.1 correspond to the most optimized conditions for each case; for example, the most successful AsS_3^{3-} exchanges were performed using chloroform and FA as the nonpolar-polar solvent pair, which is discussed further in the next section. Close study of the characteristic C-H stretching region ($\sim 3100\text{-}2800\text{ cm}^{-1}$) reveals an incomplete exchange when DAS and BA ligands were used, suggesting that multiple exchanges or elevated temperatures may be required to drive these exchanges to completion. The exchanges involving NH_4OH and the AsS_3^{3-} ion are efficient at removing OLA from LUZ NPs, though they leave residues characteristic of amides ($\sim 1700\text{-}1400\text{ cm}^{-1}$). It is likely that FA and other amides will evaporate cleanly from the film without reacting with sulfur at high temperatures [1]; Raman spectroscopy will be used to monitor undesired reactions this later in this chapter.

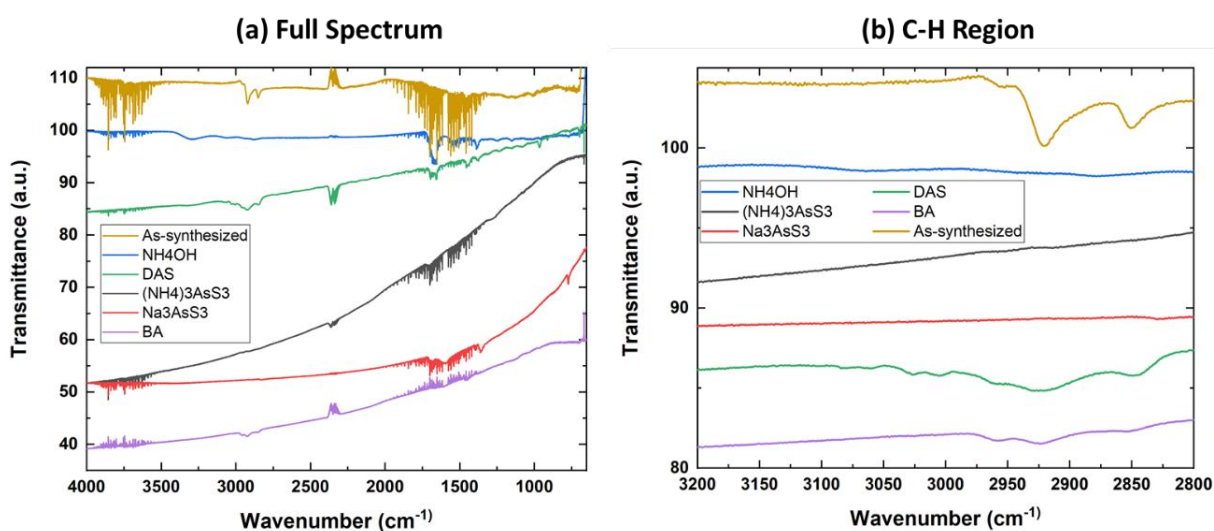


Figure 5.1. FTIR spectra on LUZ NPs exchanged with a variety of ligands.

NH_4OH , AsS_3^{3-} , or a combination of the two seem like promising candidates for ligand exchange with OLA-capped LUZ NPs, as they remove characteristic C-H stretches from the LUZ NP completely. However, the use of hydroxide should be avoided to avoid potential oxidation of the surface. Furthermore, exchange with just NH_4OH occurs very rapidly, sometimes within ~30 seconds. However, AsS_3^{3-} did not exchange completely without NH_4OH present, demonstrating the need for additional exploration of the properties of AsS_3^{3-} .

5.3.2 Optimizing Ligand Exchange with AsS_3^{3-} Ligands

AsS_3^{3-} is an ideal candidate ligand for LUZ NPs. Besides completely displacing OLA under certain conditions, it also contains elements that are native to Cu_3AsS_4 , meaning that it may suppress elemental losses during heating of LUZ NPs and supply an in-situ As-S liquid for growth of thin films. These changes mean that moving to processing outside of sealed ampoules is possible, an important step towards module-scale processing.

The initial experiments involved As_2S_3 dissolved in a DAS-water solution with no additional modifications. Such a configuration only allowed for complete ligand exchange when NH_4OH was present, suggesting that the exchange is either pH dependent or that water complexes with AsS_3^{3-} , impeding its binding to a LUZ NP surface. To eliminate the effects of water in ligand exchange studies, solid $(\text{NH}_4)_3\text{AsS}_3$ and Na_3AsS_3 were isolated by centrifugation after As_2S_3 dissolution in aqueous $(\text{NH}_4)_2\text{S}$ and Na_2S solutions, respectively. This solid powder was then dried and redispersed in various solvents. Table 5.3 gives the dissolution properties of the AsS_3^{3-} solid ligands in various polar solvents at ~20 mg/mL.

Table 5.3. Dissolution of AsS_3^{3-} -based ligands in various polar solvents at ~20 mg/mL.

Solvent	$(\text{NH}_4)_3\text{AsS}_3$	Na_3AsS_3
Acetonitrile	Reaction – white opaque	Reaction – white opaque
Dimethylsulfoxide	Dissolved – green	Partial dissolution
Ethylene Glycol	Dissolved – yellow	Dissolved – orange
Formamide	Dissolved – yellow	Dissolved – orange
Glycerol	Very slow dissolution	Very slow dissolution
Methanol	Partial dissolution	Dissolved – red, unstable
N,N-dimethylformamide	Dissolved – yellow	Partial dissolution
Water	Dissolved – yellow	Partial dissolution, unstable

From Table 5.3, several candidate solvents are identified for use in ligand exchange of LUZ with AsS_3^{3-} -based ligands. Ethylene glycol and FA are good candidates for both the NH_4^- - and Na-based ligands; other solvents only dissolve the ammonium-based ligands. To check the effects of different solvents on the ligand exchange of $(\text{NH}_4)_3\text{AsS}_3$ with OLA on LUZ NPs, FTIR was again utilized (Figure 5.2). Small C-H stretches are observed with ethylene glycol-toluene and hexane-DMF combinations, but the remainder are effective at removing OLA from the NPs, as noted from the flat C-H regions.

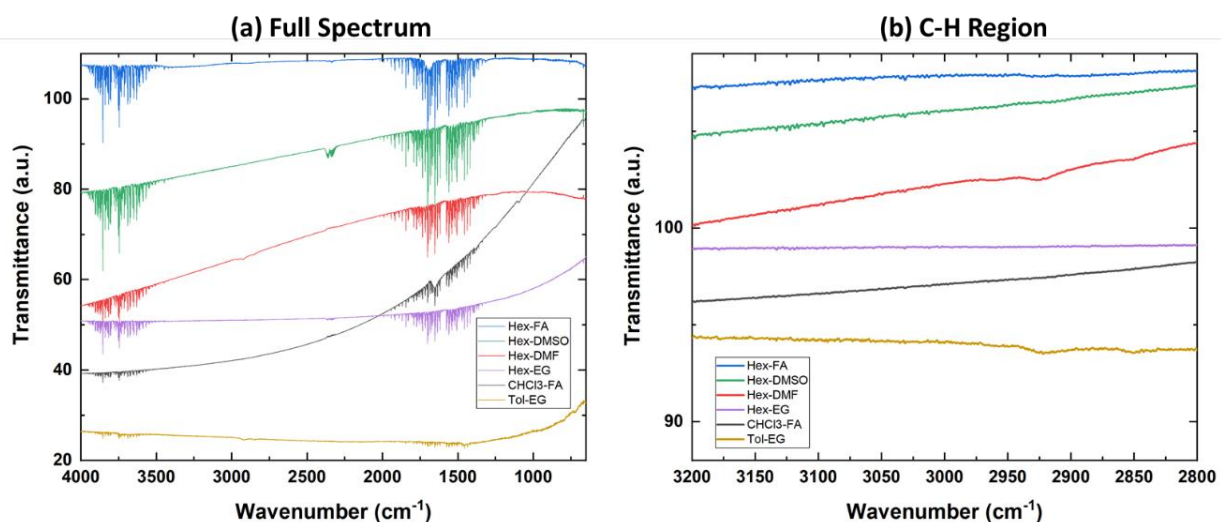


Figure 5.2. FTIR spectra of OLA-capped LUZ NPs exchanged with $(\text{NH}_4)_3\text{AsS}_3$ in various solvent combinations.

There are several solvent systems which can be used for the exchange of LUZ NPs with $(\text{NH}_4)_3\text{AsS}_3$; CHCl_3 -FA was selected for further investigation. CHCl_3 is denser than the polar solvents used, so during a two-phase ligand exchange, particles must overcome gravitational forces to transfer to the polar phase, eliminating the possibility of particles aggregating and settling without undergoing significant ligand exchange. FA is immiscible with chloroform, contains fewer oxygen atoms than ethylene glycol, and does not turn green as a DMSO - $(\text{NH}_4)_3\text{AsS}_3$ solution did.

The CHCl_3 -FA ligand exchange was optimized to completely remove OLA from the LUZ NPs and maintain colloidal stability of the resulting NP pellet; the concentrations of ligands and NPs were critical. For a NP concentration of 25 mg/mL in CHCl_3 , a ligand concentration of 0.15 M in FA was required; lower concentrations did not lead to phase transfer of every particle. These concentrations correspond to roughly $\sim 8\times$ excess ligand relative to the amount of OLA on the NP

surface (calculated in Appendix A). Additionally, longer exchange times gave NPs with better colloidal stability. Exchanges ran for ~ 36 hours, even though the phase transfer was complete after 12 hours. This indicates that ligand adsorption and desorption is a dynamic process that continues in the polar FA solvent; further studies are needed to fully elucidate the exchange kinetics. XRF measurements were used to verify compositional changes upon the addition of new ligands; a typical result indicated that the Cu/As ratio decreased from 2.89 to 2.23 due to the exchange, indicating successful capping of the LUZ NPs with As-containing ligands.

Several persistent challenges regarding the ligand exchange procedure must be addressed in future work. The colloidal stability of LUZ NPs is delicate, and generally disappears if the NPs are dried during the process. Consequently, NP drying is not performed at any step, meaning that all stated concentrations are only estimated. Loss of colloidal stability can either mean the ligand desorbs and evaporates, which is unlikely due to the low vapor pressure of OLA and the charged nature of AsS_3^{3-} , or that the particles agglomerate. OLA provides good colloidal stability to other NP systems, but the presence of other species on the surface of LUZ NPs cannot be ruled out. Figure 5.3 gives the NMR spectra of NP pellets after successive CHCl_3 -EtOH washes during a standard LUZ NP synthesis routine. The chemical shift near 5.5 ppm is attributed to the C=C bond in OLA, and its relative intensity decreases with each successive wash, indicating removal from the system. Furthermore, the relative intensity of the ethanol $-\text{CH}_2-$ (~ 3.72 ppm) shift increases with each wash; the stripping of ligands from NP surface and replacements by alkoxide groups has been reported previously [23]. While it is unclear whether ethanol is binding to the surface of the NPs here or is just entrained with the pellet, its persistent presence after extensive drying leads to a high probability of surface NP oxidation.

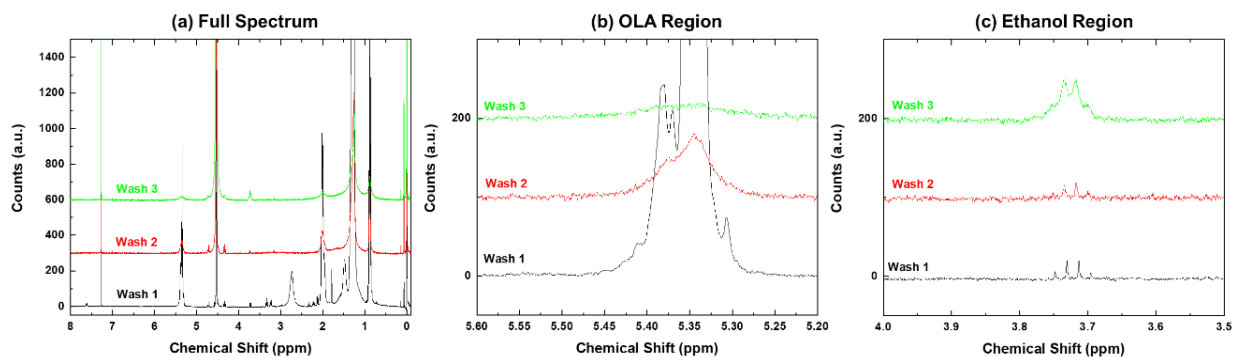


Figure 5.3. NMR spectra in deuterated chloroform of LUZ NPs after successive washes in chloroform-ethanol mixtures. The regions for OLA and EtOH are magnified for clarity.

In addition to alcohol/alkoxide groups, it is possible that chloride ions used in the NP synthesis bind to the NP surface. Quantifying chloride ions on the surface of NPs is difficult without high-resolution transmission electron microscopes, but during an ICP-MS analysis of Cu_3AsS_4 NPs, a line with a m/z ratio of 77 was detected. This corresponds to an adduct of argon-40 and chlorine-37, suggesting that chlorine is still present even in well-washed NP pellets.

Because of colloidal stability loss, uniform coatings of ligand exchanged LUZ NPs have been difficult to achieve. Heated doctor blading from DMSO inks in both the glovebox and air has made films that are relatively crack free and continuous, but significant roughness and agglomerates are still observed. A more fundamental understanding of the LUZ NP surface chemistry and ligand exchange procedure is needed to fully achieve reproducible, high-quality thin films for heat treatments and device fabrication.

5.3.3 Ligand Exchange of AsS_3^{3-} with Copper(I) Sulfide Nanoparticles

The surface chemistry of Cu_2S NPs should be simpler than that of LUZ NPs because there are only two elements present. Cu_2Se NPs have been used as precursors for the fabrication of CIGSe and CZTSe thin films when In-, Ga-, Zn-, and Sn- containing ligands were attached to the surface and the resulting film was annealed; the ligands reacted with the core NPs to form ternary and quaternary phases with near-stoichiometric compositions [24]. Extension of such a scheme to sulfide NPs seems possible. Cu_2S NPs were synthesized according to the recipe of Wu et al and then exchanged with NH_4^- and Na-based AsS_3^{3-} ligands [21]. These NPs are capped with a combination of DDT and OA, both of which likely bind as charged X-type ligands (i.e. forming a bond using one electron from the surface atom and one from the ligand) to a copper-rich surface. Furthermore, copper is a softer acid than arsenic, and the arsenic sulfide-derived ligands have been shown to bind well cadmium selenide NPs (which have a “borderline” hard-soft Cd^{2+} surface), so HSAB theory can be used to deduce that the ligand exchange of AsS_3^{3-} with Cu_2S should proceed more easily than with LUZ NPs.

Figure 5.4 gives the FTIR spectra of Cu_2S NPs exchanged with $(\text{NH}_4)_3\text{AsS}_3$ and Na_3AsS_3 ligands using a CHCl_3 -FA mixture. The C-H region is free of any stretches, indicating removal of OLA from the film; FA residues appear in the 1700-1400 cm^{-1} range. Additionally, this ligand exchange phase transferred within 2 hours, as compared to the 12+ hours required for LUZ NP

exchanges. The use of Cu₂S NPs capped with As-containing ligands as precursors for Cu-As-S thin films is explored later in this chapter.

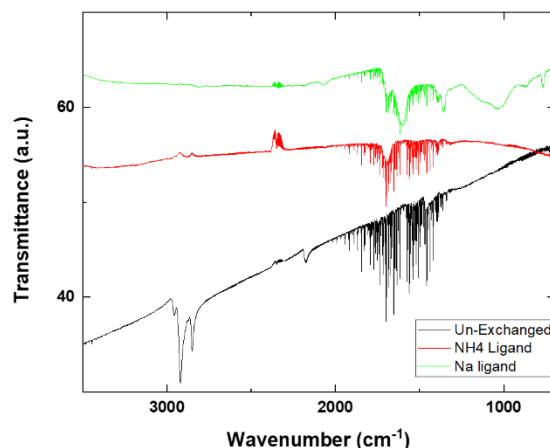


Figure 5.4. FTIR spectra of copper(I) sulfide NPs ligand exchanged with (NH₄)₃AsS₃ and Na₃AsS₃ ligands.

5.3.4 Heat Treatments of Ligand Exchanged Luzonite Nanoparticles

As mentioned earlier in this chapter, obtaining uniform coatings of ligand exchanged LUZ NPs that are suitable for fabrication into devices has proven to be a challenge, and further work is required. However, as a preliminary investigation into grain growth and phase transformations in this carbon-free system, ligand exchanged LUZ NP films capped with (NH₄)₃AsS₃ were heated in a sealed ampoule with As₂S₅ for 30 min at 425 °C. The GIXRD and Raman spectra (Figures 5.5a and 5.5b) demonstrate conversion of the LUZ NPs to the ENG phase as was seen in heat treatments of OLA-capped NPs. Importantly, there is no trace of the impurity peak at 490 cm⁻¹ in Raman, suggesting that these films are free of the carbonaceous secondary phase that has plagued the standard procedure. This confirms that residual amides seen in FTIR do not contribute to the formation of a secondary phase in ligand exchanged films. Note that Na₃AsS₃-capped films were also tested, but an unidentified secondary phase was present in the GIXRD spectra, so they were not pursued further.

The plan-view SEM image (Figure 5.5c) indicates that micron-sized grains grew, similar to those seen in OLA-capped NP heat treatments. However, there is significantly more void space in between the grains, rendering the film wholly unsuitable for device applications. It is likely that the initial film was too thin, and the growing grains consequently pulled in too much material from

the surroundings; a very thin film is confirmed by a cross-sectional SEM image (Figure 5.5d) which shows columnar grains that are only ~200-300 nm thick.

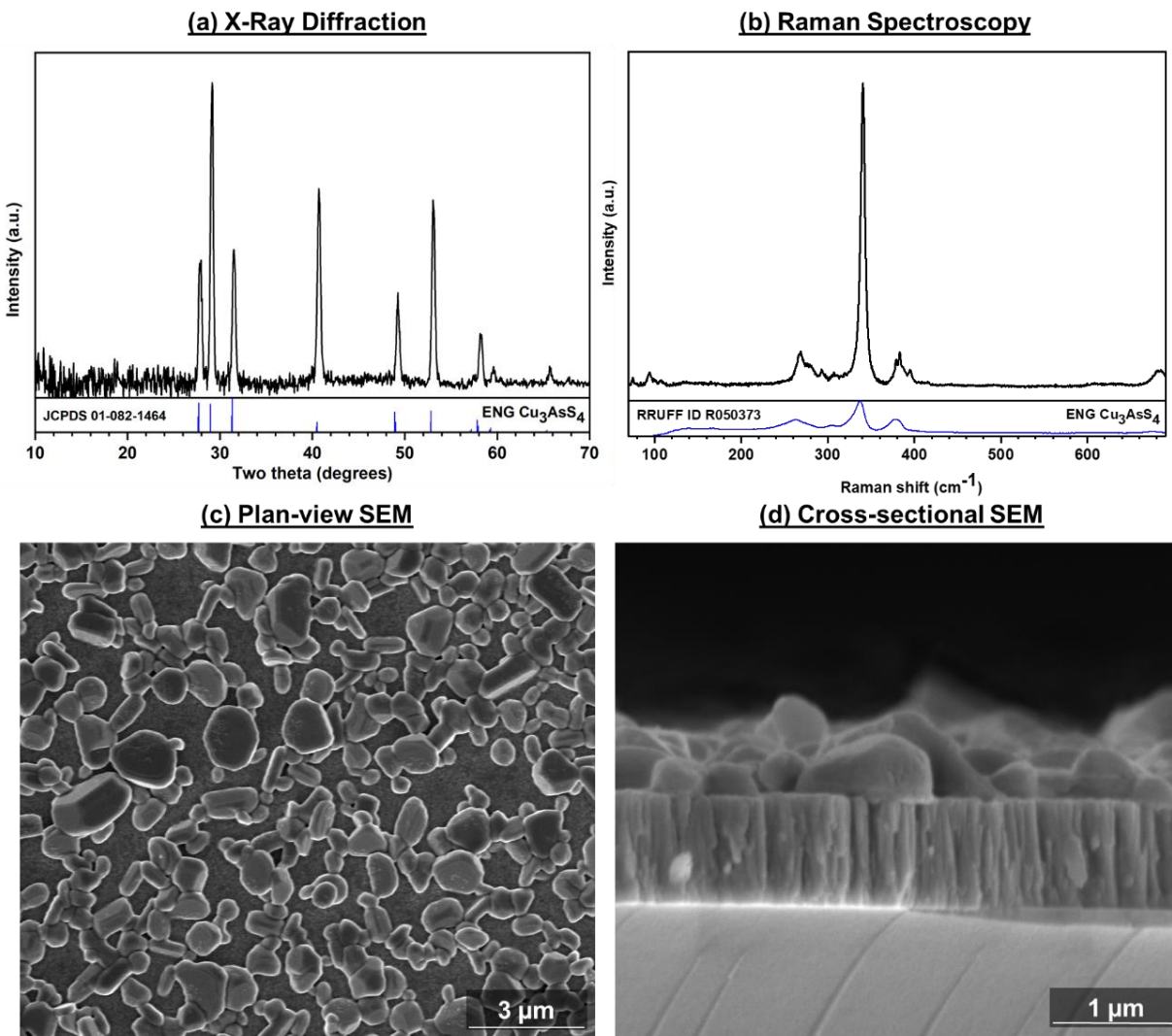


Figure 5.5. (a) GIXRD spectrum, (b) Raman spectrum, (c) Plan-view SEM image, and (d) cross-sectional SEM image of a ligand exchanged LUZ NP film heat treated in a sealed ampoule with As_2S_5 powder for 30 min at 425°C .

The behavior of ligand exchanged LUZ NPs in a sealed ampoule at 350°C without any added powder was also investigated. Figures 5.6a and 5.6b indicate a partial transition of the LUZ structure to tennantite $\text{Cu}_{12}\text{As}_4\text{S}_{13}$, consistent with some sulfur loss from the film. The EDX-determined Cu/As ratio was 2.17 ± 0.05 , which is not a statistically significant change from the 2.24 ± 0.04 ratio measured for this coating. The similar Cu/As ratios suggest that the AsS_3^{3-} ligands are effective at suppressing arsenic losses from the film that were shown to occur starting above

300 °C in Chapter 2. The plan-view SEM image (Figure 5.6c) does not indicate significant grain growth, though it does appear that small nuclei form by 350 °C. Further study of the heat treatment conditions may lead to significant grain growth in Cu-As-S films without needing to supply As-S powders.

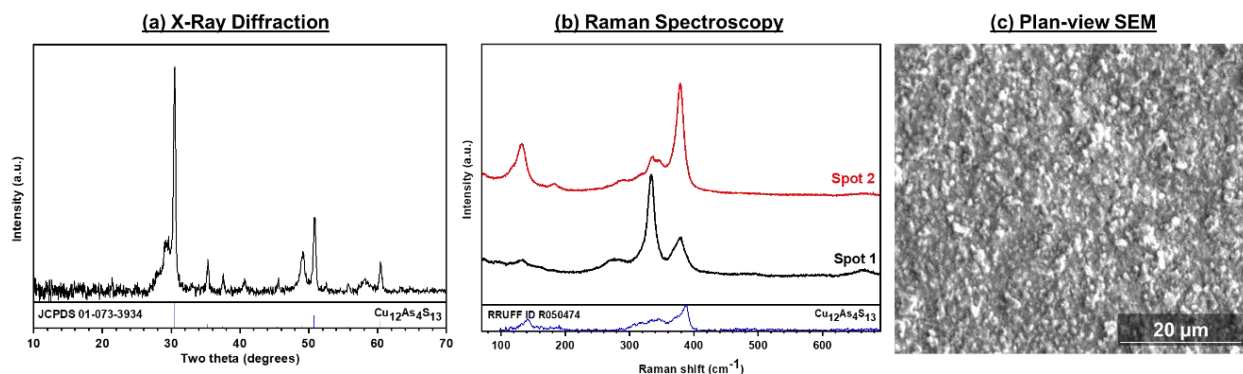


Figure 5.6. (a) GIXRD spectrum, (b) Raman spectrum, and (c) plan-view SEM image of ligand exchanged LUZ NPs heat treated in an ampoule with no added powders at 350 °C for 1 h.

These preliminary heat treatments demonstrate that phase transformations for ligand exchanged LUZ NPs proceed in a similar manner as what was observed in standard OLA-capped NPs. Further improvements to the coatings will ultimately result in thin films with micron-sized dense grains suitable for photovoltaic device applications.

5.3.5 Heat Treatments of Ligand Exchanged Copper Sulfide Nanoparticles

Copper(I) sulfide NPs capped with $(\text{NH}_4)_3\text{AsS}_3$ ligands were heat treated in various atmospheres to check for the formation of ternary phases, confirm the lack of a secondary phase, and compare the grain growth to that of LUZ NP precursor films. Jiang et al. fabricated thin films of CIGSe and CZTSe by annealing Cu_2S NPs capped with various metal molecular chalcogenide ligands; the ligands reacted with the core to form ternary and quaternary phases [24]. Such a procedure allows for high atom economy and minimal volume change upon heat treatment.

Figure 5.7 gives the GIXRD and Raman characterization of ligand exchanged Cu_2S NPs heat treated in argon, 1% H_2S in argon, dilute sulfur in argon, and an As_2S_5 -filled ampoule. All experiments were conducted at 400 °C except for the argon flow, which was at 300 °C because the 400 °C sample did not yield usable characterization data. The argon and H_2S treatments formed TEN along with some small Cu_{2-x}S impurity phases, and the sulfur and As_2S_5 treatments resulted

in an ENG/LUZ mixture and ENG, respectively. No secondary phases are noted in the Raman spectra. The first three treatments indicate that the As-containing ligands did indeed react with the Cu_2S NP core.

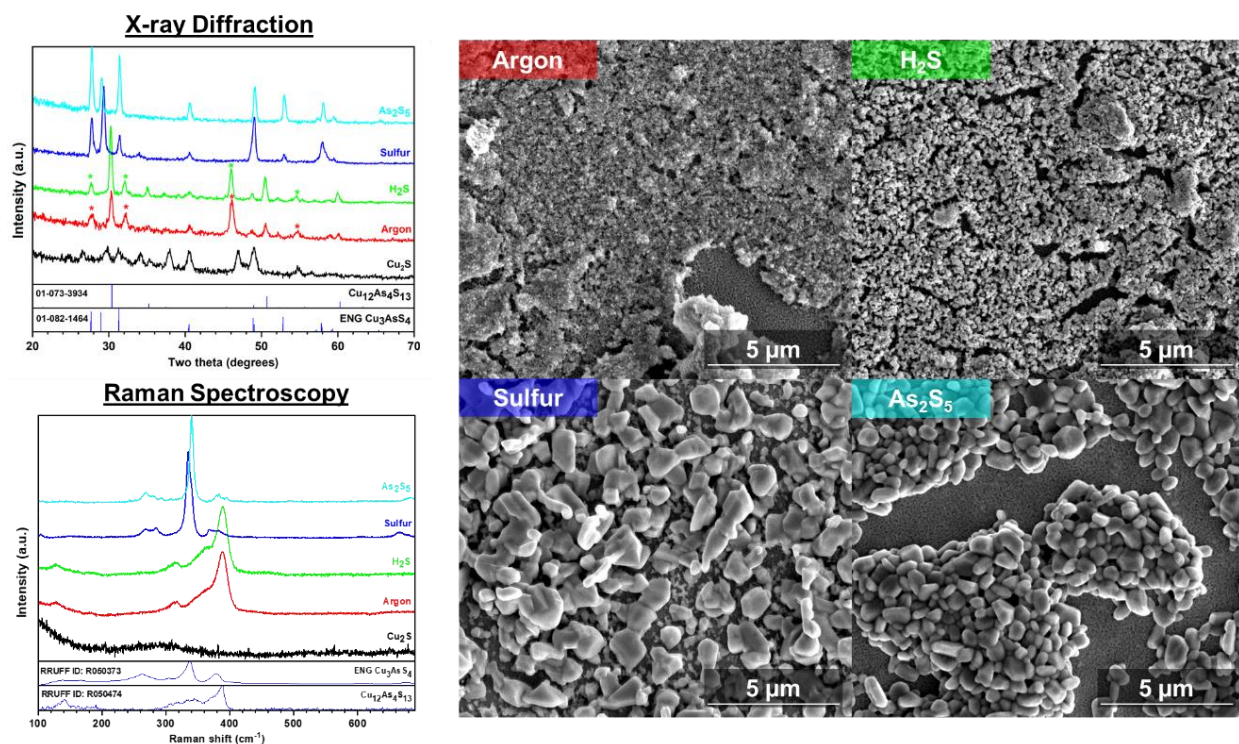


Figure 5.7. GIXRD spectra, Raman spectra, and plan-view SEM images of ligand exchanged Cu_2S NPs heat treated in various atmospheres at 400 °C for 30 min. In the GIXRD spectra, a * indicates a peak attributable to copper sulfide Cu_{2-x}S .

The plan-view SEM images in Figure 5.7 indicate minimal grain growth in the argon and H_2S cases and significant grain growth in both the sulfur and As_2S_5 cases. The grain growth in the As_2S_5 treatment was expected, but the sulfur one is the most exciting, as it represents a method by which relatively dense micron-sized grains were achieved without the use of a sealed glass ampoule. Such a development allows for scale-up to larger substrate (and ultimately, solar cell) sizes and can eliminate nonuniformity concerns associated with the distribution of powders in the ampoules. Overall, the ligand exchanged Cu_2S heat treatments represent a promising step towards fabricating carbon-free films of ternary Cu-As-S phases without the need to supply an external atmosphere of arsenic-containing vapor. Further improvements to the ligand exchange and coating procedures will yield denser films more suited for device applications.

5.4 Conclusions

In this chapter, preliminary studies on ligand exchange of both luzonite and copper(I) sulfide nanoparticles were presented. Several ligands were screened, and ultimately, arsenic sulfide-derived materials were chosen as the best ligands for both particles. Optimization revealed the need for high concentrations and long exchange times to exchange of LUZ NPs in a chloroform-formamide mixture. Preliminary heat treatments in As_2S_5 , sulfur, and argon were then presented, demonstrating similar grain sizes and phase transformations as in the standard OLA-capped NP heat treatments presented earlier in this thesis. Treatments with Cu_2S -capped NPs also indicated that ligands can be used as the sole arsenic source for formation of ternary films. While the initial results are promising, there is significant work to be done to achieve thin films appropriate for device applications. Colloidal stability of the NPs is very difficult to maintain, so a fundamental study involving detailed NMR, FTIR, and possibly XPS studies is critical to determine the nature of the NP surface and design an optimal ligand exchange scheme for these materials. The work presented in this chapter represents a springboard by which carbon-free films of ENG for high-efficiency solar cells may be fabricated.

5.5 Acknowledgements

S.A.M. acknowledges funding support from the National Science Foundation (grant #DMR-1534691) and Purdue University (Bilsland Dissertation Fellowship). He would like to give special thanks to Louie Schroeder for his hard work on initial ligand exchange experiments, some heat treatments and characterization, and the design of the n-butylamine exchanges. He also expresses thanks to Ryan Ellis for useful discussions and insights, to David Rokke and Swapnil Deshmukh for assistance with NMR measurements, and to Arlene Rothwell and Karl Wood for assistance with ICP-MS measurements. He declares no competing financial interests.

5.6 References

- [1] T. J. Huang, X. Yin, C. Tang, G. Qi, and H. Gong, "Influence of Ligands on the Formation of Kesterite Thin Films for Solar Cells: A Comparative Study," *ChemSusChem*, vol. 9, no. 9, pp. 1032–1041, May 2016.
- [2] D. V. Talapin, J.-S. Lee, M. V. Kovalenko, and E. V. Shevchenko, "Prospects of Colloidal Nanocrystals for Electronic and Optoelectronic Applications," *Chem. Rev.*, vol. 110, no. 1, pp. 389–458, Jan. 2010.
- [3] D. Celik *et al.*, "Performance enhancement of CdSe nanorod-polymer based hybrid solar cells utilizing a novel combination of post-synthetic nanoparticle surface treatments," *Sol. Energy Mater. Sol. Cells*, vol. 98, pp. 433–440, Mar. 2012.
- [4] N. C. Anderson, M. P. Hendricks, J. J. Choi, and J. S. Owen, "Ligand Exchange and the Stoichiometry of Metal Chalcogenide Nanocrystals: Spectroscopic Observation of Facile Metal-Carboxylate Displacement and Binding," *J. Am. Chem. Soc.*, vol. 135, no. 49, pp. 18536–18548, Dec. 2013.
- [5] R. Dierick *et al.*, "Annealing of sulfide stabilized colloidal semiconductor nanocrystals," *J. Mater. Chem. C*, vol. 2, no. 1, pp. 178–183, 2014.
- [6] S. Yakunin *et al.*, "High infrared photoconductivity in films of arsenic-sulfide-encapsulated lead-sulfide nanocrystals," *ACS Nano*, vol. 8, no. 12, pp. 12883–12894, 2014.
- [7] A. Carrete *et al.*, "Antimony-Based Ligand Exchange To Promote Crystallization in Spray-Deposited $\text{Cu}_2\text{ZnSnSe}_4$ Solar Cells," *J. Am. Chem. Soc.*, vol. 135, no. 43, pp. 15982–15985, Oct. 2013.
- [8] H. Zhang, J. M. Kurley, J. C. Russell, J. Jang, and D. V. Talapin, "Solution-Processed, Ultrathin Solar Cells from CdCl_3^- -Capped CdTe Nanocrystals: The Multiple Roles of CdCl_3^- Ligands," *J. Am. Chem. Soc.*, vol. 138, no. 24, pp. 7464–7467, 2016.
- [9] M. V. Kovalenko, M. Scheele, and D. V. Talapin, "Colloidal Nanocrystals with Molecular Metal Chalcogenide Surface Ligands," *Science (80-.)*, vol. 324, no. 5933, pp. 1417–1420, Jun. 2009.
- [10] M. V. Kovalenko, M. I. Bodnarchuk, J. Zaumseil, J.-S. Lee, and D. V. Talapin, "Expanding the Chemical Versatility of Colloidal Nanocrystals Capped with Molecular Metal Chalcogenide Ligands," *J. Am. Chem. Soc.*, vol. 132, no. 29, pp. 10085–10092, Jul. 2010.

- [11] M. V. Kovalenko, M. I. Bodnarchuk, and D. V. Talapin, "Nanocrystal Superlattices with Thermally Degradable Hybrid Inorganic–Organic Capping Ligands," *J. Am. Chem. Soc.*, vol. 132, no. 43, pp. 15124–15126, Nov. 2010.
- [12] A. Nag, M. V. Kovalenko, J.-S. Lee, W. Liu, B. Spokoyny, and D. V. Talapin, "Metal-free Inorganic Ligands for Colloidal Nanocrystals: S^{2-} , HS^- , Se^{2-} , HSe^- , Te^{2-} , HTe^- , TeS_3^{2-} , OH^- , and NH_4^+ as Surface Ligands," *J. Am. Chem. Soc.*, vol. 133, no. 27, pp. 10612–10620, Jul. 2011.
- [13] M. V. Kovalenko, R. D. Schaller, D. Jarzab, M. a. Loi, and D. V. Talapin, "Inorganically Functionalized PbS–CdS Colloidal Nanocrystals: Integration into Amorphous Chalcogenide Glass and Luminescent Properties," *J. Am. Chem. Soc.*, vol. 134, no. 5, pp. 2457–2460, Feb. 2012.
- [14] M. A. Boles, D. Ling, T. Hyeon, and D. V. Talapin, "The surface science of nanocrystals," *Nat. Mater.*, vol. 15, no. 2, pp. 141–153, Jan. 2016.
- [15] J. S. Owen, J. Park, P. Trudeau, and a P. Alivisatos, "Reaction Chemistry and Ligand Exchange at Cadmium–Selenide Nanocrystal Surfaces," *J. Am. Chem. Soc.*, vol. 130, no. 37, pp. 12279–12281, Sep. 2008.
- [16] J. Owen, "Nanocrystal Structure. The Coordination Chemistry of Nanocrystal Surfaces.," *Science (80-.)*, vol. 347, no. 6222, pp. 615–616, 2015.
- [17] B. Fritzing, I. Moreels, P. Lommens, R. Koole, Z. Hens, and J. C. Martins, "In Situ Observation of Rapid Ligand Exchange in Colloidal Nanocrystal Suspensions Using Transfer NOE Nuclear Magnetic Resonance Spectroscopy," *J. Am. Chem. Soc.*, vol. 131, no. 8, pp. 3024–3032, Mar. 2009.
- [18] R. Gomes *et al.*, "Binding of phosphonic acids to CdSe quantum dots: A solution NMR study," *J. Phys. Chem. Lett.*, vol. 2, no. 3, pp. 145–152, 2011.
- [19] R. B. Balow, E. J. Sheets, M. M. Abu-Omar, and R. Agrawal, "Synthesis and Characterization of Copper Arsenic Sulfide Nanocrystals from Earth Abundant Elements for Solar Energy Conversion," *Chem. Mater.*, vol. 27, no. 7, pp. 2290–2293, Apr. 2015.
- [20] R. B. Balow, C. K. Miskin, M. M. Abu-Omar, and R. Agrawal, "Synthesis and Characterization of $Cu_3(Sb_{1-x}As_x)S_4$ Semiconducting Nanocrystal Alloys with Tunable Properties for Optoelectronic Device Applications," *Chem. Mater.*, vol. 29, no. 2, pp. 573–578, Jan. 2017.

- [21] Y. Wu, C. Wadia, W. Ma, B. Sadler, and A. P. Alivisatos, "Synthesis and Photovoltaic Application of Copper(I) Sulfide Nanocrystals," *Nano Lett.*, vol. 8, no. 8, pp. 2551–2555, Aug. 2008.
- [22] R. Dierick *et al.*, "Surface Chemistry of CuInS₂ Colloidal Nanocrystals, Tight Binding of L-Type Ligands," *Chem. Mater.*, vol. 26, no. 20, pp. 5950–5957, Oct. 2014.
- [23] A. Hassinen, I. Moreels, K. De Nolf, P. F. Smet, J. C. Martins, and Z. Hens, "Short-Chain Alcohols Strip X-Type Ligands and Quench the Luminescence of PbSe and CdSe Quantum Dots, Acetonitrile Does Not," *J. Am. Chem. Soc.*, vol. 134, no. 51, pp. 20705–20712, Dec. 2012.
- [24] C. Jiang, J. Lee, and D. V. Talapin, "Soluble Precursors for CuInSe₂, CuIn_{1-x}Ga_xSe₂, and Cu₂ZnSn(S,Se)₄ Based on Colloidal Nanocrystals and Molecular Metal Chalcogenide Surface Ligands," *J. Am. Chem. Soc.*, vol. 134, no. 11, pp. 5010–5013, Mar. 2012.

6. OPTOELECTRONIC CHARACTERIZATION OF ENARGITE THIN FILMS AND DEVICES

Significant parts of this chapter, including figures and excerpts of text, have been previously published in the proceedings of a conference: Scott A. McClary, Siming Li, Xinxing Yin, Patricia Diplo, Darius Kuciauskas, Yanfa Yan, Jason B. Baxter, and Rakesh Agrawal, “Optoelectronic characterization of emerging solar absorber Cu_3AsS_4 ”, *46th IEEE Photovoltaics Specialists Conference*, June 2019. The work is © IEEE, 2019 and reprinted here with permission. Additional work that was not included in the conference proceedings is also included here, and the work published in the conference proceedings has been supplemented with additional details.

6.1 Introduction

The previous chapters of this thesis have focused on the development and improvement of enargite (ENG) Cu_3AsS_4 thin films from morphological and compositional purity standpoints; little attention has been paid to the material’s defect and optoelectronic properties. Optimized films have been fabricated into devices, but the power conversion efficiencies have remained low, failing to surpass 0.35% in a field where the top-tier technologies have efficiencies far exceeding 20% [1]. While efficiencies are a convenient bottom line for comparing various materials, they are highly sensitive to band alignment, interface recombination, and other factors that are not readily apparent, so the true potential of a material can be difficult to determine from efficiencies alone. It is therefore prudent to evaluate the performance of new materials (such as ENG) independently of device fabrication.

In this chapter, a suite of characterization techniques is used to evaluate the defect properties and carrier dynamics of ENG films fabricated from oleylamine (OLA)-capped nanoparticle (NP) precursors unless otherwise noted. Photoluminescence (PL) spectroscopy is used to investigate the shallow defect properties at room and cryogenic temperatures. Hall effect measurements are used to determine the carrier concentrations and mobilities that frame the subsequent discussions of carrier dynamics. Time-resolved terahertz spectroscopy (TRTS) is used to investigate carrier lifetimes and determine the dominant recombination mechanisms; the conclusions from TRTS measurements are reinforced by time-resolved photoluminescence (TRPL)

measurements. The mobilities, lifetimes, and general defect characteristics indicate that ENG-based solar cells should have significantly higher efficiencies than what has been achieved so far. A combination of experimental measurements (cyclic voltammetry) and simulations is then presented, demonstrating that the device architecture currently used for ENG is completely inappropriate. Suggestions for an alternative buffer layer are then presented, based on a combination of simulations and literature results. This chapter ultimately demonstrates that ENG-based solar cells have the potential to achieve high efficiencies, provided that the device architecture is significantly upgraded in parallel with continued improvements to absorber layer morphology and properties.

6.2 Experimental Methods

6.2.1 Materials

All chemicals were used as received and stored in a nitrogen-filled glovebox unless otherwise noted. Details regarding all chemicals used for NP synthesis and ligand exchange were described in previous chapters. Tetrabutylammonium hexafluorophosphate (TBAPF₆, >99%, for electrochemical analysis), acetonitrile (MeCN, >99.8%, anhydrous) and diammonium sulfide (DAS, (NH₄)₂S, 40-48 wt% in water) were obtained from Sigma-Aldrich.

6.2.2 Characterization Methods

Photoluminescence (PL) spectroscopy was conducted at the National Renewable Energy Laboratory (NREL) using a 633 nm He:Ne laser excitation and a helium closed-cycle cryostat to reach temperatures of 4.25 K. Hall effect measurements were conducted at Purdue University in the van der Pauw geometry on an Ecopia AHT55T5 system using a magnetic field of 0.556 T. Time-resolved terahertz (TRTS) spectroscopy was conducted at Drexel University in both transmission and reflection geometry using a regeneratively amplified Ti:sapphire laser operating at 1 kHz repetition rate and 50 fs pulses. THz pulses were generated and detected by optical rectification and free-space electro-optic sampling with ZnTe crystals [2]. An optical parametric amplifier was used to tune the pump wavelength, and the pump-probe delay time was controlled using an optical delay line. Time-resolved photoluminescence (TRPL) measurements were conducted at Purdue University on a custom optical setup using a 447 nm diode laser or 600 nm variable wavelength laser for excitation and a PDM photon counting module for signal detection.

Cyclic voltammetry (CV) measurements were conducted using a home-built three-electrode system with 0.1 M TBAPF₆ in MeCN as the electrolyte and a platinum wire as the counter electrode. Admittance spectroscopy (AS) was conducted using an Agilent A4294A impedance analyzer. The measurements were done in the dark using a 20 mV_{rms} AC signal under a liquid nitrogen-cooled vacuum chamber starting at low temperatures.

Unless otherwise noted, the measurements presented here were conducted on ENG Cu₃AsS₄ thin films fabricated from oleylamine-capped luzonite nanoparticles (NPs), as described in previous chapters of this thesis. Some measurements (including some TRTS and TRPL) were conducted on ligand exchanged films, and some were conducted after a DAS etch depending on the substrate, but there were not major differences noted in the overall conclusions of these experiments.

The TRPL setup in the Agrawal lab at Purdue was not appropriate to evaluate the TRPL response of ENG thin films because the sensitivity range of the photomultiplier tube is ~910-1400 nm, and the main emission line for ENG occurs at ~880 nm. Therefore, a collaboration with Prof. Libai Huang's lab (Purdue Chemistry) was developed.

6.2.3 Simulation Methods

Two programs were used for simulation of the band diagrams and current-voltage (J-V) curves of ENG-based solar cells. The band diagrams shown in this chapter were simulated using ADEPT [3], while the J-V curves were simulated using SCAPS [4]. The simulated results were similar between the two programs, but ADEPT's band diagram data was more easily extractable, and SCAPS enabled much faster and user-friendly simulation of multiple data points, hence the use of outputs from both programs here.

6.3 Results and Discussion

6.3.1 Photoluminescence

Photoluminescence (PL) spectroscopy measures the emission spectra of semiconducting materials when they are illuminated with above-bandgap photons, such as those from a monochromatic laser. The spectra provide information about electronic transitions and band structure, and by varying the sample temperature and laser intensity, one can assign various peaks to different radiative transitions such as band-to-band or donor-acceptor pair (DAP)

recombination. Here, PL was used to investigate the electronic structure of ENG thin films fabricated using NPs as precursors. A 633 nm laser was used, corresponding to an approximate absorption coefficient (α) of approximately $60,000 \text{ cm}^{-1}$ (or a characteristic absorption depth ($1/\alpha$) of 167 nm), so it is expected that all signal results from the $\sim 1 \mu\text{m}$ ENG absorber layer rather than the fine grain layer underneath [5].

Figure 6.1 gives the room-temperature PL emission spectra for an ENG film illuminated with a 633 nm He:Ne laser operating at 1 mW and 10 mW. The spectra can be fit with two peaks centered near 1.37 and 1.41 eV. The peak at 1.41 eV agrees well with the reported bandgap [6], [7], and the peak at 1.37 eV is only $\sim 40 \text{ meV}$ below the bandgap, signifying emission from shallow defect states. The increased width of the shallow defect peak relative to the band edge peak indicates a broad distribution of energies, which may be related to compensation, donor-acceptor pair effects, or band tailing.

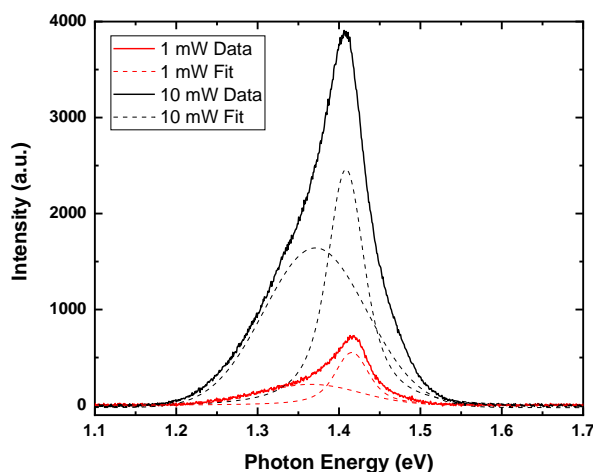


Figure 6.1. Room-temperature photoluminescence spectra of ENG thin films using a 633 nm laser excitation. Solid lines indicate raw data, while dashed lines indicate the best fit Voigt curves.

Figure 6.2a gives the PL emission spectra from the center of an ENG thin film mounted in a helium-cooled cryostat ($T = 4.25 \text{ K}$) at laser intensities spanning three orders of magnitude. (Note that the spectrum collected from the edge of the sample displayed a prominent peak at 1.15 eV, suggesting the presence of a deep defect and the need to mitigate edge effects in ENG thin films.) The spectra display multiple overlapping peaks, corresponding to distinct luminescence events. At cryogenic temperatures, new radiative recombination pathways become accessible because there

is not enough thermal energy to facilitate excitation of carriers into or out of trap states; additionally, excitonic luminescence must also be considered. Excitonic binding energies have not previously been calculated for ENG, but using a simple hydrogenic model [8], [9] and density functional theory-derived (DFT) data published by Wallace et al [10], the excitonic binding energies are calculated as 44, 76, and 74 meV, depending on the local orientation of the film. These binding energies are a first approximation and may vary somewhat; they are inversely proportional to the square of the dielectric constant, which has not been measured experimentally for ENG and may vary from the published DFT-derived values of 5.70, 5.89, and 5.91.

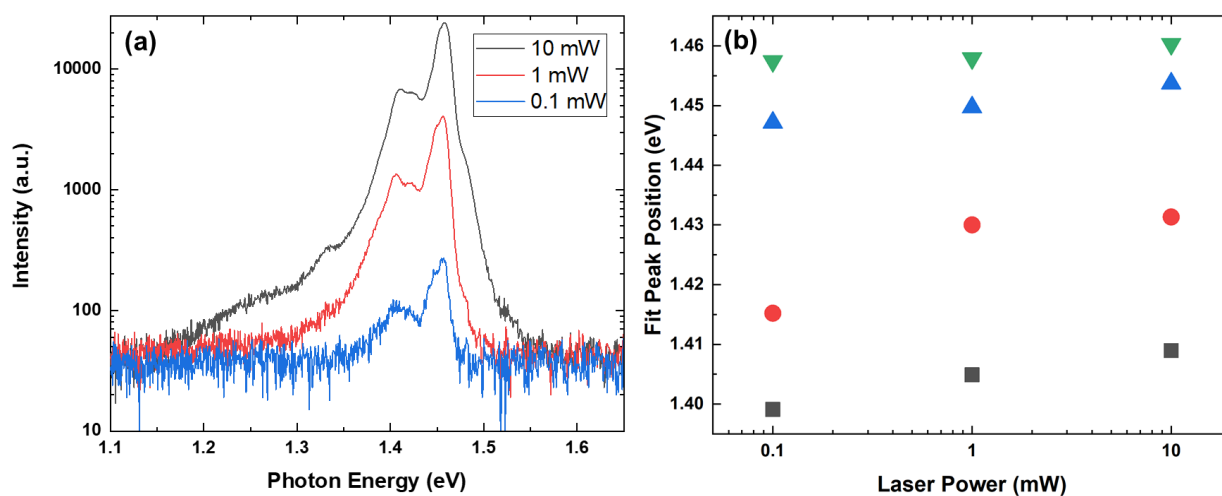


Figure 6.2. (a) Cryogenic (4.25 K) photoluminescence spectra of an ENG thin film at various laser powers. [© 2019, IEEE] (b) Estimated peak position from Voigt-fit peaks as a function of incident laser power.

Deconvolution of each spectrum in Figure 6.2a was attempted, but the fitting was not completed to an acceptable level using Gaussian, Lorentzian, or Voigt peaks; in particular, the region between 1.40 and 1.44 eV was not fit well in any scheme. Therefore, it is not currently possible to draw definite conclusions regarding the origins of each peak, though a preliminary analysis based on the Voigt peak fitting (which fit the spectra better than either Gaussian or Lorentzian peaks alone did) is presented here. Figure 6.2b gives the center of the best fit peaks for each spectrum. The peak positions shift slightly with increasing laser power, with values of ~5-8 meV/decade for the two lower energy peaks and ~2-5 meV/decade for the two higher energy peaks. Blue shifts with increasing power are often attributed to donor-acceptor pair (DAP) recombination due to the shorter average distance between donors and acceptors and hence a larger coulombic

force to contribute to the emitted photon's energy [8], [9]. However, another quantity to check is the integrated PL intensity as a function of laser intensity, which generally follows a power law $I_{PL} = aP^k$, where a and k are constants [11]. For $k < 1$, DAP recombination and free-to-bound exciton transitions are expected, while $1 < k < 2$ signifies free or bound-exciton recombination. Because the peaks cannot be unambiguously deconvoluted here, a definitive value of k cannot be determined. To assign the PL peaks to specific transitions, data must be taken at additional temperatures and laser powers; a higher wavelength resolution may also be needed. Temperature-dependent PL would allow for a Varshni fit for ENG's bandgap, something that has not yet been reported.

Despite the current uncertainty in the interpretation of the 4.25 K PL spectra, there are several key takeaways that suggest promise for ENG. First is that all peaks (including a low-intensity peak around 1.33 eV in the 10 mW spectrum) are relatively shallow in relation to the band edge, implying that they will not significantly impede carrier transport at operating conditions for solar cells. Additionally, the peaks are sharp when compared to the room temperature case, which is not typically seen in semiconductors such as CIGSe and CZTSSe. Broad peaks are caused by strong potential fluctuations in a material resulting from defect compensation, and blueshifts in the PL emission energies are much larger than those seen for DAP transitions [8]. This implies that any shallow defects present in ENG are relatively localized in low concentrations, suggesting the potential for relatively straightforward defect mitigation in ENG. More PL measurements must be taken to estimate the temperature-dependent bandgap of ENG and any peak quenching. Additionally, DFT calculations should supplement future measurements and allow for assignment of PL peaks to specific defect- and exciton-related recombination events.

6.3.2 Hall Effect Measurements

Hall effect measurements, which involve the application of a magnetic field to a sample and subsequent measurement of the laterally induced current and voltage, can be used to determine the carrier type, carrier concentration, carrier mobility, and conductivity of thin film materials [12]. Table 6.1 gives the average value and standard deviation of these quantities for an ENG thin film fabricated on quartz; an Ohmic contact was made by soldering indium onto each corner of the ENG. A positive Hall coefficient indicated a p-type sample.

Table 6.1. ENG carrier concentration, conductivity, and mobility derived from Hall measurements.

Quantity	Average Value	Standard Deviation
Carrier Concentration (cm ⁻³)	8.1 * 10 ¹⁵	1.8 * 10 ¹⁵
Conductivity (S/cm)	1.9*10 ⁻³	1.2*10 ⁻⁵
Mobility (cm ² /Vs)	1.54	0.33

The three parameters derived from Hall effect measurements are critical information for modeling, as discussed later in this section. The carrier concentration is acceptable for semiconducting applications and was checked using simple 4-point probe resistivity measurements on an ENG film on soda-lime glass; an approximate value of $5 \times 10^{15} \text{ cm}^{-3}$ was obtained, confirming the order of magnitude for the carrier concentrations. The mobility is 1-2 orders of magnitude lower than what is typically seen for high-efficiency materials, but improvements to the film (such as removal of carbon) will likely result in a significant increase of this value. Hall effect measurements must be used to monitor the effects of various processing changes on the properties of ENG thin films in future work.

6.3.3 Time-Resolved Terahertz Spectroscopy

Time-resolved terahertz (TRTS) spectroscopy is a technique used to study the transient photoconductivity on the femtosecond (fs) to nanosecond (ns) timescale in thin-film and single crystal semiconductors [2], [13]. It is a pump-probe technique in which the sample of interest is photoexcited by a pulsed visible laser, and then the attenuation of a THz pulse passing through the film is measured. The changing pulse strength directly relates to the photoconductivity, which decreases over time due to the recombination of electrons and holes. Photoconductivity is directly related to the material's mobility and carrier concentration, so the carrier dynamics may be determined. Additionally, the incident wavelength can be tuned to investigate recombination mechanisms at various depths in the material, and the laser power can be adjusted to vary the initial carrier density, allowing one to distinguish between Shockley-Read-Hall (SRH), surface, radiative, and Auger recombination.

Figure 6.3 shows $\Delta E/E$ from TRTS measurements on an ENG film as a function of time. Note that the film used here were fabricated on quartz, rather than molybdenum-coated soda-lime glass (Mo-SLG) typically used for devices, as THz radiation transmits through quartz. The photoconductivity ($\Delta\sigma = q\Delta n\mu$) is directly proportional to $\Delta E/E$. Assuming that mobility is independent of time, the decrease of $\Delta E/E$ is only from carrier recombination [14]. When the initial

carrier density is $4 \times 10^{17} \text{ cm}^{-3}$, the total mobility, $\mu_e + \mu_h$, is $11 \text{ cm}^2/(\text{Vs})$, or $\sim 7x$ higher than the hole mobility (μ_h) of $1.5 \text{ cm}^2/(\text{Vs})$ from Hall effect measurements. This allows for extraction of the electron mobility (μ_e) as $\sim 9 \text{ cm}^2/(\text{Vs})$.

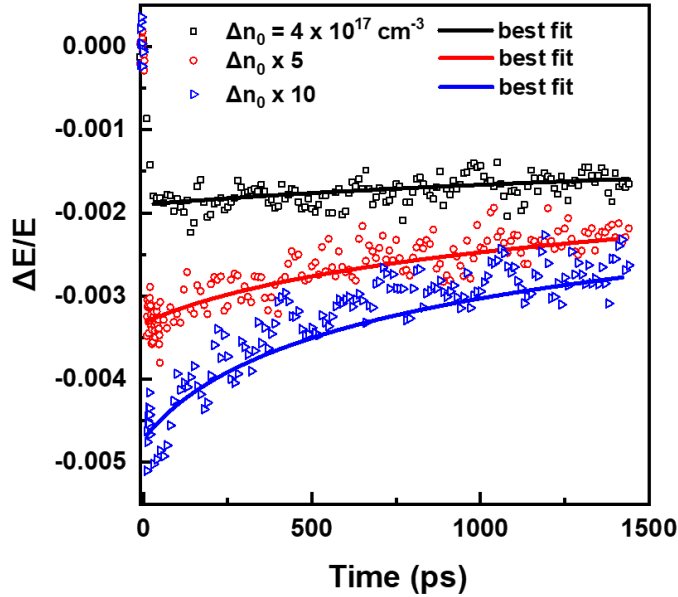


Figure 6.3. Change in electric field from TRTS measurements as a function of delay time (excitation wavelength is 740 nm). Solid lines are the global fits of the diffusion-recombination model assuming third-order recombination kinetics with $\alpha = 3 \times 10^4 \text{ cm}^{-1}$, $D = 0 \text{ cm}^2/\text{s}$, and $k_{Aug} = 3.4 \times 10^{-27} \text{ cm}^6/\text{s}$. [© 2019, IEEE]

The fluence-dependent decay (i.e. the time constants) in Figure 6.3 indicate that, under TRTS experimental conditions, either radiative or Auger recombination dominates, rather than SRH or surface recombination [15]. These dynamics suggest that any deep defects present in ENG films do not dominate the transport of charge carriers, either because of low concentrations or small capture cross sections. Furthermore, the photoconductivity persists beyond the detection limit of the TRTS setup (1.4 ns), suggesting carrier lifetimes on the order of nanoseconds, a promising value for an emerging photovoltaic material.

To quantify the radiative and Auger recombination rates, the carrier dynamics were fit with a global diffusion-recombination model (Equation 6.1):

$$\frac{\partial n}{\partial t} = D \frac{\partial^2 n}{\partial x^2} - k_{SRH}n - k_{rad}n^2 - k_{Aug}n^3 \quad (6.1)$$

By fitting the model assuming exclusively third-order recombination, an upper limit for the Auger rate constant is $3.4 \cdot 10^{-27} \text{ cm}^6/\text{s}$, and the time constant is 1.6 ns for $\Delta n_0 = 4 \cdot 10^{17} \text{ cm}^{-3}$. By assuming exclusively second-order recombination, the radiative rate constant is $1.27 \cdot 10^{-9} \text{ cm}^3/\text{s}$, and the time constant is 1.8 ns. The similarity of the time constants suggests that both types of recombination play a significant role in carrier transport. Because radiative and Auger recombination dominate at the high-injection conditions used here (recall that the hole concentration is $\sim 10^{16} \text{ cm}^{-3}$ from Hall effect measurements), the SRH time constant exceeds 1.6 ns. At lower injection levels more relevant to TFSC operation, radiative and Auger recombination are expected to be less significant, so SRH recombination may become more dominant. However, the SRH lifetime is independent of fluence, so it will remain on the order of nanoseconds. At this point, it is not clear if carrier trapping and de-trapping have a significant impact on carrier dynamics, as has been seen in CZTSSe absorbers [16]; further studies (such as temperature-dependent measurements) are needed.

The measurements just discussed were taken on ENG films that were fabricated on quartz, which was necessary for the THz *transmission* measurements. To obtain data that is more relevant to device operation, ENG films were fabricated on Mo-SLG for THz *reflection* measurements. The use of reflection mode allows for use of different substrates, which enables study of the impacts of molybdenum and sodium on film properties. Figure 6.4 gives the THz reflection response for ENG films fabricated on quartz, bare SLG, and Mo-coated SLG at an excitation wavelength of 800 nm. The quartz signal (Figure 6.4a) indicates that the dynamics are similar between transmission and reflection mode, justifying the use of either setup for the study of ENG films.

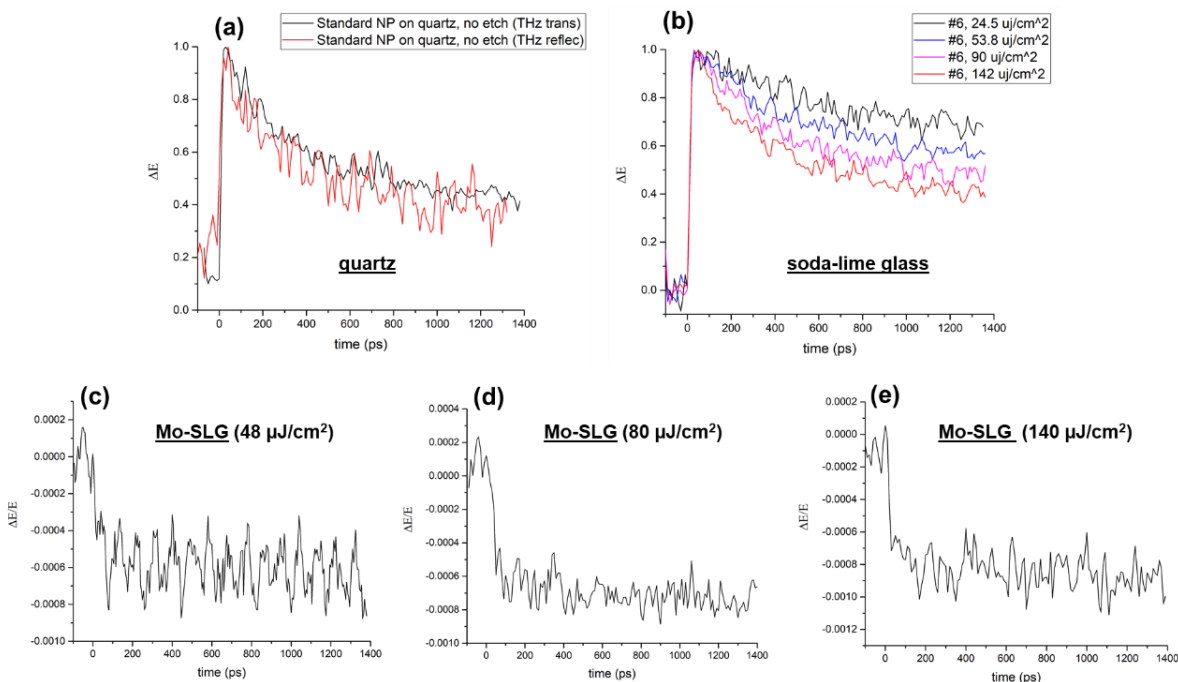


Figure 6.4. Change in electric field from TRTS reflection mode measurements. All spectra were taken with an 800 nm excitation source. (a) ENG response on quartz for both reflection and transmission mode. (b) ENG response for a soda-lime glass (no Mo) substrate at a variety of fluences. (c) – (e) ENG response on Mo-coated soda-lime glass substrate at the indicated fluence.

Figure 6.4b shows that the carrier decay rate in an ENG film on SLG depends on the initial carrier density, meaning that Auger or radiative recombination dominate; this situation is similar to what is seen on quartz substrates and suggests that sodium does not have a large impact on carrier dynamics. Figures 6.4c-e, however, demonstrate a relatively flat decay for ENG on Mo-SLG substrates at all fluences, suggesting a longer carrier lifetime at these conditions. It is unclear which type of recombination dominates the signal, as the data is somewhat noisy, though it does appear that second- and third-order processes are less relevant for ENG fabricated on Mo substrates. Higher-resolution data from Mo-SLG samples is also critical but challenging due to the high refractive index (~ 70) of Mo relative to quartz (~ 1.5), which results in a much lower signal-to-noise ratio.

Figure 6.5 gives the TRTS response of ENG films on various substrates at 400 nm and 800 nm. The differences in absorption coefficients ($\sim 1.17 \times 10^5 \text{ cm}^{-1}$ for 400 nm and $1.3 \times 10^4 \text{ cm}^{-1}$ for 800 nm) allow for the probing of recombination mechanisms at the surface of the film and throughout the bulk of the film [5]. As shown in Figures 6.5a-c, the decay of ENG films fabricated

on quartz and soda-lime glass occurs more rapidly at 800 nm than 400 nm, suggesting that the surface of ENG is well-passivated relative to the bulk; this reinforces the earlier conclusion that surface recombination (a first-order process) does not dominate. However, Figures 6.5d-e demonstrate a similar response for 400 nm and 800 nm excitation when ENG is grown on a Mo-SLG substrate, implying that there is no significant difference between bulk and surface recombination. This suggests that Mo may effectively passivate bulk defects, though it must again be stressed that higher-resolution data is needed to make a definite conclusion. Mo may diffuse into the bulk of the ENG film and alter its defect chemistry by creating new point defects and complexes. Such diffusion is not typically seen in CIGS or CZTS films, which are processed at higher temperatures, though it is possible that the As-S liquids used may enhance diffusivity of Mo along the grain boundaries in the film. Experiments at additional wavelengths would help determine the depth at which bulk recombination is effectively suppressed, and a depth-dependent composition profile may be obtained using secondary ion mass spectrometry (SIMS) or glow discharge optical emission spectroscopy (GDOES) for correlation with wavelength-dependent results.

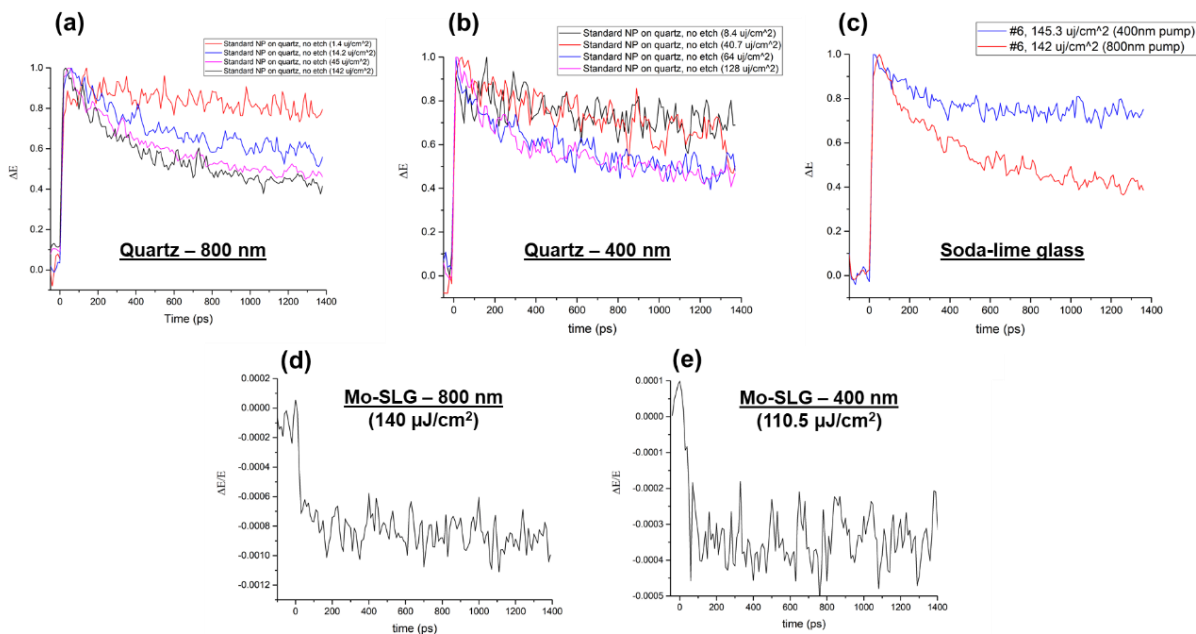


Figure 6.5. Change in electric field from TRTS reflection mode measurements on the indicated substrates and laser fluences at 400 and 800 nm.

The TRTS measurements discussed so far have used the maximum time range that the detector can access (~ 1.4 ns). By increasing the temporal resolution to sub-picosecond levels, more information regarding the initial carrier dynamics in ENG films can be gathered. Figure 6.6 gives the short-time TRTS measurements for ENG films in transmission mode on quartz and in reflection mode on Mo-SLG. A rapid decay of roughly half of the carriers is noted within the first ~ 5 ps. The origins of this decay are unclear and will require temperature-dependent measurements to fully understand. Several theories are that the decay is due to rapid thermalization of hot carriers to the band edge or interactions with defect states very close to the band edge [17], [18].

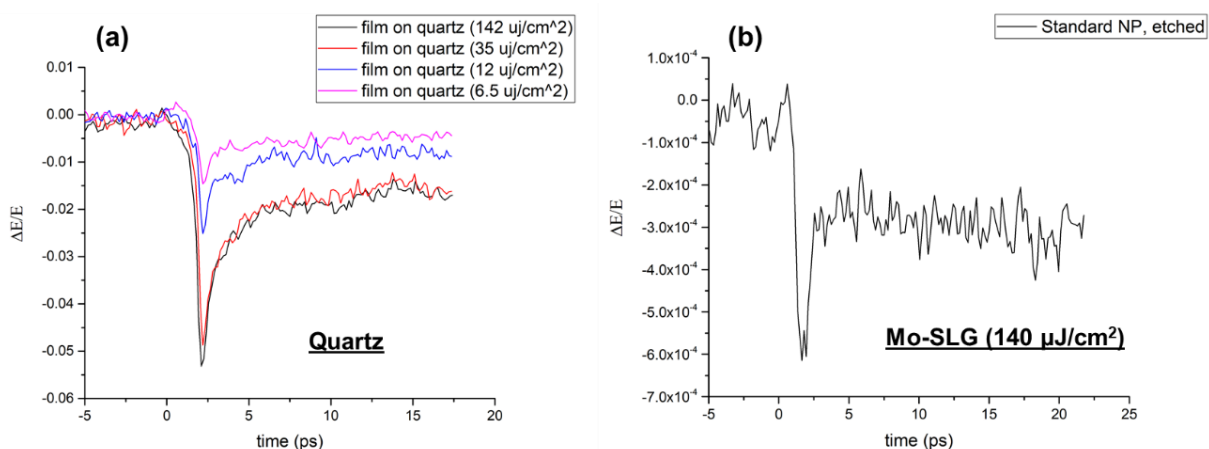


Figure 6.6. Change in electric field from short-time TRTS measurements on ENG films fabricated on quartz and Mo-SLG. Pump wavelength is 800 nm.

While additional TRTS measurements are needed to fully understand ENG's carrier dynamics, initial results demonstrate promising characteristics that justify its further use in thin-film solar cells. Because the response on quartz is dominated by radiative and Auger recombination, deep defects are not prominent in the material, suggesting that long lifetimes may be achievable in ENG films. Lifetimes are already on the nanosecond scale, a promising benchmark value for emerging absorber materials. Comparing the response of films on bare SLG and Mo-coated SLG demonstrate that molybdenum has an impact on the carrier dynamics of Cu_3AsS_4 thin films. Further investigation is needed to determine the specific impacts of Mo on defect chemistry, carrier lifetimes, mobilities, etc.; such a study may result in the need to alter the substrate on which ENG films are grown.

6.3.4 Time-Resolved Photoluminescence Spectroscopy

Time-resolved photoluminescence (TRPL) spectroscopy is a technique in which a pulsed laser is used to photoexcite carriers in a sample, and emission due to radiative recombination over time is measured. The data can then be fit by a sum of exponential decay functions to estimate the minority carrier lifetime. However, nonidealities within the absorber layer can make extraction of the true minority carrier lifetime challenging [16]. A range of voltages, intensities, wavelengths, and temperatures is often necessary to accurately assess carrier lifetimes from TRPL measurements. Here, TRPL measurements on ENG thin film absorbers are presented with the aims of extracting the minority carrier lifetime for device modeling and comparing the results to those of the TRTS measurements discussed in the previous section.

TRPL was used to estimate the minority carrier lifetime of ENG films fabricated on a variety of substrates (including quartz, soda-lime glass, Mo-SLG, and Mo-borosilicate glass), with a variety of thicknesses, with and without DAS etching (depending on the substrate), and using ligand exchanged and non-ligand exchanged NPs as the starting point. Figure 6.7 gives the TRPL response from a sample fabricated on quartz using standard OLA-capped NPs as the starting layer. The excitation source was a pulsed blue laser ($\lambda = 447 \text{ nm}$) at $3.35 \mu\text{W}$, corresponding to an initial carrier density of roughly $3.1 \times 10^{18} \text{ cm}^{-3}$ (i.e. high injection conditions). The signal is fit well by a biexponential decay with $\tau_1 = 0.42 \text{ ns}$ and $\tau_2 = 2.08 \text{ ns}$. Due to ENG's high predicted absorption coefficient ($1.3 \times 10^5 \text{ cm}^{-1}$) at 447 nm [5], most absorption will occur near the surface of the film. It is therefore likely that the short τ_1 results from diffusion to and recombination at the surface and that τ_2 is more representative of the bulk lifetime. Note that τ_2 exceeds the minimum Auger and radiative lifetimes estimated from TRTS measurements. Using τ_2 and a $9 \text{ cm}^2/(\text{Vs})$ electron mobility from TRTS and Hall measurements, the diffusion length for minority carriers in the bulk is estimated as $\sim 200 \text{ nm}$.

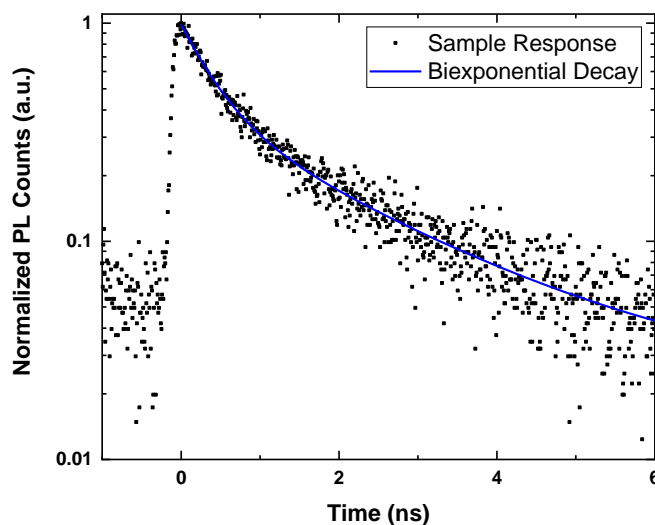


Figure 6.7. TRPL response of an ENG film on quartz at 447 nm excitation wavelength. The curve is well fit by a biexponential decay with $\tau_1 = 0.42$ ns and $\tau_2 = 2.08$ ns, with relative weights for each curve as 24% and 76%, respectively.

TRPL was also conducted at a variety of conditions using the same batch of NPs as precursors; the lifetimes and relative weights are summarized in Table 6.2. The lifetimes are all lower than those presented for the sample in Figure 6.7; these samples were exposed to ambient conditions for a longer period, which may have caused the lifetimes to deteriorate. Note that the lifetimes for the samples on molybdenum are consistently higher than those on quartz, supporting the TRTS reflection measurements that suggest that Mo passivates bulk defects in ENG.

Table 6.2. TRPL-derived time constants and relative weights for ENG samples fabricated on various substrates. Excitation wavelength was 447 nm.

Sample	τ_1 (ps)	Rel. wt.	τ_2 (ps)	Rel. wt.
Quartz (thin)	124 ± 2	32%	748 ± 14	68%
Quartz (thick)	105 ± 1	35%	955 ± 19	65%
Mo-SLG (no etch)	135 ± 2	24%	1264 ± 22	76%
Mo-SLG (etched)	126 ± 1	40%	1189 ± 30	60%
Mo-BSG	148 ± 2	25%	1438 ± 26	75%

By varying the power of the laser, the initial carrier density can be tuned and used to distinguish between various recombination mechanisms in the film. The PL intensity is proportional to the radiative radiation from the absorber layer [16], [19]. For a p-type semiconductor such as ENG, the decay should proceed according to Equation 6.2.

$$I_{pL} = B(\Delta n^2 + p_0 \Delta n) \quad (6.2)$$

In Equation 6.2, Δn represents the excess carrier density, p_0 represents the initial carrier density of the film, and B is a constant. Because the only variable quantity in Equation 6.2 is the excess carrier density, one can time-shift the TRPL data from different curves to match carrier densities in time. The excess carrier density typically follows a mono-exponential or biexponential decay curve as in Equation 6.3.

$$\Delta n = Ae^{-\frac{t}{\tau_1}} + Be^{-\frac{t}{\tau_2}} \quad (6.3)$$

In Equation 6.3, the lifetimes τ_1 and τ_2 are constant for SRH and surface recombination-dominated samples. Figure 6.8 gives the time-shifted TRPL for a Mo-SLG ENG sample at different injection intensities. The two traces do not align when shifted to the same carrier densities; this suggests that τ is not independent of time. Therefore, it varies with Δn , suggesting that radiative or Auger recombination dominate the carrier dynamics at these test conditions.

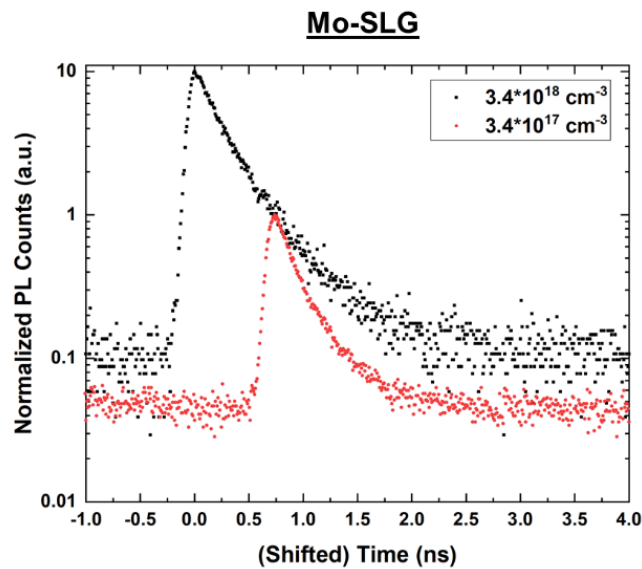


Figure 6.8. TRPL for ENG films fabricated on Mo-SLG substrates, time-shifted such that the initial carrier densities match.

The TRPL experiments discussed to this point have used pulsed 447 nm excitation, which means that recombination centers at the surface may play a significant role. Figure 6.9 compares the TRPL response of an ENG sample fabricated on Mo-SLG at excitation wavelengths of 447 nm and 600 nm; the initial carrier densities are within a factor of 2, and the lifetimes are relatively similar. The relative similarity between bulk and surface recombination was also noted on Mo-SLG samples in TRTS and suggests that surface states are effectively passivated in air.

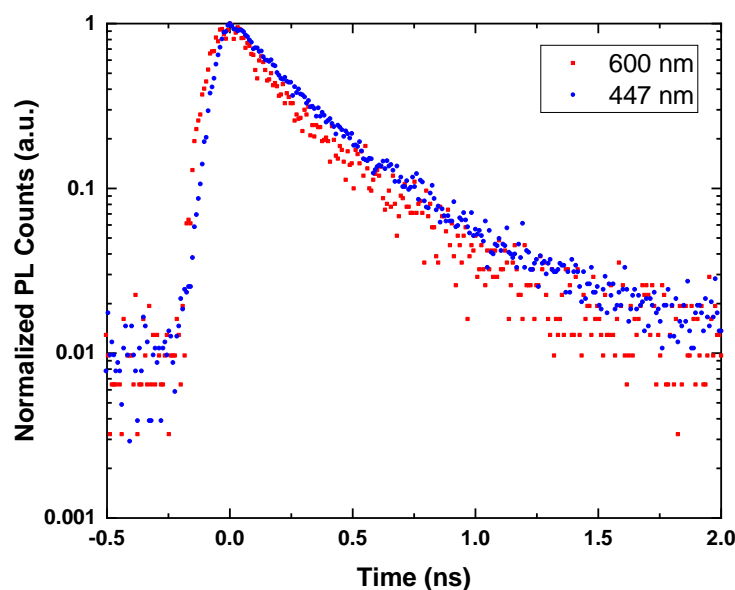


Figure 6.9. TRPL response from an ENG sample fabricated on Mo-SLG at 447 and 600 nm excitation wavelengths.

The data associated with Figures 6.7-6.9 and Table 6.2 took an extended amount of time to collect, significantly longer than high-quality perovskite materials that had been tested previously on the same system. There are several plausible reasons for this, including that the detector efficiency in the 880-910 nm range is only ~5%, the films are rough and hence have a significant reflectance, the system has poor optics for collecting all signal emitted from the ENG films, and/or that the absolute photoluminescence efficiency of ENG is low. By performing a 1 minute etch in diammonium sulfide $[(\text{NH}_4)_2\text{S}]$, the count rate increases significantly, suggesting that a passivating layer may form on the surface of ENG films when they are exposed to air. This phenomenon should be further explored, and films must be exposed to the environment minimally to maximize device performance.

The TRPL presented in this section reveals promising characteristics for ENG-based thin film solar cells. In some cases, the minority carrier lifetime is on the order of nanoseconds, though future experiments must carefully consider the effects of a passivating layer on the ENG surface. Additionally, radiative and/or Auger recombination appear to be significant at experimental conditions used (i.e. high injection), meaning that the relative impact of SRH recombination, and hence deep defects, is low. Future TRPL experiments should be resolved over more orders of magnitude to ensure the highest accuracy in interpreting data, and exciting at low injection would be useful to lessen the overall impact of radiative and Auger recombination processes. Additionally, voltage and temperature-dependent measurements may further elucidate the carrier lifetimes and recombination mechanisms in ENG.

6.3.5 On the Origins of Poor Enargite Device Performance

The previous sections in this chapter have shown that ENG thin films have promising shallow and deep defect characteristics, carrier concentrations on the order of $1 \times 10^{16} \text{ cm}^{-3}$, hole (electron) mobilities of 1.5 (9.5) cm^2/Vs , and carrier lifetimes on the nanosecond timescale. In literature, solar cells with comparable or worse properties have achieved power conversion efficiencies around 5% [20], [21]. Though there are many improvements that can be made to the ENG absorber layer, it is worthwhile check for other factors that may limit the device performance of ENG-based solar cells.

The architecture used for ENG-based solar cells involves a molybdenum back contact and a cadmium sulfide (CdS) n-type layer, identical to what is used for most CIGSe and CZTSSe-based solar cells. However, this architecture was initially adopted for ENG without any knowledge of its valence band maximum (VBM) or conduction band minimum (CBM). Ultraviolet photoelectron spectroscopy (UPS) is often used to determine the VBM and Fermi levels of semiconducting materials, but it is very sensitive to surface conditions. Chapter 4 demonstrated that the surface of as-prepared ENG films is significantly arsenic- and sulfur-rich, so any measurements on such films will not represent the bulk properties of the material. Additionally, the effects of an $(\text{NH}_4)_2\text{S}$ etch on the surface composition and secondary phases in ENG are not known, and UPS is an expensive and difficult-to-access technique, so an alternative technique is necessary.

Cyclic voltammetry (CV) is an electrochemical technique that can be used to estimate the VBM of a material [22], [23]. Briefly, a semiconductor film of interest is immersed in an electrochemical solution, and a voltage is applied in a cyclic manner, usually starting from 0 V and going first in the positive direction. A rapid onset of current will occur, corresponding to carrier injection into the valence band. By referring the onset potential to a known standard, the absolute VBM can be estimated, and then the CBM may also be deduced from the measured band gap.

CV measurements for an ENG thin film immersed in a solution of 0.1 M TBAPF₆ in MeCN are given in Figure 6.10. The onset of current occurs around 0.67 V relative to a Ag⁺/AgCl reference electrode. Since reference electrodes drift slightly over time, ferrocene, which has a well-defined redox potential of -4.80 V vs. vacuum, was used as an internal standard [24]. Ferrocene's onset occurs at 0.46 V, so it follows that the VBM of ENG occurs at -5.01 eV vs vacuum. When combined with the 1.4 eV bandgap from EQE measurements, the conduction band edge lies at -3.61 eV vs. vacuum. The reliability of this CV measurement has been confirmed in two distinct ways. The VBM of a related material, Cu₃PS₄, was determined as -5.05 eV through CV [25]. Theoretical work has shown that the Cu₃PS₄ and Cu₃AsS₄ valence bands mainly consist of Cu and S orbitals, so the similarity in the VBM between the two is expected [5], [26]. Additionally, CV measurements on Ag₂ZnSnSe₄ films were conducted internally and compared with results from UPS; the computed VBM were nearly identical.

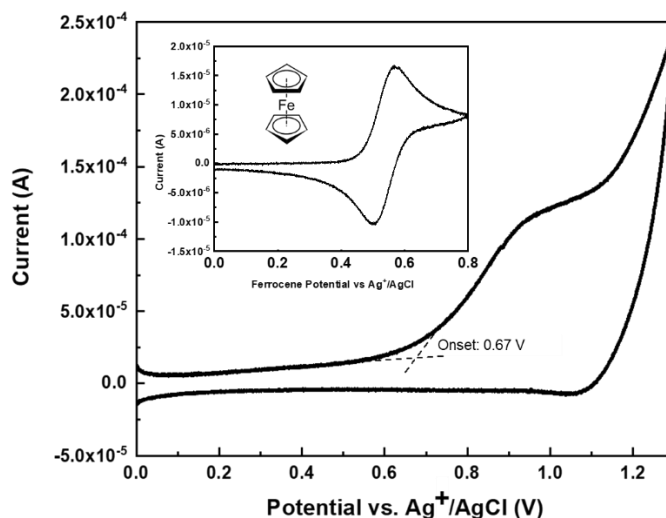


Figure 6.10. Cyclic voltammetry of an ENG thin film in 0.1 M tetrabutylammonium hexafluorophosphate in acetonitrile. The inset shows the CV response of a ferrocene internal standard. [© 2019, IEEE]

Now that the VBM and CBM (and other material properties such as mobility and carrier lifetime) of ENG are known, simulated band diagrams and current-voltage (J-V) curves can be generated to explore the impact of band alignment and material properties on expected device performance. Figure 6.11a gives the ADEPT-simulated band diagram for the ENG-CdS interface. A severe cliff offset at the junction is noted, which may lead to significant electron-hole pair recombination; additionally, there is very limited band bending in the absorber layer. Both factors severely limit the open-circuit voltage (V_{oc}), and hence the efficiency, of solar cells in this architecture. Note that the molybdenum back contact was not simulated here. The work function of (100)-oriented molybdenum is -4.95 eV [27], which is relatively close to the estimated ENG VBM of -5.01 eV, so this is not expected to be a major barrier to device performance at this point.

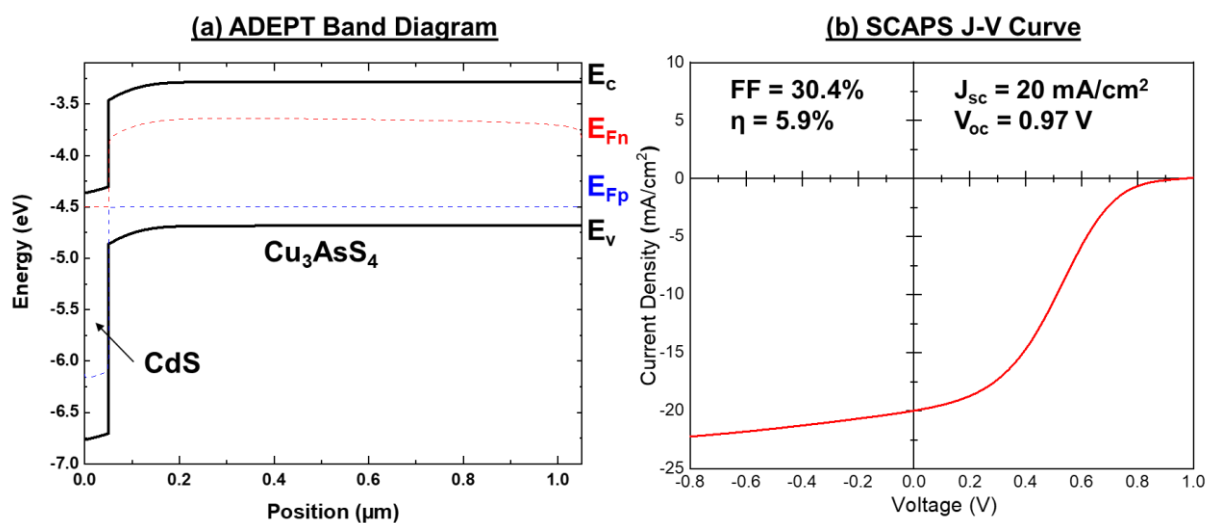


Figure 6.11. (a) ADEPT-simulated band diagram for the ENG-CdS interface. (b) SCAPS-simulated J-V curve for an ENG-CdS solar cell assuming 100 ns lifetime and no interfacial recombination. [© 2019, IEEE]

The large cliff offset suggests that alternative buffer layers are needed to pair with an ENG absorber layer for high-efficiency devices. This is reinforced by the simulated J-V curve shown in Figure 6.11b, which is the result of a SCAPS simulation of an ENG-CdS interface in the limit of long lifetimes (100 ns) and zero interfacial defects. The maximum efficiency that can be achieved in this configuration is only 5.9%, with a very low fill factor primarily contributing to the low performance. The full set of parameters used for SCAPS simulations are given in Table 6.3.

Table 6.3. Parameters used for simulation of J-V curves in SCAPS.

Cu₃AsS₄ Enargite			CdS (ZnS)		
Parameter	Value	Basis	Parameter	Value	Basis
Thickness	1 μm	SEM	Thickness	50 nm	SEM
Bandgap	1.4 eV	EQE	Bandgap	2.4 eV (3.5 eV)	[16] ([28])
Electron Affinity	3.61 eV	CV	Electron Affinity	4.45 eV (3.5 eV)	[29] ([28])
ϵ	5.83	[10]	ϵ	10	[16]
CB DOS	$1 * 10^{18} \text{ cm}^{-3}$		CB DOS	$2 * 10^{18} \text{ cm}^{-3}$	[16]
VB DOS	$1 * 10^{19} \text{ cm}^{-3}$		VB DOS	$2 * 10^{19} \text{ cm}^{-3}$	[16]
$v_{\text{th}}(e^-)$	$1 * 10^7 \text{ cm/s}$		$v_{\text{th}}(e^-)$	$1 * 10^7 \text{ cm/s}$	[16]
$v_{\text{th}}(h^+)$	$1 * 10^7 \text{ cm/s}$		$v_{\text{th}}(h^+)$	$1 * 10^7 \text{ cm/s}$	[16]
μ_e	$7 \text{ cm}^2 \text{ V}^{-1} \text{ s}^{-1}$	TRTS	μ_e	$50 \text{ cm}^2 \text{ V}^{-1} \text{ s}^{-1}$	[16]
μ_h	$1.5 \text{ cm}^2 \text{ V}^{-1} \text{ s}^{-1}$	Hall	μ_h	$20 \text{ cm}^2 \text{ V}^{-1} \text{ s}^{-1}$	[16]
N_A	$8 * 10^{15} \text{ cm}^{-3}$	Hall	N_D	$1.1 * 10^{16} \text{ cm}^{-3}$	[16]
τ_e	100 ns		τ_e	110 ns	[16]
τ_h	1000 ns		τ_h	1.1 ps	[16]
Contact	Flat bands		Contact	Flat bands	

The fact that device performance has not yet approached 5.9% (or even 3.0%, the efficiency from a SCAPS simulation assuming no interfacial recombination and a 2 ns lifetime) suggests that there may be significant interfacial states present at the ENG-CdS interface. One technique used to investigate defects in completed devices is admittance spectroscopy (AS), in which the capacitance of a completed device is measured as a function of frequency; the temperature and applied DC voltage can also be modified. Capacitance measurements involve the application of a small AC bias to a material; if the frequency is low enough, defect states can be filled, modifying the junction's capacitance. As the frequency is increased, the defects are no longer filled, and the capacitance decreases. The capacitance signature therefore shows the number of distinct defects in the material, and by performing temperature-dependent measurements, the activation energy of a defect can be determined by an Arrhenius plot.

The preliminary results of zero-bias AS on a completed ENG-CdS device (fabricated using a Cu film as the starting layer, rather than LUZ NPs) is given in Figure 6.12a. While the absolute values of capacitance do not follow the expected trend due to the difficulty in making stable contacts to the completed device, extraction of the inflection points is still possible. One inflection point is observed in each of the capacitance-frequency sweeps (Figure 6.12a), suggesting the

presence of one shallow defect in an ENG thin film. This demarcation frequency (ω_0) (i.e. the inflection point) can then be transformed and used in an Arrhenius plot (Figure 6.12b) to extract the activation energy of the defect. For 0 V applied DC bias, the activation energy is approximately 65.9 meV.

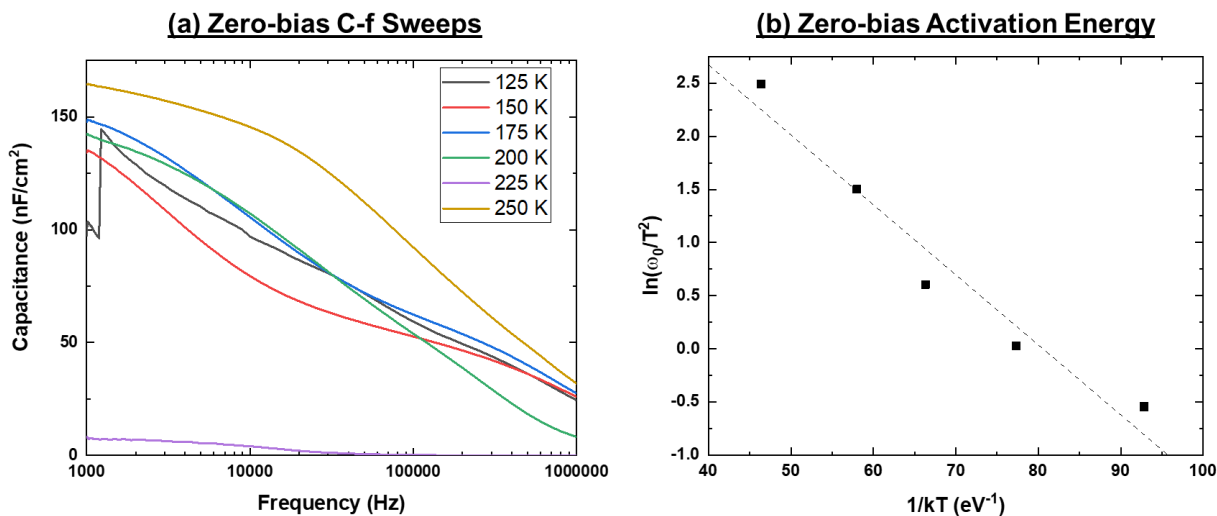


Figure 6.12. Admittance spectroscopy measurements at zero bias on ENG-based solar cells with a CdS buffer layer.

AS measurements were also conducted at -0.25 and -0.50 V applied DC bias; activation energies of 77.3 and 87.2 meV were extracted. This voltage-dependent activation energy is characteristic of a defect that is present in the space-charge region, rather than the bulk [30]. Therefore, it is highly likely that this defect causes interfacial recombination that severely impedes device performance. It is possible that there is interdiffusion of atoms between ENG and CdS, forming a highly defective layer; further investigation is required to find out the exact nature of these defects, but it will likely not be a worthwhile study due to the impracticality of using CdS as a buffer layer

The CV and AS measurements, along with SCAPS simulations, demonstrate that alternative buffer layers are needed for the development of high-efficiency ENG-based solar cells. One candidate is zinc sulfide (ZnS), which has a CBM closer to vacuum and would consequently form a more favorable p-n junction with ENG. Zinc sulfide has been applied to several different materials successfully, including CIGSe and CZTSSe, and can be deposited by variety of techniques including chemical bath deposition and sputtering [31]–[34].

Figure 6.13 gives the simulated results of the pairing between a ZnS buffer layer and an ENG absorber layer. The simulated band diagram (Figure 6.13a) demonstrates a much more favorable alignment at the p-n junction, with only a small spike offset that does not impede the transport of electrons. The simulated J-V curve (Figure 6.13b) indicates that a maximum efficiency of 18.9% can be reached, with a significant improvement to the fill factor noted in comparison with the CdS case. The simulation assumed no interfacial recombination and 100 ns lifetime, both parameters that need to be thoroughly studied in future work. Note that the properties of ZnS are not well-agreed upon in the literature, with CBM's reported over a range spanning more than 1 eV. Additionally, deposition using a chemical bath may result in significant oxygen incorporation, which adjusts the band gap and CBM/VBM of the material. Figure 6.13c depicts the maximum efficiency of a ZnS-ENG solar cell as a function of ZnS CBM (i.e. the electron affinity) and ENG carrier lifetime, showing that both areas are critical to improve in future research. Note that the band gap in this set of simulations was set to 3.0 eV to account for potential oxygen incorporation and to facilitate convergence in SCAPS. The efficiency of ZnS-ENG solar cells may be boosted beyond 20% by tuning the carrier concentration in both layers, thinning the ZnS buffer layer to reduce parasitic light absorption, and introducing reflectors at the back contact to promote additional light absorption.

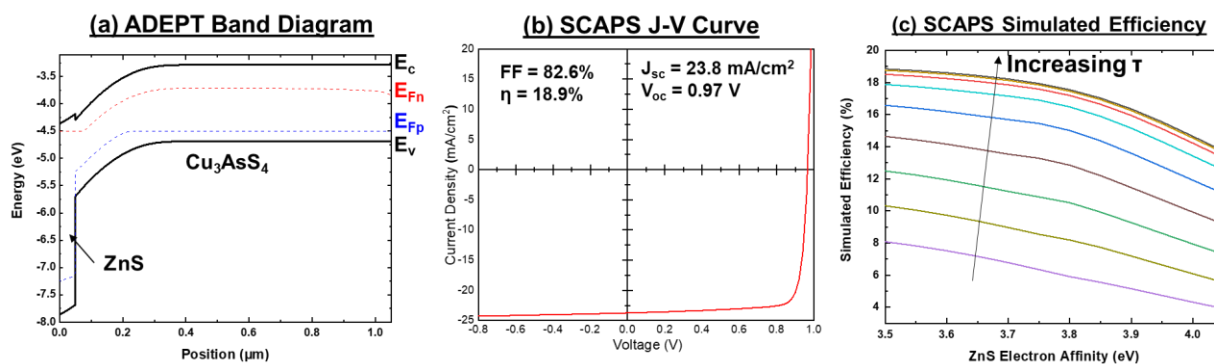


Figure 6.13. Simulations of ENG-ZnS solar cell. (a) ADEPT-simulated band diagram for the ZnS-ENG interface, assuming a ZnS conduction band minimum of -3.5 eV. [© 2019, IEEE] (b) SCAPS-simulated J-V curve assuming no interfacial recombination and 100 ns ENG lifetime. [© 2019, IEEE] (c) SCAPS-simulated efficiencies as a function of ZnS electron affinity and carrier lifetime (0.01 ns to 100 ns).

ZnS is one promising candidate buffer layer for ENG solar cells, but due to its high band gap, it has an intrinsically high resistivity that may render it difficult to achieve sufficiently high

carrier concentrations. A recent computational work by Wallace et al. studied the conduction band offsets and lattice strains of various n-type buffer layers with different surfaces of ENG [35]. They calculated an electron affinity for the (100) and (110) planes as 5.0 eV, very similar to the measured result from CV, and a 5.2 eV electron affinity for the (010)a plane. Some candidate buffer layers they identify to pair with these surfaces are cerium(III) oxide (Ce_2O_3), cerium(III) sulfide (Ce_2S_3), zinc telluride (ZnTe), and dysprosium sulfide (Dy_2S_3). With the number of candidate buffer layers available, the replacement of CdS in ENG solar cells should proceed, though it must be noted that the orientation of the ENG films must be monitored for optimal band alignments.

6.4 Conclusions

The characterization presented in this chapter is an early indication that enargite Cu_3AsS_4 is promising for future photovoltaic applications. Photoluminescence spectroscopy showed relatively promising shallow defect characteristics and the possible presence of excitons, both signs of a high-quality electronic material. Time-resolved terahertz and time-resolved photoluminescence spectroscopies showed that Shockley-Read-Hall recombination in ENG thin films proceeds on the timescale of nanoseconds at a minimum, a promising value for an emerging solar absorber. Carrier concentrations and mobilities were determined through Hall effect measurements. When all of these characteristics are jointly considered, it is evident that the factor currently limiting ENG-based solar cells is NOT the properties of the absorber layer itself. Rather, cadmium sulfide is a completely inappropriate n-type material to pair with ENG. By using simulations, a path towards high efficiency solar cells using zinc sulfide or another buffer layer was suggested. Future work should focus not only on the development of new buffer layers, but also on improving film morphology (particularly roughness) for better ability to measure optical data (such as refractive index and absorption coefficients), characterizing changes to absorber processing using PL, TRPL, and TRTS, and evaluating the radiative efficiency (a.k.a. the photoluminescence quantum yield) of ENG to determine the maximum open-circuit voltage achievable from ENG-based devices.

6.5 Acknowledgements

Many collaborators were involved in the characterization methods applied in this chapter. S.A.M. would like to thank Darius Kuciauskas and Patricia Dippo of NREL for their assistance with PL measurements, Yining Feng and Prof. Luna Lu of Purdue University for their assistance with Hall Effect measurements, Siming Li, Mohammad Taheri, and Prof. Jason Baxter of Drexel University for their assistance with TRTS measurements, Daria Blach and Prof. Libai Huang of Purdue University for their assistance with TRPL measurements, Xinxing Yin and Prof. Yanfa Yan of the University of Toledo for their assistance with cyclic voltammetry measurements, Prof. Marc Burgelman and his team at the University of Ghent for developing the SCAPS program, and Prof. Jeff Gray and his team at Purdue University for developing the ADEPT program. S.A.M. acknowledges funding from the NSF under the DMREF program (grant #1534691) and from Purdue University under a Bilsland Dissertation Fellowship. He declares no competing financial interests.

6.6 References

- [1] M. A. Green *et al.*, “Solar cell efficiency tables (Version 53),” *Prog. Photovoltaics Res. Appl.*, vol. 27, no. 1, pp. 3–12, 2019.
- [2] J. B. Baxter and G. W. Guglietta, “Terahertz Spectroscopy,” *Anal. Chem.*, vol. 83, no. 12, pp. 4342–4368, Jun. 2011.
- [3] J. L. Gray, X. Wang, R. V. K. Chavali, X. Sun, A. Kanti, and J. R. Wilcox, “ADEPT 2.1.” nanohub.org, 2015.
- [4] M. Burgelman, “SCAPS 3.3.07.” 2019.
- [5] L. Yu, R. S. Kokenyesi, D. A. Keszler, and A. Zunger, “Inverse Design of High Absorption Thin-Film Photovoltaic Materials,” *Adv. Energy Mater.*, vol. 3, no. 1, pp. 43–48, Jan. 2013.
- [6] T. Pauporté and D. Lincot, “Electrical, optical and photoelectrochemical properties of natural enargite, Cu_3AsS_4 ,” *Adv. Mater. Opt. Electron.*, vol. 5, no. 6, pp. 289–298, Nov. 1995.
- [7] S. A. McClary, J. Andler, C. A. Handwerker, and R. Agrawal, “Solution-processed copper arsenic sulfide thin films for photovoltaic applications,” *J. Mater. Chem. C*, vol. 5, no. 28, pp. 6913–6916, 2017.

- [8] T. Unold and L. Gutay, "Photoluminescence Analysis of Thin-Film Solar Cells," in *Advanced Characterization Techniques for Thin Film Solar Cells*, 2011, pp. 151–175.
- [9] M. D. McCluskey and E. E. Haller, *Dopants and Defects in Semiconductors*, 2nd ed. Taylor and Francis, 2018.
- [10] S. K. Wallace *et al.*, "Candidate photoferroic absorber materials for thin-film solar cells from naturally occurring minerals: enargite, stephanite, and bournonite," *Sustain. Energy Fuels*, vol. 1, no. 6, pp. 1339–1350, 2017.
- [11] T. Schmidt, K. Lischka, and W. Zulehner, "Excitation-power dependence of the near-band-edge photoluminescence of semiconductors," *Phys. Rev. B*, vol. 45, no. 16, pp. 8989–8994, 1992.
- [12] D. K. Schroder, *Semiconductor Material and Device Characterization*, 3rd ed. Hoboken, NJ: John Wiley & Sons, Inc., 2006.
- [13] C. A. Schmuttenmaer, "Exploring Dynamics in the Far-Infrared with Terahertz Spectroscopy," *Chem. Rev.*, vol. 104, no. 4, pp. 1759–1780, Apr. 2004.
- [14] G. W. Guglietta, K. R. Choudhury, J. V. Caspar, and J. B. Baxter, "Employing time-resolved terahertz spectroscopy to analyze carrier dynamics in thin-film $\text{Cu}_2\text{ZnSn}(\text{S},\text{Se})_4$ absorber layers," *Appl. Phys. Lett.*, vol. 104, no. 25, p. 253901, Jun. 2014.
- [15] S. Dastidar, S. Li, S. Y. Smolin, J. B. Baxter, and A. T. Fafarman, "Slow Electron-Hole Recombination in Lead Iodide Perovskites Does Not Require a Molecular Dipole," *ACS Energy Lett.*, vol. 2, no. 10, pp. 2239–2244, 2017.
- [16] C. J. Hages *et al.*, "Identifying the Real Minority Carrier Lifetime in Nonideal Semiconductors: A Case Study of Kesterite Materials," *Adv. Energy Mater.*, vol. 7, no. 18, p. 1700167, Sep. 2017.
- [17] X. Deng *et al.*, "Ultrafast Carrier Dynamics in Methylammonium Lead Bromide Perovskite," *J. Phys. Chem. C*, vol. 120, no. 5, pp. 2542–2547, 2016.
- [18] D. Hayes *et al.*, "Electronic and nuclear contributions to time-resolved optical and X-ray absorption spectra of hematite and insights into photoelectrochemical performance," *Energy Environ. Sci.*, vol. 9, no. 12, pp. 3754–3769, 2016.
- [19] B. C. Connelly, G. D. Metcalfe, H. Shen, and M. Wraback, "Direct minority carrier lifetime measurements and recombination mechanisms in long-wave infrared type II superlattices using time-resolved photoluminescence," *Appl. Phys. Lett.*, vol. 97, no. 25, pp. 95–98, 2010.

- [20] A. W. Welch *et al.*, “Trade-Offs in Thin Film Solar Cells with Layered Chalcostibite Photovoltaic Absorbers,” *Adv. Energy Mater.*, p. 1601935, Jan. 2017.
- [21] H. Guo *et al.*, “Enhancement in the Efficiency of Sb₂S₃ Thin-Film Solar Cells by Increasing Carrier Concentration and Inducing Columnar Growth of the Grains,” *Sol. RRL*, vol. 1800224, p. 1800224, 2018.
- [22] S. K. Haram, B. M. Quinn, and A. J. Bard, “Electrochemistry of CdS Nanoparticles: A Correlation between Optical and Electrochemical Band Gaps,” *J. Am. Chem. Soc.*, vol. 123, no. 36, pp. 8860–8861, 2001.
- [23] Y. Li, H. Zhong, R. Li, Y. Zhou, C. Yang, and Y. Li, “High-yield fabrication and electrochemical characterization of tetrapodal CdSe, CdTe, and CdSe_xTe_{1-x} nanocrystals,” *Adv. Funct. Mater.*, vol. 16, no. 13, pp. 1705–1716, 2006.
- [24] R. R. Gagne, C. A. Koval, and G. C. Lisensky, “Ferrocene as an Internal Standard for Electrochemical Measurements,” *Inorg. Chem.*, vol. 19, no. 9, pp. 2854–2855, 1980.
- [25] X. Yin *et al.*, “A Cu₃PS₄ nanoparticle hole selective layer for efficient inverted perovskite solar cells,” *J. Mater. Chem. A*, vol. 7, no. 9, pp. 4604–4610, 2019.
- [26] T. Shi, W.-J. Yin, M. Al-Jassim, and Y. Yan, “Structural, electronic, and optical properties of Cu₃-V-VI₄ compound semiconductors,” *Appl. Phys. Lett.*, vol. 103, no. 15, p. 152105, Oct. 2013.
- [27] S. Berge, P. O. Gartland, and B. J. Slagsvold, “Photoelectric work function of a molybdenum single crystal for the (100), (110), (111), (112), (114), and (332) faces,” *Surf. Sci.*, vol. 43, no. 1, pp. 275–292, May 1974.
- [28] M. Mostefaoui, H. Mazari, S. Khelifi, A. Bouraiou, and R. Dabou, “Simulation of High Efficiency CIGS Solar Cells with SCAPS-1D Software,” *Energy Procedia*, vol. 74, pp. 736–744, 2015.
- [29] A. Chirilă *et al.*, “Highly efficient Cu(In,Ga)Se₂ solar cells grown on flexible polymer films,” *Nat. Mater.*, vol. 10, no. 11, pp. 857–861, 2011.
- [30] J. Heath and P. Zabierowski, “Capacitance Spectroscopy of Thin-Film Solar Cells,” *Adv. Charact. Tech. Thin Film Sol. Cells Second Ed.*, vol. 1–2, pp. 93–119, 2016.
- [31] K. Sun *et al.*, “Over 9% Efficient Kesterite Cu₂ZnSnS₄ Solar Cell Fabricated by Using Zn_{1-x}Cd_xS Buffer Layer,” *Adv. Energy Mater.*, vol. 6, no. 12, p. 1600046, Jun. 2016.

- [32] D.-H. Jeon, D.-K. Hwang, D.-H. Kim, J.-K. Kang, and C.-S. Lee, "Optimization of the ZnS Buffer Layer by Chemical Bath Deposition for Cu(In,Ga)Se₂ Solar Cells," *J. Nanosci. Nanotechnol.*, vol. 16, no. 5, pp. 5398–5402, 2016.
- [33] T. Kato, "Cu(In,Ga)(Se,S)₂ solar cell research in Solar Frontier: Progress and current status," *Jpn. J. Appl. Phys.*, vol. 56, no. 4S, p. 04CA02, Apr. 2017.
- [34] J. K. Larsen *et al.*, "Cadmium Free Cu₂ZnSnS₄ Solar Cells with 9.7% Efficiency," *Adv. Energy Mater.*, vol. 1900439, p. 1900439, 2019.
- [35] S. K. Wallace, K. T. Butler, Y. Hinuma, and A. Walsh, "Finding a junction partner for candidate solar cell absorbers enargite and bournonite from electronic band and lattice matching," *J. Appl. Phys.*, vol. 125, no. 5, p. 055703, Feb. 2019.

7. ROLE OF ANNEALING ATMOSPHERE ON THE CRYSTAL STRUCTURE AND COMPOSITION OF TETRAHEDRITE-TENNANTITE ALLOY NANOPARTICLES

A version of this chapter has been previously published as a journal article: Scott A. McClary, Robert B. Balow, and Rakesh Agrawal, "Role of annealing atmosphere on the crystal structure and composition of tetrahedrite-tennantite alloy nanoparticles," *Journal of Materials Chemistry C*, vol. 6, no. 39, pp. 10538-10546, 2018. It is reproduced here with permission from the Royal Society of Chemistry. The main journal article and supporting information have been merged, and the text and figures have been modified where appropriate.

7.1 Introduction

Semiconducting nanoparticles (NPs) offer many advantages over bulk materials for the fabrication of thin-film electronic devices due to their size-dependent characteristics. Optoelectronic properties of NPs are correlated with NP size due to quantum confinement effects, and NP surfaces can be functionalized with a variety of ligands for colloidal stability in many solvents, thus enabling the use of low-cost and high-throughput manufacturing methods such as direct inkjet printing [1]–[3]. These qualities have spurred significant scientific effort into synthesizing novel NP-based semiconducting compounds for use in energy-related applications. High-efficiency photovoltaic devices have been demonstrated for NP-based CdTe [4], [5] and Cu(In,Ga)Se₂ [6], and a high figure of merit has been reported for NP-based Bi₂Te₃ thermoelectric devices [7].

While long-chained carbonaceous ligands enable facile solution-phase deposition of NP films, they typically hinder final device performance due to their electrically insulating nature. As such, as-deposited NP thin films are often heat treated to remove or modify the surface-bound ligands and improve electronic transport. For sulfide-based materials, a variety of thermal anneals have been incorporated into thin film fabrication protocols. Elemental sulfur and hydrogen sulfide (H₂S) have both been used to remove ligands and densify NP films of Cu₂ZnSnS₄ and Cu(In,Ga)S₂, respectively [8], [9]. The use of a reactive selenium atmosphere to convert CuInS₂ and CuInSe₂ NP films into micron-sized grains of CuInSe₂ was first demonstrated by Guo et al [10], [11]. This heat treatment is now a widely-used method to convert sulfide-based materials into their selenide

analogous and aggregate carbonaceous ligands into a “fine-grain” layer whose effect on device performance appears to be relatively benign [12]–[15].

Recent energy-related research has seen an increased focus on semiconductors comprised of earth-abundant elements to minimize feedstock expenses and alleviate concerns regarding large-scale materials availability for terawatt-scale manufacturing [16]. One such class of materials is the copper antimony sulfide (Cu-Sb-S) family, which has been studied in both thermoelectric and photovoltaic contexts. Extensive research on tetrahedrite (TET, $\text{Cu}_{12}\text{Sb}_4\text{S}_{13}$), has revealed promising thermoelectric properties in natural, synthetic, and alloyed samples [17]–[25]. Additionally, TET and its derivatives are candidates for use in solar energy conversion due to predicted conversion efficiencies exceeding 20% and ideal band gap energies of ~ 1.5 eV [26], [27].

The isostructural analog of TET, achieved by substituting antimony with the more earth abundant element arsenic, is tennantite (TEN, $\text{Cu}_{12}\text{As}_4\text{S}_{13}$) [28]–[30]. The TET-TEN system forms a complete solid series between Sb and As, enabling the tuning of optoelectronic properties via alloying [31], [32]. Furthermore, the mismatch of Sb and As radii in a mixed alloy crystal lattice may improve thermoelectric performance by increasing phonon scattering without significantly hindering carrier transport [33]. Sb-As alloying has been shown to tune the optical band gap in $\text{Cu}_3\text{As}_{1-x}\text{Sb}_x\text{S}_4$ NPs [30], improve the power factor (a thermoelectric parameter) of $\text{Cu}_3\text{As}_{1-x}\text{Sb}_x\text{Se}_4$ NP films [34], and boost the thermoelectric figure of merit in blended TET-TEN mineral sample [17], [18].

Controlled syntheses of TET ([35]–[38]) and TEN ([39]) NPs have been previously reported in the literature. Development of a solution-based synthesis represents a more scalable route to Sb- and As-based chalcogenide films when compared to more common techniques such as spark plasma sintering. Developing thermal treatments to remove surface-bound ligands and densify NP-based TET-TEN films is necessary for future optoelectronic device development; however, there have been no reports detailing a synthetic protocol for TET-TEN NP alloys or heat treatments for thin films formed from such NPs. In this manuscript, we report the first synthesis of impurity-free TET-TEN NP alloys and demonstrate the effects of elemental sulfur, H_2S , and inert atmospheres on the phase stability and composition of TET-TEN NP alloy films at elevated temperatures. We show that the oxidation state of sulfur during heat treatment is critical for controlling the final bulk phase of the film, and that antimony, arsenic, and sulfur are prone to

escaping from the films at elevated temperatures. These data are critical knowledge for future development of Cu-Sb-S, Cu-As-S, and related material systems.

7.2 Experimental Methods

7.2.1 Materials

All materials were used as received with standard air-free handling procedures. Antimony (III) chloride (SbCl_3 , 99.99%), arsenic (III) chloride (AsCl_3 , 99.95%), and sulfur flakes (S, 99.99%) were obtained from Sigma-Aldrich. Copper (I) chloride (CuCl , 99.99%) was obtained from Strem. Oleylamine (80-90%, OLA) was obtained from Acros Organics; it was degassed by three freeze-pump-thaw (FPT) cycles and stored in a nitrogen-filled glovebox before use in making stock solutions. Ethanol (EtOH, 200 proof) was obtained from Koptec, hexanes (98.5%, mixture of isomers) were obtained from Fisher, and toluene (99.5%) was obtained from Macron. Hydrogen sulfide (H_2S , 1%; balance argon) was obtained from Airgas (an Air Liquide Company). *Note that AsCl_3 is highly toxic and must be handled under an inert atmosphere using proper personal protective equipment at all times!*

7.2.2 Nanoparticle Alloy Synthesis and Washing Procedure

To synthesize TET-TEN NP alloys, a two-step hot injection method was adapted from previous reports by Balow et al [30], [39]. All syntheses were performed using standard air-free techniques. Three stock solutions were prepared in a nitrogen-filled glovebox. Solution A contained 1.6 mmol CuCl , 0.571 mmol SbCl_3 , and 8 mL FPT OLA; Solution B contained 1.6 mmol CuCl , 0.571 mmol AsCl_3 , and 8 mL FPT OLA; Solution C contained 9 mmol S flakes and 6 mL FPT OLA. All solutions were sealed and placed on a stir plate and heated to 65 °C for dissolution. Solutions A and B stirred with heat for 2 h, while Solution C stirred for 0.5 h with heat and the remaining 1.5 h without heat. Immediately prior to injection, mixed cation precursor solutions were made by combining Solutions A and B in nitrogen-purged vials sealed with Teflon septa. The $\text{Cu}_{12}\text{Sb}_4\text{S}_{13}$ precursor solution contained 3.0 mL of Solution A, the $\text{Cu}_{12}(\text{As}_{0.25}\text{Sb}_{0.75})_4\text{S}_{13}$ solution contained 2.25 mL of Solution A and 0.75 mL of Solution B, the $\text{Cu}_{12}(\text{As}_{0.50}\text{Sb}_{0.50})_4\text{S}_{13}$ solution contained 1.5 mL of Solution A and 1.5 mL of Solution B, the $\text{Cu}_{12}(\text{As}_{0.75}\text{Sb}_{0.25})_4\text{S}_{13}$ solution contained 0.75 mL of Solution A and 2.25 mL of Solution B, and the $\text{Cu}_{12}\text{As}_4\text{S}_{13}$ solution contained 3.0 mL of Solution B.

A three-neck reaction flask containing 7.0 mL OLA and a Teflon stir bar was sealed and attached to a Schlenk line. The flask was evacuated and refilled three times with argon. The flask was then heated under vacuum to reflux (~ 115 °C) for 1 h. The flask was then refilled with argon, and the temperature was increased to 250 °C. Once the temperature reached 250 °C, 0.8 mL of S-OLA (Solution C) was injected into the vessel, and 2.0 mL of the appropriate mixed cation solution was injected 20 s later, inducing a rapid nucleation event. The reaction was maintained at 250 °C for 30 min and then cooled naturally to room temperature. Once the vessel was below 40 °C, the flask contents were extracted into a 25 mL centrifuge tube for washing and purification. The centrifuge tube was topped with EtOH and centrifuged at 14,000 rpm (~ 17100 xG) for 5 min. The supernatant was discarded, and the pellet was resuspended in ~ 10 mL hexane by vortexing. The tube was then topped with EtOH, vortexed, and centrifuged as described previously. The hexane-ethanol wash was repeated one final time. The remaining NP pellet was suspended in ~ 5 mL toluene and stored for later use.

7.2.3 Heat Treatments

Samples were prepared for heat treatments by drop-casting ~ 200 μ L of the toluene NP ink onto glass and silicon substrates. The toluene was then slowly evaporated at room temperature in air to form thin films. For each heat treatment, the five samples of distinct compositions were treated together in the same vessel.

7.2.3.1 Sulfur Anneal

The sulfur anneals occurred in a three-zone tube furnace (Applied Test Systems, Inc. Series 3210) with a quartz tube. Zone 1 contained sulfur flakes, Zone 2 contained the samples, and Zone 3 was left empty. The tube was evacuated and refilled with argon three times to purge the system of oxygen and moisture. Zone 1 was heated to 200 °C, and the other two zones were heated to the desired reaction temperature (350 °C or 450 °C). A steady backflow of argon (10 sccm) was introduced to minimize sulfur transport towards the samples during the initial heat up. Once the temperatures had equilibrated, a graphite box containing sulfur flakes was pushed into Zone 1 to heat the sulfur flakes and generate sulfur vapor (15 min). Then, the five thin films were inserted into Zone 2 using a manual push-pull rod, and the argon flow was reversed to carry sulfur vapor towards the samples for 1 h. After the sulfurization, the furnace was opened, and the heaters were

turned off. The direction of the argon flow was again reversed to purge the atmosphere and minimize condensation of sulfur onto the thin films. The samples were naturally cooled below 40 °C before removing the samples to ambient air.

7.2.3.2 Hydrogen Sulfide (H₂S) Anneal

The five samples were loaded into a graphite sample holder and secured outside the heating zone of a vertical tube furnace (Applied Test Systems, Inc., Series 3210). A quartz tube was placed over the samples and sealed within the furnace. The H₂S and argon gas lines were purged with argon for 10 min. The tube was then evacuated and refilled with argon three times and then heated to the annealing temperature (350 °C or 450 °C) under 100 sccm argon flow. Once the target temperature was reached, the argon lines were closed, and H₂S/Ar gas flow was initiated (20 sccm). After 1 min, the samples were pushed into the center of the tube furnace using a manual push-pull rod and treated for 1 h. The heaters were then turned off, the H₂S/Ar flow was halted, and a 100 sccm argon flow was initiated. The furnace jacket was opened, allowing the samples to cool naturally to 40 °C before opening the tube to ambient air.

Hydrogen sulfide is highly toxic and corrosive. To ensure safe operation, both the hydrogen sulfide tank and annealing furnace are stored within a fume hood. The furnace is equipped with an H₂S detector with a solenoid shutoff valve that will close in the event of a detectable leak above 10 ppm. The concentration of H₂S is 1%, which is below the lower flammability limit (LFL) of 4%; more stringent safety precautions must be taken when working at higher concentrations. The gas outlet of the furnace is also equipped with an aqueous 0.5 M copper (II) sulfate solution to scrub any residual H₂S gas from the exhaust.

7.2.3.3 Nitrogen Anneal

The five samples were placed on a ceramic hot plate and isolated from the ambient atmosphere using a custom-made bell jar that was sealed to the hot plate with vacuum grease. The top of the bell jar was connected to a vacuum and nitrogen purge line. The apparatus was evacuated and refilled with nitrogen three times. The inlet nitrogen flow was set to 7 cfm using a rotameter, and the vacuum pump was adjusted such that the internal pressure of the bell jar was maintained at 100 torr. The hot plate was set to the desired temperature (350 °C or 450 °C) for 1 h. After the

treatment, the samples were cooled naturally to 40 °C before returning to atmospheric pressure and opening to the ambient environment.

7.2.4 Characterization

Grazing incidence X-ray diffraction (GIXRD) data were collected on a Rigaku Smartlab diffractometer equipped with a copper $K\alpha$ x-ray source. Parallel beam geometry was used with an incidence angle of 0.5°. Raman spectra were collected using a Horiba/Jobin-Yvon LabRAM HR800 confocal microscope equipped with a 633 nm He:Ne laser through a 100x objective lens. Scanning electron microscopy (SEM) images were taken using either an FEI Nova NanoSEM at an accelerating voltage of 5 kV or a FEI Quanta 3D FEG dual-beam field emission SEM at an accelerating voltage of 7 kV. Scanning electron microscopy energy dispersive X-ray spectroscopy data (SEM-EDS) were collected using a FEI Quanta 3D FEG dual-beam field emission SEM at an accelerating voltage of 20 kV with an Oxford INCA Xstream-2 silicon drift detector. All SEM-EDS was analyzed using AZtec software. Rietveld refinement was conducted using MAUD software.

7.3 Results and Discussion

7.3.1 Characterization of Synthesized $\text{Cu}_{12}(\text{As}_{1-x}\text{Sb}_x)_4\text{S}_{13}$ Nanoparticles

The as-synthesized alloy NPs have a cubic crystal structure (space group I-43m) as determined using GIXRD (Figure 7.1). All observed diffraction peaks in the endmember TET and TEN compositions are assignable to references for $\text{Cu}_{12}\text{Sb}_4\text{S}_{13}$ (JCPDS 01-075-2211) and $\text{Cu}_{12}\text{As}_4\text{S}_{13}$ (JCPDS 01-073-3934), respectively. The most intense reflections are indexed to the (222), (440), and (622) planes for both cubic TET and TEN. The cubic alloy series displays a linear shift in lattice parameter, as predicted by Vegard's Law for alloy materials (Figure 7.2) [40], [41]. No extraneous diffraction planes are observed in the GIXRD patterns, suggesting an impurity-free synthesis.

Raman spectra of the $\text{Cu}_{12}(\text{As}_{1-x}\text{Sb}_x)_4\text{S}_{13}$ NPs were collected to check for amorphous impurity phases (Figure 7.1). The TET and TEN endmember compositions closely match reference spectra for mineral $\text{Cu}_{12}\text{Sb}_4\text{S}_{13}$ (RRUFF ID R040164) and $\text{Cu}_{12}\text{As}_4\text{S}_{13}$ (RRUFF ID R050474), respectively, with slight discrepancies resulting from heavier elemental impurities (e.g. Zn, Ag) in the reference spectra. All mixed compositions exhibit lattice vibrational modes (100 – 150 cm^{-1})

and symmetric (Sb/As)-S stretching modes ($350 - 390 \text{ cm}^{-1}$) similar to those found in the endmember reference spectra. The peaks display two-mode behavior, and the position of each peak shifts slightly with changing composition; both observations are consistent with a previous report [42]. Only the vibrational modes reported for TET and TEN spectra were detected, further indicating impurity-free NPs.

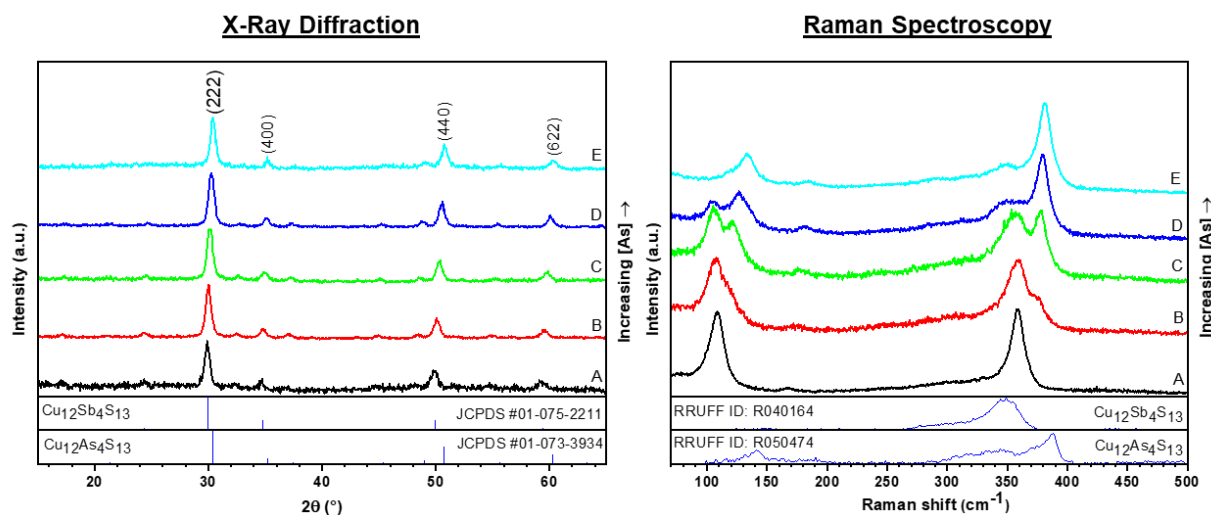


Figure 7.1. Grazing incidence X-ray diffraction (GIXRD) and Raman spectra of as-synthesized (A) $\text{Cu}_{12}\text{Sb}_4\text{S}_{13}$, (B) $\text{Cu}_{12}(\text{As}_{0.25}\text{Sb}_{0.75})_4\text{S}_{13}$, (C) $\text{Cu}_{12}(\text{As}_{0.50}\text{Sb}_{0.50})_4\text{S}_{13}$, (D) $\text{Cu}_{12}(\text{As}_{0.75}\text{Sb}_{0.25})_4\text{S}_{13}$, and (E) $\text{Cu}_{12}\text{As}_4\text{S}_{13}$ NPs. No secondary peaks were detected, suggesting the formation of impurity-free NPs.

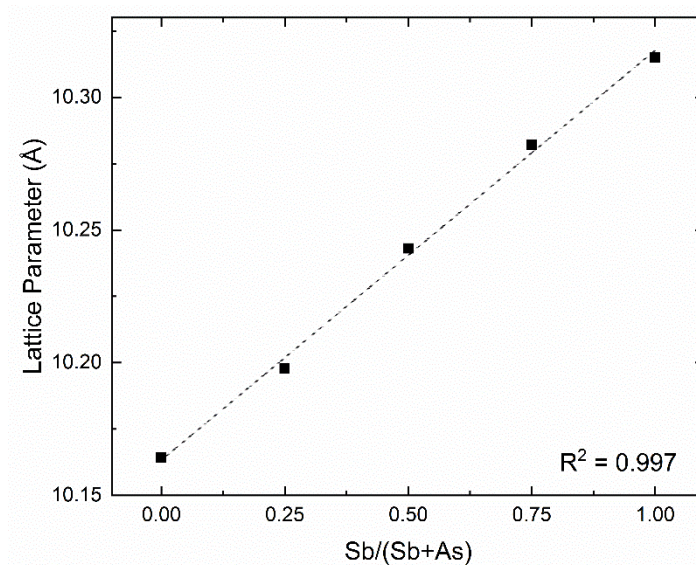


Figure 7.2. Calculated lattice parameter for as-synthesized TET-TEN NPs using Rietveld refinement. A linear shift in lattice parameter is observed with increasing Sb content, consistent with Vegard's law for alloy materials.

The bulk elemental composition of the nano-sized particles (Figure 7.3) was investigated by SEM-EDS (Table 7.1); the results suggest off-stoichiometric compositions. Such off-stoichiometry is not surprising, as NP surfaces are commonly cation-rich due to preferential binding of electron-donating ligands to under-coordinated metallic surface sites [43]. Furthermore, variable composition ranges (particularly copper-rich compositions) in both the TET and TEN systems have been reported previously [28], [29], [44]–[47].

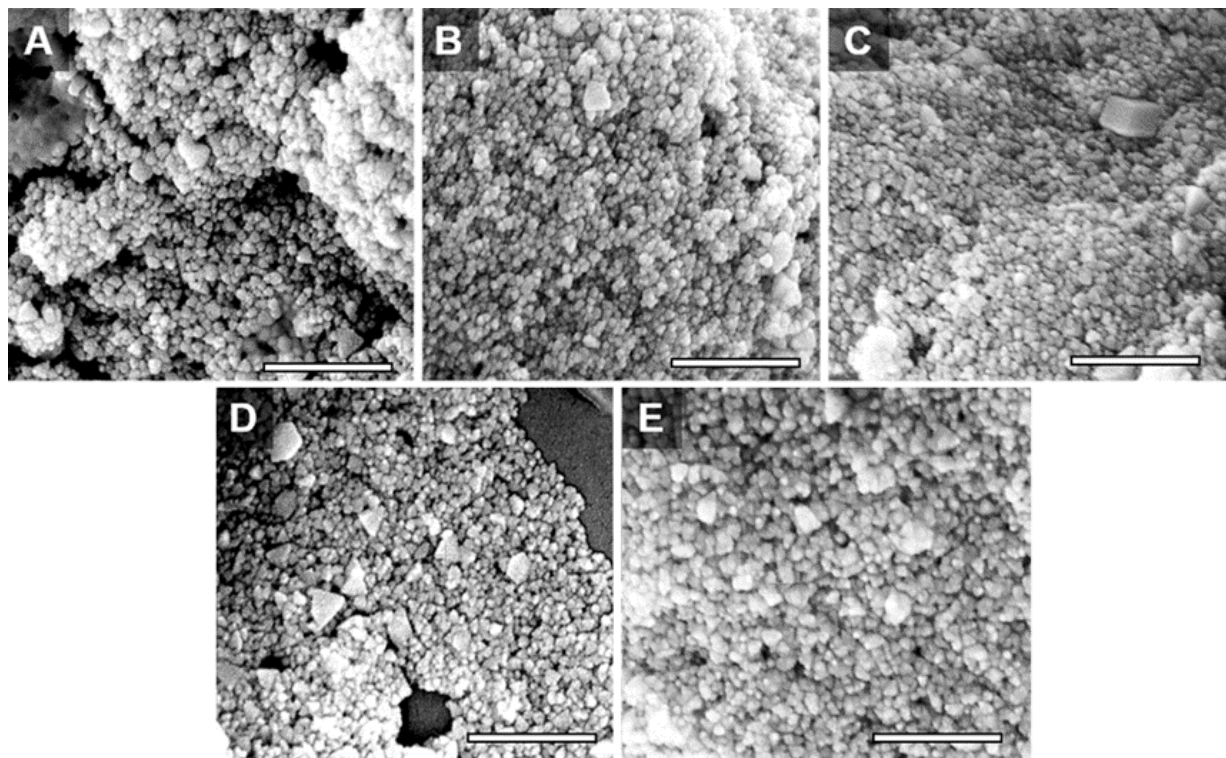


Figure 7.3. SEM micrographs of (A) $\text{Cu}_{12}\text{Sb}_4\text{S}_{13}$, (B) $\text{Cu}_{12}(\text{As}_{0.25}\text{Sb}_{0.75})_4\text{S}_{13}$ (C) $\text{Cu}_{12}(\text{As}_{0.50}\text{Sb}_{0.50})_4\text{S}_{13}$, (D) $\text{Cu}_{12}(\text{As}_{0.75}\text{Sb}_{0.25})_4\text{S}_{13}$, and (E) $\text{Cu}_{12}\text{As}_4\text{S}_{13}$ nanoparticles. Scale bars are 300 nm.

Table 7.1. Calculated elemental ratios of as-synthesized $\text{Cu}_{12}(\text{As}_{1-x}\text{Sb}_x)_4\text{S}_{13}$ NPs from SEM-EDS data. The standard deviations are based on three measurements from random areas of each sample. Note that the stoichiometric ratios for $\text{Cu}/(\text{Sb}+\text{As})$ and $(\text{Cu}+\text{Sb}+\text{As})/\text{S}$ are 3.00 and 1.23, respectively.

<i>Target Composition</i>	$\frac{\text{Cu}}{\text{Sb} + \text{As}}$	$\frac{\text{Sb}}{\text{Sb} + \text{As}}$	$\frac{\text{Cu} + \text{Sb} + \text{As}}{\text{S}}$
$\text{Cu}_{12}\text{Sb}_4\text{S}_{13}$	2.86 ± 0.05	1.00 ± 0.00	1.32 ± 0.02
$\text{Cu}_{12}(\text{As}_{0.25}\text{Sb}_{0.75})_4\text{S}_{13}$	3.09 ± 0.05	0.76 ± 0.00	1.39 ± 0.01
$\text{Cu}_{12}(\text{As}_{0.50}\text{Sb}_{0.50})_4\text{S}_{13}$	3.28 ± 0.07	0.55 ± 0.00	1.40 ± 0.04
$\text{Cu}_{12}(\text{As}_{0.75}\text{Sb}_{0.25})_4\text{S}_{13}$	3.45 ± 0.21	0.28 ± 0.01	1.45 ± 0.06
$\text{Cu}_{12}\text{As}_4\text{S}_{13}$	3.10 ± 0.02	0.00 ± 0.00	1.35 ± 0.01

7.3.2 Characterization of Nanoparticles Annealed in Sulfur

GIXRD data (Figure 7.4) indicate complete conversion from the cubic TET-TEN alloy series to structures containing fully oxidized arsenic and antimony with a nominal stoichiometry of $\text{Cu}_3\text{As}_{1-x}\text{Sb}_x\text{S}_4$. These alloys have a tetragonal crystal structure corresponding to the famatinite-luzonite (FAM-LUZ, Cu_3SbS_4 - Cu_3AsS_4) mineral series. The diffraction patterns of the purely Sb and As samples match with the respective FAM and LUZ references (JCPDS 01-071-0555 and JCPDS 01-074-1125); we attribute a slight difference in peak position between the Cu_3AsS_4 reference and heat treated sample to the presence of antimony in reference spectrum JCPDS 01-074-1125. A shift to higher 2θ was observed as the ratio of arsenic to antimony increased, suggesting a contraction of the unit cell as arsenic occupies antimony sites in the lattice. Arsenic-rich compositions show an additional, but minor reflection around $28^\circ 2\theta$ that is assignable to the (210) plane of the orthorhombic polymorph enargite (ENG, Cu_3AsS_4 , JCPDS 01-082-1464). Additionally, the intensity of this peak is reduced with increasing antimony concentration, suggesting that the tetragonal crystal structure is stabilized by the incorporation of antimony in the lattice. Rietveld refinement (Table 7.2) confirms that increasing the antimony concentration decreases the relative proportion of the orthorhombic phase in the final film. The preferential formation of the tetragonal phase at high Sb concentrations is expected, as the FAM-LUZ series freely substitutes Sb and As at pnictogen lattice sites, while the ENG phase only remains stable up to ~12 at. % Sb substitution at As sites [29], [48].

Raman spectroscopy data (Figure 7.4) also indicate the conversion of TET-TEN NP films to the FAM-LUZ alloy series upon heat treatment in a sulfur atmosphere at 450°C . The vibrational

modes of the Sb endmember match well with the Cu_3SbS_4 reference mineral (RRUFF ID R110021), while the As endmember is slightly shifted from the Cu_3AsS_4 reference mineral (RRUFF ID R060390); this discrepancy is again attributed to the presence of Sb in the reference spectrum. The characteristic ν_1 bands, resulting from Sb-S and As-S stretching vibrations, shift to higher wavenumbers with increasing arsenic composition between 320 and 340 cm^{-1} , with peak positions in close agreement with the FAM-LUZ alloy NP series [30]. In each spectrum, there is a fixed vibrational mode near 494 cm^{-1} that is not present in the Raman spectra of the reference minerals; this stretch is likely due to elemental sulfur (S-S modes) that has reacted with the OLA ligands remaining in the film [49]–[51].

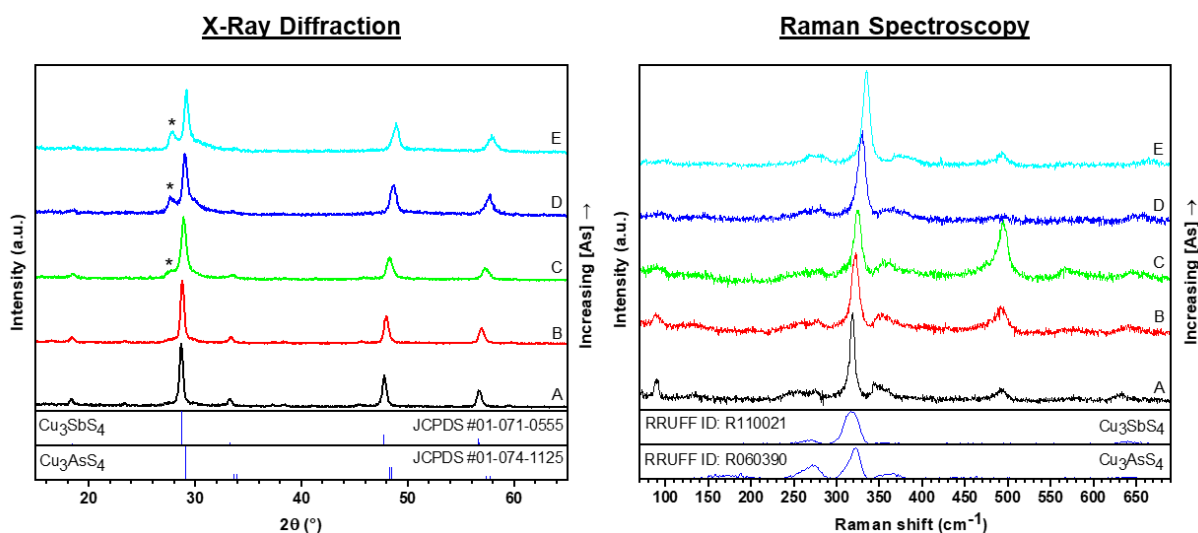


Figure 7.4. GIXRD and Raman spectra of nanoparticles treated in a sulfur atmosphere at $450\text{ }^\circ\text{C}$ for 1 h. (A) $\text{Cu}_{12}\text{Sb}_4\text{S}_{13}$, (B) $\text{Cu}_{12}(\text{As}_{0.25}\text{Sb}_{0.75})_4\text{S}_{13}$, (C) $\text{Cu}_{12}(\text{As}_{0.50}\text{Sb}_{0.50})_4\text{S}_{13}$, (D) $\text{Cu}_{12}(\text{As}_{0.75}\text{Sb}_{0.25})_4\text{S}_{13}$, and (E) $\text{Cu}_{12}\text{As}_4\text{S}_{13}$. Peaks marked with a * correspond to the (210) plane in orthorhombic enargite Cu_3AsS_4 (JCPDS 01-082-1464).

Table 7.2. Rietveld refinement-determined weight percent of resulting phases after $\text{Cu}_{12}(\text{As}_{1-x}\text{Sb}_x)_4\text{S}_{13}$ NPs were annealed in sulfur for 1 h at $450\text{ }^\circ\text{C}$. The more As-rich phases partially formed a mixture of the orthorhombic enargite and tetragonal famatinite/luzonite crystal structures. The tendency to form the orthorhombic phase was suppressed with increasing Sb concentration.

Resultant Phases	Starting Composition				
	x = 0	x = 0.25	x = 0.50	x = 0.75	x = 1
Famatinite/Luzonite	28.0	38.8	55.3	100.0	100.0
Enargite	72.0	61.2	44.7	0.0	0.0

SEM-EDS measurements (Table 7.3) were taken to determine bulk compositions of the films after the sulfur heat treatments. The Cu/(Sb+As) ratios are expected to remain identical for stoichiometric TET-TEN and FAM-LUZ compositions. However, after sulfurization, the Cu/(Sb+As) atomic ratios increased relative to the starting NP compositions, indicating a slight loss of pnictogen species. The Sb/(Sb+As) ratios of the mixed-composition samples also increased compared to their starting values, suggesting that arsenic is more readily lost from the films than antimony. Furthermore, Sb was observed in the treated TEN endmember and vice versa, implying that pnictogen species were carried between samples through the vapor phase, as all samples were heated together. Similar phase conversions were observed for NPs heat treated at 350 °C (Figure 7.5).

Table 7.3. SEM-EDS calculated elemental ratios of $\text{Cu}_{12}(\text{As}_{1-x}\text{Sb}_x)_4\text{S}_{13}$ nanoparticles treated in a sulfur atmosphere at 450 °C for 1 h. The standard deviations are based on three measurements from random areas of the samples.

<i>Starting Composition</i>	$\frac{\text{Cu}}{\text{Sb} + \text{As}}$	$\frac{\text{Sb}}{\text{Sb} + \text{As}}$	$\frac{\text{Cu} + \text{Sb} + \text{As}}{\text{S}}$
$\text{Cu}_{12}\text{Sb}_4\text{S}_{13}$	3.06 ± 0.05	0.95 ± 0.01	0.99 ± 0.01
$\text{Cu}_{12}(\text{As}_{0.25}\text{Sb}_{0.75})_4\text{S}_{13}$	3.33 ± 0.03	0.80 ± 0.01	1.03 ± 0.05
$\text{Cu}_{12}(\text{As}_{0.50}\text{Sb}_{0.50})_4\text{S}_{13}$	3.41 ± 0.12	0.66 ± 0.01	1.06 ± 0.04
$\text{Cu}_{12}(\text{As}_{0.75}\text{Sb}_{0.25})_4\text{S}_{13}$	3.51 ± 0.05	0.46 ± 0.03	1.02 ± 0.06
$\text{Cu}_{12}\text{As}_4\text{S}_{13}$	3.24 ± 0.02	0.16 ± 0.03	1.08 ± 0.01

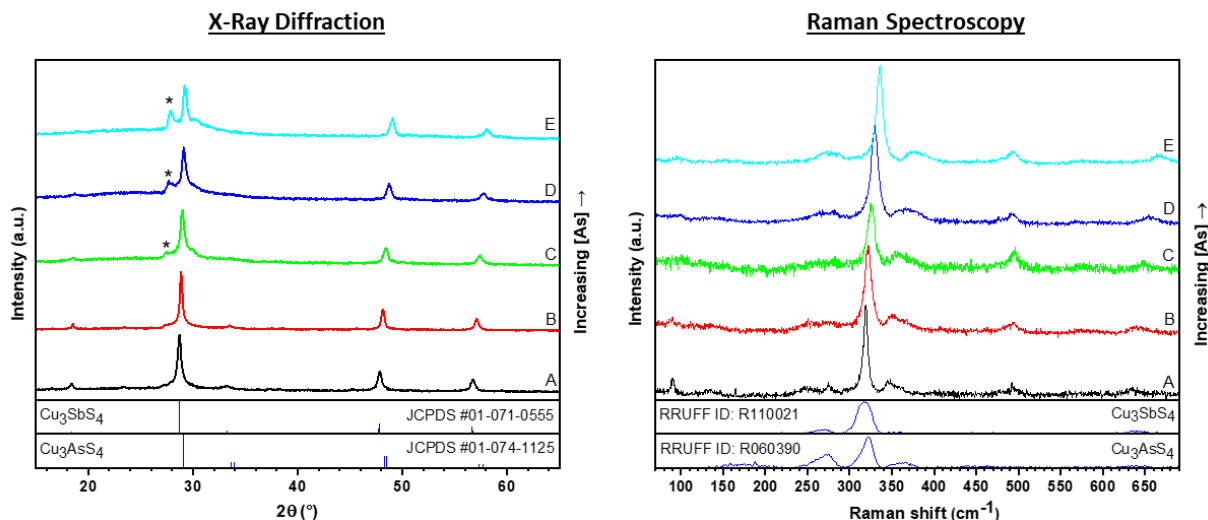


Figure 7.5. GIXRD and Raman spectra of nanoparticles treated in a sulfur atmosphere at 350 °C for 1 h. (A) $\text{Cu}_{12}\text{Sb}_4\text{S}_{13}$, (B) $\text{Cu}_{12}(\text{As}_{0.25}\text{Sb}_{0.75})_4\text{S}_{13}$, (C) $\text{Cu}_{12}(\text{As}_{0.50}\text{Sb}_{0.50})_4\text{S}_{13}$, (D) $\text{Cu}_{12}(\text{As}_{0.75}\text{Sb}_{0.25})_4\text{S}_{13}$, and (E) $\text{Cu}_{12}\text{As}_4\text{S}_{13}$. Peaks marked with a * correspond to the (210) plane in enargite $\text{Cu}_3\text{As}_4\text{S}_{13}$ (JCPDS 01-082-1464). In the GIXRD and Raman spectra, slight deviations of the purely arsenic endmember from the reference spectra are attributed to Sb impurities in the reference spectra themselves. The Raman peaks near 490 cm^{-1} are likely due to surface condensed elemental sulfur [49]–[51].

7.3.3 Characterization of Nanoparticles Annealed in H_2S

GIXRD data (Figure 7.6) obtained for the TET-TEN NP films heat treated in H_2S at 450 °C for 1 h show maintenance of the cubic TET-TEN crystal structure in the mixed Sb and As compositions. These results differ from those of the elemental sulfur treatments, as the phases that exist after H_2S anneals contain Sb or As in the nominal +3 state, rather than +5. In contrast to the stabilized alloy compositions, the endmember NP films underwent phase changes and decomposition at 450 °C. The heat treated $\text{Cu}_{12}\text{Sb}_4\text{S}_{13}$ NP film displays crystallographic planes characteristic of the monoclinic skinnerite phase (SKI, Cu_3SbS_3 , JCPDS 01-083-0563), as well as a smaller diffraction peak at $29.8^\circ 2\theta$ that is assignable to TET. Note that SKI is not observed in the sample annealed at 350 °C (Figure 7.7), consistent with previous studies in which SKI was only formed at higher temperatures [44], [52]. Additionally, the heat treated $\text{Cu}_{12}\text{As}_4\text{S}_{13}$ film predominately contains digenite $\text{Cu}_{1.8}\text{S}$ (JCPDS 01-088-2045) impurity peaks. Rietveld refinement (Table 7.4) was used to quantify the phases present after annealing; the data confirm that the endmember films decompose most readily during the H_2S heat treatment. These observations are supported by a previous report suggesting that TEN is unstable at elevated temperature and

decomposes into copper sulfide and arsenic sulfide intermediates [53]. However, this decomposition does not occur at 350 °C (Figures 7.7 and 7.8).

The obtained Raman spectra (Figure 7.6) corroborate the stabilization of the TET-TEN cubic crystal structure in the mixed alloy compositions, with peak positions matching those of the starting NP alloys. The treated $\text{Cu}_{12}\text{As}_4\text{S}_{13}$ film also displays peaks characteristic of the TEN phase, though digenite $\text{Cu}_{1.8}\text{S}$ was not detected in the Raman spectra. These data suggest the formation of localized copper sulfide impurities that are difficult to detect due to the relatively small sampling area. Raman spectra taken on the $\text{Cu}_{12}\text{Sb}_4\text{S}_{13}$ film suggest a multiphase material. The modes near 130 cm^{-1} and 309 cm^{-1} have been reported in SKI thin films [54], and the mode at 333 cm^{-1} matches closely with the Raman mode of chalcostibite CuSbS_2 [55]. The presence of multiple phases in the treated film is unsurprising, as TET decomposes to SKI through a CuSbS_2 intermediate phase [56]. Note that the Raman spectra of treated $\text{Cu}_{12}\text{Sb}_4\text{S}_{13}$ varied across the surface with some spectra closely matching TET references (Figure 7.9), suggesting inhomogeneous surface composition after heat treatment. In the mixed pnictogen films, the TEN ν_1 vibrational mode (near 390 cm^{-1}) was significantly reduced in intensity relative to the TET ν_1 vibrational mode (near 350 cm^{-1}), implying more significant losses in As-rich compositions during the H_2S heat treatments [42]. To quantify the losses, SEM-EDS data (Table 7.5) were acquired on the treated films. The $\text{Cu}/(\text{Sb}+\text{As})$ ratios increased above the starting values, significantly more than the NPs that were heat treated in elemental sulfur vapors. There was also As present in the Sb endmember (and vice versa), again suggesting the mobility of Sb and As species in the vapor phase. The magnitude of these elemental losses suggests that H_2S is less effective at suppressing decomposition than elemental sulfur.

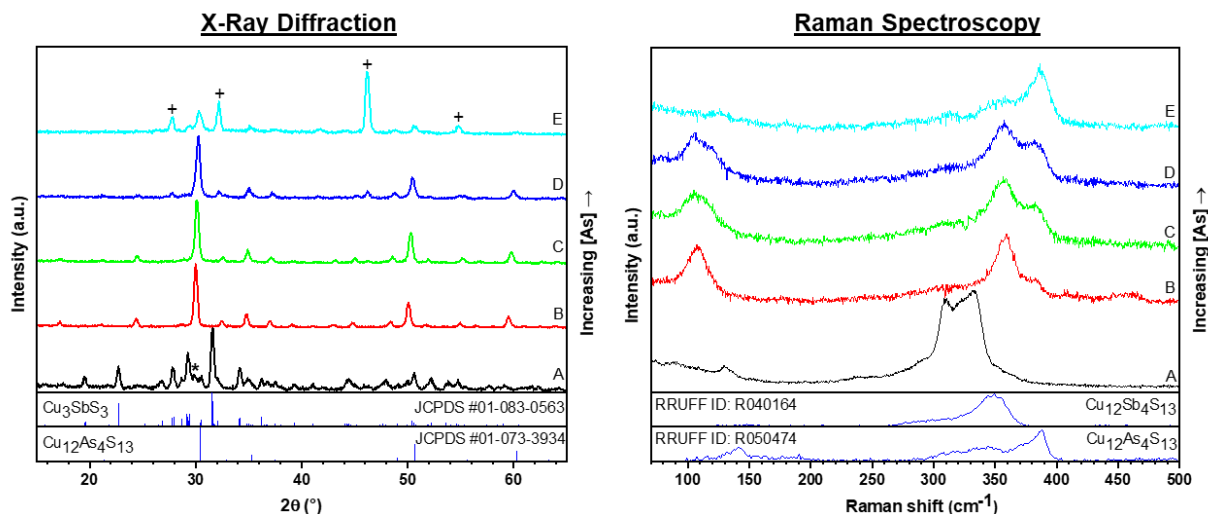


Figure 7.6. GIXRD and Raman spectra of nanoparticles treated in an H_2S atmosphere at $450\text{ }^\circ\text{C}$ for 1h. (A) $\text{Cu}_{12}\text{Sb}_4\text{S}_{13}$, (B) $\text{Cu}_{12}(\text{As}_{0.25}\text{Sb}_{0.75})_4\text{S}_{13}$, (C) $\text{Cu}_{12}(\text{As}_{0.50}\text{Sb}_{0.50})_4\text{S}_{13}$, (D) $\text{Cu}_{12}(\text{As}_{0.75}\text{Sb}_{0.25})_4\text{S}_{13}$, and (E) $\text{Cu}_{12}\text{As}_4\text{S}_{13}$. The peak marked with (*) in GIXRD spectrum A is attributable to the (222) stretch of tetrahedrite $\text{Cu}_{12}\text{Sb}_4\text{S}_{13}$ (JCPDS #42-560), and the peaks marked with (+) in spectrum E are attributable to digenite $\text{Cu}_{1.8}\text{S}$ (JCPDS 01-088-2045).

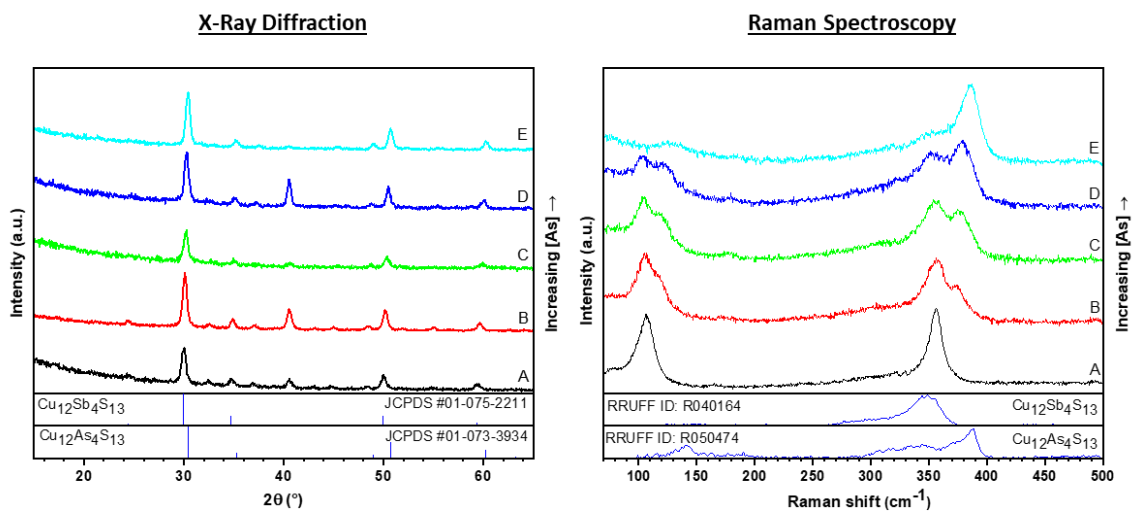


Figure 7.7. GIXRD and Raman spectra of nanoparticles treated in H_2S at $350\text{ }^\circ\text{C}$ for 1 h. (A) $\text{Cu}_{12}\text{Sb}_4\text{S}_{13}$, (B) $\text{Cu}_{12}(\text{As}_{0.25}\text{Sb}_{0.75})_4\text{S}_{13}$, (C) $\text{Cu}_{12}(\text{As}_{0.50}\text{Sb}_{0.50})_4\text{S}_{13}$, (D) $\text{Cu}_{12}(\text{As}_{0.75}\text{Sb}_{0.25})_4\text{S}_{13}$, and (E) $\text{Cu}_{12}\text{As}_4\text{S}_{13}$. In the Raman spectrum, deviations of the antimony endmember from the reference spectrum are attributed to Zn impurities in the reference spectrum itself.

Table 7.4. Rietveld refinement-determined weight percent of resulting phases after $\text{Cu}_{12}(\text{As}_{1-x}\text{Sb}_x)_4\text{S}_{13}$ NPs were annealed in H_2S for 1 h at 450 °C. Significant decomposition is observed in the purely Sb- and As-samples, while the mixed alloy compositions displayed significantly higher resistance to decomposition into crystalline secondary phases.

Resultant Phases	Starting Composition				
	x = 0	x = 0.25	x = 0.50	x = 0.75	x = 1
$\text{Cu}_{12}(\text{As}_{1-x}\text{Sb}_x)_4\text{S}_{13}$	25.4	88.3	99.5	100.0	7.7
Digenite $\text{Cu}_{1.8}\text{S}$	74.6	11.7	0.5	0.0	0.0
Skinnerite Cu_3SbS_3	0.0	0.0	0.0	0.0	92.3

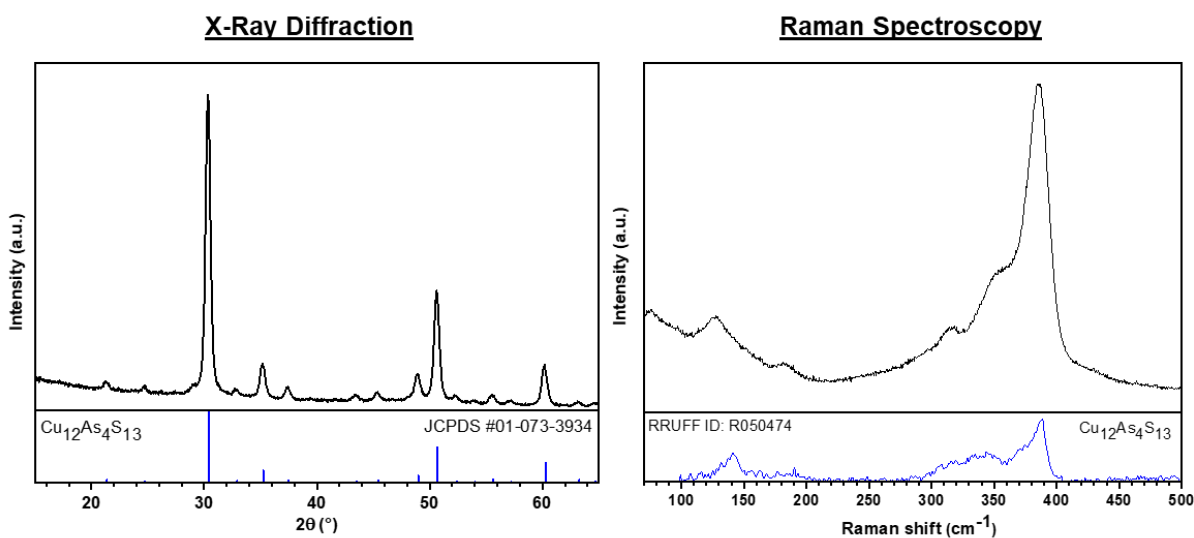


Figure 7.8. GIXRD and Raman spectra of $\text{Cu}_{12}\text{As}_4\text{S}_{13}$ nanoparticles treated in an H_2S atmosphere for 1 h at 350 °C with H_2S flow maintained during the cool down procedure. The $\text{Cu}_{12}\text{As}_4\text{S}_{13}$ phase is maintained both here and in the case where H_2S flow is stopped during the cool down procedure (Figure 7.6, spectrum E). This result eliminates the possibility of a phase change during the cool down procedure, further confirming that H_2S promotes the formation of the cubic $\text{Cu}_{12}\text{As}_4\text{S}_{13}$ phase.

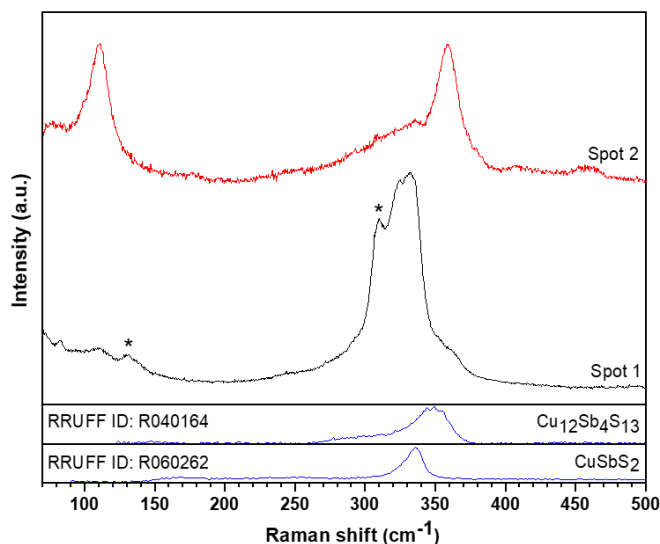


Figure 7.9. Raman spectra of two different spots on the $\text{Cu}_{12}\text{Sb}_4\text{S}_{13}$ NP film treated in H_2S for 1 h at $450\text{ }^\circ\text{C}$. Peaks corresponding to tetrahedrite $\text{Cu}_{12}\text{Sb}_4\text{S}_{13}$, chalcostibite CuSbS_2 , and skinnerite Cu_3SbS_3 (denoted with *) are observed, suggesting an inhomogeneous film after heat treatment.

Table 7.5. SEM-EDS calculated elemental ratios of $\text{Cu}_{12}(\text{As}_{1-x}\text{Sb}_x)_4\text{S}_{13}$ nanoparticles treated in an H_2S atmosphere at $450\text{ }^\circ\text{C}$ for 1 h. The standard deviations are based on three measurements from random areas of the samples.

<i>Starting Composition</i>	$\frac{\text{Cu}}{\text{Sb} + \text{As}}$	$\frac{\text{Sb}}{\text{Sb} + \text{As}}$	$\frac{\text{Cu} + \text{Sb} + \text{As}}{\text{S}}$
$\text{Cu}_{12}\text{Sb}_4\text{S}_{13}$	3.64 ± 0.05	0.95 ± 0.01	1.78 ± 0.04
$\text{Cu}_{12}(\text{As}_{0.25}\text{Sb}_{0.75})_4\text{S}_{13}$	4.22 ± 0.17	0.83 ± 0.01	1.67 ± 0.08
$\text{Cu}_{12}(\text{As}_{0.50}\text{Sb}_{0.50})_4\text{S}_{13}$	4.33 ± 0.64	0.66 ± 0.02	1.60 ± 0.12
$\text{Cu}_{12}(\text{As}_{0.75}\text{Sb}_{0.25})_4\text{S}_{13}$	5.40 ± 0.56	0.52 ± 0.02	1.56 ± 0.07
$\text{Cu}_{12}\text{As}_4\text{S}_{13}$	5.33 ± 1.72	0.07 ± 0.05	1.64 ± 0.25

7.3.4 Characterization of Nanoparticles Annealed in Nitrogen

GIXRD (Figure 7.10) data show a cubic crystal structure for all TET-TEN compositions, with some Sb-endmember decomposition into skinnerite Cu_3SbS_3 (JCPDS 01-083-0563) and As-endmember decomposition into digenite $\text{Cu}_{1.8}\text{S}$ (JCPDS 01-088-2045) after heating in nitrogen. Rietveld refinement (Table 7.6) of the GIXRD spectra confirms the relative stability of the mixed alloy compositions when compared with the endmembers. Similar to the H_2S treatments, the Raman spectra (Figure 7.10) display peak shifts consistent with the cubic alloy phases, and the magnitude of the TEN ν_1 modes are significantly reduced relative to the TET ν_1 modes, suggesting

more extensive decomposition in As-rich films. SEM-EDS measurements (Table 7.7) also show a greater loss of arsenic compared to antimony, with Sb/(Sb+As) ratios significantly higher than the starting NP values. The elemental analysis also reveals pnictogen losses in excess of the maximum observed stable composition ratio of $\text{Cu}/(\text{Sb}+\text{As}) = \sim 3.5:1$ [28], [44]. With the severe losses of arsenic and antimony, it is likely that highly localized copper sulfide species are scattered throughout the film but are undetectable by XRD or Raman. Significant compositional variations were observed across the film's surface, as evidenced by the high standard deviations of the SEM-EDS elemental ratios. It is evident that a nitrogen atmosphere is even less effective at suppressing elemental losses than sulfur and H_2S atmospheres. Note that the cubic crystal structure was unchanged at $350\text{ }^\circ\text{C}$ (Figure 7.11).

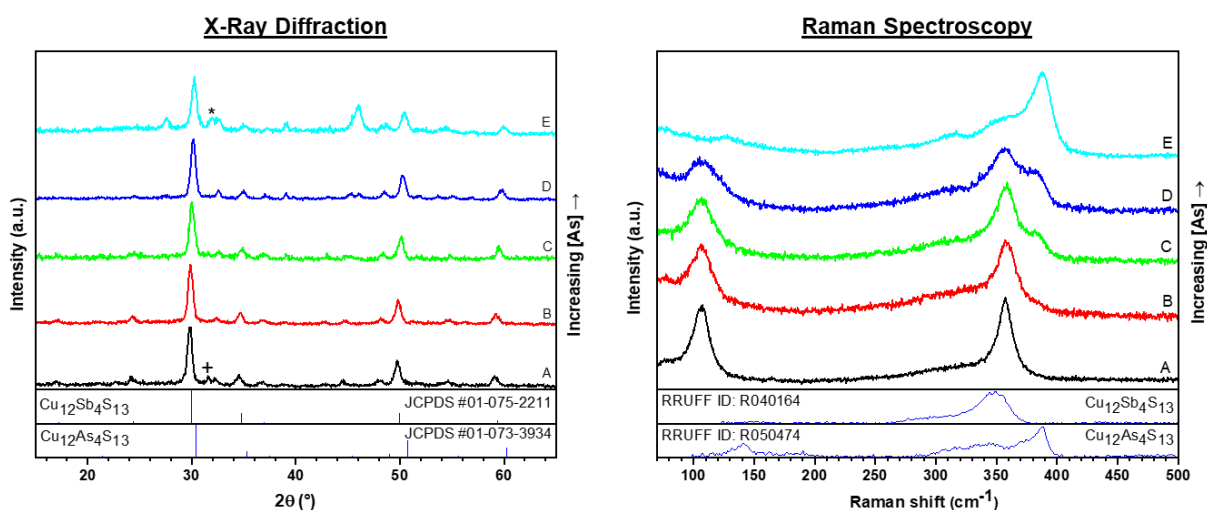


Figure 7.10. GIXRD and Raman spectra of nanoparticles treated in a nitrogen atmosphere at $450\text{ }^\circ\text{C}$ for 1 h. (A) $\text{Cu}_{12}\text{Sb}_4\text{S}_{13}$, (B) $\text{Cu}_{12}(\text{As}_{0.25}\text{Sb}_{0.75})_4\text{S}_{13}$, (C) $\text{Cu}_{12}(\text{As}_{0.50}\text{Sb}_{0.50})_4\text{S}_{13}$, (D) $\text{Cu}_{12}(\text{As}_{0.75}\text{Sb}_{0.25})_4\text{S}_{13}$, and (E) $\text{Cu}_{12}\text{As}_4\text{S}_{13}$. The (+) in GIXRD spectrum (A) denotes a skinnerite Cu_3SbS_3 (JCPDS 01-083-0563) impurity phase, and the (*) in GIXRD spectrum (E) denotes a digenite $\text{Cu}_{1.8}\text{S}$ impurity phase (JCPDS-01-088-2045).

Table 7.6. Rietveld refinement-determined weight percent of resulting phases after $\text{Cu}_{12}(\text{As}_{1-x}\text{Sb}_x)_4\text{S}_{13}$ NPs were annealed in nitrogen for 1 h at 450 °C. Significant decomposition is observed in the purely Sb- and As-samples, while the mixed alloy compositions displayed significantly higher resistance to decomposition into crystalline secondary phases.

Resultant Phases	Starting Composition				
	x = 0	x = 0.25	x = 0.50	x = 0.75	x = 1
$\text{Cu}_{12}(\text{As}_{1-x}\text{Sb}_x)_4\text{S}_{13}$	46.1	93.2	99.6	100.0	94.4
Digenite $\text{Cu}_{1.8}\text{S}$	53.9	6.8	0.4	0.0	0.0
Skinnerite Cu_3SbS_3	0.0	0.0	0.0	0.0	5.6

Table 7.7. SEM-EDS calculated elemental ratios of $\text{Cu}_{12}(\text{As}_{1-x}\text{Sb}_x)_4\text{S}_{13}$ nanoparticles heat treated in a nitrogen atmosphere at 450 °C for 1 h. The standard deviations are based on three measurements from random areas of the samples.

Starting Composition	$\frac{\text{Cu}}{\text{Sb} + \text{As}}$	$\frac{\text{Sb}}{\text{Sb} + \text{As}}$	$\frac{\text{Cu} + \text{Sb} + \text{As}}{\text{S}}$
	$\text{Cu}_{12}\text{Sb}_4\text{S}_{13}$	3.56 ± 0.07	0.98 ± 0.00
$\text{Cu}_{12}(\text{As}_{0.25}\text{Sb}_{0.75})_4\text{S}_{13}$	7.08 ± 3.63	0.92 ± 0.09	1.51 ± 0.13
$\text{Cu}_{12}(\text{As}_{0.50}\text{Sb}_{0.50})_4\text{S}_{13}$	5.27 ± 0.15	0.81 ± 0.02	1.62 ± 0.07
$\text{Cu}_{12}(\text{As}_{0.75}\text{Sb}_{0.25})_4\text{S}_{13}$	9.71 ± 1.81	0.64 ± 0.00	1.72 ± 0.22
$\text{Cu}_{12}\text{As}_4\text{S}_{13}$	11.5 ± 2.8	0.00 ± 0.00	1.71 ± 0.02

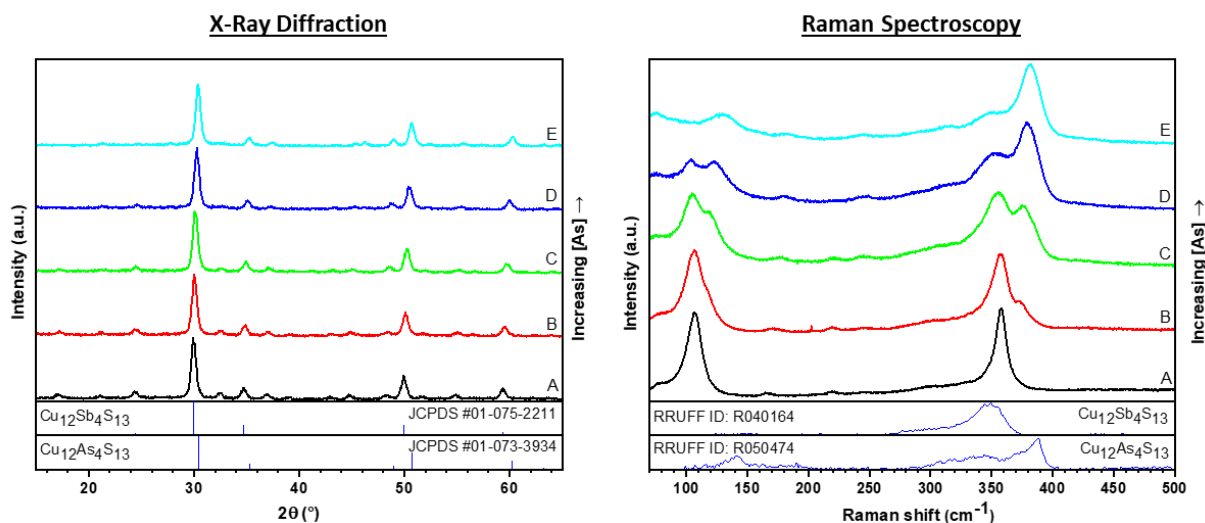


Figure 7.11. GIXRD and Raman spectra of nanoparticles treated in a nitrogen atmosphere at 350 °C for 1 h. (A) $\text{Cu}_{12}\text{Sb}_4\text{S}_{13}$, (B) $\text{Cu}_{12}(\text{As}_{0.25}\text{Sb}_{0.75})_4\text{S}_{13}$, (C) $\text{Cu}_{12}(\text{As}_{0.50}\text{Sb}_{0.50})_4\text{S}_{13}$, (D) $\text{Cu}_{12}(\text{As}_{0.75}\text{Sb}_{0.25})_4\text{S}_{13}$, and (E) $\text{Cu}_{12}\text{As}_4\text{S}_{13}$. In the Raman spectrum, slight deviations of the purely antimony endmember from the reference spectrum are attributed to Zn impurities in the reference spectrum itself.

7.3.5 Grain Growth for All Three Heat Treatments

In all three atmospheres (Figures 7.12-7.14), grain growth was observed, indicating that the heat treatment protocols may be fine-tuned to produce thin films with uniformly dense grains.

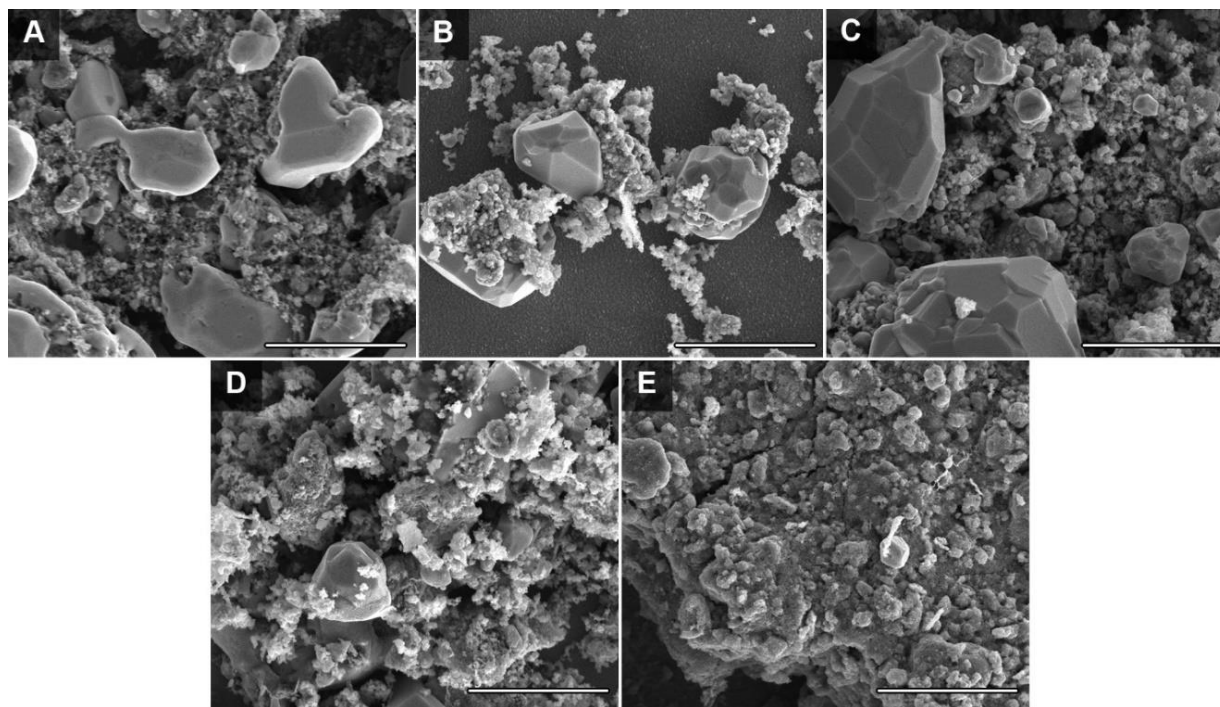


Figure 7.12. SEM micrographs of (A) $\text{Cu}_{12}\text{Sb}_4\text{S}_{13}$, (B) $\text{Cu}_{12}(\text{As}_{0.25}\text{Sb}_{0.75})_4\text{S}_{13}$ (C) $\text{Cu}_{12}(\text{As}_{0.50}\text{Sb}_{0.50})_4\text{S}_{13}$, (D) $\text{Cu}_{12}(\text{As}_{0.75}\text{Sb}_{0.25})_4\text{S}_{13}$, and (E) $\text{Cu}_{12}\text{As}_4\text{S}_{13}$ nanoparticles heat treated in a flowing 1% H_2S (balance argon) atmosphere at 450 °C for 1 h. Scale bars are 5 μm .

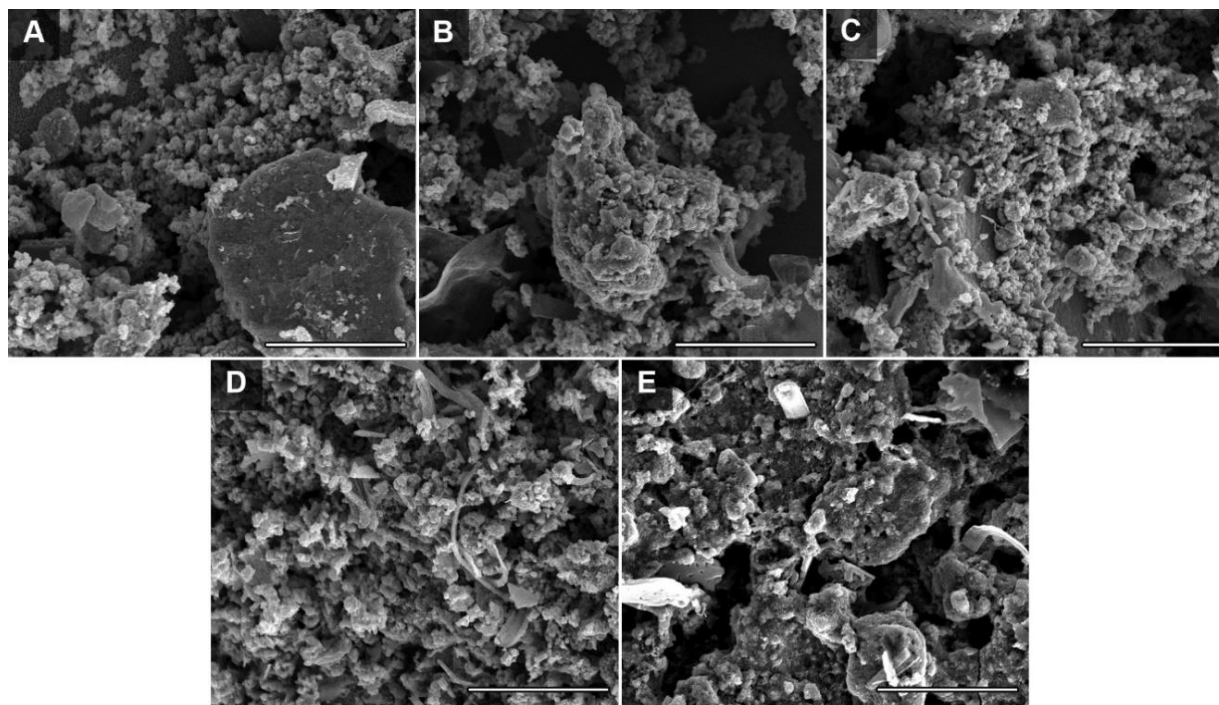


Figure 7.13. SEM micrographs of (A) $\text{Cu}_{12}\text{Sb}_4\text{S}_{13}$, (B) $\text{Cu}_{12}(\text{As}_{0.25}\text{Sb}_{0.75})_4\text{S}_{13}$ (C) $\text{Cu}_{12}(\text{As}_{0.50}\text{Sb}_{0.50})_4\text{S}_{13}$, (D) $\text{Cu}_{12}(\text{As}_{0.75}\text{Sb}_{0.25})_4\text{S}_{13}$, and (E) $\text{Cu}_{12}\text{As}_4\text{S}_{13}$ nanoparticles heat treated in a flowing nitrogen atmosphere at 450 °C for 1 h. Scale bars are 5 μm .

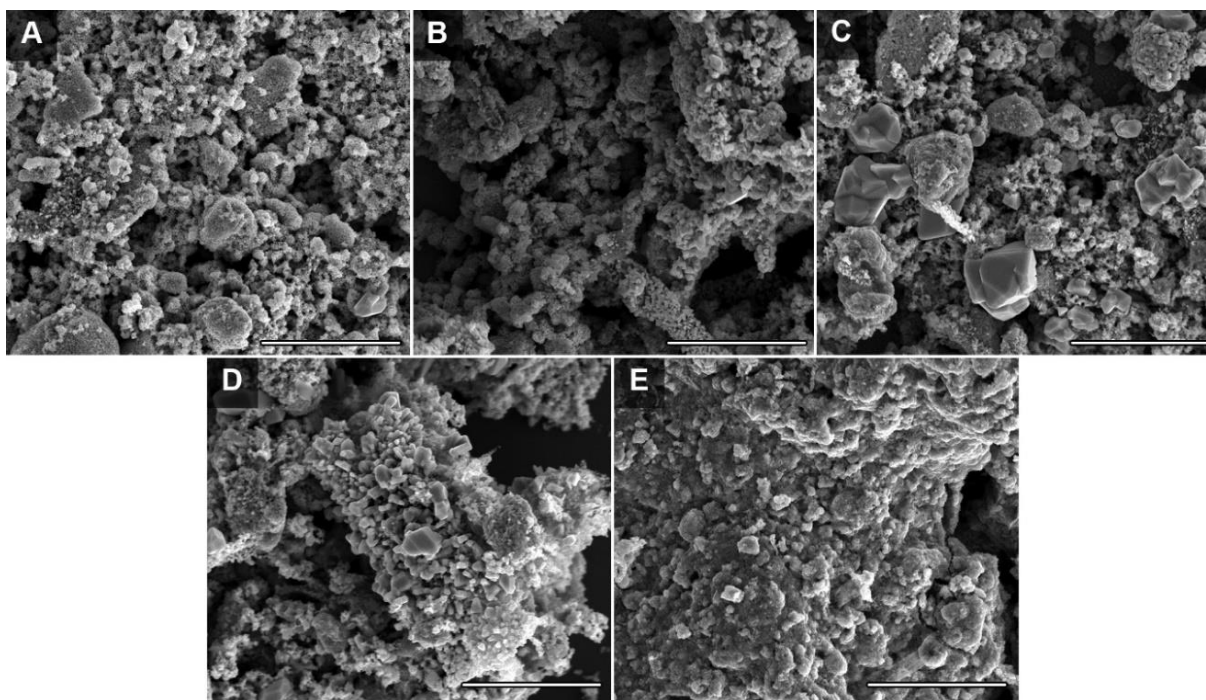
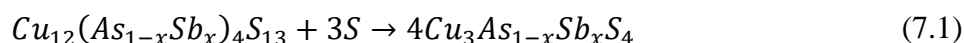


Figure 7.14. SEM micrographs of (A) $\text{Cu}_{12}\text{Sb}_4\text{S}_{13}$, (B) $\text{Cu}_{12}(\text{As}_{0.25}\text{Sb}_{0.75})_4\text{S}_{13}$ (C) $\text{Cu}_{12}(\text{As}_{0.50}\text{Sb}_{0.50})_4\text{S}_{13}$, (D) $\text{Cu}_{12}(\text{As}_{0.75}\text{Sb}_{0.25})_4\text{S}_{13}$, and (E) $\text{Cu}_{12}\text{As}_4\text{S}_{13}$ nanoparticles heat treated in a flowing sulfur/argon atmosphere at 450 °C for 1 h. Scale bars are 5 μm .

7.3.6 Discussion

The nature of the heat treatment atmosphere was critical for controlling the final phase of the TET-TEN NP alloys. It has been shown that Sb and As exist exclusively in the +5 state in the FAM-LUZ system and mostly in the +3 state in TET-TEN [22], [35], [57]. Under an elemental sulfur atmosphere, the cubic NPs converted to a tetragonal phase upon annealing at 450 °C. This may be achieved by the simultaneous oxidation of Sb and As (from +3 to +5) and reduction of sulfur (from 0 to -2), forming Cu_3SbS_4 - Cu_3AsS_4 alloy phases as described in Equation 7.1:



Annealing the TET-TEN NPs in 1% H_2S still provides a sulfur-rich atmosphere, but it is slightly reducing instead of oxidizing. Consequently, the Sb and As cations remain in the nominal +3 state rather than the more oxidized +5 state. Additionally, the copper in the digenite $\text{Cu}_{1.8}\text{S}$ impurity phases primarily exists in the +1 state instead of +2, highlighting the role of H_2S in controlling the nominal oxidation state of the multivalent atoms. The net effect of the H_2S treatments was to form larger grains of the TET-TEN phases, as evidenced by SEM micrographs (Figure 7.12). These outcomes are not surprising, as H_2S has been used to promote grain growth in other semiconductor systems, albeit in higher concentrations than used here [58], [59].

The loss of Sb and As species from the films is a critical observation with far-reaching implications. As seen in Table 7.8, pnictogen losses were greatest under a nitrogen atmosphere, followed by H_2S , and finally sulfur vapor. Additionally, As-rich alloys demonstrated greater elemental losses after heat treatment. The SEM-EDS elemental ratios show losses in both the H_2S and nitrogen-treated films, but the GIXRD-calculated ratios suggest less loss. Because the GIXRD data can only provide information regarding the crystalline portion of a material, it is likely that amorphous Cu-S phases exist throughout the treated films. Previous reports on the decomposition mechanisms of TET-TEN and related systems note such elemental sulfur and pnictogen sulfide losses during decomposition, as well as the formation of copper sulfides [21], [53], [60]–[63]. It is therefore plausible that the TET-TEN alloy films decompose into binary sulfides and elemental sulfur upon heating. The decomposition phases such as Sb_2S_3 / As_2S_3 and sulfur have relatively high vapor pressures and are likely removed during heat treatment in the effluent gas stream. Copper sulfide phases remain and may form crystallites (and hence become detectable by GIXRD) or

become trapped at grain boundaries in the final films. It is also important to note that the lattice parameters of the heat treated films also shift linearly as expected from Vegard's law (Figure 7.15), suggesting that the compositions of crystalline grains remain relatively unchanged when compared with the pre-heat treated films.

Table 7.8. Cu/(Sb+As) ratios for the various 450 °C heat treatments. SEM-EDS data is reproduced from Tables 7.1, 7.3, 7.5, and 7.7, and the XRD-calculated results are computed using weight fractions estimated by Rietveld refinement (Tables 7.4 and 7.6). GIXRD-calculated results were not determined for the starting NPs or sulfur due to the lack of binary phases appearing in the GIXRD spectra.

Nominal Composition	NPs (EDS)	Sulfur (EDS)	H ₂ S (EDS)	H ₂ S (XRD)	N ₂ (EDS)	N ₂ (XRD)
Cu ₁₂ Sb ₄ S ₁₃	2.86	3.06	3.64	3.01	3.56	3.13
Cu ₁₂ (As _{0.25} Sb _{0.75}) ₄ S ₁₃	3.09	3.33	4.22	3.14	7.08	3.14
Cu ₁₂ (As _{0.50} Sb _{0.50}) ₄ S ₁₃	3.28	3.41	4.33	3.17	5.27	3.15
Cu ₁₂ (As _{0.75} Sb _{0.25}) ₄ S ₁₃	3.45	3.51	5.40	3.68	9.71	3.43
Cu ₁₂ As ₄ S ₁₃	3.10	3.24	5.33	15.10	11.5	7.91

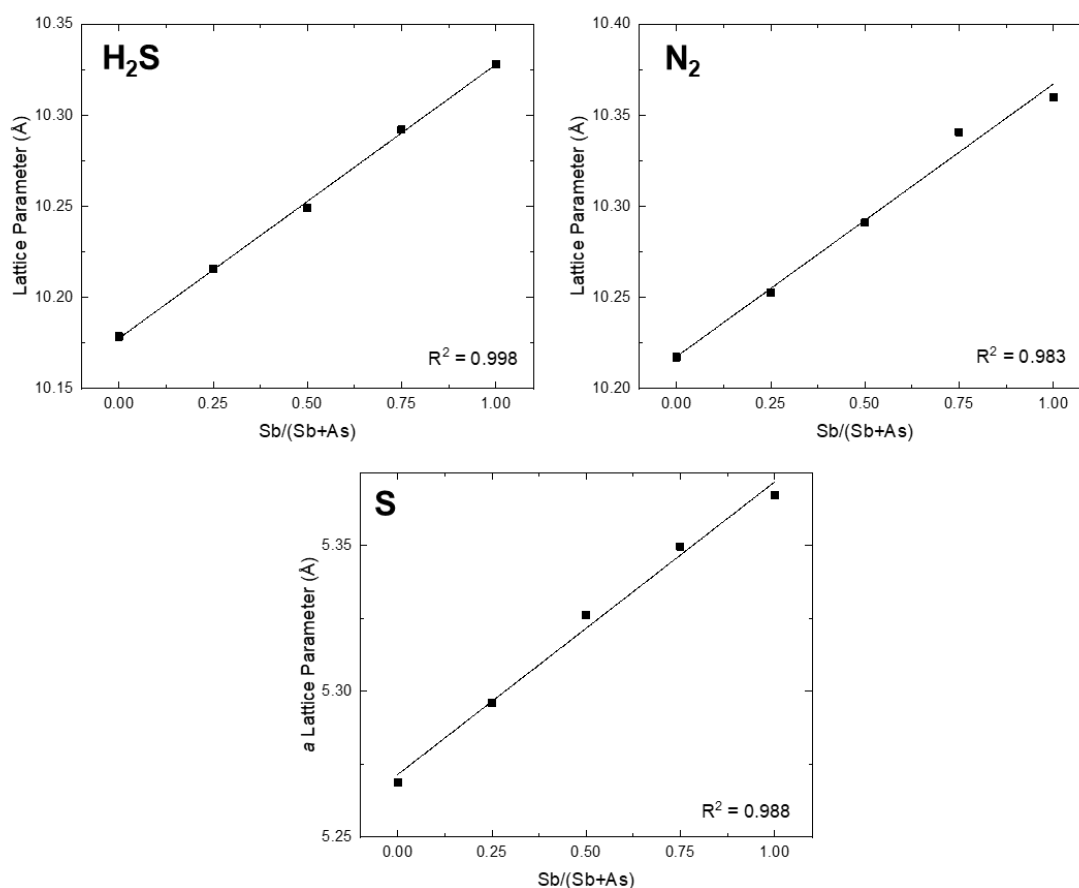


Figure 7.15. Calculated lattice parameters of $\text{Cu}_{12}(\text{As}_{1-x}\text{Sb}_x)_4\text{S}_{13}$ NP films after heat treatment at $450\text{ }^\circ\text{C}$ for 1 h in the indicated atmospheres. A nearly linear trend is observed as expected from Vegard's law, implying that the crystalline portion of the material retained its original $\text{Sb}/(\text{Sb}+\text{As})$ ratio.

One possible solution to mitigate elemental losses at higher temperatures is to supply an atmosphere containing a partial pressure of pnictogen and sulfur species. Selection of the appropriate atmosphere must be done carefully, as the nominal oxidation state of sulfur in the annealing atmosphere can modify the final phase of the material. Implementation of a closed annealing system [51] or maintaining a vapor pressure of volatile pnictogen sulfide species above the samples [64] are two methods that have been utilized in closely related material systems (Cu_3AsS_4 and CuSbS_2 , respectively) and may be applied to the TET-TEN family.

The interconversion between cubic TET-TEN NPs and tetragonal FAM-LUZ NPs appears to be reversible if an appropriate annealing atmosphere is used. The FAM-LUZ NP alloy series was synthesized according to a previous report [30] and then heat treated in sulfur, H_2S , and

nitrogen atmospheres as described in this manuscript. Under the elemental sulfur atmosphere, the FAM-LUZ phases were maintained, while H₂S and nitrogen anneals resulted in conversion to the TET-TEN phases (Figures 7.16-7.18). These two material systems have the same nominal copper-to-pnictogen ratio, suggesting that oxidation or reduction of the cations and the addition or removal of sulfur would result in interconversion between these crystallographic phases [30]. This may be achieved using reducing H₂S (if TET-TEN is desired) or oxidizing sulfur (if FAM-LUZ is desired) atmospheres during heat treatment; however, controlling pnictogen losses in this setup remains a challenge. Introducing a gas stream of elemental As or Sb in conjunction with H₂S may be an additional route to control these elemental losses. Our results demonstrate the feasibility of stabilizing and/or interconverting the TET-TEN and FAM-LUZ material families by rational selection of an annealing atmosphere, allowing for fabrication of materials with desired crystal structures and optoelectronic properties. Similar chalcogenide NP systems may also display comparable behavior, offering new insight and methodologies for synthesis of novel materials.

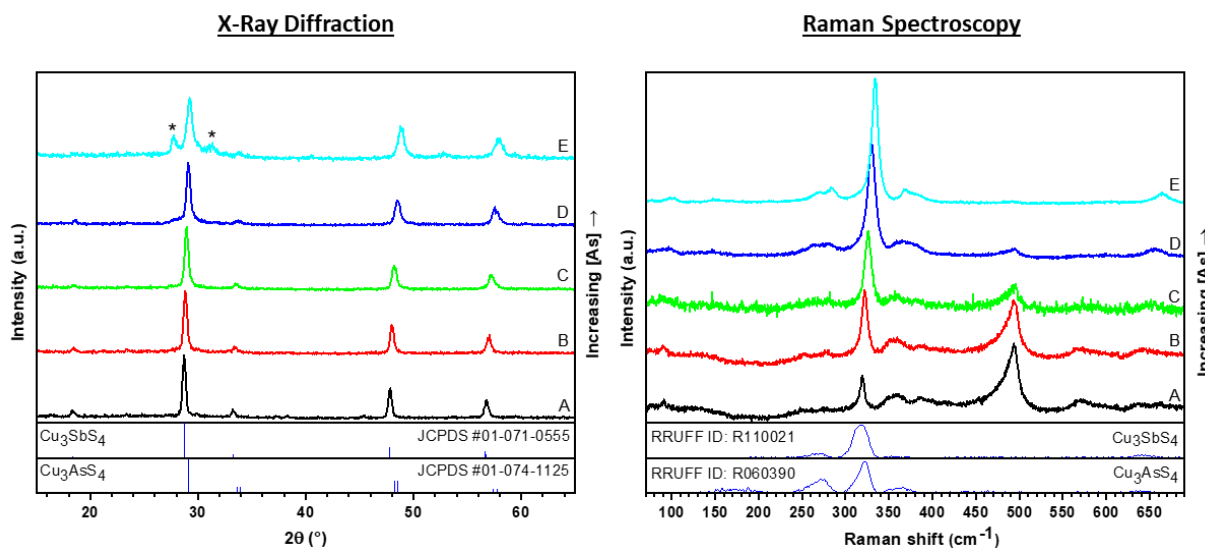


Figure 7.16. GIXRD and Raman spectra of nanoparticles treated in an elemental sulfur atmosphere at 450 °C for 1 h. (A) Cu₃SbS₄, (B) Cu₃As_{0.25}Sb_{0.75}S₄, (C) Cu₃As_{0.50}Sb_{0.50}S₄, (D) Cu₃As_{0.75}Sb_{0.25}S₄, and (E) Cu₃AsS₄. Peaks marked with a * correspond to orthorhombic enargite Cu₃AsS₄ (JCPDS 01-082-1464). In the GIXRD and Raman spectra, slight deviations of the purely arsenic endmember from the reference spectra are attributed to Sb impurities in the reference spectra themselves. The Raman peaks around 490 cm⁻¹ are attributed to excess sulfur on the surface. [49]–[51]

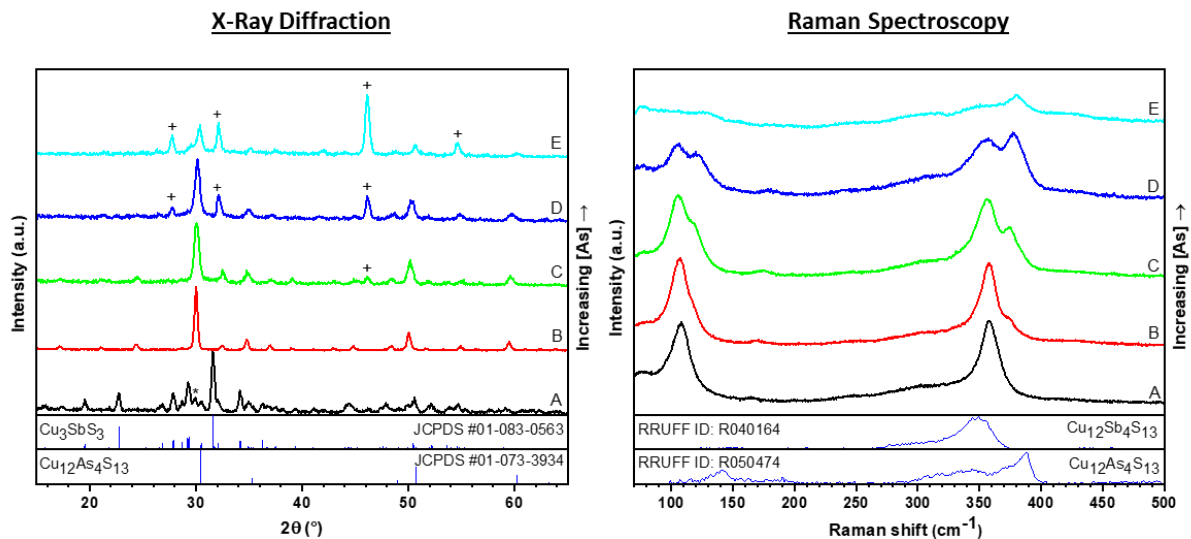


Figure 7.17. GIXRD and Raman spectra of nanoparticles treated in an H_2S atmosphere at $450\text{ }^\circ\text{C}$ for 1 h. (A) Cu_3SbS_4 , (B) $\text{Cu}_3\text{As}_{0.25}\text{Sb}_{0.75}\text{S}_4$, (C) $\text{Cu}_3\text{As}_{0.50}\text{Sb}_{0.50}\text{S}_4$, (D) $\text{Cu}_3\text{As}_{0.75}\text{Sb}_{0.25}\text{S}_4$, and (E) Cu_3AsS_4 . In the GIXRD spectra, the peak marked with (*) in A is attributable to the (222) stretch of tetrahedrite $\text{Cu}_{12}\text{Sb}_4\text{S}_{13}$ (JCPDS #42-560), and the peaks marked with (+) in spectra C-E are attributable to digenite $\text{Cu}_{1.8}\text{S}$ (JCPDS 01-088-2045). In the Raman spectra, slight deviations of the purely antimony endmember from the reference spectrum are attributed to Zn impurities in the reference spectrum itself. Severe reductions in the $\text{Cu}_{12}\text{As}_4\text{S}_{13}$ ν_1 stretch relative to the $\text{Cu}_{12}\text{Sb}_4\text{S}_{13}$ ν_1 stretch imply more significant decomposition in the arsenic-rich compositions relative to the antimony-rich compositions. Cu_3SbS_3 was not detected by Raman in these films; the reader is referred elsewhere for a reference spectrum [54].

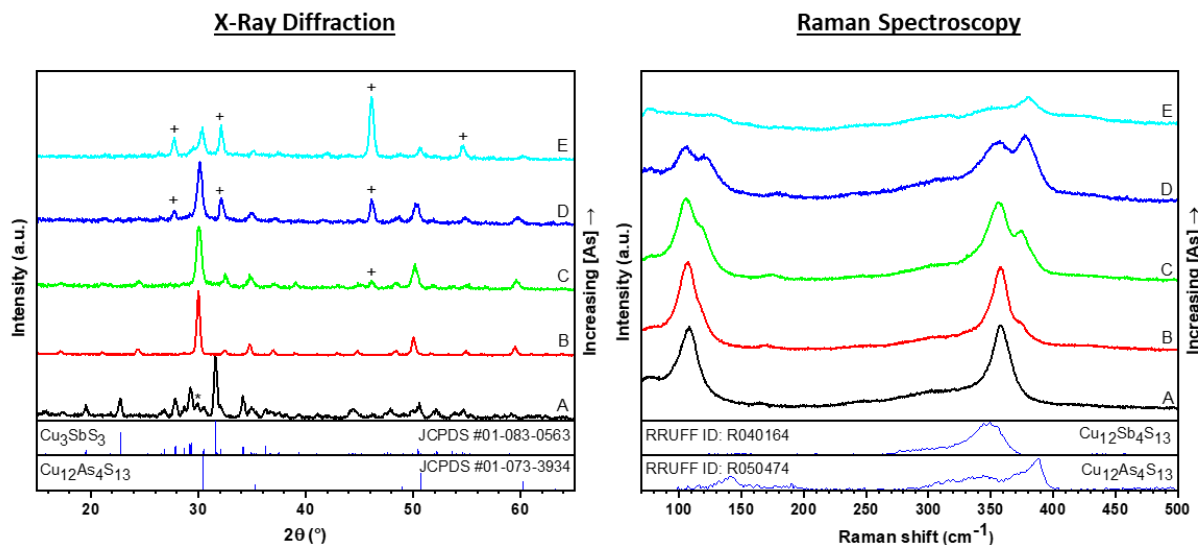


Figure 7.18. GIXRD and Raman spectra of nanoparticles treated in a nitrogen atmosphere at $450\text{ }^\circ\text{C}$ for 1 h. (A) Cu_3SbS_4 , (B) $\text{Cu}_3\text{As}_{0.25}\text{Sb}_{0.75}\text{S}_4$, (C) $\text{Cu}_3\text{As}_{0.50}\text{Sb}_{0.50}\text{S}_4$, (D) $\text{Cu}_3\text{As}_{0.75}\text{Sb}_{0.25}\text{S}_4$, and (E) Cu_3AsS_4 . In GIXRD spectra D and E, the (*) correspond to a digenite $\text{Cu}_{1.8}\text{S}$ impurity phase (JCPDS 01-088-2045). In the Raman spectrum, slight deviations of the purely antimony endmember from the reference spectrum are attributed to Zn impurities in the reference spectrum itself. Additionally, severe reductions in the $\text{Cu}_{12}\text{As}_4\text{S}_{13}$ ν_1 stretch relative to the $\text{Cu}_{12}\text{Sb}_4\text{S}_{13}$ ν_1 stretch imply more significant decomposition in the arsenic-rich compositions relative to the antimony-rich compositions.

7.4 Conclusions

We have reported the first synthesis of $\text{Cu}_{12}(\text{As}_{1-x}\text{Sb}_x)_4\text{S}_{13}$ NPs alloys via a two-step hot-injection. NP-based thin films were heat treated in oxidizing (sulfur), reducing (H_2S), and inert (nitrogen) environments to control the phase and composition of the synthesized $\text{Cu}_{12}(\text{As}_{1-x}\text{Sb}_x)_4\text{S}_{13}$ NP alloys. Heat treating under an elemental sulfur atmosphere oxidized the antimony and arsenic in the $\text{Cu}_{12}(\text{As}_{1-x}\text{Sb}_x)_4\text{S}_{13}$ materials, converting the cubic crystal structure to tetragonal $\text{Cu}_3\text{As}_{1-x}\text{Sb}_x\text{S}_4$. Conversely, the oxidation states of antimony and arsenic were maintained when heat treating in H_2S . Additionally, an increase in grain size was observed after all heat treatments. Elemental losses were observed when heating the $\text{Cu}_{12}(\text{As}_{1-x}\text{Sb}_x)_4\text{S}_{13}$ films in sulfur, H_2S , and nitrogen, likely due to volatilization of sulfur and binary pnictogen sulfide species. These data provide insight into the stability of this material system and reveal the importance of the heat treatment atmosphere in both stabilizing and controllably converting between the TET-TEN and FAM-LUZ crystal systems. These results provide a foundation for future development of antimony and arsenic chalcogenide-based materials and offer insight into heat treatment conditions necessary for tuning and optimizing the optoelectronic properties for future device applications.

7.5 Acknowledgements

This work was supported by the National Science Foundation under grant #1534691-DMR (DMREF: Rapid Design of Earth Abundant Inorganic Materials for Future PVs). The authors would like to acknowledge Joseph Andler for assisting with the table of contents graphic design. The authors declare no competing financial interests.

7.6 Statement of Data Access

The data associated with this manuscript can be found at the project's website: <https://datacenterhub.org/groups/dmref1534691>

7.7 References

- [1] D. V. Talapin, J.-S. Lee, M. V. Kovalenko, and E. V. Shevchenko, "Prospects of Colloidal Nanocrystals for Electronic and Optoelectronic Applications," *Chem. Rev.*, vol. 110, no. 1, pp. 389–458, Jan. 2010.
- [2] P. Reiss, M. Carrière, C. Lincheneau, L. Vaure, and S. Tamang, "Synthesis of Semiconductor Nanocrystals, Focusing on Nontoxic and Earth-Abundant Materials," *Chem. Rev.*, vol. 116, no. 18, pp. 10731–10819, Sep. 2016.
- [3] C. Coughlan, M. Ibáñez, O. Dobrozhan, A. Singh, A. Cabot, and K. M. Ryan, "Compound Copper Chalcogenide Nanocrystals," *Chem. Rev.*, vol. 117, no. 9, pp. 5865–6109, May 2017.
- [4] M. G. Panthani *et al.*, "High Efficiency Solution Processed Sintered CdTe Nanocrystal Solar Cells: The Role of Interfaces," *Nano Lett.*, vol. 14, no. 2, pp. 670–675, Feb. 2014.
- [5] R. W. Crisp *et al.*, "Nanocrystal Grain Growth and Device Architectures for High-Efficiency CdTe Ink-Based Photovoltaics," *ACS Nano*, vol. 8, no. 9, pp. 9063–9072, Sep. 2014.
- [6] S. M. McLeod, C. J. Hages, N. J. Carter, and R. Agrawal, "Synthesis and characterization of 15% efficient CIGSSe solar cells from nanoparticle inks," *Prog. Photovoltaics Res. Appl.*, vol. 23, no. 11, pp. 1550–1556, Nov. 2015.
- [7] M. Scheele, N. Oeschler, K. Meier, A. Kornowski, C. Klinker, and H. Weller, "Synthesis and Thermoelectric Characterization of Bi₂Te₃ Nanoparticles," *Adv. Funct. Mater.*, vol. 19, no. 21, pp. 3476–3483, Nov. 2009.
- [8] B. Ananthoju, J. Mohapatra, M. K. Jangid, D. Bahadur, N. V. Medhekar, and M. Aslam, "Cation/Anion Substitution in Cu₂ZnSnS₄ for Improved Photovoltaic Performance," *Sci. Rep.*, vol. 6, no. 1, p. 35369, Dec. 2016.
- [9] M. R. Golobostanfard and H. Abdizadeh, "All solution processable graded CIGS solar cells fabricated using electrophoretic deposition," *RSC Adv.*, vol. 6, no. 14, pp. 11903–11910, 2016.
- [10] Q. Guo *et al.*, "Development of CuInSe₂ Nanocrystal and Nanoring Inks for Low-Cost Solar Cells," *Nano Lett.*, vol. 8, no. 9, pp. 2982–2987, 2008.
- [11] Q. Guo, G. M. Ford, H. W. Hillhouse, and R. Agrawal, "Sulfide Nanocrystal Inks for Dense Cu(In_{1-x}Ga_x)(S_{1-y}Se_y)₂ Absorber Films and Their Photovoltaic Performance," *Nano Lett.*, vol. 9, no. 8, pp. 3060–3065, 2009.

- [12] W. Wu *et al.*, “Studies of the fine-grain sub-layer in the printed CZTSSe photovoltaic devices,” *J. Mater. Chem. C*, vol. 2, no. 19, p. 3777, 2014.
- [13] C. K. Miskin *et al.*, “9.0% efficient $\text{Cu}_2\text{ZnSn}(\text{S},\text{Se})_4$ solar cells from selenized nanoparticle inks,” *Prog. Photovoltaics Res. Appl.*, vol. 23, no. 5, pp. 654–659, May 2015.
- [14] T. R. Martin, J. K. Katahara, C. N. Bucherl, B. W. Krueger, H. W. Hillhouse, and C. K. Luscombe, “Nanoparticle Ligands and Pyrolyzed Graphitic Carbon in CZTSSe Photovoltaic Devices,” *Chem. Mater.*, vol. 28, no. 1, pp. 135–145, Jan. 2016.
- [15] C. J. Hages, M. J. Koeper, C. K. Miskin, K. W. Brew, and R. Agrawal, “Controlled Grain Growth for High Performance Nanoparticle-Based Kesterite Solar Cells,” *Chem. Mater.*, vol. 28, no. 21, pp. 7703–7714, Nov. 2016.
- [16] C. Wadia, a. P. Alivisatos, and D. M. Kammen, “Materials Availability Expands the Opportunity for Large-Scale Photovoltaics Deployment,” *Environ. Sci. Technol.*, vol. 43, no. 6, pp. 2072–2077, Mar. 2009.
- [17] X. Lu *et al.*, “High Performance Thermoelectricity in Earth-Abundant Compounds Based on Natural Mineral Tetrahedrites,” *Adv. Energy Mater.*, vol. 3, no. 3, pp. 342–348, Mar. 2013.
- [18] X. Lu and D. T. Morelli, “Natural mineral tetrahedrite as a direct source of thermoelectric materials,” *Phys. Chem. Chem. Phys.*, vol. 15, no. 16, p. 5762, 2013.
- [19] K. Suekuni *et al.*, “High-performance thermoelectric mineral $\text{Cu}_{12-x}\text{Ni}_x\text{Sb}_4\text{S}_{13}$ tetrahedrite,” *J. Appl. Phys.*, vol. 113, no. 4, p. 043712, Jan. 2013.
- [20] X. Lu and D. Morelli, “The Effect of Te Substitution for Sb on Thermoelectric Properties of Tetrahedrite,” *J. Electron. Mater.*, vol. 43, no. 6, pp. 1983–1987, Jun. 2014.
- [21] R. Chetty, A. Bali, and R. C. Mallik, “Tetrahedrites as thermoelectric materials: an overview,” *J. Mater. Chem. C*, vol. 3, no. 48, pp. 12364–12378, 2015.
- [22] R. Chetty *et al.*, “Thermoelectric properties of Co substituted synthetic tetrahedrite,” *Acta Mater.*, vol. 100, pp. 266–274, Nov. 2015.
- [23] R. Chetty *et al.*, “Thermoelectric properties of a Mn substituted synthetic tetrahedrite,” *Phys. Chem. Chem. Phys.*, vol. 17, no. 3, pp. 1716–1727, 2015.
- [24] Y. Bouyrie, C. Candolfi, A. Dauscher, B. Malaman, and B. Lenoir, “Exsolution Process as a Route toward Extremely Low Thermal Conductivity in $\text{Cu}_{12}\text{Sb}_{4-x}\text{Te}_x\text{S}_{13}$ Tetrahedrites,” *Chem. Mater.*, vol. 27, no. 24, pp. 8354–8361, Dec. 2015.

- [25] S. Harish, D. Sivaprahasam, M. Battabyal, and R. Gopalan, "Phase stability and thermoelectric properties of $\text{Cu}_{10.5}\text{Zn}_{1.5}\text{Sb}_4\text{S}_{13}$ tetrahedrite," *J. Alloys Compd.*, vol. 667, pp. 323–328, May 2016.
- [26] J. Heo, R. Ravichandran, C. F. Reidy, J. Tate, J. F. Wager, and D. A. Keszler, "Design Meets Nature: Tetrahedrite Solar Absorbers," *Adv. Energy Mater.*, vol. 5, no. 7, p. 1401506, Apr. 2015.
- [27] L. Wang *et al.*, "Synthesis and characterization of hydrazine solution processed $\text{Cu}_{12}\text{Sb}_4\text{S}_{13}$ film," *Sol. Energy Mater. Sol. Cells*, vol. 144, pp. 33–39, Jan. 2016.
- [28] S. Maske and B. J. Skinner, "Studies of the sulfosalts of copper I. Phases and phase relations in the system Cu-As-S," *Econ. Geol.*, vol. 66, no. 6, pp. 901–918, Oct. 1971.
- [29] F. D. Luce, C. L. Tuttle, and B. J. Skinner, "Studies of sulfosalts of copper: V. Phases and phase relations in the system Cu-Sb-As-S between 350° and 500°C," *Econ. Geol.*, vol. 72, no. 2, pp. 271–289, Apr. 1977.
- [30] R. B. Balow, C. K. Miskin, M. M. Abu-Omar, and R. Agrawal, "Synthesis and Characterization of $\text{Cu}_3(\text{Sb}_{1-x}\text{As}_x)\text{S}_4$ Semiconducting Nanocrystal Alloys with Tunable Properties for Optoelectronic Device Applications," *Chem. Mater.*, vol. 29, no. 2, pp. 573–578, Jan. 2017.
- [31] T. Shi, W.-J. Yin, M. Al-Jassim, and Y. Yan, "Structural, electronic, and optical properties of $\text{Cu}_3\text{-V-VI}_4$ compound semiconductors," *Appl. Phys. Lett.*, vol. 103, no. 15, p. 152105, Oct. 2013.
- [32] L. Yu, R. S. Kokenyesi, D. A. Keszler, and A. Zunger, "Inverse Design of High Absorption Thin-Film Photovoltaic Materials," *Adv. Energy Mater.*, vol. 3, no. 1, pp. 43–48, Jan. 2013.
- [33] G. J. Snyder and E. S. Toberer, "Complex thermoelectric materials," *Nat. Mater.*, vol. 7, no. 2, pp. 105–114, Feb. 2008.
- [34] R. B. Balow, E. P. Tomlinson, M. M. Abu-Omar, B. W. Boudouris, and R. Agrawal, "Solution-based synthesis and characterization of earth abundant $\text{Cu}_3(\text{As,Sb})\text{Se}_4$ nanocrystal alloys: towards scalable room-temperature thermoelectric devices," *J. Mater. Chem. A*, vol. 4, no. 6, pp. 2198–2204, 2016.
- [35] J. van Embden, K. Latham, N. W. Duffy, and Y. Tachibana, "Near-Infrared Absorbing $\text{Cu}_{12}\text{Sb}_4\text{S}_{13}$ and Cu_3SbS_4 Nanocrystals: Synthesis, Characterization, and Photoelectrochemistry," *J. Am. Chem. Soc.*, vol. 135, no. 31, pp. 11562–11571, Aug. 2013.

- [36] K. Ramasamy, H. Sims, W. H. Butler, and A. Gupta, "Selective Nanocrystal Synthesis and Calculated Electronic Structure of All Four Phases of Copper–Antimony–Sulfide," *Chem. Mater.*, vol. 26, no. 9, pp. 2891–2899, May 2014.
- [37] S. Suehiro *et al.*, "Synthesis of Copper–Antimony–Sulfide Nanocrystals for Solution-Processed Solar Cells," *Inorg. Chem.*, vol. 54, no. 16, pp. 7840–7845, Aug. 2015.
- [38] K. Chen, J. Zhou, W. Chen, P. Zhou, F. He, and Y. Liu, "Size-Dependent Synthesis of $\text{Cu}_{12}\text{Sb}_4\text{S}_{13}$ Nanocrystals with Bandgap Tunability," *Part. Part. Syst. Charact.*, vol. 32, no. 11, pp. 999–1005, Nov. 2015.
- [39] R. B. Balow, E. J. Sheets, M. M. Abu-Omar, and R. Agrawal, "Synthesis and Characterization of Copper Arsenic Sulfide Nanocrystals from Earth Abundant Elements for Solar Energy Conversion," *Chem. Mater.*, vol. 27, no. 7, pp. 2290–2293, Apr. 2015.
- [40] L. Vegard, "Die Konstitution der Mischkristalle und die Raumfüllung der Atome," *Zeitschrift für Phys.*, vol. 5, no. 1, pp. 17–26, Jan. 1921.
- [41] A. R. Denton and N. W. Ashcroft, "Vegard's law," *Phys. Rev. A*, vol. 43, no. 6, pp. 3161–3164, Mar. 1991.
- [42] S. Kharbish, E. Libowitzky, and A. Beran, "The effect of As-Sb substitution in the Raman spectra of tetrahedrite-tennantite and pyrrargyrite-proustite solid solutions," *Eur. J. Mineral.*, vol. 19, no. 4, pp. 567–574, Aug. 2007.
- [43] M. A. Boles, D. Ling, T. Hyeon, and D. V. Talapin, "The surface science of nanocrystals," *Nat. Mater.*, vol. 15, no. 2, pp. 141–153, Jan. 2016.
- [44] B. J. Skinner, F. D. Luce, and E. Makovicky, "Studies of the Sulfosalts of Copper III. Phases and Phase Relations in the System Cu-Sb-S," *Econ. Geol.*, vol. 67, no. 7, pp. 924–938, Nov. 1972.
- [45] M. L. Johnson and R. Jeanloz, "A Brillouin-zone model for compositional variation in tetrahedrite," *Am. Mineral.*, vol. 68, pp. 220–226, 1983.
- [46] Y. Bouyrie *et al.*, "Crystal structure, electronic band structure and high-temperature thermoelectric properties of Te-substituted tetrahedrites $\text{Cu}_{12}\text{Sb}_{4-x}\text{Te}_x\text{S}_{13}$ ($0.5 \leq x \leq 2.0$)," *J. Mater. Chem. C*, vol. 3, no. 40, pp. 10476–10487, 2015.
- [47] P. Vaqueiro *et al.*, "The Influence of Mobile Copper Ions on the Glass-Like Thermal Conductivity of Copper-Rich Tetrahedrites," *Chem. Mater.*, vol. 29, no. 9, pp. 4080–4090, May 2017.

- [48] M. Posfai and P. R. Buseck, "Relationships between microstructure and composition in enargite and luzonite," *Am. Mineral.*, vol. 83, pp. 373–382, Apr. 1998.
- [49] B. Meyer, "Elemental sulfur," *Chem. Rev.*, vol. 76, no. 3, pp. 367–388, Jun. 1976.
- [50] B. D. Chernomordik, A. E. Béland, D. D. Deng, L. F. Francis, and E. S. Aydil, "Microstructure Evolution and Crystal Growth in $\text{Cu}_2\text{ZnSnS}_4$ Thin Films Formed By Annealing Colloidal Nanocrystal Coatings," *Chem. Mater.*, vol. 26, no. 10, pp. 3191–3201, May 2014.
- [51] S. A. McClary, J. Andler, C. A. Handwerker, and R. Agrawal, "Solution-processed copper arsenic sulfide thin films for photovoltaic applications," *J. Mater. Chem. C*, vol. 5, no. 28, pp. 6913–6916, 2017.
- [52] P. Maiello, G. Zoppi, R. W. Miles, N. Pearsall, and I. Forbes, "Chalcogenisation of Cu–Sb metallic precursors into $\text{Cu}_3\text{Sb}(\text{Se}_x\text{S}_{1-x})_3$," *Sol. Energy Mater. Sol. Cells*, vol. 113, pp. 186–194, Jun. 2013.
- [53] R. Padilla, Y. Fan, and I. Wilkomirsky, "Decomposition of Enargite in Nitrogen Atmosphere," *Can. Metall. Q.*, vol. 40, no. 3, pp. 335–342, Jan. 2001.
- [54] A. Hussain, R. Ahmed, N. Ali, A. Shaari, J.-T. Luo, and Y. Q. Fu, "Characterization of Cu_3SbS_3 thin films grown by thermally diffusing Cu_2S and Sb_2S_3 layers," *Surf. Coatings Technol.*, vol. 319, pp. 294–300, Jun. 2017.
- [55] C. L. McCarthy, P. Cottingham, K. Abuyen, E. C. Schueller, S. P. Culver, and R. L. Brutchey, "Earth abundant CuSbS_2 thin films solution processed from thiol–amine mixtures," *J. Mater. Chem. C*, vol. 4, no. 26, pp. 6230–6233, 2016.
- [56] T. Barbier *et al.*, "Structural stability of the synthetic thermoelectric ternary and nickel-substituted tetrahedrite phases," *J. Alloys Compd.*, vol. 634, pp. 253–262, Jun. 2015.
- [57] X. Lu *et al.*, "Band structure engineering in highly degenerate tetrahedrites through isovalent doping," *J. Mater. Chem. A*, pp. 17096–17103, 2016.
- [58] W. Septina, S. Ikeda, Y. Iga, T. Harada, and M. Matsumura, "Thin film solar cell based on CuSbS_2 absorber fabricated from an electrochemically deposited metal stack," *Thin Solid Films*, vol. 550, pp. 700–704, Jan. 2014.
- [59] M. G. Gang *et al.*, "A 5.1% efficient kesterite $\text{Cu}_2\text{ZnSnS}_4$ (CZTS) thin film solar cell prepared using modified sulfurization process," *Phys. status solidi c*, vol. 12, no. 6, pp. 713–716, Jun. 2015.

- [60] P. Balaz, J. Briancin, and L. Turcaniova, "Thermal decomposition of mechanically activated tetrahedrite," *Thermochim. Acta*, vol. 249, pp. 375–381, 1995.
- [61] F.-H. Sun *et al.*, "Powder metallurgically synthesized $\text{Cu}_{12}\text{Sb}_4\text{S}_{13}$ tetrahedrites: phase transition and high thermoelectricity," *RSC Adv.*, vol. 7, no. 31, pp. 18909–18916, 2017.
- [62] P. Lemoine, C. Bourgès, T. Barbier, V. Nassif, S. Cordier, and E. Guilmeau, "High temperature neutron powder diffraction study of the $\text{Cu}_{12}\text{Sb}_4\text{S}_{13}$ and $\text{Cu}_4\text{Sn}_7\text{S}_{16}$ phases," *J. Solid State Chem.*, vol. 247, pp. 83–89, Mar. 2017.
- [63] G. H. Albuquerque *et al.*, "Multimodal characterization of solution-processed Cu_3SbS_4 absorbers for thin film solar cells," *J. Mater. Chem. A*, vol. 6, no. 18, pp. 8682–8692, 2018.
- [64] F. W. de Souza Lucas *et al.*, "Effects of Thermochemical Treatment on CuSbS_2 Photovoltaic Absorber Quality and Solar Cell Reproducibility," *J. Phys. Chem. C*, vol. 120, no. 33, pp. 18377–18385, Aug. 2016.

8. SYNTHESIS AND CHARACTERIZATION OF SEMICONDUCTING SINNERITE ($\text{Cu}_6\text{As}_4\text{S}_9$) THIN FILMS

8.1 Introduction

Thin-film photovoltaic (PV) materials are a promising low-cost method for harvesting solar radiation and converting it into electricity that can meet the human race's energy demands for the foreseeable future. Building on decades of laboratory-scale research, CdTe and Cu(In,Ga)Se₂ solar cells have been commercialized [1], but their widespread deployment may be challenging due to the volatility and relative scarcity of In, Ga, and Te sources [2], [3]. Thus, a significant fraction of the PV community has begun to focus on alternative materials consisting of earth-abundant elements, with substantial research into compounds that are either derivatives of existing compounds (such as $\text{Cu}_2\text{ZnSn}(\text{S},\text{Se})_4$ [4]–[6] and ZnSnP_2 [7], [8]) or entirely new classes of materials (such as Sb_2Se_3 [9] and lead halide perovskites [10]). However, none have yet achieved the combination of efficiency and stability that warrant large-scale manufacturing and commercialization.

Cu-As-S compounds have recently emerged as potential PV materials due to their constituent earth abundant elements that possess dissimilar cation sizes, a characteristic which typically results in high formation energies and hence lower concentrations of harmful antisite defects. The most widely researched Cu-As-S material is orthorhombic enargite (ENG) Cu_3AsS_4 , which has been studied in its natural mineral [11] and synthetic nanoparticle [12] (NP) forms. Prototype ENG-based solar cells have also been fabricated from NP precursors [13], and computational work has elucidated ENG's optoelectronic properties and accelerated the development of ideal device architectures [14], [15]. Besides ENG, two other phases have been explored in semiconducting contexts: tetragonal luzonite (LUZ) Cu_3AsS_4 has an appropriate bandgap for PV and generates more photocurrent than its Sb-based analog [16]–[18], and cubic tennantite (TEN) $\text{Cu}_{12}\text{As}_4\text{S}_{13}$ has attracted attention for medium-temperature thermoelectric applications [19]–[21].

One Cu-As-S phase that has received less attention from the research community is sinnerite (SIN), which has nominal composition $\text{Cu}_6\text{As}_4\text{S}_9$. Previous experimental studies on SIN have been restricted to solving its triclinic crystal structure and measuring optoelectronic properties of amorphous $\text{Cu}_6\text{As}_4\text{S}_9$ glasses [22]–[27]. Recent theoretical studies indicate that SIN

may display high absorption coefficients and PV device efficiencies exceeding 20%, as well as low lattice thermal conductivity for enhanced thermoelectric transport [19], [28]. To the best of our knowledge, the electrical and optical properties of crystalline SIN have not been measured experimentally. In this work, we report the synthesis and preliminary optoelectronic characterization of SIN thin films for potential use in PV applications. SIN films were fabricated from solution-processed NP precursors and display micron-sized dense grains, an ideal bandgap (1.16 eV) for solar energy conversion, and significant current production under simulated solar illumination. The results detailed here motivate further research and development of sinnerite thin films and PV devices.

8.2 Experimental Methods

Caution: Arsenic compounds are highly toxic! Consult the safety data sheets (SDS) for each specific compound before use. To reduce the risk of exposure and undesired reactions, it is highly recommended that any arsenic-containing compound is handled under an inert environment unless necessary, especially arsenic (III) chloride ($AsCl_3$)!

8.2.1 Materials

Table 8.1 lists the chemicals, abbreviations, purities, and suppliers of the chemicals used in this chapter. All materials were used as received and stored in a nitrogen-filled glovebox unless otherwise noted. Oleylamine (OLA) used in nanoparticle (NP) synthesis was degassed using three freeze-pump-thaw (FPT) cycles and stored in the glovebox prior to use.

Table 8.1. Detailed information for chemicals used in this chapter.

Chemical	Abbreviation	Purity	Supplier
1-hexanethiol	HT	>95%	Sigma-Aldrich
Acetone	--	>99.5% (certified ACS)	Fisher
Acetonitrile	--	>99.8% anhydrous	Sigma-Aldrich
Ammonium sulfide	$(NH_4)_2S$	40-48 wt% in water	Sigma-Aldrich
Arsenic (II) sulfide	As_2S_2	>95%	Sigma-Aldrich
Arsenic (III) chloride	$AsCl_3$	>99.99%	Sigma-Aldrich
Arsenic (III) sulfide	As_2S_3	>99.9%	Strem Chemicals
Arsenic (V) sulfide	As_2S_5	>99.99%	Sigma-Aldrich
Chloroform	$CHCl_3$	>99.8% (certified ACS)	Fisher
Copper (I) chloride	$CuCl$	>99.99%	Strem Chemicals

Table 8.1 continued

Dimethylsulfoxide	DMSO	>99.9% anhydrous	Sigma-Aldrich
Ethanol	EtOH	200 proof	Fisher
Europium (III) chloride	EuCl ₃	>99.9% (hydrate)	VWR
Ferrocene	Fc	>98%	Sigma-Aldrich
Formamide	FA	>99.5%	Sigma-Aldrich
Molybdenum	Mo	>99.95%	Kurt J. Lesker
Oleylamine	OLA	>70% (technical grade)	Sigma-Aldrich
Sulfur	S	>99.99%, flakes	Sigma-Aldrich
Tetrabutylammonium hexafluorophosphate	TBAPF ₆	>99% for electrochemical analysis	Sigma-Aldrich

8.2.2 Nanoparticle Synthesis and Coating

Luzonite Cu₃AsS₄ nanoparticles (NPs) were fabricated according to our group's previous reports [13], [17], [18]. Precursor stock solutions were formed by dissolving sulfur (1 M) or CuCl/AsCl₃ (2.8/1 Cu:As molar ratio, 0.2 M CuCl) in FPT OLA for ~2 h at 65 °C with magnetic stirring. A 100 mL three-neck flask containing 10.5 mL OLA was attached to a Schlenk line, evacuated and refilled with argon three times, and refluxed under vacuum for 1 h at 110 °C to remove dissolved gases and light impurities. The flask temperature was increased to 175 °C, at which point 1.2 mL of the S solution was injected, followed by 3.0 mL of the cation solution 20 s later. The reaction mixture immediately turned black and reacted for 10 min before removing from heat and cooling naturally to room temperature. NPs were washed via three precipitation and redissolution cycles with ethanol/chloroform mixtures; centrifugations took place at 8 krpm (~9800 xG) for 10 min.

NPs were dried under argon, dispersed in HT (200 mg/mL), and blade coated onto 2" by 1" molybdenum-coated soda-lime glass substrates at room temperature. The Mo was 800 nm thick and was deposited using DC sputtering. Between coats, substrates were dried at 75 °C for 5 min.

8.2.3 Ampoule Preparation and Heat Treatment

Samples were cut to ¼" by 1" and placed in a 10 mL borosilicate glass ampoule from ChemGlass. ~10 mg As₂S₂ powder was then added to the ampoule in a nitrogen-filled glovebox, and the ampoule was removed and attached to a Schlenk line while maintaining the inert atmosphere. The ampoule was evacuated and refilled with argon three times, then evacuated again and sealed using a butane flame.

Sealed ampoules were treated in a horizontal tube furnace (Applied Test Systems, Inc. Series 3210). The furnace was set to the desired temperature and allowed to equilibrate, at which point the ampoule was inserted into the furnace. After a set time, the furnace was opened and allowed to cool by natural convection. After cooling, the ampoules were broken around the neck by scribing with a diamond tip pen and snapping the neck while wearing cut-resistant gloves.

8.2.4 Ligand Exchange

In order to eliminate carbonaceous residue that could impact optoelectronic measurements, we used a ligand exchange procedure to replace OLA with an As_2S_3 -based molecular metal chalcogenide complex; this method was adapted from previous work [29], [30]. 1 mmol As_2S_3 was dissolved in 0.43 mL $(\text{NH}_4)_2\text{S}$ and 5 mL ultrapure water, and the resulting yellow liquid was filtered. Then, solid yellow $(\text{NH}_4)_3\text{AsS}_3$ was isolated by adding acetone and centrifuging, followed by an additional washing step with water and acetone. This ligand was dried and dispersed in FA (0.15 M).

To conduct the ligand exchange, undried LUZ NPs were dispersed in CHCl_3 at a concentration of ~ 25 mg/mL and taken into a glovebox, where an equal volume of FA- $(\text{NH}_4)_3\text{AsS}_3$ was added. The two-phase mixture was stirred until the FA phase turned dark and the CHCl_3 phase became transparent. The clear CHCl_3 was drawn off and replaced with fresh CHCl_3 for an additional hour of stirring. Then, the CHCl_3 was discarded, and 6 mL acetonitrile was added to the FA phase. The mixture was centrifuged at 14 krpm (~ 17100 xG) for 5 min, and the yellow supernatant was discarded. The pellet was resuspended in 2 mL DMSO followed by 8 mL acetonitrile; this mixture was centrifuged at 14 krpm for 5 min. The supernatant was discarded, and the pellet was resuspended in DMSO (~ 200 mg/mL) for coating. Removal of carbonaceous ligands was verified by baking this ink at 200°C in nitrogen and then performing Fourier transform infrared spectroscopy (FTIR).

Ligand exchanged NPs were coated onto desired substrates (Mo-coated soda-lime glass, quartz) by blade coating at 85°C in air. Between coatings, the sample was dried at 85°C for 5 min. After all layers were applied, the sample was baked at 130°C and then 200°C for 5 min each.

8.2.5 Characterization

Grazing incidence X-ray diffraction (GIXRD) data were collected on a Rigaku SmartLab diffractometer using a copper $K\alpha$ X-ray source in parallel beam mode at a grazing incidence angle of 0.5° . X-ray fluorescence (XRF) data were taken at an accelerating voltage of 50 kV with a Ni filter (10 μm thickness) using a Fisherscope X-Ray XAN 250 with He flow. Raman spectra were taken at an excitation wavelength of 633 nm using a Horiba/Jobin-Yvon LabRAM HR800 confocal microscope system. Scanning Electron Microscopy (SEM) images were taken on an FEI Quanta scanning electron microscope at an accelerating voltage of 7 kV and a working distance of 10 mm. Fourier Transform Infrared Spectroscopy (FTIR) data were acquired using a Nicolet Nexus 670 FTIR. Reflectance data was acquired using a Perkin-Elmer Lambda 950 spectrometer with an integrating sphere. Electrochemical measurements were conducted using a home-built quartz cell with a SIN film as the working electrode, a platinum wire (BASi, Inc.) as the counter electrode, and Ag^+/AgCl as the reference electrode; the electrodes were attached to a Digi-Ivy D2011 single channel potentiostat. All measurements were taken at a scan rate of 50 mV/s after the open-circuit potential had equilibrated. A xenon arc lamp with AM1.5G filters was used to provide artificial sunlight for photoelectrochemical measurements, and a Si reference cell was used for intensity calibration to 100 mW/cm^2 . Time-resolved photoluminescence (TRPL) measurements were acquired using a Horiba Fluorolog equipped with a 637 nm laser operating at 1 MHz pulse rate and an InGaAs photomultiplier tube (Hamamatsu H10330-45) for signal detection. Hall effect measurements were performed in the van der Pauw geometry on an Ecopia AHT55T5 system.

8.3 Results and Discussion

In a previous publication, we reported the first synthesis of ENG thin films with micron-sized dense grains; this was achieved by heating LUZ NPs in a sealed glass ampoule with As_2S_5 powder [13]. At moderate temperatures ($\sim 300 - 500^\circ\text{C}$) typically used to promote grain growth in NP-based thin films, solid ENG is in equilibrium with an extensive range of liquids containing mostly As and S with a small amount ($\sim 1-3\%$) of Cu [22]. The proposed mechanism for grain growth is that a liquid As-S phase initially condenses on the surface of and nanopores within the NP film, a phenomenon driven by supersaturation of the vapor space and the nanoporosity of the initial film. This binary liquid absorbs Cu from decomposing NPs until a saturation point is reached;

solid Cu_3AsS_4 can nucleate from this liquid either upon cooling or upon any disruption to the equilibrium. A close examination of Cu-As-S phase relations reveals that while ternary liquids are in equilibrium with Cu_3AsS_4 at high sulfur compositions (>55 at%), they are instead in equilibrium with $\text{Cu}_6\text{As}_4\text{S}_9$ at lower sulfur compositions (~40-55 at%) [22]. Therefore, we hypothesized that by increasing the amount of As relative to S sealed in the ampoule, we could alter the liquid composition and form SIN, rather than ENG as seen previously.

Figure 8.1a gives the grazing incidence X-ray diffraction (GIXRD) pattern of a LUZ NP film that was heated in a glass ampoule with commercially available As_2S_2 powder for 10 min at 400 °C. The major reflections suggest a tetragonal or cubic crystal structure, such as those seen in the XRD patterns of both luzonite and lazarevicite Cu_3AsS_4 , along with an exaggerated peak at 40° 2 θ resulting from the Mo substrate. This observed pattern is not surprising – even though many additional reflections are expected due to its triclinic crystal structure, SIN has a sphalerite sublattice with strong reflections that obscure signal from the true triclinic cell [23], [24], [27]. Figure 8.1b gives the same GIXRD spectra with an exaggerated reference spectrum, which shows that the small peaks near 20.8°, 22.5°, 35.3°, 36.4°, 44.0°, and 45.5° in the measured spectrum do appear weakly in single crystal samples; additionally, they do not match with any potential elemental, binary, or ternary impurity phases that may occur in the reaction scheme used in this work.

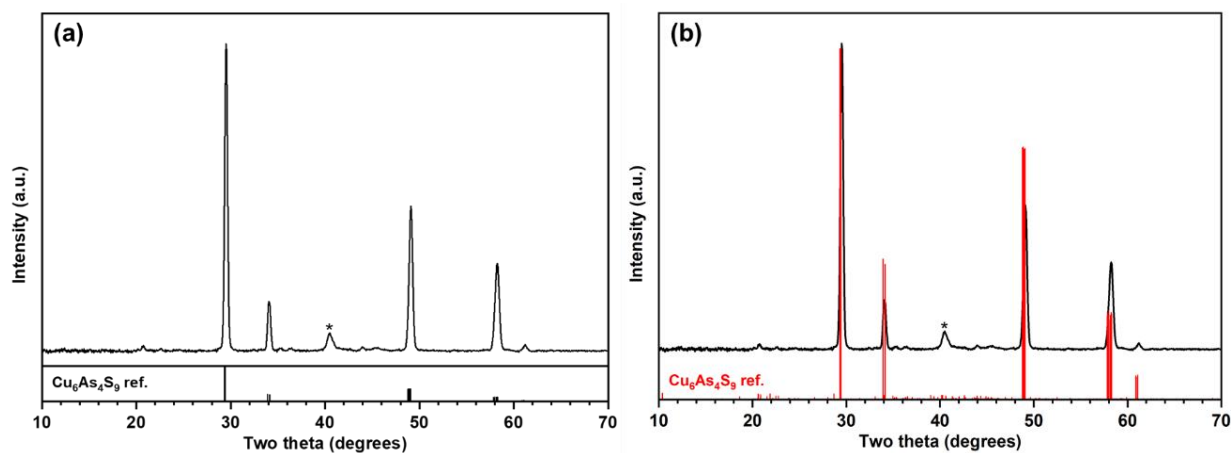


Figure 8.1. (a) GIXRD spectrum of a luzonite Cu_3AsS_4 NP film that was treated in an As_2S_2 atmosphere at 400 °C for 10 min. The pattern agrees with a reference standard for sinnerite $\text{Cu}_6\text{As}_4\text{S}_9$ (ICSD collection code 236895) and is free of detectable impurity phases [27]. The peak marked with (*) is attributed to the Mo substrate. (b) The same GIXRD spectrum with an enlarged reference showing spectrum, showing that other visible minor peaks (e.g. 20.8°) exist but are obscured by the sphalerite subcell reflections.

To further distinguish between SIN and other ternary phases, one can take advantage of the vastly different ideal Cu/As ratios (1.5 for SIN, 3.0 for LUZ). X-ray fluorescence (XRF) measurements were used to estimate the composition of as-treated thin films. For a sample treated at 400 °C for 10 min, the Cu/As ratio is 1.30, which is much closer to the ratio for SIN than for other competing phases; however, it appears that a significant excess of As remains in the film. Because of the sealed environment associated with the heat treatment, As-S vapors likely condense on the film's surface during cooldown, leading to artificially low Cu/As ratios. Since an aqueous solution of ammonium sulfide $[(\text{NH}_4)_2\text{S}]$ may dissolve arsenic sulfides, a short etch was conducted to remove any excess material from the surface [29], [31], [32]. After a 1 min immersion, the Cu/As ratio increased to 1.38, indicating that As-containing phases were preferentially etched, though there still may be excess As beneath the surface of the film.

Raman spectroscopy is often used to identify the phases present in thin films, but to the best of our knowledge, a spectrum has not been reported in previous SIN studies, so comparison of our sample with a known standard is not possible. However, as seen in Figure 8.2, the Raman spectrum obtained from an As_2S_2 -treated film etched in $(\text{NH}_4)_2\text{S}$ is significantly different than that of a LUZ or ENG standard, providing further evidence that Cu_3AsS_4 was not formed. The observed stretches do not align with other potential impurity phases such as copper sulfides and arsenic sulfides. It is noteworthy that there is no impurity peak at 494 cm^{-1} (corresponding to S-S bonds entrained with residual carbon) as seen in our previous report on ENG films; this is likely due to reduced sulfur content in the atmosphere [13]. When the XRD, XRF, and Raman data are jointly considered, it is evident that $\text{Cu}_6\text{As}_4\text{S}_9$ was formed from As_2S_2 heat treatments, rather than Cu_3AsS_4 or other ternary Cu-As-S phases.

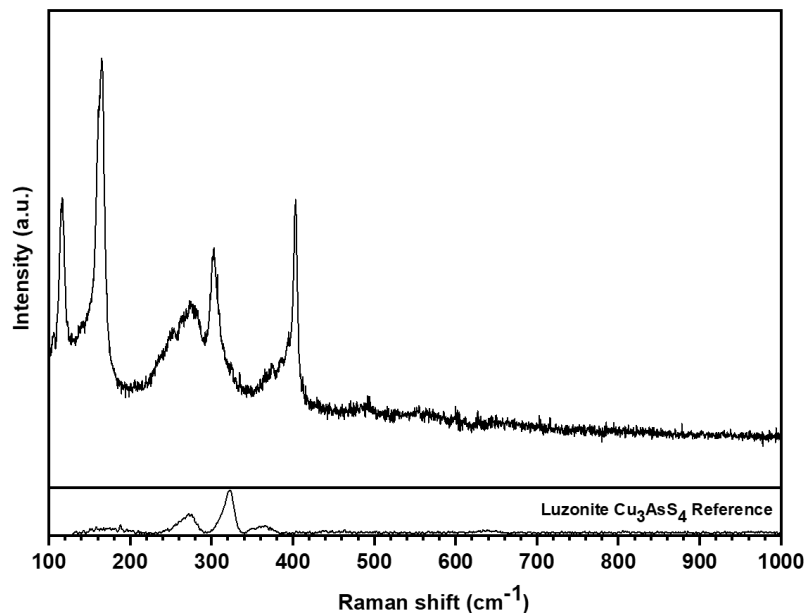


Figure 8.2. Raman spectrum of a LUZ NP film heat treated in an ampoule with As_2S_2 for 10 min at $400\text{ }^\circ\text{C}$. As discussed in the main text, there is not a reference spectrum available for sinnerite $\text{Cu}_6\text{As}_4\text{S}_9$, but the obtained spectrum is significantly different than that of a mineral for Cu_3AsS_4 (RRUFF ID R060390), ruling out the possibility of luzonite formation.

The formation of SIN in an As_2S_2 atmosphere (rather than ENG as in As_2S_5 or As_2S_3) [13] suggests that the ternary material formed after heat treatment is dictated by the composition of the As-S liquid, as opposed to the phase of the precursor film. To further support this point, heat treatments were conducted using evaporated Cu films as the starting material; GIXRD and Raman (Figure 8.3) indicate that SIN was formed in As_2S_2 and ENG was formed in As_2S_5 . We hypothesize, but do not further explore in this chapter, that any convenient precursor material (e.g. Cu, Cu_3AsS_4 NPs, Cu_{2-x}S , etc.) can be used for growth of $\text{Cu}_6\text{As}_4\text{S}_9$ or Cu_3AsS_4 films, so long as it contains enough copper to saturate a condensing As-S liquid.

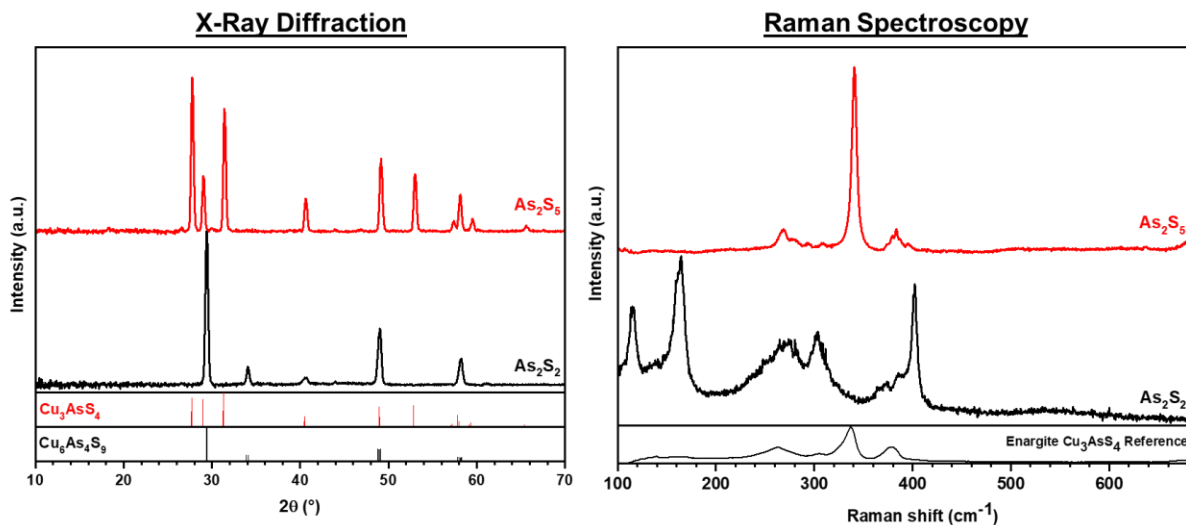


Figure 8.3. GIXRD and Raman spectra of 300 nm evaporated Cu films treated in As_2S_2 at 400 $^\circ C$ for 10 min or As_2S_5 at 425 $^\circ C$ for 30 min. The GIXRD spectrum for the As_2S_2 treatment matches well with a reference $Cu_6As_4S_9$ spectrum (ICSD collection code 236895), and the Raman spectrum matches closely with that obtained in Figure 8.2. The GIXRD and Raman spectra for the As_2S_5 treatment match well with enargite Cu_3AsS_4 references (JCPDS 01-082-1464 and RRUFF ID R050373, respectively).

For solid-state device applications, micron-sized dense grains are desirable so that the density of grain boundaries and effects of electrical shunting are minimized. Grain growth mechanisms are strongly dependent on the annealing temperatures and times. Initially, several temperatures were explored for the growth of SIN thin films over a duration of 30 minutes. Plan-view scanning electron microscopy (SEM) images (Figure 8.4) indicate that the 350-400 $^\circ C$ range is optimal for growing SIN films, as grains with relatively high packing densities are formed. Higher temperatures result in island grain growth and some decomposition to TEN (Figure 8.5). To further optimize the film morphology, a range of annealing times at 400 $^\circ C$ was tested. Figure 8.6 depicts plan-view SEM images for anneals of 5, 10, 15, 30, and 60 min, all of which were SIN (Figure 8.7). The 5 min treatment resulted in a film with significant void space, while the 60 min treatment gave a film with significant surface nonuniformity and poor grain packing. For the remainder of this manuscript, the 10 min treatment is studied, as it represents the best combination of uniform grain size and dense coverage. A cross-sectional SEM image (Figure 8.8) shows a bilayer morphology typical of many NP-based thin films, with a layer of micron-thick grains on top of a ~ 300 nm “fine grain” layer. This layer often contains residual carbon stemming from NP ligands [33]–[35], and its presence suggests that grain growth was initiated at the top of the NP

film, similar to $\text{Cu}(\text{In,Ga})\text{S}_2$ and $\text{Cu}_2\text{ZnSnS}_4$ absorber layers that undergo liquid-assisted grain growth in a selenium atmosphere [36], [37].

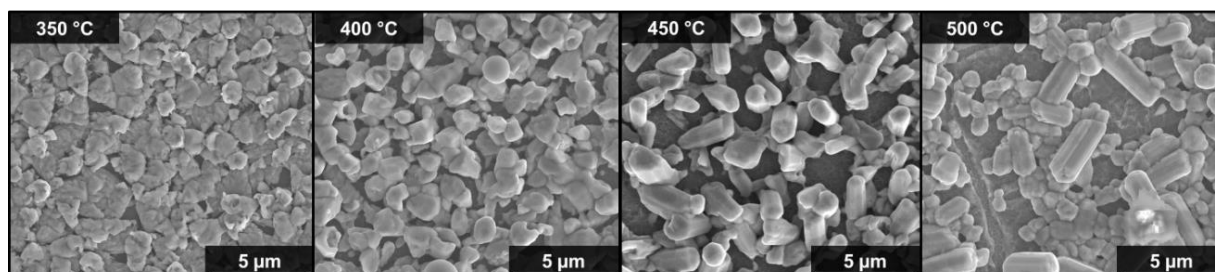


Figure 8.4. Plan-view SEM images of LUZ NPs heat treated in As_2S_2 at the indicated temperature for 30 min. The 350 °C and 400 °C treatments resulted in micron-sized grains with relatively high packing density, whereas the 450 °C and 500 °C treatments gave isolated groups of grains with significant portions of the substrate exposed.

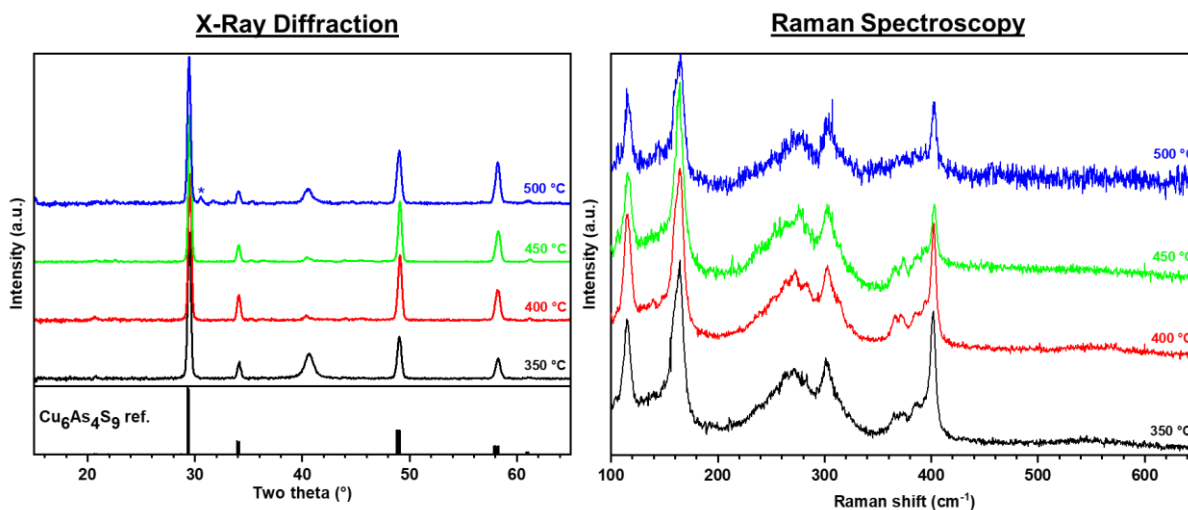


Figure 8.5. GIXRD and Raman spectra of LUZ NPs heat treated in As_2S_2 at the indicated temperature for 30 min. GIXRD spectra match with reference spectrum #236895 on the ICSD, and the Raman spectra match well with the spectrum depicted in Figure 8.2. In the 500 °C GIXRD spectrum, the peak marked with an asterisk (*) matches with the (222) plane of tennantite $\text{Cu}_{12}\text{As}_4\text{S}_{13}$ (reference spectrum JCPDS #01-073-3934). The Cu/As ratios (as determined by XRF) were 1.17, 1.19, 1.22, and 1.09 for the un-etched 350 °C, 400 °C, 450 °C, and 500 °C treatments, respectively.

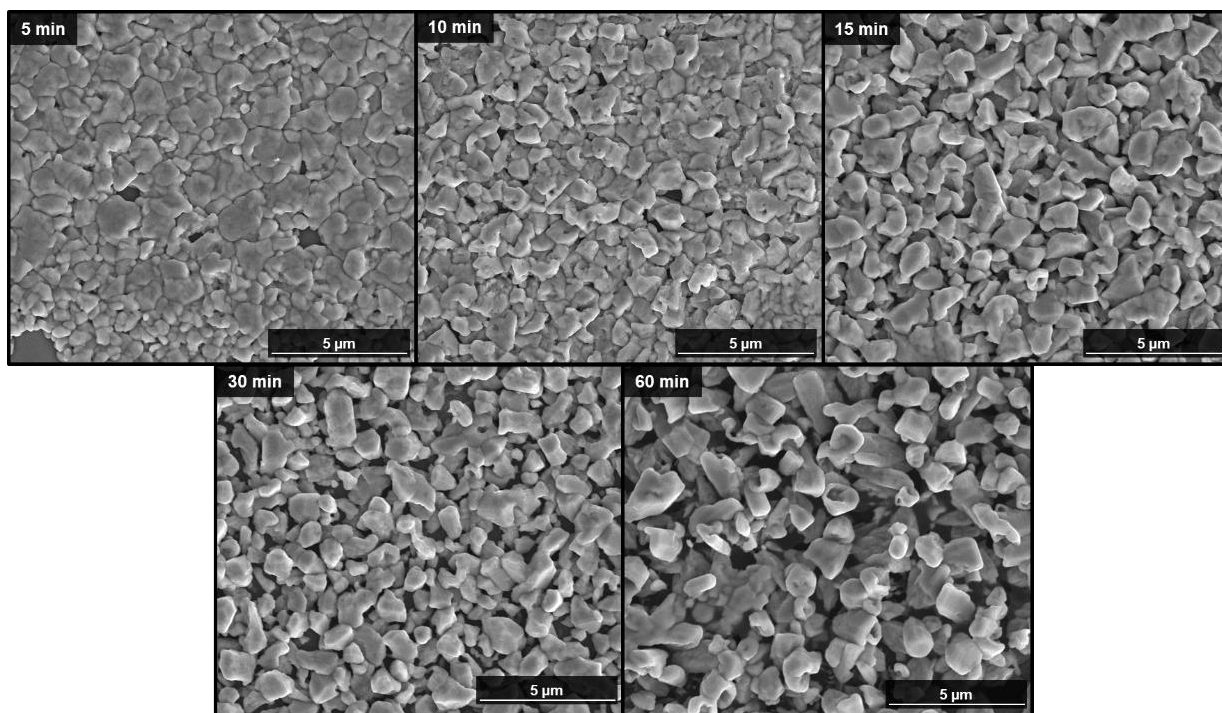


Figure 8.6. Plan-view SEM images of LUZ NP films heated with As_2S_2 at $400\text{ }^\circ\text{C}$ for 5, 10, 15, 30, and 60 min.

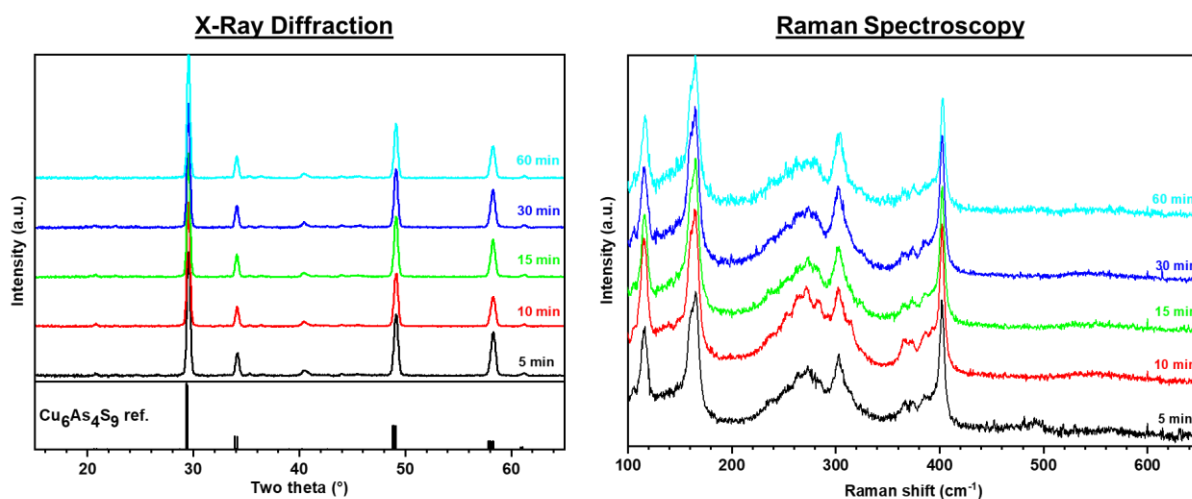


Figure 8.7. GIXRD and Raman spectra of LUZ NPs heat treated in As_2S_2 at $400\text{ }^\circ\text{C}$ for the indicated time. GIXRD spectra match with reference spectrum #236895 on the ICSD, and the Raman spectra match well with the spectrum depicted in Figure 8.2. The Cu/As ratios (as measured by XRF) were 1.33, 1.30, 1.29, 1.22, and 1.21 for the 5, 10, 15, 30, and 60 min treatments, respectively.

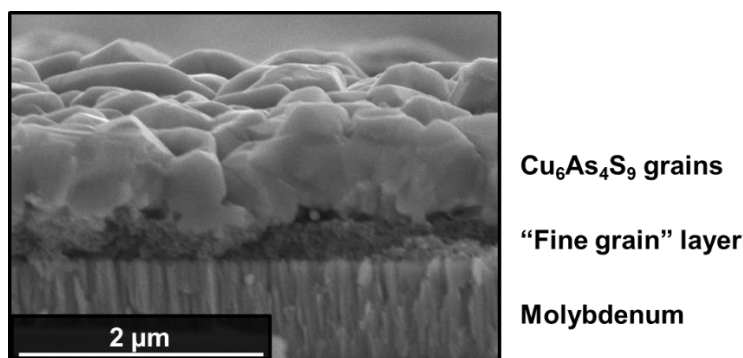


Figure 8.8. Cross-sectional SEM image of LUZ NPs heat treated in As₂S₂ for 10 min at 400 °C. The film demonstrates a bilayer morphology, with micron-thick grains on top of a thinner "fine-grain" layer.

Most of this thesis (Chapters 2-6 and 9) has focused on enargite Cu₃AsS₄ as an absorber for thin-film solar cells. The only difference between conditions that form SIN and ENG is the composition of the atmosphere that is supplied to thin films of LUZ NPs; specifically, the amount of sulfur is critical. To test for the possibility of interconversion between ENG and SIN, SIN films that were formed via LUZ treatment in As₂S₂ were sealed in a glass ampoule with sulfur and heated at 425 °C for 1 h. Figure 8.9 gives the XRD and Raman characterization data, indicating that the SIN film converted to ENG under the influence of a simple sulfur atmosphere. One interesting note is that the carbonaceous impurity peak near 490 cm⁻¹ is quite minimal when compared with that of a typical LUZ NP film heat treated in As₂S₅. A two-step heat treatment process may therefore be useful in mitigating the carbonaceous secondary phase, though it must be noted that one drawback is much more nonuniformity in the grain sizes and apparent film roughness (Figure 8.9).

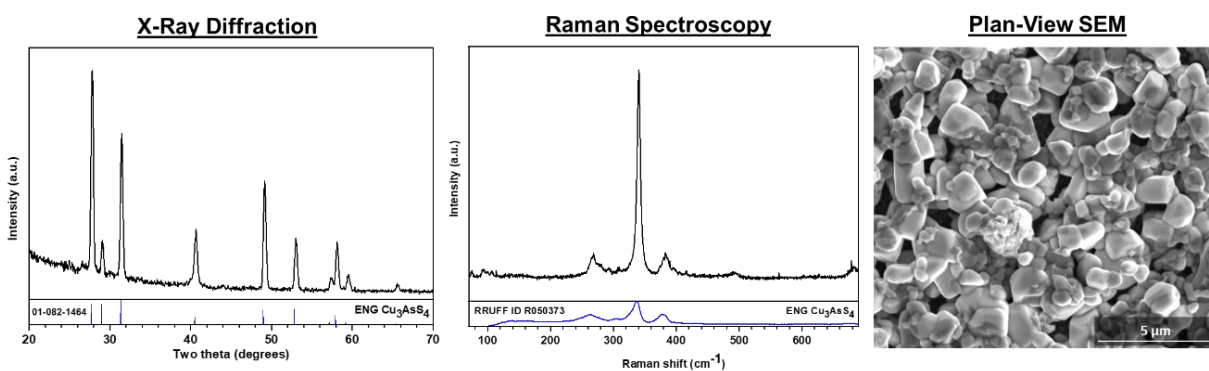


Figure 8.9. GIXRD spectrum, Raman spectrum, and plan-view SEM image of a SIN film heat treated in a sulfur-containing ampoule at 425 °C for 1 h.

The reverse process of what was just described was also studied, i.e. heat treating in sulfur and then in As_2S_2 . The XRD and Raman spectra (Figure 8.10) indicate conversion to ENG after the sulfur treatment as expected, followed by conversion to SIN after heat treatment in As_2S_2 . This further suggests that the ratio of the external supply of As and S determines the final phase, rather than any As and S already present in the film. The plan-view SEM images (Figure 8.10) display large island grains after heat treatment in sulfur, and some of these island grains are maintained even after subsequent treatment in As_2S_2 . This result suggests that the grain growth mechanisms by which a sulfur liquid and an As-S liquid operate are fundamentally different and may ultimately result in different grain structure and packing density. When using a material such as As_2S_5 , which can break into sulfur and As_2S_3 at high temperatures, during heat treatments, both grain growth mechanisms are likely present and must be controlled to produce films with appropriate grain density and size.

Critical optoelectronic properties of SIN films were measured to determine the material's relevance in semiconducting applications. To eliminate any effects resulting of carbonaceous residue, the carbonaceous oleylamine ligands were exchanged with an As_2S_3 -derived complex [29]–[31], and films were fabricated from these carbon-free NPs (Figure 8.11). One property of paramount importance for PV applications is the optical bandgap, which may be estimated using diffuse reflectance spectroscopy (Figure 8.12A). A clear decrease in the reflectance of SIN films around 1.1 eV is noted. To estimate the bandgap, the Kubelka-Munk function is used to transform the reflectance data [38], [39]. By extrapolating the function's square to the x-axis, a direct band gap of 1.16 eV is estimated. This value closely matches with a previous calculation and is within the ideal range for solar energy conversion (1-1.5 eV) [28].

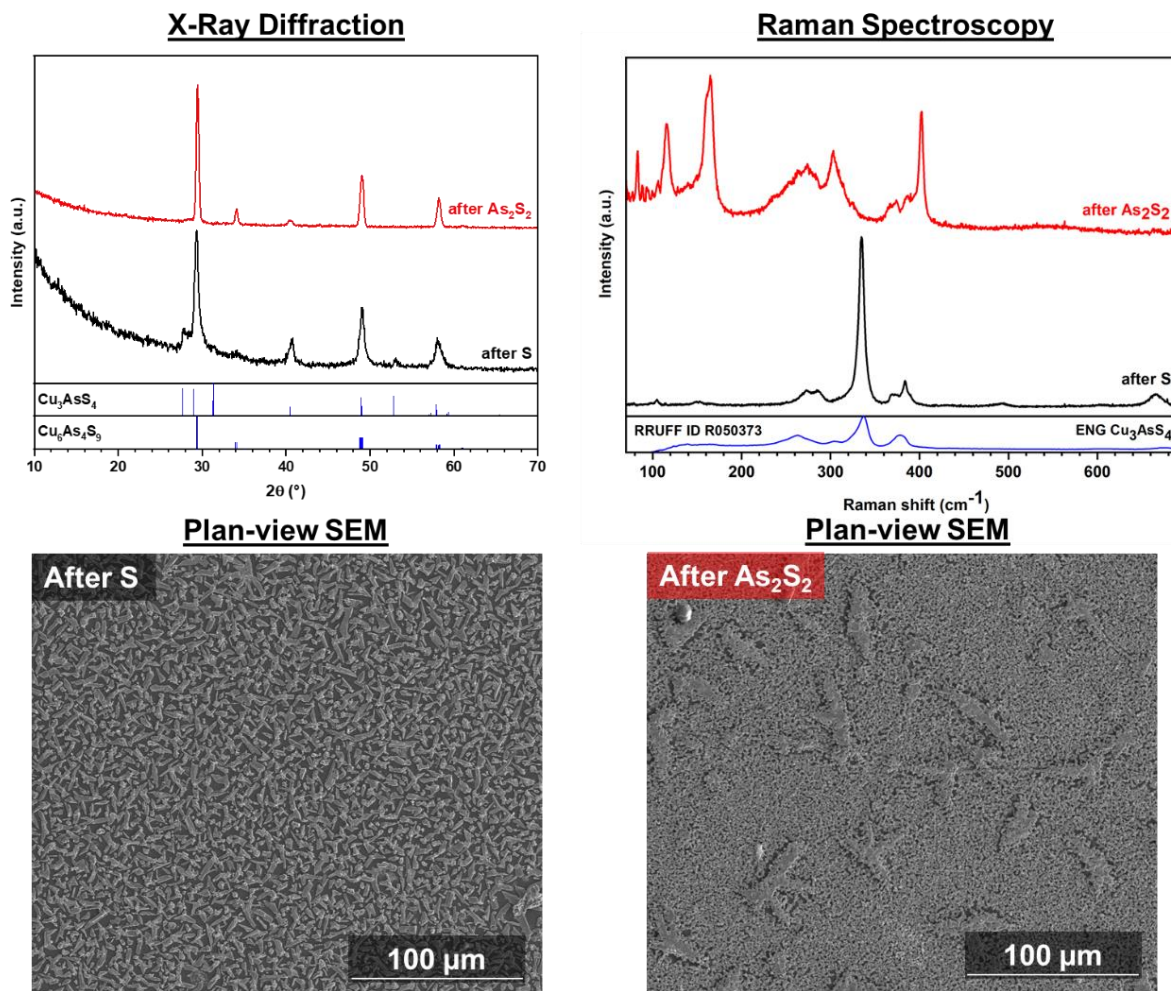


Figure 8.10. GIXRD spectrum, Raman spectrum, and plan-view SEM images of a LUZ NP film that was first heated in a sulfur-containing ampoule for 1 h at 425 °C, and then heated in an As_2S_2 -containing ampoule for 1 h at 425 °C.

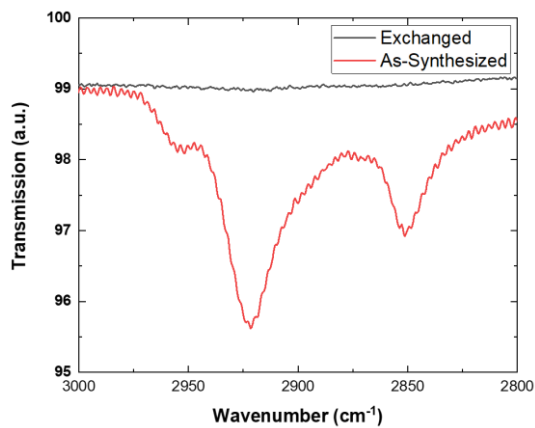


Figure 8.11. Fourier transform infrared spectroscopy (FTIR) spectra of as-synthesized LUZ NPs and ligand exchanged LUZ NPs. The removal of characteristic oleylamine C-H stretches demonstrates the effectiveness of the ligand exchange protocol.

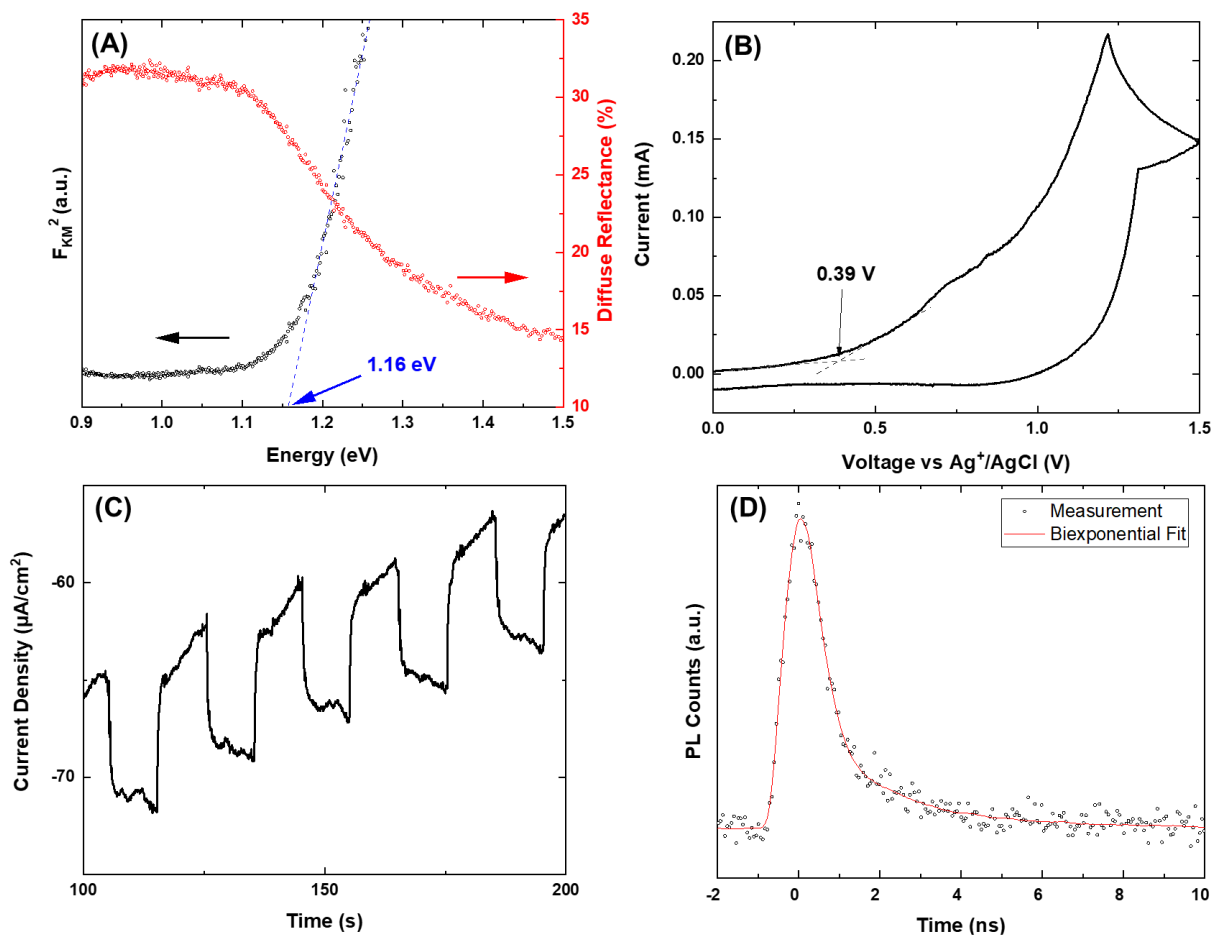


Figure 8.12. Optoelectronic characterization of sinnerite $\text{Cu}_6\text{As}_4\text{S}_9$ thin films. A) Diffuse reflectance spectroscopy data and Tauc plot of the Kubelka-Munk function. Linear extrapolation gives a direct band gap of 1.16 eV. B) Cyclic voltammetry in 0.1 M tetrabutylammonium hexafluorophosphate in acetonitrile electrolyte. The current onset occurs at 0.39 V vs Ag^+/AgCl . C) Photoelectrochemical current generation in aqueous EuCl_3 electrolyte under chopped AM1.5G illumination. D) Time-resolved photoluminescence decay and biexponential fit to the measured data.

For SIN-based device applications, the energy levels of the valence and conduction bands must be measured so that an appropriate pn junction partner can be found. Cyclic voltammetry (CV) was performed on a SIN film using 0.1 M tetrabutylammonium hexafluorophosphate in acetonitrile as the electrolyte (Figure 8.12B). The onset of current, corresponding to carrier injection to the valence band, occurs at approximately 0.39 V vs. Ag^+/AgCl . The onset of ferrocene, an internal standard with an absolute redox potential of -4.80 eV vs vacuum, occurred at 0.33 V vs. Ag^+/AgCl (Figure 8.13) [40]. The valence band edge of SIN, therefore, lies at approximately -4.86 eV vs vacuum. When combined with the measured 1.16 eV band gap, the conduction band

edge lies near -3.70 eV vs vacuum. These measurements are critical knowledge for integrating SIN into functional prototype devices.

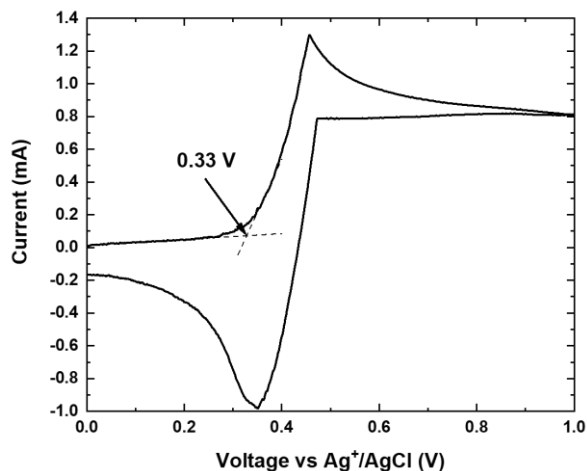


Figure 8.13. Cyclic voltammetry (scan rate = 50 mV/s) on ferrocene dissolved in 0.1 M tetrabutylammonium hexafluorophosphate/acetonitrile solution. The onset current occurs at 0.33 V vs. Ag⁺/AgCl.

The photoresponse of SIN thin films was measured in a three-electrode photoelectrochemical (PEC) cell under chopped simulated AM1.5G illumination in an aqueous EuCl₃ electrolyte. The stabilized current response of a SIN working electrode at a constant bias of -0.5 V vs. Ag⁺/AgCl is shown in Figure 8.12C. The steady generation of ~ 7 $\mu\text{A}/\text{cm}^2$ of cathodic photocurrent indicates that SIN is a p-type material that absorbs visible and near infrared light, justifying its further development for PV applications. The p-type nature of SIN was confirmed through hot-point probe and Hall effect measurements, the latter of which also revealed a carrier concentration of $(1.7 \pm 0.5) \times 10^{19} \text{ cm}^{-3}$ and a hole mobility of $0.26 \pm 0.09 \text{ cm}^2/\text{V}\cdot\text{s}$.

Figure 8.12D depicts the time-resolved photoluminescence (TRPL) decay of SIN films under pulsed laser illumination ($\lambda = 637 \text{ nm}$). The response is well fit by a biexponential function with time constants $\tau_1 = 334 \text{ ps}$ and $\tau_2 = 2.4 \text{ ns}$, suggesting that a fraction of the minority carriers have high lifetimes, which can lead to high minority carrier diffusion lengths and greater carrier collection within a solar cell. As improvements to the SIN processing conditions are made, the carrier lifetimes are expected to improve significantly.

8.4 Conclusions

We have fabricated the first crystalline sinnerite $\text{Cu}_6\text{As}_4\text{S}_9$ thin films through a heat treatment scheme that exploits equilibrium phase relations in the Cu-As-S system. The films are free of detectable secondary phases and possess micron-sized dense grains suitable for device applications. The films display a direct band gap of 1.16 eV, appreciable photocurrent generation under simulated sunlight, and minority carrier lifetimes exceeding 1 ns. The valence and conduction band edges were estimated to lie at -4.86 and -3.70 eV vs. vacuum, respectively. Future work in developing this promising material should focus on continued measurement of fundamental material properties, as well as finding an appropriate n-type layer to pair with SIN for a robust pn junction.

8.5 Acknowledgements

The authors acknowledge the National Science Foundation for funding under grant #1534691-DMR (Rapid Design of Earth Abundant Inorganic Materials for Future PVs). S.A.M. acknowledges Purdue University for a Bilsland Dissertation Fellowship. The authors thank Kyle Weideman, Yining Feng, and Professor Luna Lu for Hall effect measurements, Joseph Andler, Essam AlRuqobah, and Xianyi Hu for providing Mo and Cu films, Apurva Pradhan for helpful comments on the manuscript, and Alexei Lagoutchev for helpful discussions regarding the collection of reflectance data. The authors declare no competing financial interests.

8.6 Statement of Data Access

The data associated with this manuscript can be found at the project's website: <https://datacenterhub.org/groups/dmref1534691/>

8.7 References

- [1] M. A. Green *et al.*, “Solar cell efficiency tables (Version 53),” *Prog. Photovoltaics Res. Appl.*, vol. 27, no. 1, pp. 3–12, 2019.
- [2] C. Wadia, a. P. Alivisatos, and D. M. Kammen, “Materials Availability Expands the Opportunity for Large-Scale Photovoltaics Deployment,” *Environ. Sci. Technol.*, vol. 43, no. 6, pp. 2072–2077, Mar. 2009.

- [3] C. Candelise, M. Winkler, and R. Gross, "Implications for CdTe and CIGS technologies production costs of indium and tellurium scarcity," *Prog. Photovoltaics Res. Appl.*, vol. 20, no. 6, pp. 816–831, Sep. 2012.
- [4] W. Wang *et al.*, "Device Characteristics of CZTSSe Thin-Film Solar Cells with 12.6% Efficiency," *Adv. Energy Mater.*, vol. 4, no. 7, p. 1301465, May 2014.
- [5] C. K. Miskin *et al.*, "9.0% efficient $\text{Cu}_2\text{ZnSn}(\text{S},\text{Se})_4$ solar cells from selenized nanoparticle inks," *Prog. Photovoltaics Res. Appl.*, vol. 23, no. 5, pp. 654–659, May 2015.
- [6] S. Giraldo, Z. Jehl, M. Placidi, V. Izquierdo-Roca, A. Pérez-Rodríguez, and E. Saucedo, "Progress and Perspectives of Thin Film Kesterite Photovoltaic Technology: A Critical Review," *Adv. Mater.*, vol. 31, no. 16, p. 1806692, Apr. 2019.
- [7] E. J. Sheets, R. B. Balow, W.-C. Yang, E. A. Stach, and R. Agrawal, "Solution-based synthesis and purification of zinc tin phosphide nanowires," *Nanoscale*, vol. 7, no. 45, pp. 19317–19323, 2015.
- [8] S. Akari, J. Chantana, S. Nakatsuka, Y. Nose, and T. Minemoto, "ZnSnP₂ solar cell with (Cd,Zn)S buffer layer: Analysis of recombination rates," *Sol. Energy Mater. Sol. Cells*, vol. 174, no. June 2017, pp. 412–417, Jan. 2018.
- [9] Z. Li *et al.*, "9.2%-Efficient Core-Shell Structured Antimony Selenide Nanorod Array Solar Cells," *Nat. Commun.*, vol. 10, no. 1, p. 125, 2019.
- [10] W. A. Dunlap-Shohl, Y. Zhou, N. P. Padture, and D. B. Mitzi, "Synthetic Approaches for Halide Perovskite Thin Films," *Chem. Rev.*, vol. 119, no. 5, pp. 3193–3295, Mar. 2019.
- [11] T. Pauporté and D. Lincot, "Electrical, optical and photoelectrochemical properties of natural enargite, Cu_3AsS_4 ," *Adv. Mater. Opt. Electron.*, vol. 5, no. 6, pp. 289–298, Nov. 1995.
- [12] A. Das, A. Shamirian, and P. T. Snee, "Arsenic Silylamide: An Effective Precursor for Arsenide Semiconductor Nanocrystal Synthesis," *Chem. Mater.*, vol. 28, no. 11, pp. 4058–4064, Jun. 2016.
- [13] S. A. McClary, J. Andler, C. A. Handwerker, and R. Agrawal, "Solution-processed copper arsenic sulfide thin films for photovoltaic applications," *J. Mater. Chem. C*, vol. 5, no. 28, pp. 6913–6916, 2017.

- [14] S. K. Wallace *et al.*, “Candidate photoferroic absorber materials for thin-film solar cells from naturally occurring minerals: enargite, stephanite, and bournonite,” *Sustain. Energy Fuels*, vol. 1, no. 6, pp. 1339–1350, 2017.
- [15] S. K. Wallace, K. T. Butler, Y. Hinuma, and A. Walsh, “Finding a junction partner for candidate solar cell absorbers enargite and bournonite from electronic band and lattice matching,” *J. Appl. Phys.*, vol. 125, no. 5, p. 055703, Feb. 2019.
- [16] T. Shi, W.-J. Yin, M. Al-Jassim, and Y. Yan, “Structural, electronic, and optical properties of $\text{Cu}_3\text{-V-VI}_4$ compound semiconductors,” *Appl. Phys. Lett.*, vol. 103, no. 15, p. 152105, Oct. 2013.
- [17] R. B. Balow, E. J. Sheets, M. M. Abu-Omar, and R. Agrawal, “Synthesis and Characterization of Copper Arsenic Sulfide Nanocrystals from Earth Abundant Elements for Solar Energy Conversion,” *Chem. Mater.*, vol. 27, no. 7, pp. 2290–2293, Apr. 2015.
- [18] R. B. Balow, C. K. Miskin, M. M. Abu-Omar, and R. Agrawal, “Synthesis and Characterization of $\text{Cu}_3(\text{Sb}_{1-x}\text{As}_x)\text{S}_4$ Semiconducting Nanocrystal Alloys with Tunable Properties for Optoelectronic Device Applications,” *Chem. Mater.*, vol. 29, no. 2, pp. 573–578, Jan. 2017.
- [19] R. Zhang, K. Chen, B. Du, and M. J. Reece, “Screening for Cu–S based thermoelectric materials using crystal structure features,” *J. Mater. Chem. A*, vol. 5, no. 10, pp. 5013–5019, 2017.
- [20] S. A. McClary, R. B. Balow, and R. Agrawal, “Role of annealing atmosphere on the crystal structure and composition of tetrahedrite–tennantite alloy nanoparticles,” *J. Mater. Chem. C*, vol. 6, no. 39, pp. 10538–10546, 2018.
- [21] P. Levinsky, C. Candolfi, A. Dauscher, J. Tobola, J. Hejtmánek, and B. Lenoir, “Thermoelectric properties of the tetrahedrite–tennantite solid solutions $\text{Cu}_{12}\text{Sb}_{4-x}\text{As}_x\text{S}_{13}$ and $\text{Cu}_{10}\text{Co}_2\text{Sb}_{4-y}\text{As}_y\text{S}_{13}$ ($0 \leq x, y \leq 4$),” *Phys. Chem. Chem. Phys.*, 2019.
- [22] S. Maske and B. J. Skinner, “Studies of the sulfosalts of copper I. Phases and phase relations in the system Cu-As-S,” *Econ. Geol.*, vol. 66, no. 6, pp. 901–918, Oct. 1971.
- [23] E. Makovicky and B. J. Skinner, “Studies of the Sulfosalts of Copper II. The Crystallography and Composition of Sinnerite, $\text{Cu}_6\text{As}_4\text{S}_9$,” *Am. Mineral.*, vol. 57, pp. 824–834, 1972.

- [24] E. Makovicky and B. J. Skinner, "Studies of the sulfosalts of copper. IV. Structure and twinning of sinnerite, $\text{Cu}_6\text{As}_4\text{S}_9$," *Am. Mineral.*, vol. 60, pp. 998–1012, 1975.
- [25] J. Hautala and P. C. Taylor, "A review of optical properties of metal chalcogenide glasses," *J. Non. Cryst. Solids*, vol. 141, no. C, pp. 24–34, 1992.
- [26] B. Yan, S. Giralani, and P. C. Taylor, "Defect structure and conductivity in tetrahedrally coordinated metal chalcogenide amorphous semiconductors," *Phys. Rev. B*, vol. 56, no. 16, pp. 10249–10254, 1997.
- [27] L. Bindi, E. Makovicky, F. Nestola, and L. De Battisti, "Sinnerite, $\text{Cu}_6\text{As}_4\text{S}_9$, from the Lengenbach Quarry, Binn Valley, Switzerland: Description and Re-Investigation of the Crystal Structure," *Can. Mineral.*, vol. 51, no. 6, pp. 851–860, Dec. 2013.
- [28] L. Yu, R. S. Kokenyesi, D. A. Keszler, and A. Zunger, "Inverse Design of High Absorption Thin-Film Photovoltaic Materials," *Adv. Energy Mater.*, vol. 3, no. 1, pp. 43–48, Jan. 2013.
- [29] M. V. Kovalenko, M. I. Bodnarchuk, J. Zaumseil, J.-S. Lee, and D. V. Talapin, "Expanding the Chemical Versatility of Colloidal Nanocrystals Capped with Molecular Metal Chalcogenide Ligands," *J. Am. Chem. Soc.*, vol. 132, no. 29, pp. 10085–10092, Jul. 2010.
- [30] S. Yakunin *et al.*, "High infrared photoconductivity in films of arsenic-sulfide-encapsulated lead-sulfide nanocrystals," *ACS Nano*, vol. 8, no. 12, pp. 12883–12894, 2014.
- [31] M. V. Kovalenko, M. I. Bodnarchuk, and D. V. Talapin, "Nanocrystal Superlattices with Thermally Degradable Hybrid Inorganic–Organic Capping Ligands," *J. Am. Chem. Soc.*, vol. 132, no. 43, pp. 15124–15126, Nov. 2010.
- [32] Z. Xia *et al.*, "Generalized Water-Processed Metal Chalcogenide Complexes: Synthesis and Applications," *Chem. Mater.*, vol. 27, no. 23, pp. 8048–8057, Dec. 2015.
- [33] Q. Guo *et al.*, "Development of CuInSe_2 Nanocrystal and Nanoring Inks for Low-Cost Solar Cells," *Nano Lett.*, vol. 8, no. 9, pp. 2982–2987, 2008.
- [34] W. Wu *et al.*, "Studies of the fine-grain sub-layer in the printed CZTSSe photovoltaic devices," *J. Mater. Chem. C*, vol. 2, no. 19, p. 3777, 2014.
- [35] T. J. Huang, X. Yin, C. Tang, G. Qi, and H. Gong, "Influence of Ligands on the Formation of Kesterite Thin Films for Solar Cells: A Comparative Study," *ChemSusChem*, vol. 9, no. 9, pp. 1032–1041, May 2016.

- [36] C. J. Hages, M. J. Koeper, C. K. Miskin, K. W. Brew, and R. Agrawal, "Controlled Grain Growth for High Performance Nanoparticle-Based Kesterite Solar Cells," *Chem. Mater.*, vol. 28, no. 21, pp. 7703–7714, Nov. 2016.
- [37] S. McLeod, E. Alruqobah, and R. Agrawal, "Liquid assisted grain growth in solution processed Cu(In,Ga)(S,Se)₂," *Sol. Energy Mater. Sol. Cells*, vol. 195, no. February, pp. 12–23, 2019.
- [38] P. Kubelka and F. Munk, "Ein Beitrag zur Optik der Farbanstriche (Contribution to the optic of paint)," *Zeitschrift fur Tech. Phys.*, vol. 12, pp. 593–601, 1931.
- [39] V. Džimbeg-Malčić, Ž. Barbarić-Mikočević, and K. Itrić, "Kubelka-Munk Theory in Describing Optical Properties of Paper (I)," *Tech. Gaz.*, vol. 18, no. 1, pp. 117–124, 2011.
- [40] R. R. Gagne, C. A. Koval, and G. C. Lisensky, "Ferrocene as an Internal Standard for Electrochemical Measurements," *Inorg. Chem.*, vol. 19, no. 9, pp. 2854–2855, 1980.

9. MOLECULAR PRECURSOR ROUTES TO THIN FILMS OF COPPER ARSENIC SULFIDE

9.1 Introduction

The previous chapters in this thesis focused on nanoparticle-based (NP) routes to thin films of copper arsenic sulfides. While NPs generally allow for control over thin film packing densities and optoelectronic properties through shape and size tunability, they also have several disadvantages, especially the presence of bulky organic ligands that are often difficult to remove by thermal annealing. An alternative route is the molecular precursor approach, which involves forming homogeneous solutions of metal salts, metal chalcogenides, pure metals, etc., depositing these onto a substrate, baking away the solvent, and annealing the remaining materials to crystallize them into a functional thin film [1]–[3]. This approach avoids the use of long-chained carbonaceous species and may simplify processing by bypassing the NP synthesis and purification steps.

A variety of solvents (both organic and aqueous) have been successfully used in the molecular precursor approach, but one of the most versatile is the organic amine-thiol system, which has been applied to many materials including $\text{Cu}(\text{In,Ga})\text{Se}_2$ (CIGSe) [4]–[6], $\text{Cu}_2\text{ZnSn}(\text{S,Se})_4$ (CZTSSe) and its derivatives [7]–[9], CdTe [10], and CuSbS_2 [11]. The amine-thiol system can dissolve a large suite of metal salts and even pure metals because a proton is transferred from a thiol to an amine with relative ease, forming thiolate anions and alkylammonium cations that can coordinate with ions present in bulk salts or react to form soluble complexes with pure metals [12], [13]. Many reports have used the amine-thiol solvent system to dissolve copper and its salts, but reports on the dissolution of arsenic-based compounds are limited [12], [14], [15].

In this chapter, preliminary research on the fabrication of Cu-As-S films via molecular precursors is presented. The dissolution properties of Cu, As, and S compounds in amine-thiol mixtures is presented; a combination of 1-butylamine and ethanethiol is explored further due to the low boiling points of the two solvents and relative ease of removal through annealing. Low-temperature routes involving drop-casting of precursors onto a substrate in air and a glovebox are then presented; ternary Cu-As-S phases are formed, but stability and uniformity concerns necessitate the development of spin coating techniques and high-temperature annealing processes. The results presented here reveal a complex interplay between three different sulfur sources (solid

precursors, the liquid thiol, and the gaseous annealing atmosphere) that must be investigated in more detail. Preliminary thin film growth experiments indicate that a film consisting of micron-sized grains can be made, similar to what has already been demonstrated in the NP-based Cu-As-S system; one added benefit is that there is no evidence of a carbonaceous secondary phase. The work presented in this chapter represents a significant step towards the development of high-efficiency molecular-precursor based Cu-As-S thin film devices.

9.2 Experimental Methods

9.2.1 Materials

All chemicals were used as received from Sigma-Aldrich and stored in a nitrogen-filled glovebox unless otherwise noted. The liquids used were n-butylamine (BA, >99.5%), n-hexylamine (HA, >99%), oleylamine (OLA, 80-90%, Acros Organics), 1,2-ethylenediamine (EDA, >99.5%), ethanethiol (ET, >97%), 1-propanethiol (PT, >99%), 1-butanethiol (BT, >99%), and 1,2-ethanedithiol (EDT, >98%). The solids used were copper(I) chloride (CuCl, >99.99%, Strem Chemicals), copper(I) sulfide (Cu₂S), copper(II) sulfide (CuS), arsenic(III) sulfide (As₂S₃, Alfa Aesar), arsenic(V) sulfide (As₂S₅, Santa Cruz Biotechnology), and sulfur (S, >99.98% powder and >99.99% flakes). The gases used were argon (>99.997%, Indiana Oxygen) and hydrogen sulfide (H₂S, 0.97%, balance argon, Airgas).

9.2.2 Low-Temperature Baking

Precursor solutions were made by adding the desired amount of one powder (typically enough for a 0.1 M solution) to a 4 mL glass vial, then slowly pipetting in the desired amine, and finally pipetting the desired thiol in dropwise. For low-temperature baking, microscope slide glasses were cleaned with isopropanol and placed on a hot plate, which was preheated to the desired baking temperature (75 or 150 °C). In an empty 4 mL vial, individual precursor solutions were mixed together and then immediately drop cast onto the microscope glass slide and annealed for the desired amount of time. To make thicker films, a second layer was often drop cast after 5 min of annealing. For inert environment spin coating experiments, a 1" by 1" Mo-coated soda-lime glass substrate was cleaned and vacuumed onto the spin coater chuck. 350 μL of a precursor solution was dropped on the substrate, which was spun at 1500 rpm for 5 s and 2500 rpm for 25 s,

forming a uniform thin film. This film was then baked at 150 °C for 2 min and cooled before repeating to build up a film of the desired thickness.

9.2.3 High-Temperature Annealing

High-temperature anneals in various gases proceeded according to methods outlined in Chapters 2 and 7 of this thesis. Briefly, treatments in the argon and H₂S atmospheres (40 sccm) took place in a vertical three-zone tube furnace (see Chapter 7); the samples were held in place using a custom graphite sample holder and push-pull rod. Treatments in sulfur took place in a horizontal three-zone tube furnace (see Chapter 7) with a graphite box containing sulfur flakes at 200 °C, which produced sulfur vapor that effused through a small hole in the side of the box. The sulfur was carried by argon (10 sccm) to the samples in an uncovered graphite boat in another zone of the furnace. Treatments in As₂S₅ (see Chapter 2) took place in sealed glass ampoules with added As₂S₅ powder; they had been purged three times with argon on a Schlenk line and sealed under vacuum with a butane torch. In all cases, the furnace temperature equilibrated at the setpoint before inserting the samples, and the samples were cooled naturally to < 40 °C before exposing to the ambient atmosphere.

9.2.4 Characterization

X-ray diffraction (XRD) data were collected on a Rigaku Smartlab diffractometer in parallel beam geometry with a 0.5° incident angle and a copper K α X-ray source ($\lambda = 1.5406 \text{ \AA}$). Raman spectra were acquired using a 633 nm He:Ne laser coupled with a custom Horiba/Jobin-Yvon LabRAM HR800 confocal microscope system. Scanning electron microscopy (SEM) images were collected using an FEI Quanta 3D FEG dual-beam field emission SEM at a 7 kV accelerating voltage.

9.3 Results and Discussion

9.3.1 Precursor Solubility

Table 9.1 gives qualitative dissolution results at 0.1 M for a variety of Cu, As, and S precursors that were mixed with an amine-thiol solvent (9:1 v:v amine:thiol), vortexed, and stirred overnight at a temperature of 85 °C. Note that some solids dissolved upon vortexing (before heat was applied), and others partially dissolved or reacted with the solvent and may undergo further

dissolution at higher temperatures or over longer periods of time. The experiments here are not an exhaustive study of the solubility of Cu, As, and S precursors in the amine-thiol system but are rather an exploratory study of the most readily available materials.

Table 9.1. Qualitative solubility results for Cu, As, and S precursors in amine-thiol mixtures (9:1 v:v amine:thiol). A green box indicates complete solubility at 0.1 M, a yellow box indicates either partial solubility or a color change in the solvent, a red box indicates no dissolution and no interaction with the solvent, and a black box indicates that the combination was not tested.

Amine	Thiol	CuS	Cu ₂ S	CuCl	As ₂ S ₃	As ₂ S ₅	S
OLA	EDT	Yellow	Yellow	Green	Yellow	Green	Green
HA	EDT	Yellow	Yellow	Green	Yellow	Green	Green
BA	EDT	Yellow	Yellow	Green	Yellow	Green	Green
EDA	HT	Red	Red	Green	Red	Green	Green
EDA	PT	Red	Red	Green	Red	Green	Green
HA	ET	Red	Red	Green	Yellow	Green	Green
BA	ET	Red	Red	Green	Yellow	Green	Green
HA	PT	Black	Black	Green	Black	Green	Green
BA	None	Black	Black	Green	Green	Green	Green
BA	BT	Black	Black	Green	Black	Green	Green

In addition to those combinations listed in the table, several other precursors were tested in one solvent mixture: arsenic(III) chloride, thiourea, copper(II) acetate, and copper(II) nitrate dissolve in a 9:1 v:v BA:ET solvent, and copper(I) oxide and arsenic(V) oxide dissolve in a 9:1 v:v HA:PT solvent. Arsenic(III) chloride was particularly reactive and required cooling with dry ice to slow reaction kinetics.

The dissolution experiments show that CuCl, As₂S₅, and S are soluble in many amine-thiol combinations. To facilitate facile removal of the solvents during film fabrication, the combination of BA (b.p. 77 °C) and ET (35 °C) was chosen as the model system for future experiments. Note that this combination avoids the use of toxic and malodorous 1,2-ethanedithiol, which is typically required for the dissolution of copper chalcogenides (as opposed to a mono-thiol) [6], [8]. Also note that the difficulty in dissolving As₂S₃ was unexpected, as its dissolution in amine-thiol mixtures (and even just amines) has been reported previously [12], [16]. The As₂S₃ used here was in the form of fused pieces with diameters up to 1 mm; by grinding them into a fine powder, it is likely that the dissolution will proceed as expected.

The stability of combined BA/ET precursor solutions (i.e. mixtures of CuCl, As₂S₅, and S) is poor; precipitation of a dark brown or black solid occurred in as little as five minutes at 0.1 M.

As a result, before each drop casting or spin coating step, a fresh combined precursor solution was made in a separate vial. When multiple layers were cast on one substrate, the layers that were already present did not dissolve, suggesting that ternary Cu-As-S phases are insoluble in BA/ET. Combined precursor solutions were stabilized for longer periods of time by adding small amounts of EDT (1:1 Cu:EDT molar ratio), but removal of EDT from the film at 150 °C was difficult. Combined As_2S_5 and S solutions appear to be stable and may be mixed in whatever ratio is desired.

9.3.2 Low-Temperature Baking

Air synthesis is attractive for the fabrication of thin-film electronics because it does not require expensive high-vacuum or inert environment processing. To probe the processability of Cu_3AsS_4 films in air, CuCl, As_2S_5 , and S precursors were mixed in various ratios and drop cast on glass microscope slides preheated to temperatures exceeding the boiling points of BA and ET. The films were annealed to remove the solvent, leaving behind solid species that reacted to form various compounds. Figure 9.1 gives the XRD and Raman spectra of a solution with atomic ratios of 2.6:1:6 (Cu:As:S, a copper-poor and sulfur-rich solution) that was annealed at 150 °C for 3 h in air. The XRD and Raman spectra match well with reference spectra for tetragonal luzonite (LUZ) Cu_3AsS_4 , with slight shifts from the Raman standard attributed to the presence of antimony in the reference spectrum RRUFF ID R060390. The XRD peaks are slightly broadened, indicating the presence of nanocrystalline domains. No secondary phases are noted, likely due in part to the use of a Cu-poor composition that suppresses the formation of binary copper sulfide phases [17].

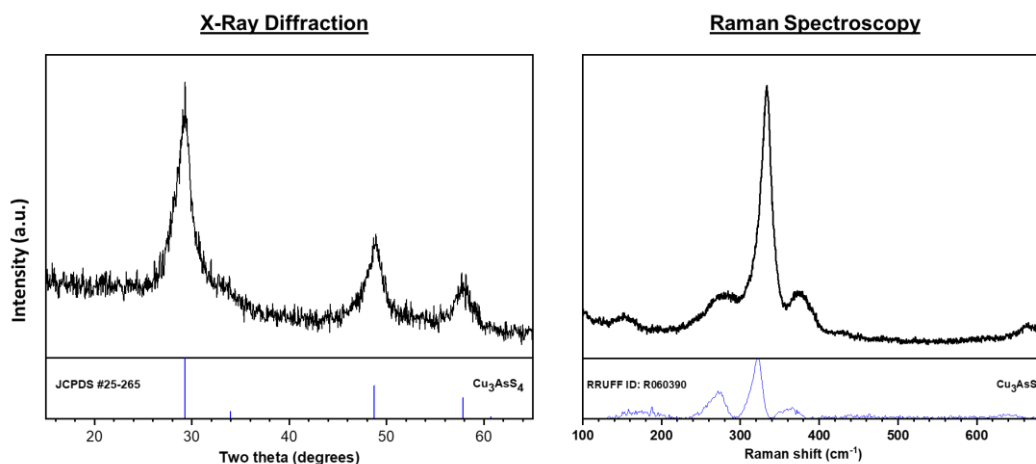


Figure 9.1. XRD and Raman spectra of a 0.1 M solution of CuCl, As_2S_5 , and S (2.6:1:6 Cu:As:S ratio) drop cast on a microscope glass slide and annealed for 3 h at 150 °C in air.

While the formation of phase-pure LUZ in air has been demonstrated, it must be stressed that there were many uncontrolled variables in the experimental setup, especially the moisture content and rate of air flow in the fume hood. When the above experiment (and others) was repeated several months later, XRD suggested the formation of some orthorhombic enargite (ENG) in addition to LUZ. Furthermore, the stability of air-processed molecular precursor films is not high, as explored further in Chapter 10. Therefore, more control over the annealing environment was required, and similar experiments were performed in a nitrogen-filled glovebox. Figure 9.2 gives the Raman spectrum of a copper-poor film annealed in the glovebox at 150 °C. The resulting film is a mixture of LUZ and TEN, suggesting that ambient conditions (i.e. an oxidizing atmosphere) suppress the reduction of arsenic from +5 to +3. Such behavior was already observed in the TET-TEN NP system (Chapter 7).

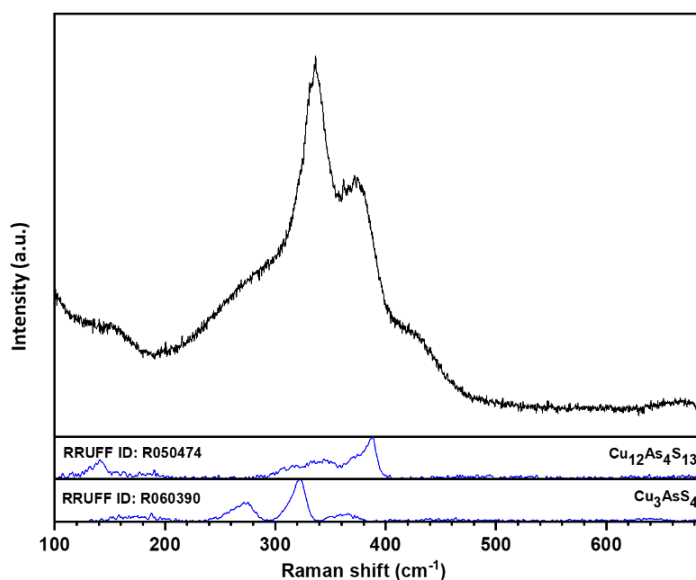


Figure 9.2. Raman spectrum of a 0.1 M solution of CuCl, As₂S₅, and S (2.6:1:4 Cu:As:S ratio) drop cast on a microscope glass slide and annealed for 2 h at 150 °C in a nitrogen-filled glovebox.

150 °C glovebox anneals did not result in a crystalline film; an increase to 200 °C was required. Figure 9.3 gives the XRD and Raman spectra of copper-poor films whose precursor solutions contained stoichiometric or 50% excess sulfur. The stoichiometric films fully converted to TEN. Films with excess sulfur formed crystalline ENG, though the Raman spectra still contains TEN peaks, suggesting its presence closer to the top surface of the film. These results reveal that

the low-temperature annealing environment is not the only factor that controls the final phase of the film; the amount of added sulfur is also relevant. Additional sulfur may very well result in reproducible phase-pure ENG films.

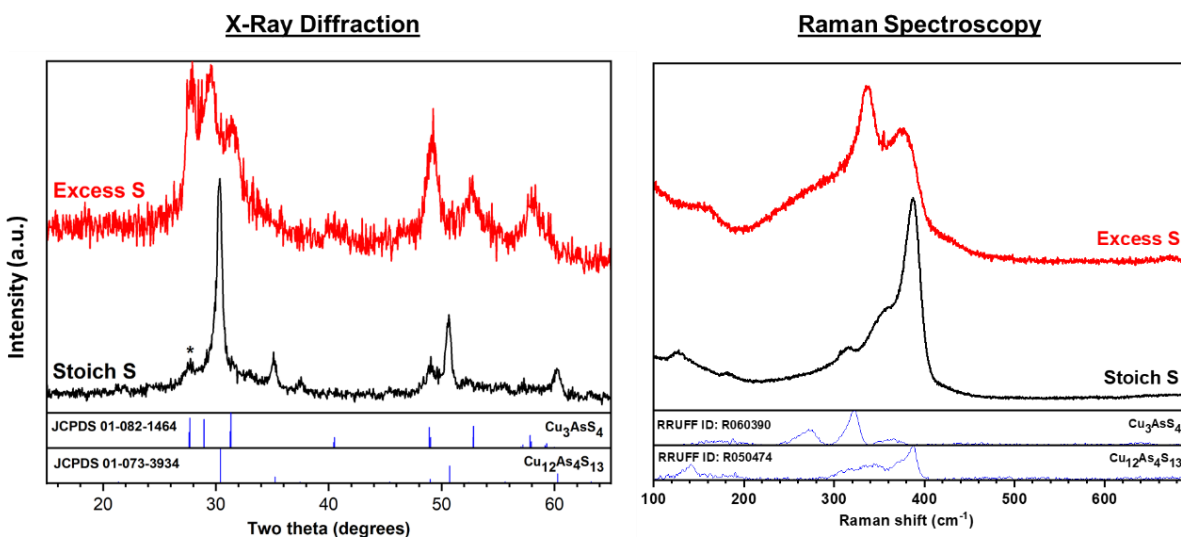


Figure 9.3. XRD and Raman spectra of a 0.1 M solution of CuCl, As₂S₅, and S (2.8:1:4 and 2.8:1:6 Cu:As:S ratios) drop cast on a microscope glass slide and annealed for 2 h at 150 °C in a nitrogen-filled glovebox. The (*) peak is attributed to incomplete filtering of tungsten L α radiation from the X-ray source.

9.3.3 High-Temperature Annealing

The drop casting and low-temperature baking procedure described in the previous section did not result in films with large crystalline grains, as evidenced by relatively broad XRD peaks. After deposition of molecular precursors and baking off the solvent, films are typically annealed at higher temperatures to promote crystallization and grain growth of the desired phase. Here, three annealing atmospheres (argon, H₂S, and dilute elemental sulfur) were explored after baking off the BA/ET solvent at low temperatures. Additionally, Table 9.1 indicates that BA alone is sufficient to dissolve CuCl, As₂S₅, and S, which allowed for exploration of the role of each sulfur source on the growth of Cu-As-S films.

Figure 9.4 gives the XRD and Raman spectra of CuCl/As₂S₅ precursor films (2.8:1 ratio; no elemental sulfur was added) that were annealed in an argon atmosphere for 1 h at the given temperature. In the films fabricated using only BA as the solvent, a mixture of either LUZ or ENG and TEN formed at 150 °C, and phase-pure TEN formed at 300 °C. This indicates that the sulfur

contained in As_2S_5 is sufficient to form ternary Cu-As-S phases. When thiol is added to the annealing mixture, however, it is not a spectator in the reaction. The decomposition to TEN is suppressed at 150 °C, suggesting that the thiol slows the transition from LUZ to TEN. However, the suppression is not uniform throughout the film, as some spots display a Raman spectrum (not shown) consisting of both LUZ and TEN. At 300 °C, a copper sulfide impurity phase (Cu_{2-x}S) forms, suggesting that ET may be forming some sort of complex with Cu and/or As that impacts reaction and decomposition kinetics; complexation of copper with thiols has been observed previously [13].

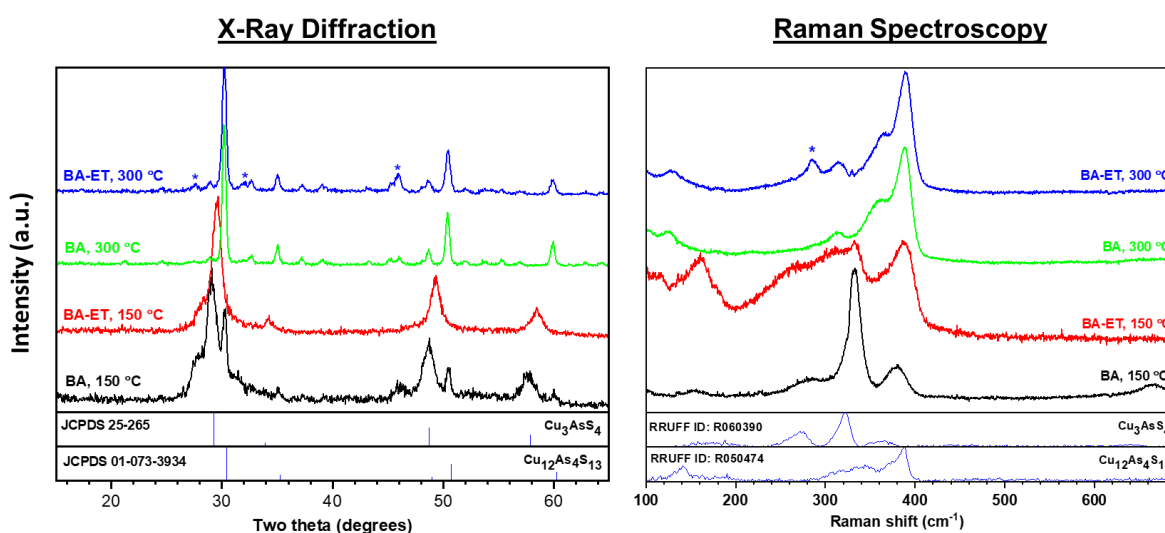


Figure 9.4. XRD and Raman spectra of Cu-As-S molecular precursor films baked in a glovebox at 75 °C and then annealed in an argon atmosphere for 1 h at the given temperature. A (*) indicates a peak attributable to copper sulfide Cu_{2-x}S .

Figure 9.5 gives the XRD and Raman spectra of molecular precursor films annealed in a dilute sulfur (balance argon) atmosphere for 1 h at the given temperatures. When there is no thiol present at 175 °C, the film partially decomposes into covellite CuS , suggesting that the gaseous sulfur preferentially reacts with copper over arsenic at low temperatures. At 400 °C, however, no secondary phases are observed, and the LUZ phase has only slightly converted to ENG, as indicated by a small shoulder on the (112) peak seen in the XRD. In contrast, when ET is present in the initial precursor solution, sulfurization results in significant conversion to the orthorhombic ENG phase. Taken together, these results suggest that the thiol plays a key role in determining the selectivity between the LUZ and the ENG phases. The use of thiols to control the crystal structure

of CZTS nanoparticles has been reported previously [18]; further work here is needed to fully elucidate the mechanism behind the selectivity between Cu-As-S phases.

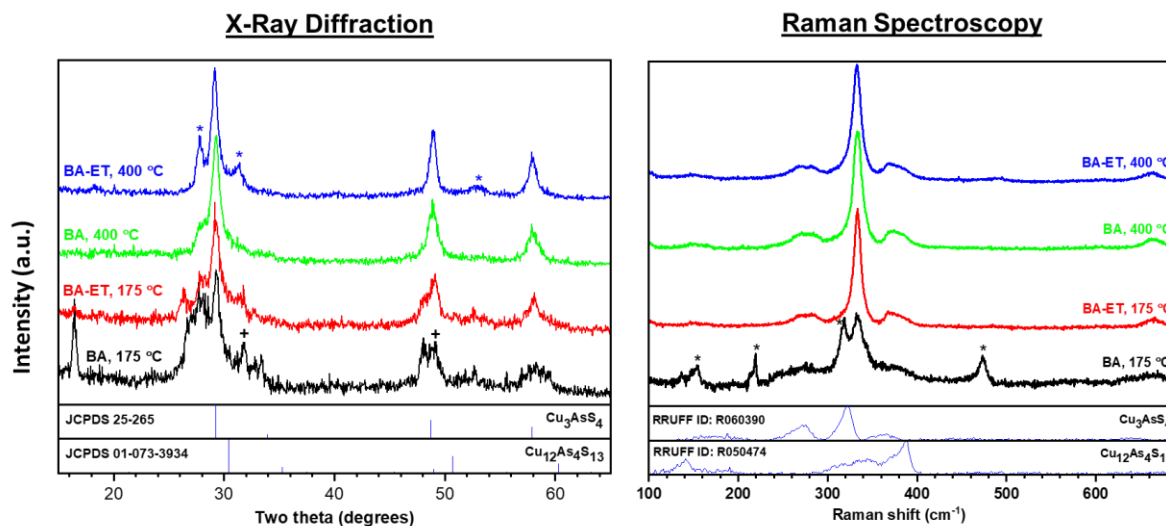


Figure 9.5. XRD and Raman spectra of Cu-As-S molecular precursor films baked in a glovebox at 75 °C and then annealed in an elemental sulfur/argon atmosphere for 1 h at the given temperature. In the XRD spectra, the (+) symbols are attributed to covellite CuS and the (*) to enargite Cu_3AsS_4 . In the Raman spectra, the (*) are attributed to covellite CuS or potential contamination from Cu-Sb-S films that were heat treated concurrently with the Cu-As-S films.

Figure 9.6 gives the XRD and Raman spectra of Cu-As-S molecular precursor films treated in a 1% H_2S (balance argon) atmosphere for 1 h at the indicated temperature. Except for the BA only film heated at 150 °C, conversion to TEN occurred, which was expected due to the reducing nature of the H_2S atmosphere as discussed in Chapter 7. At 150 °C, a Cu_2S impurity phase is noted without the presence of thiol, further demonstrating the reducing nature of the H_2S atmosphere. Interestingly, the tetragonal LUZ structure is maintained without a protective thiol at 150 °C, and the conversion to TEN is not complete even at 300 °C – a small LUZ peak is evident in the Raman spectrum. Further experiments are required to fully determine how the interplay between the nature of the gaseous sulfur source and the presence of a thiol affects the final Cu-As-S phase that is formed.

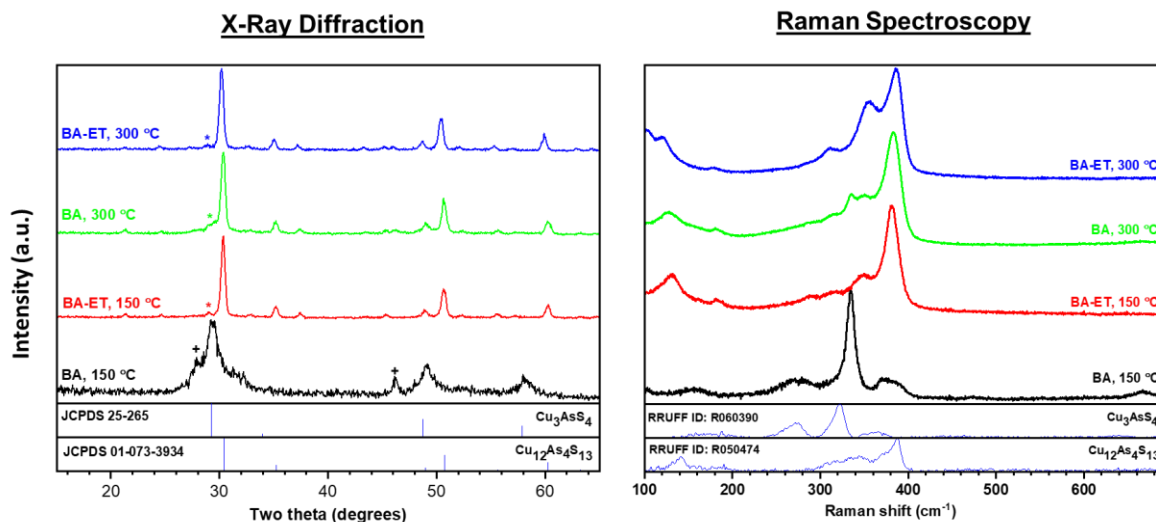


Figure 9.6. XRD and Raman spectra of Cu-As-S molecular precursor films baked in a glovebox at 75 °C and then annealed in 1% H₂S (balance argon) at the given temperature for 1 h. The (+) peak signifies a Cu₂S phase, and the (*) represent incomplete filtering of the tungsten L α peak from the X-ray source.

The experiments just outlined involved drop casting precursors on glass slides and annealing for several hours before high temperature treatments. This setup yields relatively thick films with significant nonuniformities. To fabricate more uniform films and engineer grain growth in Cu-As-S molecular precursor films, a thin precursor film was built up via spin coating on molybdenum-coated soda-lime glass. When this film was heat treated in sulfur at 400 °C for 1 h, Cu₃AsS₄ was formed as expected, but significant grain growth did not occur (Figure 9.7). Similar to what was observed with NP films (Chapters 2 and 3), an elemental sulfur atmosphere does not appear yield thin films with micron-sized dense grains.

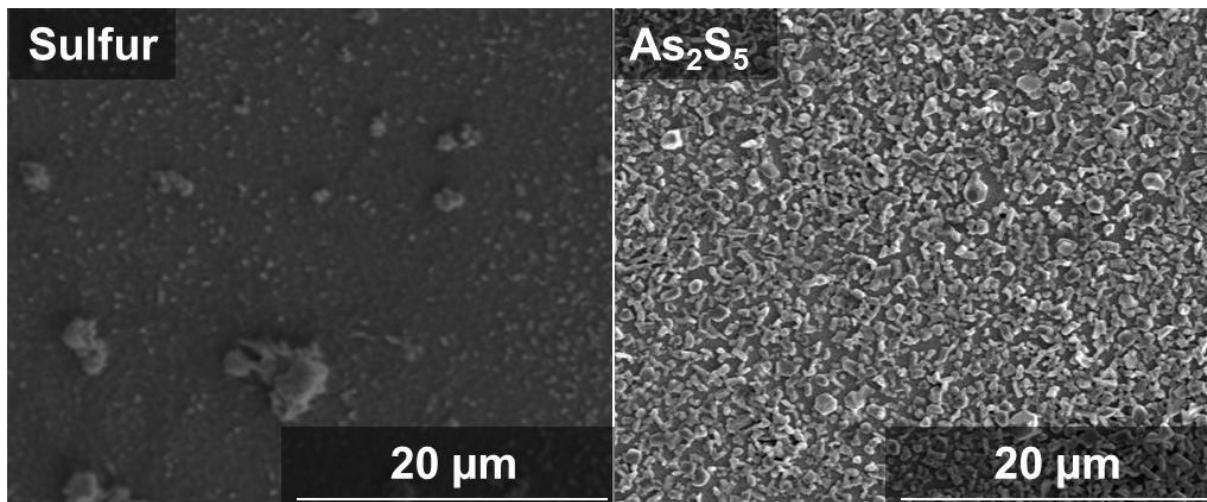


Figure 9.7. Plan-view SEM images of Cu-As-S molecular precursor films that were spin coated in a glovebox and then heated in a flowing S atmosphere at 400 °C or an As_2S_5 -filled ampoule at 425 °C for 1 h.

In Chapter 2, I outlined a method by which thin films of ENG can be grown by treating LUZ NPs in an As_2S_5 atmosphere. Figure 9.7 gives the plan view SEM image of a spin coated molecular precursor film annealed in As_2S_5 for 1 h at 425 °C. In contrast to the sulfur atmosphere treatments, numerous micron-sized grains were formed, though there is significant void space when compared with a typical film grown from NP precursors. The void space may be due to the thin initial films and should decrease as the initial film is thickened and as nucleation and kinetics are further developed for this system. Figure 9.8 gives the XRD and Raman spectra of the As_2S_5 -treated film. The XRD shows phase-pure ENG with significant orientation along the (002) plane, and the Raman spectrum confirms the phase purity of the material. In contrast to standard NP-based treatments, there is no peak around 490 cm^{-1} , indicating that the amines and thiols escape the film with relative ease, avoiding the formation of C-S secondary phases that impede Cu-As-S device performance.

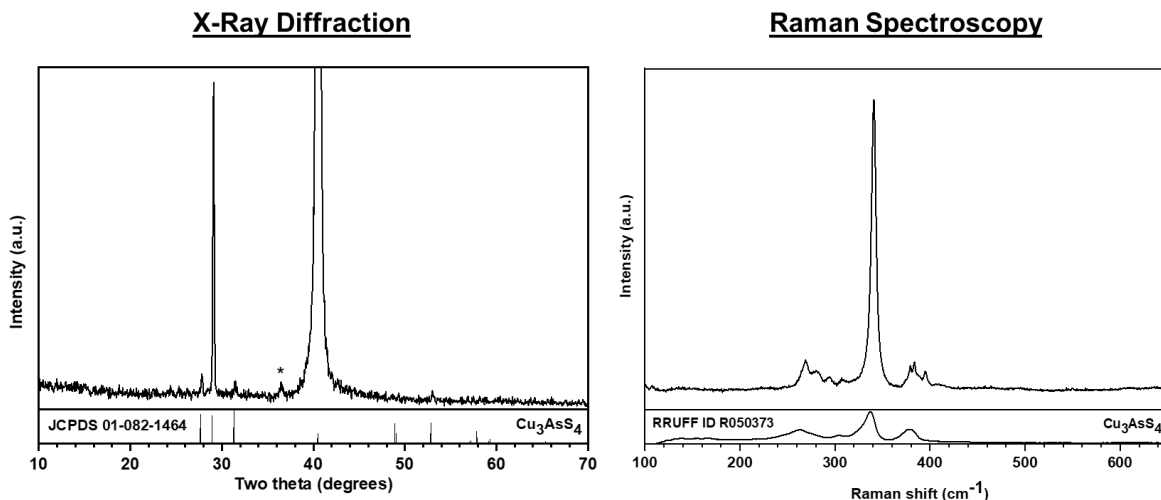


Figure 9.8. XRD and Raman spectra of a spin coated Cu-As-S molecular precursor film that was baked in the glovebox at 75 °C and heat treated in a sealed ampoule with As₂S₅ for 1 h at 425 °C. The (*) peak is attributed to incomplete filtering of the copper K β peak from the X-ray source.

9.4 Conclusions

Preliminary investigations of molecular precursor routes to thin films of copper arsenic sulfide have been presented. The amine-thiol solvent system, which has been applied to other material systems such as CIGSe and CZTSSe, was adapted to the Cu-As-S system because appropriate precursors such as CuCl and As₂S₅ can dissolve. Ternary phases were formed in air at temperatures as low as 150 °C, though the stability and reproducibility of such films were poor. By heating precursor films to higher temperatures in oxidizing and reducing atmospheres, the final phase (LUZ/ENG vs TEN) was controlled, though appropriate grain growth occurred only when films were heat treated in As₂S₅ (as has been investigated thoroughly in the NP Cu-As-S system). Future work on Cu-As-S molecular precursors must focus on the complexes formed upon precursor dissolution and the subsequent chemistry that they undergo, as the final material formed appears to depend on all three sources of sulfur present in the system. The experiments presented here demonstrate promise for forming thin films of copper arsenic sulfides that are free from carbonaceous residues, and they may ultimately be paired with an appropriate n-type material in a high-efficiency thin-film solar cell.

9.5 Acknowledgements

S.A.M. acknowledges support from the NSF Solar Economy IGERT program (0903670-DGE), the NSF DMREF program (DMR-1534691), Purdue University's Faculty Fellowship, and Purdue University's Bilslund Dissertation Fellowship. He thanks Dr. Robert Balow for helpful discussions and guidance and Louie Schroeder for insights gained through his parallel work on the aqueous Cu-As-S molecular precursor system. The author declares no competing financial interests.

9.6 References

- [1] W. Wang *et al.*, "Device Characteristics of CZTSSe Thin-Film Solar Cells with 12.6% Efficiency," *Adv. Energy Mater.*, vol. 4, no. 7, p. 1301465, May 2014.
- [2] Q. Tian, L. Huang, W. Zhao, Y. Yang, G. Wang, and D. Pan, "Metal sulfide precursor aqueous solutions for fabrication of $\text{Cu}_2\text{ZnSn}(\text{S},\text{Se})_4$ thin film solar cells," *Green Chem.*, vol. 17, no. 2, pp. 1269–1275, 2015.
- [3] C. L. McCarthy and R. L. Brutchey, "Solution Processing of Chalcogenide Materials Using Thiol-Amine 'Alkahest' Solvent Systems," *Chem. Commun.*, 2017.
- [4] D. Zhao *et al.*, "Solution-deposited pure selenide CIGSe solar cells from elemental Cu, In, Ga, and Se," *J. Mater. Chem. A*, vol. 3, no. 38, pp. 19263–19267, 2015.
- [5] D. Zhao *et al.*, "Eliminating fine-grained layers in $\text{Cu}(\text{In},\text{Ga})(\text{S},\text{Se})_2$ thin films for solution-processed high efficiency solar cells," *J. Mater. Chem. A*, vol. 4, no. 35, pp. 13476–13481, 2016.
- [6] X. Zhao, M. Lu, M. J. Koeper, and R. Agrawal, "Solution-processed sulfur depleted $\text{Cu}(\text{In},\text{Ga})\text{Se}_2$ solar cells synthesized from a monoamine–dithiol solvent mixture," *J. Mater. Chem. A*, vol. 4, no. 19, pp. 7390–7397, 2016.
- [7] R. Zhang, S. M. Szczepaniak, N. J. Carter, C. A. Handwerker, and R. Agrawal, "A Versatile Solution Route to Efficient $\text{Cu}_2\text{ZnSn}(\text{S},\text{Se})_4$ Thin-Film Solar Cells," *Chem. Mater.*, vol. 27, no. 6, pp. 2114–2120, Mar. 2015.
- [8] R. Zhang *et al.*, "Metal-metal chalcogenide molecular precursors to binary, ternary, and quaternary metal chalcogenide thin films for electronic devices," *Chem. Commun.*, vol. 52, no. 28, pp. 5007–5010, 2016.

- [9] C. L. McCarthy and R. L. Brutchey, "Solution Deposited $\text{Cu}_2\text{BaSnS}_{4-x}\text{Se}_x$ from a Thiol–Amine Solvent Mixture," *Chem. Mater.*, vol. 30, no. 2, pp. 304–308, Jan. 2018.
- [10] C. K. Miskin, A. Dubois-Camacho, M. O. Reese, and R. Agrawal, "A direct solution deposition approach to CdTe thin films," *J. Mater. Chem. C*, vol. 4, no. 39, pp. 9167–9171, 2016.
- [11] C. L. McCarthy, P. Cottingham, K. Abuyen, E. C. Schueller, S. P. Culver, and R. L. Brutchey, "Earth abundant CuSbS_2 thin films solution processed from thiol–amine mixtures," *J. Mater. Chem. C*, vol. 4, no. 26, pp. 6230–6233, 2016.
- [12] D. H. Webber and R. L. Brutchey, "Alkahest for V_2VI_3 Chalcogenides: Dissolution of Nine Bulk Semiconductors in a Diamine-Dithiol Solvent Mixture," *J. Am. Chem. Soc.*, vol. 135, no. 42, pp. 15722–15725, Oct. 2013.
- [13] P. Murria *et al.*, "Speciation of CuCl and CuCl_2 Thiol-Amine Solutions and Characterization of Resulting Films: Implications for Semiconductor Device Fabrication," *Inorg. Chem.*, vol. 56, no. 23, pp. 14396–14407, Dec. 2017.
- [14] Z. Xia *et al.*, "Generalized Water-Processed Metal Chalcogenide Complexes: Synthesis and Applications," *Chem. Mater.*, vol. 27, no. 23, pp. 8048–8057, 2015.
- [15] C. L. McCarthy, D. H. Webber, E. C. Schueller, and R. L. Brutchey, "Solution-Phase Conversion of Bulk Metal Oxides to Metal Chalcogenides Using a Simple Thiol-Amine Solvent Mixture," *Angew. Chemie - Int. Ed.*, vol. 54, no. 29, pp. 8378–8381, 2015.
- [16] J. Hautala, B. Moosman, and P. C. Taylor, "Potential p-type doping in amorphous chalcogenide films," *J. Non. Cryst. Solids*, vol. 137–138, pp. 1043–1046, Jan. 1991.
- [17] R. B. Balow, E. J. Sheets, M. M. Abu-Omar, and R. Agrawal, "Synthesis and Characterization of Copper Arsenic Sulfide Nanocrystals from Earth Abundant Elements for Solar Energy Conversion," *Chem. Mater.*, vol. 27, no. 7, pp. 2290–2293, Apr. 2015.
- [18] W.-C. Yang *et al.*, "Kesterite $\text{Cu}_2\text{ZnSn}(\text{S},\text{Se})_4$ Absorbers Converted from Metastable, Wurtzite-Derived $\text{Cu}_2\text{ZnSnS}_4$ Nanoparticles," *Chem. Mater.*, vol. 26, no. 11, pp. 3530–3534, Jun. 2014.

10. MOLECULAR PRECURSOR ROUTES TO THIN FILMS OF COPPER ANTIMONY SULFIDE

10.1 Introduction

The previous chapters in this thesis have focused primarily on copper arsenic sulfides, with only a small amount of attention paid to antimony. While the Cu-As-S system has advantages over established semiconducting materials due to its differing cationic radii and constituent earth abundant elements, it has not been explored thoroughly due to the toxicity of arsenic. Researchers have focused more on the family of copper antimony sulfides due to antimony's low toxicity and high earth abundance.

The Cu-Sb-S system has four ternary phases: tetragonal famatinite (FAM, Cu_3SbS_4), cubic tetrahedrite (TET, $\text{Cu}_{12}\text{Sb}_4\text{S}_{13}$), monoclinic skinnerite (SKI, Cu_3SbS_3), and orthorhombic chalcostibite (CHA, CuSbS_2) [1]. Most reports have focused on the synthesis and characterization of CHA nanoparticles (NPs) and thin films, though all four phases have properties that make them attractive for semiconducting applications such as photovoltaics and thermoelectrics. Yu et al. used density functional theory (DFT) to determine the optoelectronic properties of FAM, CHA, and SKI and determined that the first two have spectroscopic limited maximum efficiencies (SLME) comparable to or exceeding that of CuInSe_2 [2]. The structural, vibrational, and optoelectronic properties of TET have been thoroughly studied, revealing ultralow lattice thermal conductivities for thermoelectric applications and solar cell efficiencies potentially exceeding 20% [3]–[6]. The impacts of doping on the efficiency of SKI-based solar cells has also been investigated computationally [7].

Synthetic work in the Cu-Sb-S system has encompassed both solution- and vacuum-based processes; selected publications are highlighted here. Because there are four stable Cu-Sb-S phases, three with the same nominal Cu:Sb ratio (3:1), the selectivity between the four phases has been a key research topic. For solution-processed nanoparticles (NPs), the selectivity is governed by the specific form of sulfur in the solution; thiol ligands and dissolved sulfur powder both affect the course of the reaction [8], [9]. Aside from NPs, CHA (~1.5 eV band gap) has been fabricated through a variety of methods, including spray pyrolysis [10], electrodeposition [11], [12], thermal diffusion [13], [14], coevaporation [15], and sputtering [16], [17]. TET (band gap ~1.5 eV) has been fabricated via ball milling [18], spark plasma sintering [19], [20], and ampoule-based

synthesis from ultrapure elements [21]. SKI (band gap ~ 1.8 eV) has been synthesized through annealing of sputtered Cu-Sb precursors [22], and FAM has been synthesized through sputtering [23] and reaction of solution-deposited Cu and Sb precursors with H_2S [24].

Three of the four Cu-Sb-S phases have been successfully applied as the absorber layer in solar cells. Most reports have focused on CHA, with reported device efficiencies exceeding 3% for electrodeposition [11] and hybrid NP-based ink methods [25]. To the best of my knowledge, there is one successful report on both TET [26] and FAM [23] solar cells, with efficiencies of 0.04% and 0.46%, respectively. Significant improvements to film quality, tailoring of optoelectronic properties, and the design of an appropriate device architecture are needed to boost efficiencies to high levels. One potential route to improved film quality and property tailoring may be molecular precursors, which has been used to fabricate high-quality films of CIGSe and CZTSSe as outlined in Chapter 9. To the best of my knowledge, an amine-thiol solvent has only been applied once to the Cu-Sb-S system. McCarthy et al. used a mixture of 1,2-ethylenediamine and 2-mercaptoethanol to dissolve Cu_2S and Sb_2S_3 , which were then deposited and annealed to form phase-pure $CuSbS_2$ films [27]. However, the authors did not make a solar cell with these films, nor did they explore routes to other Cu-Sb-S phases.

In this chapter, preliminary work on discovering molecular precursor routes to all four phases of copper antimony sulfide is presented. The amine-thiol system that was applied to the Cu-As-S system extends readily to the fabrication of Cu-Sb-S thin films. Low-temperature routes to ternary Cu-Sb-S phases are explored; differentiation between ternary phases likely occurs by the formation of different copper sulfide intermediate phases. High temperature anneals in sulfur, H_2S , and Sb_2S_3 are also presented, suggesting routes to high-quality thin films of all four phases of Cu-Sb-S. The work presented here represents a significant first step in the development of Cu-Sb-S thin films with micron-sized dense grains for device applications.

10.2 Experimental Methods

10.2.1 Materials

All liquid and solid chemicals were obtained from Sigma Aldrich and were stored in a nitrogen-filled glovebox unless otherwise noted. The liquids used in this chapter were n-butylamine (BA, >99.5%), n-hexylamine (HA, >99%), ethanethiol (ET, >97%), 1-propanethiol

(PT, >99%), and 1-hexanethiol (HT, >95%). The solids used were copper(I) chloride (CuCl, >99.99%, Strem Chemicals), antimony(III) chloride (SbCl₃, >99.95%), sulfur (S, >99.98% powder and >99.99% flakes), and antimony(III) sulfide (Sb₂S₃, >99.995%). The gases used were hydrogen sulfide (H₂S, 0.97%, balance argon, Airgas) and argon (>99.997%, Indiana Oxygen).

10.2.2 Low-Temperature Baking

The methods described in Section 9.2.2 for Cu-As-S molecular precursors were adapted here for Cu-Sb-S molecular precursors. Precursor solutions were fabricated in a nitrogen-filled glovebox in glass vials by adding powders to the vial, then adding amine, and finally adding thiol dropwise. Microscope slides were cleaned with isopropanol and then heated to the target baking temperature on a ceramic hot plate. Individual precursor solutions were combined in an empty 4 mL vial and then drop cast onto the heated glass slide. If thicker films were desired, a second layer of solution was drop cast after 5 min of annealing. 1" by 1" molybdenum-coated soda-lime glass slides were used for spin coating – they were cleaned thoroughly with isopropanol, and then 350 μ L of precursor solution was drop cast onto the substrate. The substrate was then spun at 1500 rpm for 5 s and 2500 rpm for 25 s; this layer was then baked at 150 °C for 2 min and cooled. These steps were repeated to build up film thickness.

10.2.3 High-Temperature Annealing

The methods outlined in Section 9.2.3 (and Chapters 2 and 7 of this thesis) were used for high-temperature annealing of Cu-Sb-S films, often simultaneously with Cu-As-S films present in the furnace. Briefly, sulfur treatments occurred in a horizontal three-zone tube furnace with the sulfur source at 200 °C and an argon flow rate of 10 sccm that carried the vapor to a heated zone containing the samples of interest. H₂S anneals were conducted in a vertical tube furnace at a flow rate of 40 sccm. Sb₂S₃ treatments occurred in sealed glass ampoules identical to those used for As-S compounds. Sb₂S₃ and a sample were added to the ampoule, which was then attached to a Schlenk line, purged and refilled three times with argon, sealed under vacuum using a butane torch, and heat treated in a horizontal tube furnace. All samples were inserted into their respective furnaces once the temperature had equilibrated at the set point and were cooled to <40 °C naturally under argon flow before exposure to the ambient atmosphere.

10.2.4 Characterization

X-ray diffraction (XRD) data were collected on a Rigaku Smartlab diffractometer in either parallel beam (0.5° incident angle) or Bragg-Brentano geometry with a copper $K\alpha$ X-ray source ($\lambda = 1.5406 \text{ \AA}$). Raman spectra were acquired using a custom Horiba/Jobin-Yvon LabRAM HR800 confocal microscope system equipped with a 633 nm He:Ne laser. Thermogravimetric analysis (TGA) was conducted on a TA instruments SDT Q600 system at a ramp rate of $10^\circ\text{C}/\text{min}$ in a 100 mL/min helium flow. Scanning electron microscopy (SEM) images were acquired on an FEI Quanta 3D FEG dual-beam field emission microscope at a 7 kV accelerating voltage, and energy-dispersive X-ray spectroscopy (EDS) data were collected on the same system using a 20 kV accelerating voltage and an Oxford INCA Xstream-2 Si drift detector. The data was analyzed using AZtec software with a standardless quantitative analysis based on the Cliff-Lorimer method.

10.3 Results and Discussion

10.3.1 Precursor Solubility

The dissolution of copper and sulfur precursors was already discussed in Section 9.3.1 of this thesis and presented in Table 9.1. Similar dissolution experiments were conducted for antimony-based precursors. Specifically, SbCl_3 dissolved readily in every amine-thiol combination tried, though it did not dissolve in BA alone. It is also expected that Sb_2S_3 will dissolve in various amine-thiol combinations, as has been previously reported in the literature [28], [29]. To avoid the precursor stability problems like those seen between As_2S_5 and other copper precursors, Sb_2S_3 was avoided here.

Similar to the Cu-As-S system, a combination of BA and ET (v:v ratio 9:1) was used as the solvent for most molecular precursor experiments to facilitate its low-temperature removal from the film. This combination also allowed for dissolution of CuCl and SbCl_3 at higher concentrations (up to 0.3 M, though this is not the upper solubility limit) for film fabrication. Co-dissolution of CuCl and SbCl_3 resulted in a precursor solution that was stable indefinitely. When sulfur was added to a solution of CuCl and SbCl_3 , precipitation of a dark brown solid occurred, though the combined solutions remained stable longer than the $\text{CuCl}/\text{As}_2\text{S}_5/\text{S}$ precursor solutions discussed in Chapter 9.

During annealing procedures, thicker films were often desired, so a second layer was drop-cast after several minutes on top of the first. If the initial film contained elemental sulfur, it did not dissolve in the amine-thiol mixture, but if there was no added sulfur, the film dissolved and reprecipitated once the new solvent evaporated. As discussed in the next section, ternary Cu-Sb-S phases are formed only when free sulfur is present, so the lack of dissolution implies that ternary Cu-Sb-S phases are insoluble in the amine-thiol mixtures tested here.

10.3.2 Low-Temperature Baking

As discussed in Chapter 9, thin-film electronic synthesis routes that are insensitive to moisture and oxygen may be attractive because they do not require high-capital equipment such as vacuum systems. To investigate the properties of air-synthesized Cu-Sb-S films, solutions of CuCl, SbCl₃, and S were drop cast and annealed on glass microscope slides at temperatures ranging from 75 °C to 200 °C; such a temperature range exceeds the boiling points of BA and ET but also enters a regime where sulfur exceeds its melting point (~114 °C) and may evaporate as it tries to establish a vapor pressure. Initially, a BA:ET solution containing CuCl, SbCl₃, and S in a 2.8:1:4 ratio was drop cast and annealed at 150 °C for 3 h in air. During the anneal, the material changed from its initial yellow color to a dark red, and it finally became a black thin film. Figure 10.1 gives the XRD and Raman spectra of the film that was treated in this manner. The locations of the XRD and Raman peaks match well with reference spectra for tetragonal famatinite (FAM) Cu₃SbS₄ with no additional peaks detected, suggesting the formation of a phase-pure material.

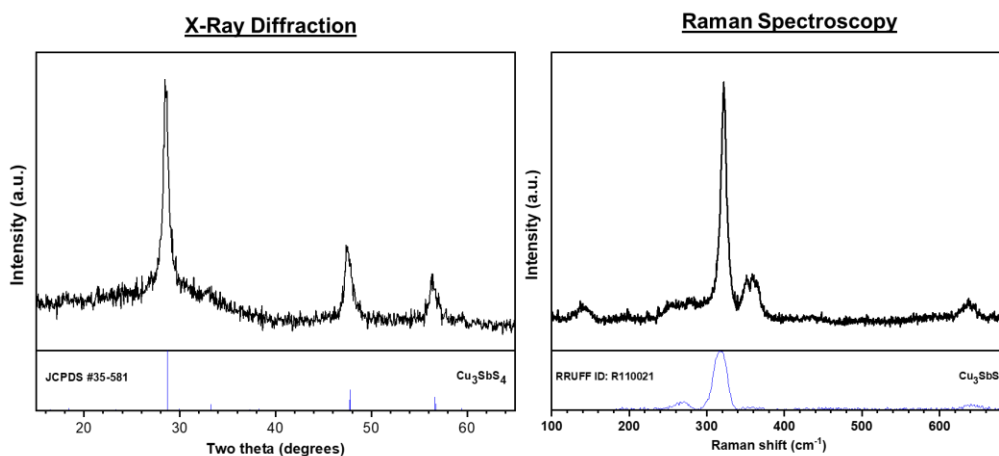


Figure 10.1. XRD and Raman spectra of a 0.1 M solution of CuCl, SbCl₃, and S (2.8:1:4 ratio) drop cast on a microscope slide and annealed for 3 h at 150 °C in air.

The formation of FAM in air is consistent with the air anneals discussed in Chapter 9, in which the oxidizing environment kept the pnictogen atom in the nominal +5 oxidation state. However, another variable that may affect the final phase formed is the Cu:Sb ratio - the value for stoichiometric FAM, TET, and SKI is 3:1, while the value for stoichiometric CHA is 1:1. Figure 10.2 gives the XRD spectra of precursor solutions with a Cu:Sb:S ratio of 1:1:3 that were annealed at 175 °C for 2 h in various amine-thiol solvent combinations; these films did not give a Raman signal. Using the lighter BA/ET and BA/PT combinations resulted in the formation of CHA, while the heavier HA/HT combination resulted in the formation of FAM. Additionally, experiments were run using 1:1:2 Cu:Sb:S ratios in BA/ET (i.e. stoichiometric sulfur instead of 50% excess); FAM was formed as the main phase, but the Raman spectra displayed stretches characteristic of both FAM and CHA. These results suggest that the annealing atmosphere is not the only factor that determines the final phase during air anneals of Cu-Sb-S molecular precursors. The chain lengths of the amines and thiols, as well as the amount of added elemental sulfur, may also have an impact.

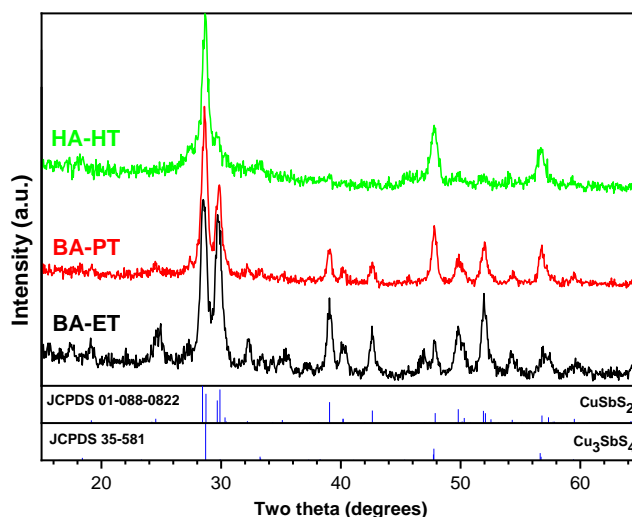


Figure 10.2. XRD spectra of a 0.1 M solution of CuCl, SbCl₃, and S (1:1:3 ratio) drop cast on a microscope slide and annealed for 2 h at 175 °C in air.

As was the case for Cu-As-S molecular precursors, the air anneals were not well-controlled, especially with respect to moisture content and air flow in the fume hood. Occasionally, additional peaks at low 2θ appeared in the XRD spectra directly after the initial anneal, a result that is tentatively attributed to the oxidation of various species, including residual amines and thiols.

Figure 10.3 gives the evolution of the XRD and Raman spectra of a BA/ET Cu:Sb:S film annealed in air at 150 °C for 2 h; the film was stored in ambient conditions between measurements. Over time, the FAM crystal structure degrades, giving rise to numerous peaks of unknown species; one potential assignment is covellite CuS, which matches well with the peaks in the 28 – 32° 2 θ range. However, the Raman spectra is invariant, suggesting that the overall Cu-Sb-S framework remains relatively intact while new species are formed.

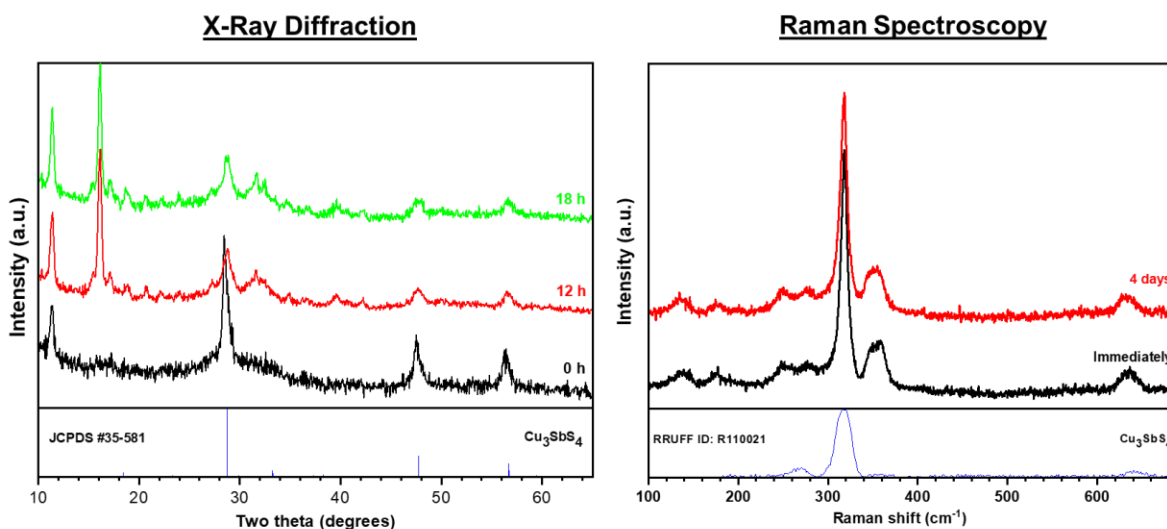


Figure 10.3. Time course of XRD and Raman spectra of 2.8:1:4 Cu:Sb:S films drop cast from a BA/ET mixture and annealed for 2 h at 175 °C.

To avoid issues associated with the stability of films fabricated in air, Cu-Sb-S solutions were instead drop cast and annealed in a nitrogen-filled glovebox. Figure 10.4 gives the XRD and Raman spectrum of solutions with a 2.8:1 Cu:Sb ratio annealed at 200 °C for 2 h. In both cases, TEN is formed with Sb in the nominal +3 oxidation state, as expected from previous nitrogen anneals involving TET-TEN NPs (Chapter 7) and Cu-As-S molecular precursors. Surprisingly, analysis of the stoichiometric sulfur sample indicates that a significant amount of CHA was formed, as indicated by the additional XRD peak around 28 ° 2 θ and additional Raman stretch at 335 cm⁻¹. This observation further supports the notion that the annealing atmosphere is not the only factor that affects the final phase in Cu-Sb-S molecular precursor films.

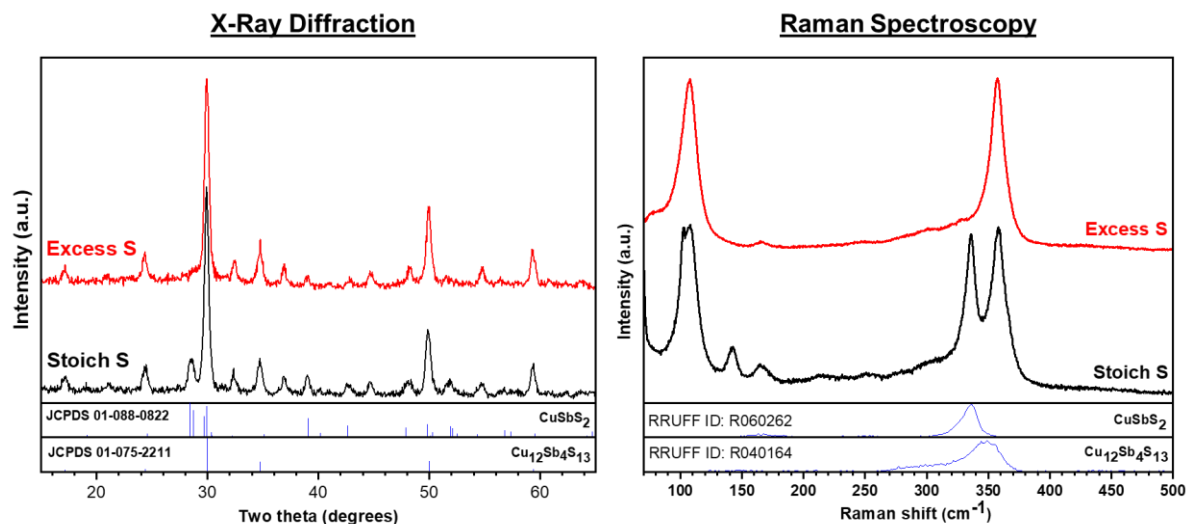


Figure 10.4. XRD and Raman spectra of CuCl/SbCl₃/S precursor solutions (2.8:1 Cu:Sb ratio) annealed at 200 °C for 2 h in a nitrogen-filled glovebox.

Several additional experiments were conducted to probe the mechanism of ternary phase formation and differentiation between phases in the Cu-Sb-S system. First, anneals of CuCl and SbCl₃ solutions without any added sulfur were conducted; the XRD did not display peaks corresponding to any ternary Cu-Sb-S phase. This suggests that ET CANNOT serve as the sole source of sulfur for air annealing; it likely leaves the film at relatively low temperatures. Second, precursors were drop cast individually on glass slides and baked for 5 min before adding another precursor on top. Figure 10.5 gives the XRD patterns of precursors that were drop cast in various orders. Interestingly, the film where copper was added last formed crystalline FAM, whereas the film where Sb was added last did not. This result suggests that the formation of stibnite Sb₂S₃ is a critical step the formation of ternary Cu-Sb-S phases.

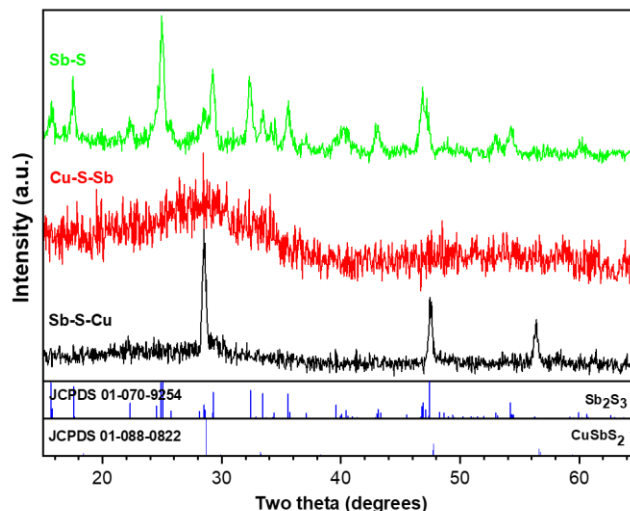


Figure 10.5. XRD spectra of CuCl, SbCl₃, and S solutions (BA/ET solvent) drop cast individually (5 min apart) and annealed at 150 °C for 2 h after the final solution was cast.

The formation of TET, FAM, and CHA under various low-temperature annealing conditions suggests that there are many variables whose interactions determine the final phase of the film. One of the key steps in the mechanism appears to be the formation of stibnite Sb₂S₃, which has been noted previously in a reaction scheme for Cu-Sb-S NPs [9]. In that report, the Sb₂S₃ reacted with various copper sulfide compounds that had formed in solution; the specific Cu_{2-x}S phases were controlled by the amount of 1-dodecanethiol added to the solution or the reactivity of the sulfur precursor dissolved in 1-octadecene (the reactivity was controlled by the temperature of the solution). Different Cu_{2-x}S phases led to different crystal structures of Cu-Sb-S nanoparticles – CuS led to FAM, Cu_{1.8}S led to TET, and Cu₃₁S₁₆ led to CHA. These observations in the NP system may be extended to the molecular precursors used here. In conditions that promote the formation of CuS with Cu in the +2 state (e.g. oxygen atmosphere, lower temperatures, heavier thiols), FAM was formed, while conditions that promote the formation of Cu_{2-x}S phases with more Cu in the +1 state (e.g. reducing atmosphere, higher temperatures, lighter thiols) led to the formation of TET and CHA. Even small temperature differences (150 °C vs 175 °C) in air resulted in different phases. Further work is needed to fully elucidate the effects of various thiols and annealing temperatures on the formation of copper sulfide phases that react with Sb₂S₃ to form ternary Cu-Sb-S phases.

10.3.3 High-Temperature Annealing

Similar to the Cu-As-S molecular system (Chapter 9), the drop casting and low-temperature baking protocols did not result in stable films with large grains suitable for device applications. Here, anneals in dilute H₂S and sulfur were conducted to probe grain growth and phase transformation mechanisms at high temperatures in the Cu-Sb-S system. Two types of films were considered throughout – some had an elemental sulfur solution added to the initial reaction mixture, while others only had the CuCl and SbCl₃ solutions. The latter was deemed a “soft bake” protocol; solutions were drop cast and baked for ~5 min to remove the majority of the amine and thiol solvent before annealing in a high-temperature sulfur-containing gas.

Figure 10.6 gives the thermogravimetric analysis (TGA) of a film that was prepared by drop casting a 2.8:1:4 CuCl:SbCl₃:S precursor solution onto a glass substrate in the glovebox and heating for 1 h at 150 °C. This film was then scraped into an alumina pan for TGA analysis in a helium atmosphere. Nearly 50% of the mass is lost by ~220 °C, with other exotherms and mass loss events noted near 350 °C and 420 °C. Because of the low solids concentrations used here (0.1 M), it is likely that most of the initial mass loss consists of residual amine-thiol compounds, though the loss of sulfur species cannot be ruled out, as sulfur melts at ~114 °C. The mass loss at higher temperature likely corresponds to the vaporization of some Sb- and S-containing compounds, consistent with previous observations in the TET-TEN NP system (Chapter 7). Because of the fast ramp rate used (10 °C/min), it is not clear if 220 °C is the absolute temperature that must be reached to remove all volatile species at low temperatures, or if baking at a lower temperature (~150 °C) for a longer period suffices. In the following discussion, some of the “high-temperature” anneals occurred at temperatures below 220 °C, so the possible effects of residual amine-thiol in the film cannot be ignored and must be carefully studied in future experiments.

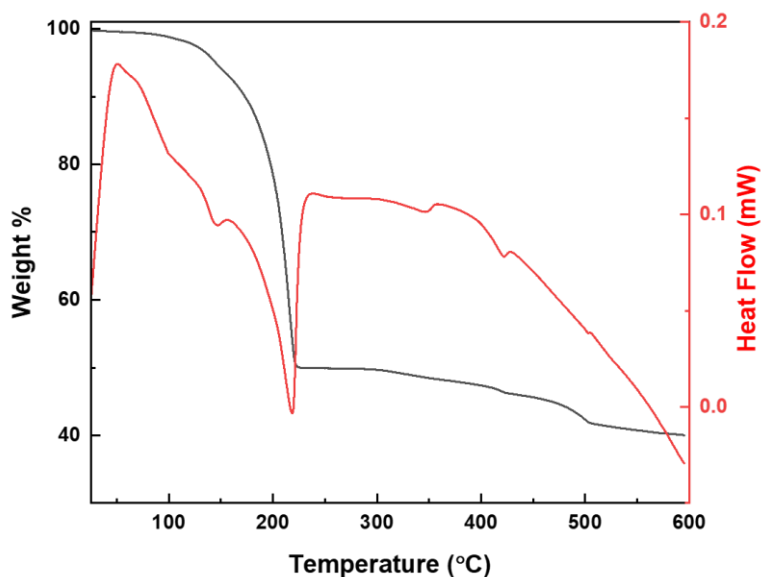


Figure 10.6. Thermogravimetric analysis (TGA) of a Cu-Sb-S molecular precursor film. The initial sample mass was 3.02 mg, and exotherms are indicated by downward spikes in the heat flow curve.

Figure 10.7 gives the XRD and Raman spectra of glovebox-prepared “soft baked” films annealed in a gaseous sulfur/argon environment for 1 h at various temperatures. At 150 °C, the XRD peaks are consistent with covellite CuS, and the Raman spectrum displays stretches consistent with both CuS and FAM. The CuS Raman peak is shifted slightly from the reference, potentially due to the presence of residual amine and thiol in the film. At higher temperatures, the copper sulfide XRD peaks gradually become less intense, while the FAM peaks become more pronounced. Also note that no peaks corresponding to stibnite Sb_2S_3 are evident. The formation of FAM and CuS (with the more oxidized Sb^{5+} and Cu^{2+}) states was expected due to the oxidizing nature of the S atmosphere. The lack of crystalline ternary phases at 150 °C suggests that the gaseous S preferentially reacts with Cu precursors instead of Sb precursors, and that higher temperatures are required to form Sb_2S_3 and drive the subsequent reaction towards FAM. There is still a CuS impurity phase present at 400 °C; further work on adjusting the precursor ratios may be required to fabricate phase-pure FAM films.

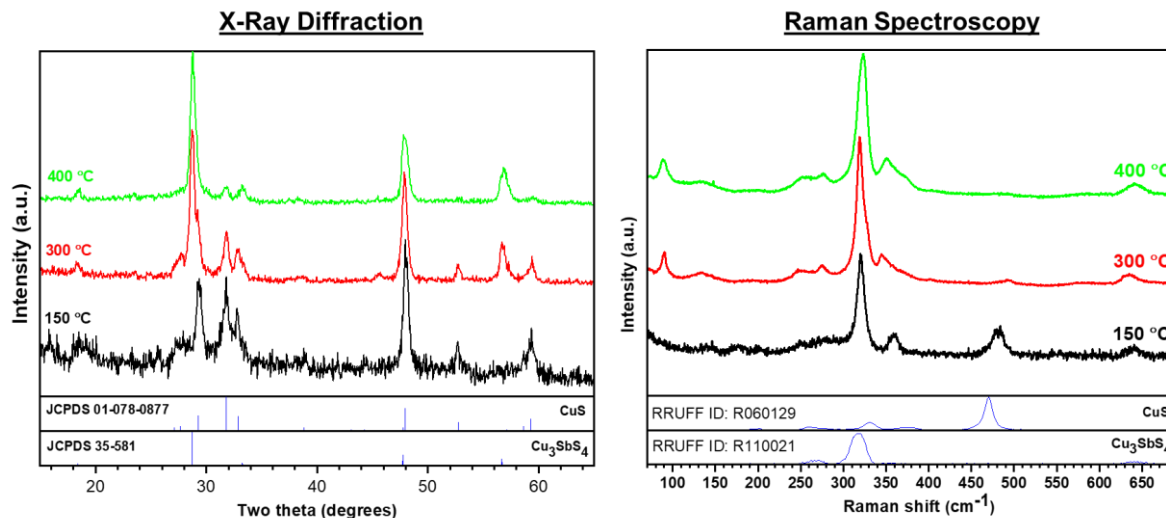


Figure 10.7. XRD and Raman spectra of Cu-Sb-S molecular precursor films soft baked in a glovebox at 75 °C (2.8:1 CuCl:SbCl₃ ratio in 9:1 v:v BA:ET) and then annealed in a sulfur/argon atmosphere for 1 h at the given temperature.

Figure 10.8 gives the XRD and Raman spectra of glovebox-prepared films that were annealed in H₂S for 1 h at the given temperatures. For the spectra labeled “no S”, the films were “soft baked” at 75 °C prior to the anneal, and the samples that had added sulfur were annealed for 2 h at 150 °C. Therefore, the comparisons here are between films that have not been impacted by a sulfur source (since ET cannot serve as the sulfur source for the formation of ternary films) and those that are TET prior to annealing – essentially a ternary phase formation vs. a ternary phase transformation. At 150 °C without added sulfur, SKI was formed, with small amounts of TET apparent in the Raman, suggesting that the H₂S may preferentially react with copper to form chalcocite Cu₂S (with all copper in the +1 state) at low temperatures [9]. When the film was instead annealed at 300 °C, TET was formed, along with a significant quantity of several copper sulfide (Cu_{2-x}S) phases. It is possible that the higher temperature resulted in a different preferential reaction between Cu and H₂S, leading to different copper sulfides. Additionally, the possibility of forming volatile Sb compounds cannot be ruled out, which would lead to their evaporation and result in a film with excess Cu. At 300 °C with added sulfur, FAM was formed as the dominant phase, with a small TET shoulder peak in the XRD. This result is somewhat surprising, as previous anneals of TET NPs in H₂S at 350 °C kept the TET structure intact. However, the presence of added sulfur, the lack of bulky carbonaceous ligands, and the lower temperature may result in conditions that are favorable for the oxidation of Sb⁺³ in TET to Sb⁺⁵ in FAM. At 450 °C, the

starting TET phase was transformed to SKI, consistent with observations in TET NP anneals. The EDX-determined elemental ratios for the SKI film were $\text{Cu}:\text{Sb} = 3.09 \pm 0.04$ and $\text{Cu}:\text{S} = 1.10 \pm 0.02$, which is relatively close to the stoichiometric value but suggests that excess copper is still present in the film. Further work is needed to fully explore the mechanisms of H_2S reactions in Cu-Sb-S molecular precursor films with respect to both initial ternary film formation and phase transformations of ternary phases.

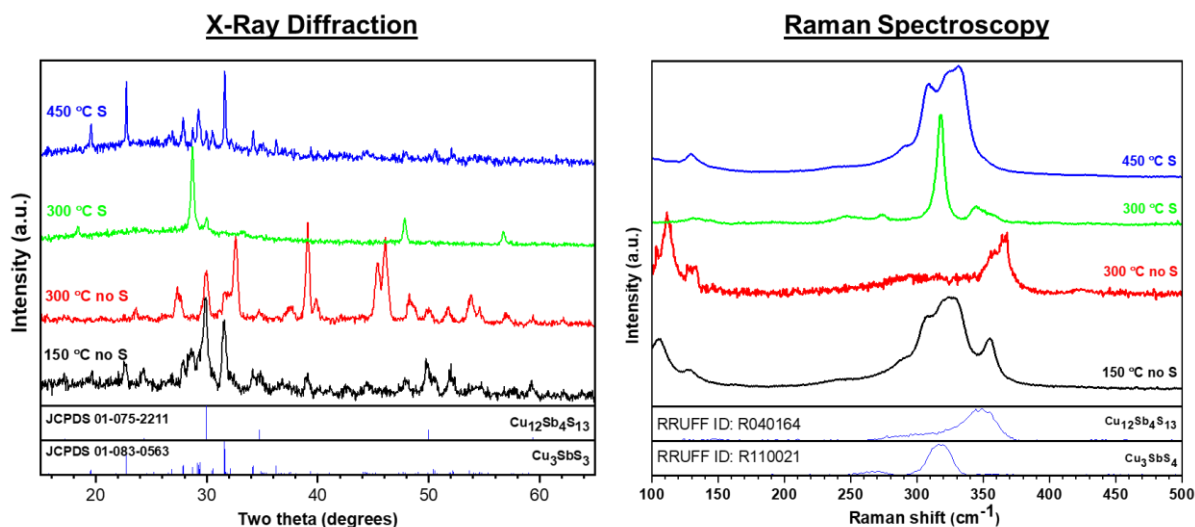


Figure 10.8. XRD and Raman spectra of Cu-Sb-S molecular precursor films annealed in H_2S for 1 h at the given temperatures and initial sulfur contents. In the “300 °C no S” spectra, additional peaks correspond to digenite $\text{Cu}_{1.8}\text{S}$ and chalcocite Cu_2S . In the “150 °C no S” and “450 °C S” films, the stretches in the 280–340 cm^{-1} do not correspond to a known mineral in the RRUFF database; the peaks are instead attributed to skinnerite Cu_3SbS_3 as described in Chapter 7.

One common feature of semiconducting thin films found in high-efficiency devices is micron-sized dense grains. While sulfur and H_2S have been previously used to grow grains of CIGSe, CZTSSe, etc., the impact of these atmospheres has not been fully elucidated in the Cu-Sb-S system. The gases do not seem to facilitate growth and densification, as seen in the SEM image for sulfur treatments presented in Figure 10.9. For many other chalcogenide semiconducting systems, the grain growth and coarsening procedure is likely aided by a liquid phase [30], [31]. While sulfur may exist as a liquid at the processing conditions used here, the decomposition of Cu-Sb-S molecular precursor films and subsequent loss of Sb and S species add additional variables to the system that must be accounted for in a future study.

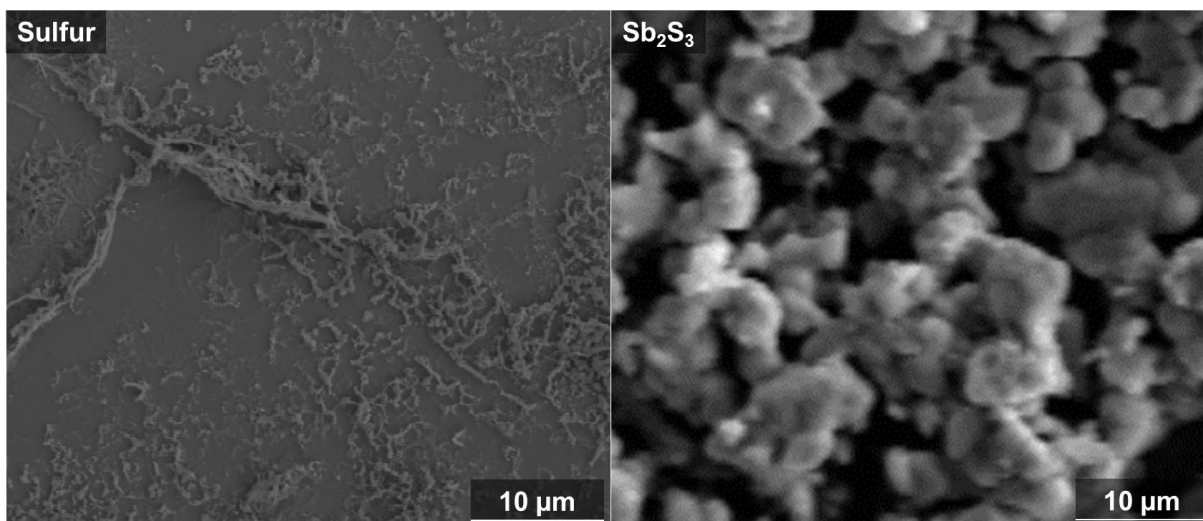


Figure 10.9. Plan view SEM images of Cu-Sb-S molecular precursor films treated in sulfur or Sb_2S_3 for 1 h at 450 °C.

As discussed in Chapter 2 of this thesis, the Cu-As-S system has a liquid phase consisting mostly of As and S at elevated temperatures. Liquid-assisted grain growth may be the mechanism responsible for growth of thin films with micron-sized dense grains. When the phase diagrams of the Cu-Sb-S system are studied, a large liquid field is not present. However, there is a very small liquid field close to the composition of Sb_2S_3 that is in equilibrium with CHA; therefore, annealing in Sb_2S_3 may result in a liquid phase from which grains of CHA can grow [1]. Figure 10.9 gives a plan view SEM image of a Cu-Sb-S molecular precursor film heated in a sealed ampoule with Sb_2S_3 powder. When compared with sulfur anneals, the grains are much larger and continuous, though further optimization is needed to promote densification of the film. Figure 10.10 gives the XRD and Raman characterization of the Sb_2S_3 -annealed films, with the formation of CHA evident at both 300 °C and 450 °C. In the XRD spectra, the peak at $40^\circ 2\theta$ is attributed to the Mo substrate, and additional peaks match with Sb_2S_3 , which may be removed through a post-annealing etch in a material such as diammonium sulfide $[(\text{NH}_4)_2\text{S}]$ [32]. The presence of TET is inferred from the Raman spectra at 300 °C, indicating that higher temperatures are required to drive the phase transformation of Cu-Sb-S films to completion.

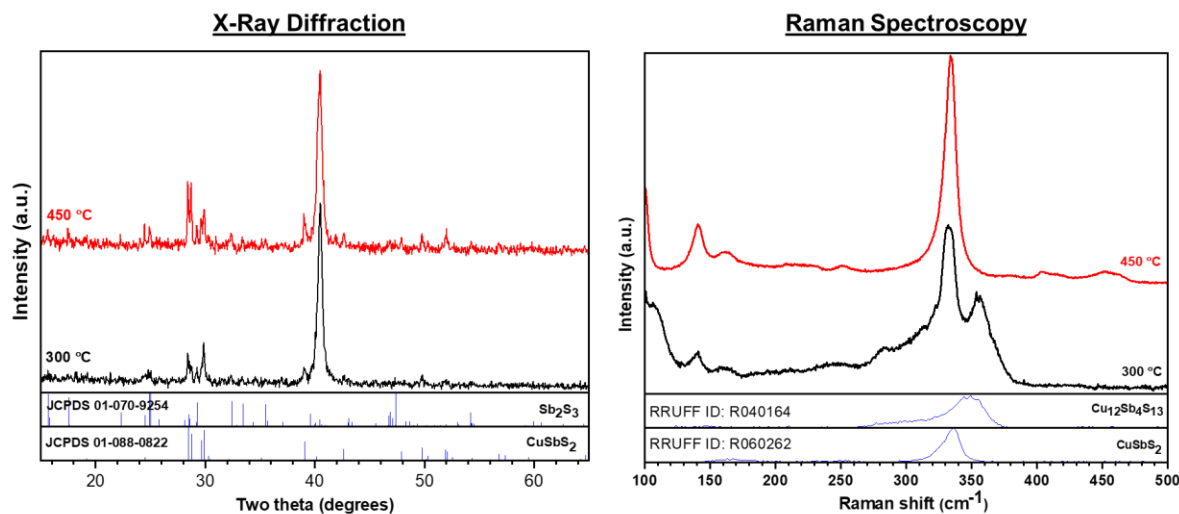


Figure 10.10. XRD and Raman spectra of a Cu-Sb-S molecular precursor film annealed in an ampoule containing Sb₂S₃ for 1 h at the given temperature. The XRD peaks at 40° 2θ correspond to the molybdenum substrate.

10.4 Conclusions

Preliminary investigations into the fabrication of molecular precursor-based copper antimony sulfide thin films have been presented. The amine-thiol solvent system, which was applied to the Cu-As-S system in Chapter 9, was adapted to the Cu-Sb-S system because Sb-based precursors can also be dissolved readily. Ternary Cu-Sb-S phases are formed at low temperatures in both air and a nitrogen-filled glovebox, and the mechanism that differentiates between the four Cu-Sb-S phases is likely the formation of different copper sulfide phases (which are, in turn, controlled by the baking atmosphere and the presence or absence of added sulfur in the molecular precursor solution). Heat treatments of precursor films have shown feasible routes to all four phases of Cu-Sb-S phases – FAM is formed in a sulfur atmosphere or low-temperature H₂S atmosphere, TET is formed at low temperatures in a glovebox, SKI is formed from TET at high temperatures in H₂S or from Cu and Sb complexes at low temperatures, and CHA is formed by annealing in Sb₂S₃ or significantly varying the Cu:Sb ratio in the precursor solutions. However, a phase-pure material remains elusive, as some copper sulfide remains in each film. Future work in this system should focus on tailoring the composition of the precursor films to avoid secondary phase formation, determining the processing windows for formation of all four phases of Cu-Sb-S compounds, discovering the chemical nature of the molecular precursor complexes, and the impacts of various amines and thiols on film phase and morphology. The preliminary work here

is significant progress towards synthesizing all four phases of copper antimony sulfide thin films, which may ultimately be paired with appropriate materials to form a high-quality pn junction for uses in photovoltaics and other applications.

10.5 Acknowledgements

S.A.M. acknowledges support from the NSF (grants 0903670-DGE and DMR-1534691) and Purdue University (Faculty and Bilsland Dissertation Fellowships). He thanks Dr. Robert Balow for helpful guidance throughout, Juan Carlos Vega-Vila and Dr. Rajamani Gounder for access to the TGA unit, and Raymond Sanfrey for insights gained through his parallel work on aqueous Cu-Sb-S molecular precursors.

10.6 References

- [1] B. J. Skinner, F. D. Luce, and E. Makovicky, "Studies of the Sulfosalts of Copper III. Phases and Phase Relations in the System Cu-Sb-S," *Econ. Geol.*, vol. 67, no. 7, pp. 924–938, Nov. 1972.
- [2] L. Yu, R. S. Kokenyesi, D. A. Keszler, and A. Zunger, "Inverse Design of High Absorption Thin-Film Photovoltaic Materials," *Adv. Energy Mater.*, vol. 3, no. 1, pp. 43–48, Jan. 2013.
- [3] C. Tablero, "Electronic and Optical Property Analysis of the Cu-Sb-S Tetrahedrites for High-Efficiency Absorption Devices," *J. Phys. Chem. C*, vol. 118, pp. 15122–15127, 2014.
- [4] W. Lai, Y. Wang, D. T. Morelli, and X. Lu, "From Bonding Asymmetry to Anharmonic Rattling in Cu₁₂Sb₄S₁₃ Tetrahedrites: When Lone-Pair Electrons Are Not So Lonely," *Adv. Funct. Mater.*, vol. 25, no. 24, pp. 3648–3657, Jun. 2015.
- [5] J. Heo, R. Ravichandran, C. F. Reidy, J. Tate, J. F. Wager, and D. A. Keszler, "Design Meets Nature: Tetrahedrite Solar Absorbers," *Adv. Energy Mater.*, vol. 5, no. 7, p. 1401506, Apr. 2015.
- [6] R. Zhang, K. Chen, B. Du, and M. J. Reece, "Screening for Cu–S based thermoelectric materials using crystal structure features," *J. Mater. Chem. A*, vol. 5, no. 10, pp. 5013–5019, 2017.
- [7] C. Tablero, "Electronic property analysis of O-doped Cu₃SbS₃," *Solar Energy Materials and Solar Cells*, vol. 104. Elsevier, pp. 180–184, 2012.

- [8] K. Ramasamy, H. Sims, W. H. Butler, and A. Gupta, "Selective Nanocrystal Synthesis and Calculated Electronic Structure of All Four Phases of Copper–Antimony–Sulfide," *Chem. Mater.*, vol. 26, no. 9, pp. 2891–2899, May 2014.
- [9] Q. Liang, K. Huang, X. Ren, W. Zhang, R. Xie, and S. Feng, "Synthesis of Cu–Sb–S nanocrystals: insight into the mechanism of composition and crystal phase selection," *CrystEngComm*, vol. 18, no. 20, pp. 3703–3710, 2016.
- [10] J. A. Ramos Aquino, D. L. Rodriguez Vela, S. Shaji, D. A. Avellaneda, and B. Krishnan, "Spray pyrolysed thin films of copper antimony sulfide as photovoltaic absorber," *Phys. Status Solidi*, vol. 13, no. 1, pp. 24–29, 2016.
- [11] W. Septina, S. Ikeda, Y. Iga, T. Harada, and M. Matsumura, "Thin film solar cell based on CuSbS₂ absorber fabricated from an electrochemically deposited metal stack," *Thin Solid Films*, vol. 550, pp. 700–704, Jan. 2014.
- [12] L. Zhang *et al.*, "Solution-processed CuSbS₂ thin film: A promising earth-abundant photocathode for efficient visible-light-driven hydrogen evolution," *Nano Energy*, vol. 28, pp. 135–142, Oct. 2016.
- [13] C. Garza *et al.*, "p-Type CuSbS₂ thin films by thermal diffusion of copper into Sb₂S₃," *Sol. Energy Mater. Sol. Cells*, vol. 95, no. 8, pp. 2001–2005, 2011.
- [14] B. Krishnan, S. Shaji, and R. Ernesto Ornelas, "Progress in development of copper antimony sulfide thin films as an alternative material for solar energy harvesting," *J. Mater. Sci. Mater. Electron.*, 2015.
- [15] L. Wan *et al.*, "Two-stage co-evaporated CuSbS₂ thin films for solar cells," *J. Alloys Compd.*, vol. 680, pp. 182–190, Sep. 2016.
- [16] A. W. Welch, P. P. Zawadzki, S. Lany, C. A. Wolden, and A. Zakutayev, "Self-regulated growth and tunable properties of CuSbS₂ solar absorbers," *Sol. Energy Mater. Sol. Cells*, vol. 132, pp. 499–506, Jan. 2015.
- [17] A. W. Welch *et al.*, "Accelerated development of CuSbS₂ thin film photovoltaic device prototypes," *Prog. Photovoltaics Res. Appl.*, vol. 24, no. 7, pp. 929–939, Jul. 2016.
- [18] T. Barbier *et al.*, "Thermoelectric Materials: A New Rapid Synthesis Process for Nontoxic and High-Performance Tetrahedrite Compounds," *J. Am. Ceram. Soc.*, vol. 99, no. 1, pp. 51–56, 2016.

- [19] R. Chetty, A. Bali, and R. C. Mallik, "Tetrahedrites as thermoelectric materials: an overview," *J. Mater. Chem. C*, vol. 3, no. 48, pp. 12364–12378, 2015.
- [20] D. P. Weller *et al.*, "Thermoelectric Performance of Tetrahedrite Synthesized by a Modified Polyol Process," *Chem. Mater.*, vol. 29, no. 4, pp. 1656–1664, 2017.
- [21] X. Lu *et al.*, "Band structure engineering in highly degenerate tetrahedrites through isovalent doping," *J. Mater. Chem. A*, pp. 17096–17103, 2016.
- [22] P. Maiello, G. Zoppi, R. W. Miles, N. Pearsall, and I. Forbes, "Chalcogenisation of Cu–Sb metallic precursors into $\text{Cu}_3\text{Sb}(\text{Se}_x\text{S}_{1-x})_3$," *Sol. Energy Mater. Sol. Cells*, vol. 113, pp. 186–194, Jun. 2013.
- [23] N. D. Franzer, N. R. Paudel, C. Xiao, and Y. Yan, "Study of RF sputtered Cu_3SbS_4 thin-film solar cells," in *2014 IEEE 40th Photovoltaic Specialist Conference (PVSC)*, 2014, pp. 2326–2328.
- [24] Y. Zhang, J. Tian, K. Jiang, J. Huang, H. Wang, and Y. Song, "Gas–solid reaction for in situ deposition of Cu_3SbS_4 on a mesoporous TiO_2 film," *RSC Adv.*, vol. 7, no. 66, pp. 41540–41545, 2017.
- [25] S. Banu, S. J. Ahn, S. K. Ahn, K. Yoon, and A. Cho, "Fabrication and characterization of cost-efficient CuSbS_2 thin film solar cells using hybrid inks," *Sol. Energy Mater. Sol. Cells*, vol. 151, pp. 14–23, Jul. 2016.
- [26] L. Wang *et al.*, "Synthesis and characterization of hydrazine solution processed $\text{Cu}_{12}\text{Sb}_4\text{S}_{13}$ film," *Sol. Energy Mater. Sol. Cells*, vol. 144, pp. 33–39, Jan. 2016.
- [27] C. L. McCarthy, P. Cottingham, K. Abuyen, E. C. Schueller, S. P. Culver, and R. L. Brutchey, "Earth abundant CuSbS_2 thin films solution processed from thiol–amine mixtures," *J. Mater. Chem. C*, vol. 4, no. 26, pp. 6230–6233, 2016.
- [28] D. H. Webber and R. L. Brutchey, "Alkahest for V_2VI_3 Chalcogenides: Dissolution of Nine Bulk Semiconductors in a Diamine-Dithiol Solvent Mixture," *J. Am. Chem. Soc.*, vol. 135, no. 42, pp. 15722–15725, Oct. 2013.
- [29] J. J. Buckley, M. J. Greaney, and R. L. Brutchey, "Ligand Exchange of Colloidal CdSe Nanocrystals with Stibanates Derived from Sb_2S_3 Dissolved in a Thiol-Amine Mixture," *Chem. Mater.*, vol. 26, no. 21, pp. 6311–6317, Nov. 2014.

- [30] C. J. Hages, M. J. Koeper, C. K. Miskin, K. W. Brew, and R. Agrawal, "Controlled Grain Growth for High Performance Nanoparticle-Based Kesterite Solar Cells," *Chem. Mater.*, vol. 28, no. 21, pp. 7703–7714, Nov. 2016.
- [31] S. McLeod, E. Alruqobah, and R. Agrawal, "Liquid assisted grain growth in solution processed Cu(In,Ga)(S,Se)₂," *Sol. Energy Mater. Sol. Cells*, vol. 195, no. February, pp. 12–23, 2019.
- [32] Z. Xia *et al.*, "Generalized Water-Processed Metal Chalcogenide Complexes: Synthesis and Applications," *Chem. Mater.*, vol. 27, no. 23, pp. 8048–8057, Dec. 2015.

11. CONCLUSIONS AND FUTURE WORK

11.1 Conclusions

This dissertation has broadly explored the Cu-As-S system, particularly enargite (ENG) Cu_3AsS_4 , with a specific focus on photovoltaic (PV) applications. The Cu-As-S system is promising for large-scale PV deployment because its constituent elements are earth abundant and have vastly different cation sizes, leading to the possibility of a relatively defect-free material. Using solution-processed nanoparticles (NPs) as precursors, the first reported thin films of ENG were fabricated by annealing in an arsenic-sulfur atmosphere. The resulting films with micron-sized dense grains were fabricated into solar cells using cadmium sulfide as the n-type buffer layer, reaching initial efficiencies of 0.18%. Further optimization of the process pushed the maximum efficiency to 0.35%; this value is certainly exciting for a new material but leaves plenty of room for improvement.

Two drawbacks of the initial fabrication procedure were the formation of a secondary phase due to the reaction of carbonaceous ligands with sulfur and the condensation of As-S residues on the surface of the film. The residues were removed by etching in ammonium sulfide $(\text{NH}_4)_2\text{S}$, but the secondary phase proved resistant to pre- and post-treatment annealing, etching, and other methods. Thus, ligand exchange of LUZ NPs was explored. Oleylamine ligands were successfully removed from the film and replaced with conductive AsS_3^{3-} ligands. Micron-sized grains grew upon heat treatment, but densification proved to be an issue, likely due to the difficulty in forming a thick, uniform coating from colloiddally stable ligand exchanged NPs.

Optoelectronic and defect properties of ENG were also probed independently of device fabrication, with the aim of evaluating the material's long-term potential for PV applications. ENG has promising optoelectronic properties that motivate continued research into the material. It has benign defect characteristics, and its mobility, carrier concentration, and carrier lifetimes are on par with what is expected for an emerging PV absorber material. The main issue plaguing ENG-based solar cells at this point is the choice of buffer layer – cadmium sulfide forms a severe cliff offset with ENG, limiting the open-circuit voltage and hence the efficiency of solar cells in this configuration. By switching to a more appropriate buffer layer, efficiencies exceeding 5% should

be relatively easy to obtain, with improvements to 10%, 15%, and 20% realistic targets over the next few years.

Other materials related to ENG were also studied. The first synthesis of alloyed tetrahedrite-tennantite $\text{Cu}_{12}\text{As}_{4-x}\text{Sb}_x\text{S}_{13}$ NPs was reported, and the role of the annealing atmosphere in controlling the crystal structure and composition of NP thin films was elucidated. The first synthesis of crystalline thin-film sinnerite $\text{Cu}_6\text{As}_4\text{S}_9$ was also discovered; it displays an appropriate band gap and a photoresponse that motivates additional research into the fundamental optoelectronic properties of the material. The related Cu-Sb-S system was also studied using a solution-based molecular precursor approach. Building off of results from Cu-As-S molecular precursors, heat treatment routes to all four phases of Cu-Sb-S were discovered.

11.2 Future Work

Publications related to new photovoltaic materials are constantly appearing, with authors claiming that their material is the next CIGSe, CdTe, or even perovskite in terms of potential transformative impacts on the solar industry. However, most studies fail to address fundamental properties such as defect chemistry, instead selling the power conversion efficiencies as the sole indicator of promise. To avoid spending 25+ years on a material (such as CZTSSe) that has fundamental flaws and will stagnate far below 20% efficiency, it is critical to measure optoelectronic properties early in enargite's development. My characterization work has shown promising shallow and deep defect characteristics, as well as appropriate mobilities, carrier concentrations, and carrier lifetimes. However, the characterization requires more work – additional temperature-dependent photoluminescence (PL) is necessary to determine the chemical origin of various peaks seen in the cryogenic PL spectra, and temperature- and voltage-dependent time-resolved photoluminescence (TRPL) will be crucial in elucidating the various recombination pathways present in ENG thin films. These experiments must be supplemented by density functional theory (DFT) calculations that can correlate PL peaks with specific point defects in the material. One other property critically important for achieving high-efficiency solar cells is the radiative efficiency [1], [2], which can be evaluated using techniques such as quantitative photoluminescence [3], [4]. Measuring the radiative efficiency of ENG will be another key step in assessing its long-term potential.

The fabrication of the first ENG thin films was achieved in this thesis, but the methods used to fabricate the films are not sufficient for achieving high-efficiency devices. The films fabricated from OLA-capped NPs are plagued by a carbon-sulfur secondary phase that likely has a high resistance. Films fabricated from ligand exchanged NPs do not have such a secondary phase, but the densification of grains has not yet been realized due to difficulties in obtaining a uniform, agglomerate-free coating. A detailed, fundamental study of the LUZ NP surface and ligand exchange procedure using techniques such as NMR, ICP-MS, FTIR, and TEM may be required to fully understand the mechanisms that cause agglomeration and uncover the requirements needed for a good initial film. Alternatively, the molecular precursor approach detailed in Chapter 9 may prove useful in fabricating high-quality thin films; it has the added benefit of simplified processing due to the lack of a NP synthesis. Regardless of the approach chosen, film fabrication progress to a point where there is no carbon remaining in the film and fully densified micron-sized grains are formed. Optoelectronic properties of these improved films (such as mobility and carrier concentration) must also be continuously investigated.

Once the optoelectronic properties of ENG have been deemed promising for long-term applications and the carbon-free films with micron-sized dense grains have been achieved, the search for an appropriate device architecture must commence. Cadmium sulfide is clearly an inappropriate n-type layer, but the optimal alternative is difficult to assess computationally. Wallace et al. have suggested various buffer layers (such as Ce_2S_3 and ZnTe) that, at a first approximation, align well with various terminating crystal planes of ENG [5], though reports on their synthesis and application in solar cells is limited. ZnS is another possible candidate that has been applied to CIGSe and CZTSSe previously. However, DFT calculations do not consider interdiffusion between the absorber and buffer layers, which may result in interfacial defects and thin impurity phases. The back contact has also not yet been addressed; as-deposited Mo has a favorable alignment with ENG, but the effects of the As_2S_5 heat treatment on Mo have not yet been elucidated. Simulations using SCAPS and ADEPT must be used to evaluate potential device performance with various buffer layer and electrical contact configurations. Then, full devices should be fabricated and measured using routine electrical characterization techniques (JV, EQE, capacitance, etc.), as well as more advanced temperature-dependent techniques to determine factors that limit device performance. At the same time, techniques such as XPS or UPS must be

used to evaluate the band alignment at the p-n junction, and high-resolution TEM must be used to examine the interface for interdiffusion and nonuniformity.

The current outlook for enargite-based solar cells is promising. If the optoelectronic characterization continues to indicate outstanding properties, improvements to the thin films and device architectures will undoubtedly result in significant efficiency boosts for ENG-based solar cells. Ultimately, ENG has the potential to be a major part in the future solar panel market, but further focused research is required to make the vision a reality.

11.3 References

- [1] M. A. Green, “Radiative efficiency of state-of-the-art photovoltaic cells,” *Prog. Photovoltaics Res. Appl.*, vol. 20, no. 4, pp. 472–476, Jun. 2012.
- [2] T. Kirchartz and U. Rau, “What Makes a Good Solar Cell?,” *Adv. Energy Mater.*, vol. 8, no. 28, 2018.
- [3] J. K. Katahara and H. W. Hillhouse, “Quasi-fermi level splitting and sub-bandgap absorptivity from semiconductor photoluminescence,” *J. Appl. Phys.*, vol. 116, no. 17, 2014.
- [4] I. L. Braly, R. J. Stoddard, A. Rajagopal, A. K. Y. Jen, and H. W. Hillhouse, “Photoluminescence and Photoconductivity to Assess Maximum Open-Circuit Voltage and Carrier Transport in Hybrid Perovskites and Other Photovoltaic Materials,” *J. Phys. Chem. Lett.*, vol. 9, no. 13, pp. 3779–3792, 2018.
- [5] S. K. Wallace, K. T. Butler, Y. Hinuma, and A. Walsh, “Finding a junction partner for candidate solar cell absorbers enargite and bournonite from electronic band and lattice matching,” *J. Appl. Phys.*, vol. 125, no. 5, p. 055703, Feb. 2019.

APPENDIX A. STUDIES ON THE COATING AND WASHING OF LUZONITE NANOPARTICLES

A.1. Introduction

In this appendix, characterization of the luzonite (LUZ) Cu_3AsS_4 nanoparticle (NP) coating and washing procedures is presented, with dynamic light scattering (DLS) and nuclear magnetic resonance (NMR) used to describe the ligands present in NP pellets and their possible impacts on particle agglomeration.

A.2. Optimization of Luzonite Nanoparticle Coatings

The established doctor blading procedure to form crack-free films of CIGS and CZTS nanoparticles (NPs) involves suspending NPs at 250 mg/mL in 1-hexanethiol (HT) and coating the ink on a Mo-coated soda-lime glass (Mo-SLG) substrate [1], [2]. A 15 μL coat is applied and then baked for 1 min at 300 °C, followed by cooling and application of a 10 μL coat. This procedure is not suitable for luzonite (LUZ) Cu_3AsS_4 NPs, as they decompose and lose arsenic at these temperatures in air.

In Chapter 2, crack-free LUZ NP films were made by blade coating HT-based inks onto Mo-SLG with no baking step to drive off the solvent. This means that the presence of HT is likely during heat treatments, contributing additional carbon that can react with sulfur to form an amorphous secondary phase. Therefore, incorporation of a baking step to remove HT is critical to minimize the formation of the secondary phase.

A wide variety of ink concentrations, baking temperatures, NP storage and ages, and ink preparation methods were tested with the goal of forming crack-free thin films for use in As_2S_5 heat treatments. An optical microscope was used to check for cracks after each coat. The most important parameter for forming crack-free films was the baking temperature. Temperatures exceeding 100 °C could not reproducibly produce crack-free films, regardless of the ink concentration or NP properties. Therefore, the baking temperature was kept at or below 100 °C for coatings involving standard OLA-capped LUZ NPs. Additionally, 250 mg/mL ink concentrations would often result in a network of cracks, so the concentration was reduced. Ultrasonication is

typically used to make more stable and well-suspended inks, but benefits seen in other NP systems did not appear to translate to the LUZ NPs used here.

The final optimized coating procedure involved preparation of a 200 mg/mL HT-based ink via simple vortexing. Anywhere from two to four coats were applied depending on the desired thickness; the first one was 15 μL and the rest were 10 μL . Between each coating step, the film was dried for 1 min at room temperature and then baked at 75 $^{\circ}\text{C}$ for 5 min before cooling and applying another coat. At the end of the final baking step, the hot plate was ramped to 100 $^{\circ}\text{C}$ for 5 min. While this procedure does not guarantee complete removal of HT, it is an important step for reducing carbon in the film. Future coating experiments may not be focused on standard NPs (due to the need to eliminate OLA), but the coating of ligand exchanged NPs, for instance, should involve full consideration of the variables outlined here, as well as the choice of solvent, coating atmosphere, and use of an automated system.

A.3. Study of the Luzonite Purification Procedure

The washing procedure outlined in Chapter 2 used a hexane solvent and ethanol (EtOH) antisolvent. However, LUZ NPs have difficulty resuspending in HT or other solvents after this washing procedure, and even resuspending in hexane during the later washes becomes difficult. Alternative washing procedures using chloroform (CHCl_3) or toluene were tested; colloidal stability was better but still not ideal for long-term applications. Therefore, detailed knowledge of the changes induced by the washing procedure is required. Two techniques were applied to investigate each step of the washing procedure: dynamic light scattering (DLS) for measuring the average hydrodynamic diameter of particles, and ^1H nuclear magnetic resonance (NMR) for determining the species in the NP pellet after purification.

Figure A.1a gives the DLS intensity-weighted spectra for LUZ NPs that were washed in hexane and EtOH. Note that the actual sizes are approximate, as quantities such as the refractive index of the NPs were not known. A bimodal distribution of hydrodynamic diameters was observed after the second and third washes, suggesting that two washes removes enough OLA ligand to induce some agglomeration of LUZ NPs. Differing particle sizes are not ideal for film growth, as they are more difficult to suspend in inks and result in initial film nonuniformity. By switching to CHCl_3 -EtOH washes, a monomodal distribution of hydrodynamic diameters is obtained (Figure A.1b). It must be noted, though, that the sizes are much larger than those seen

with hexane-EtOH washes. However, the particles washed with CHCl_3 suspended much better during subsequent washes and during coatings, so the hydrodynamic diameter measured by DLS may be artificially high due to close clustering of the NPs in solution, rather than indicating irreversible agglomeration.

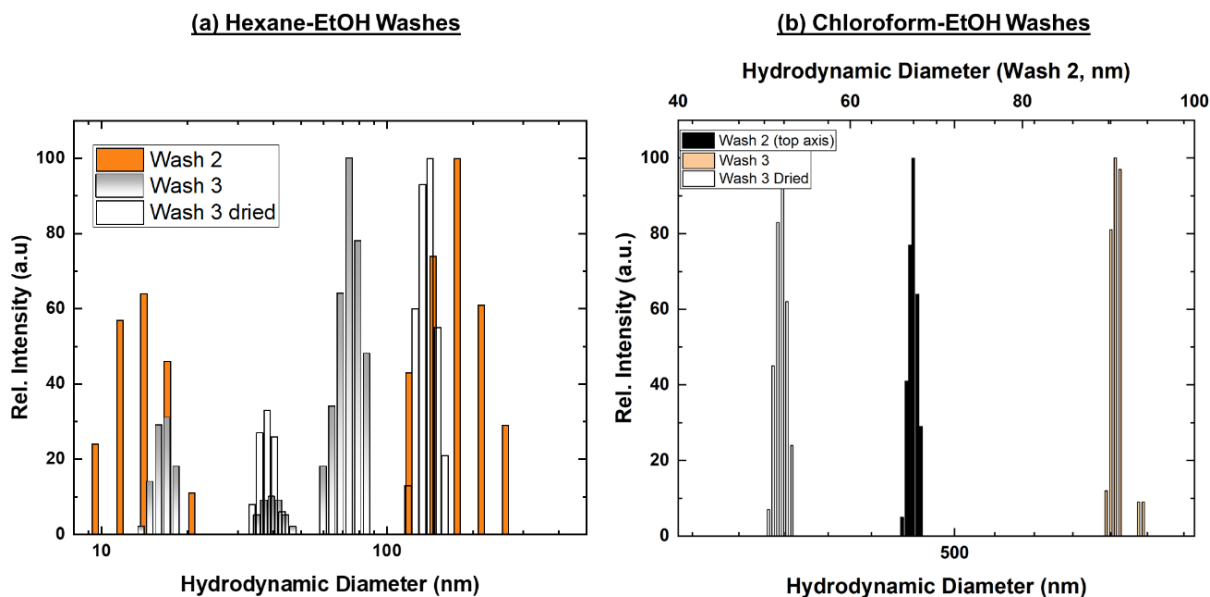


Figure A.1. Dynamic light scattering measurements (intensity normalized) for LUZ NPs washed using (a) hexane-ethanol, and (b) chloroform-ethanol.

NMR can be used to monitor the presence of free and bound ligands in NP pellets. Figure A.2 gives the NMR spectra from two pellets of LUZ NPs that were washed with different solvent combinations. Between the second and third washes, the intensity of the $\text{C}=\text{C}$ peak around 5.5 ppm decreased relative to the solvent peaks, indicating significant removal of OLA regardless of which solvent combination was used. Interestingly, the ethanol signal ($\delta = 3.72$ ppm) in the CHCl_3 -washed particles increased between the second and third washes, while its relative intensity change is unclear in the toluene-washed particles ($\delta = 3.36$ ppm). The IPA signal ($\delta = 3.65$ ppm) decreased from wash 2 to wash 3 when using toluene. These results suggest that the choice of a nonpolar solvent may have an impact on the binding or entrainment of alcohols in the NP pellet. Additionally, a less acidic alcohol such as IPA may be a better choice for washing; previous work has shown that proton transfer is an important step in the binding of alcohols to the surface of NPs, and a less acidic alcohol would slow this step [3].

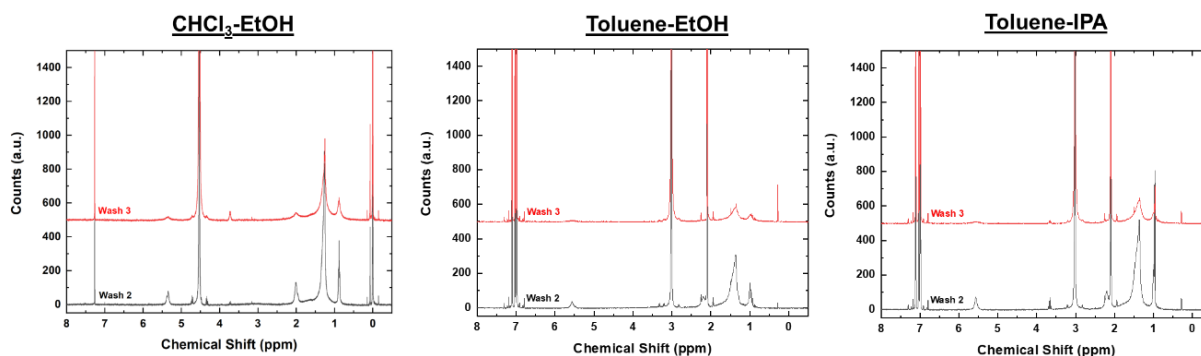


Figure A.2. NMR spectra of LUZ NP samples taken from the centrifuge tube after washes 2 and 3 in various solvents. Note that the CHCl_3 -EtOH sample was analyzed in deuterated chloroform, while the toluene-EtOH and toluene-IPA samples were analyzed in deuterated toluene.

NMR may also be used to quantify the ligands on the NP surface, and hence the overall carbon content of a NP [4]. A standard with a well-defined, simple NMR spectrum (dimethylsulfone was used here), was added to a sample tube consisting of LUZ NPs in chloroform. Then, the integrated peak intensities corresponding to the standard and to the ligand of interest (i.e. OLA) were quantified and normalized for the number of protons causing the signal. Since the concentration of the standard is known, it is a straightforward calculation to determine the concentration of OLA ligands. Using this procedure, the weight fraction of OLA in a LUZ NP pellet was estimated as ~7-8%.

A.4. Conclusions

In this appendix, the properties of LUZ NPs relevant for washing and coating were studied. LUZ NPs do not have the same surface characteristics as CIGS or CZTS NPs fabricated previously in our lab, so the washing and coating procedure was modified accordingly. Then, DLS was used to show that washing with hexane causes a bimodal distribution of hydrodynamic diameters, while washing with CHCl_3 leads to a larger average hydrodynamic diameter but a monomodal size distribution. NMR demonstrated a significant removal of OLA during the washing procedure, which may explain colloidal stability issues seen in LUZ NP work and reiterates the need to carefully control the NP purification procedure. Additionally, differences in the solvents used may also lead to different surface character of the NPs. The information here may prove useful in controlling the properties of the LUZ NP ligand shell after washing and designing subsequent

ligand exchange procedures to target all ligands present on the surface. Ligand exchanged particles should also be characterized using DLS and NMR to gain further insights into the mechanism of exchange and potential routes to overcoming colloidal stability issues.

A.5. Acknowledgements

S.A.M. would like to thank Vinny Pizzuti and Dr. Yue-Yon Won for access to the DLS instrument, and Ryan Ellis, Swapnil Deshmukh, and David Rokke for assistance with the NMR measurements.

A.6. References

- [1] C. K. Miskin *et al.*, “9.0% efficient $\text{Cu}_2\text{ZnSn}(\text{S},\text{Se})_4$ solar cells from selenized nanoparticle inks,” *Prog. Photovoltaics Res. Appl.*, vol. 23, no. 5, pp. 654–659, May 2015.
- [2] S. M. McLeod, C. J. Hages, N. J. Carter, and R. Agrawal, “Synthesis and characterization of 15% efficient CIGSSe solar cells from nanoparticle inks,” *Prog. Photovoltaics Res. Appl.*, vol. 23, no. 11, pp. 1550–1556, Nov. 2015.
- [3] A. Hassinen, I. Moreels, K. De Nolf, P. F. Smet, J. C. Martins, and Z. Hens, “Short-Chain Alcohols Strip X-Type Ligands and Quench the Luminescence of PbSe and CdSe Quantum Dots, Acetonitrile Does Not,” *J. Am. Chem. Soc.*, vol. 134, no. 51, pp. 20705–20712, Dec. 2012.
- [4] L. Tong, E. Lu, J. Pichaandi, P. Cao, M. Nitz, and M. A. Winnik, “Quantification of Surface Ligands on NaYF_4 Nanoparticles by Three Independent Analytical Techniques,” *Chem. Mater.*, vol. 27, no. 13, pp. 4899–4910, Jul. 2015.

APPENDIX B. PRELIMINARY STUDIES TOWARDS SYNTHESIS OF ALLOYED COPPER ARSENIC SULFIDE THIN FILMS

B.1. Introduction

In this appendix, preliminary investigations into isoelectronic alloying of Cu_3AsS_4 thin films with antimony and selenium are presented. Alloying is beneficial because it may tune the bandgap of a material, provide increased stability, or reduce toxic elements in the parent compound. So far, alloys of Cu_3AsS_4 have only been explored in the nanoparticle (NP) form, with a complete substitution of Sb for As published and partial substitution of Se for S achieved in the lab [1]. Here, heat treatments towards forming alloys of $\text{Cu}_3\text{Sb}_{1-y}\text{As}_y\text{S}_4$ and $\text{Cu}_3\text{As}(\text{Se}_x\text{S}_{1-x})_4$ are discussed.

B.2. Heat Treatments Towards Selenium Alloying

CIGS and CZTS NPs are transformed to their selenide analogs by heating films in a supersaturated selenium atmosphere; the excess selenium may condense on the surface, forming a liquid that aids in growth of micron-sized dense grains [2], [3]. Figure B.1 gives the XRD, Raman, and SEM images of LUZ NP samples that were annealed in the presence of selenium at 500 °C in both a graphite box under argon flow and in a sealed glass ampoule. Rather than an alloyed sulfoselenide phase or the pure selenide Cu_3AsSe_4 , a mixture of large copper selenide platelets is formed, with both $\text{Cu}_{0.87}\text{Se}$ and Cu_2Se identified. EDX measurements suggested that arsenic had left the film entirely, as no characteristic X-rays were detected in either sample. Phase diagrams of the Cu-As-Se system reveal that there is no solubility of arsenic in a liquid copper selenide phase, so growing films of $\text{Cu}_3\text{As}(\text{Se}_x\text{S}_{1-x})_4$ by standard selenization is not feasible [4].

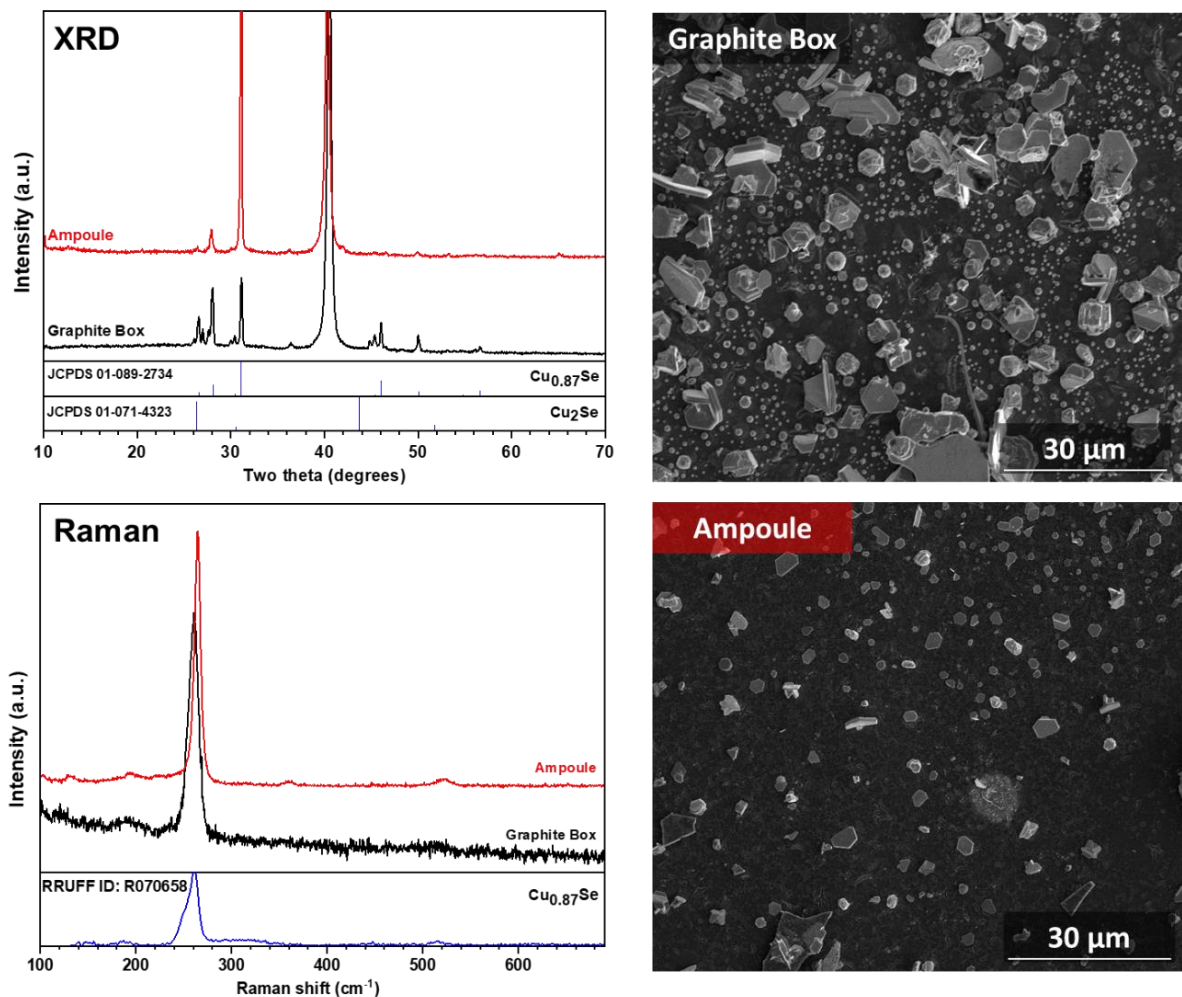


Figure B.1. XRD spectra, Raman spectra, and plan-view SEM images of LUZ NP films that were annealed in excess selenium at 500 °C for 20 min (graphite box) or 1 h (ampoule).

Much of this thesis focused on the growth of enargite Cu_3AsS_4 thin films by heating LUZ NPs in a glass ampoule with As_2S_5 powder, which is a liquid at the processing temperatures used here. By adding selenium to the ampoule with As_2S_5 , it may be possible to form a liquid phase with arsenic, sulfur, and selenium that leads to the growth of alloyed films. Figure B.2 gives XRD spectra, Raman spectra, and plan-view SEM images of LUZ NP films that were heated in a glass ampoule with added As_2S_5 powder and Se pellets. At 425 °C, the selenium does not affect the overall crystal structure, as the ENG peaks are unshifted and the Raman spectrum is dominated by the carbonaceous secondary phase. The SEM image at 425 °C shows grains that are somewhat like those grown in As_2S_5 , with larger circular regions filling the space between grains. These regions have a larger quantity of arsenic and sulfur than the surrounding grains; additionally, the overall

film has a S:Se ratio of $\sim 3:1$ indicated by EDX. At 500 °C, the XRD and Raman spectra indicate formation of a copper selenide impurity phase. The XRD spectrum suggests that some alloying may have occurred, as the peaks shifted slightly left in accordance with Vegard's law for alloy materials [5], [6]. However, the shift may be exaggerated slightly because one spectrum was collected in Bragg-Brentano mode and the other in parallel beam mode, leading to a systematic shift of the peaks. The SEM image indicates complete overgrowth of the film and significant void space.

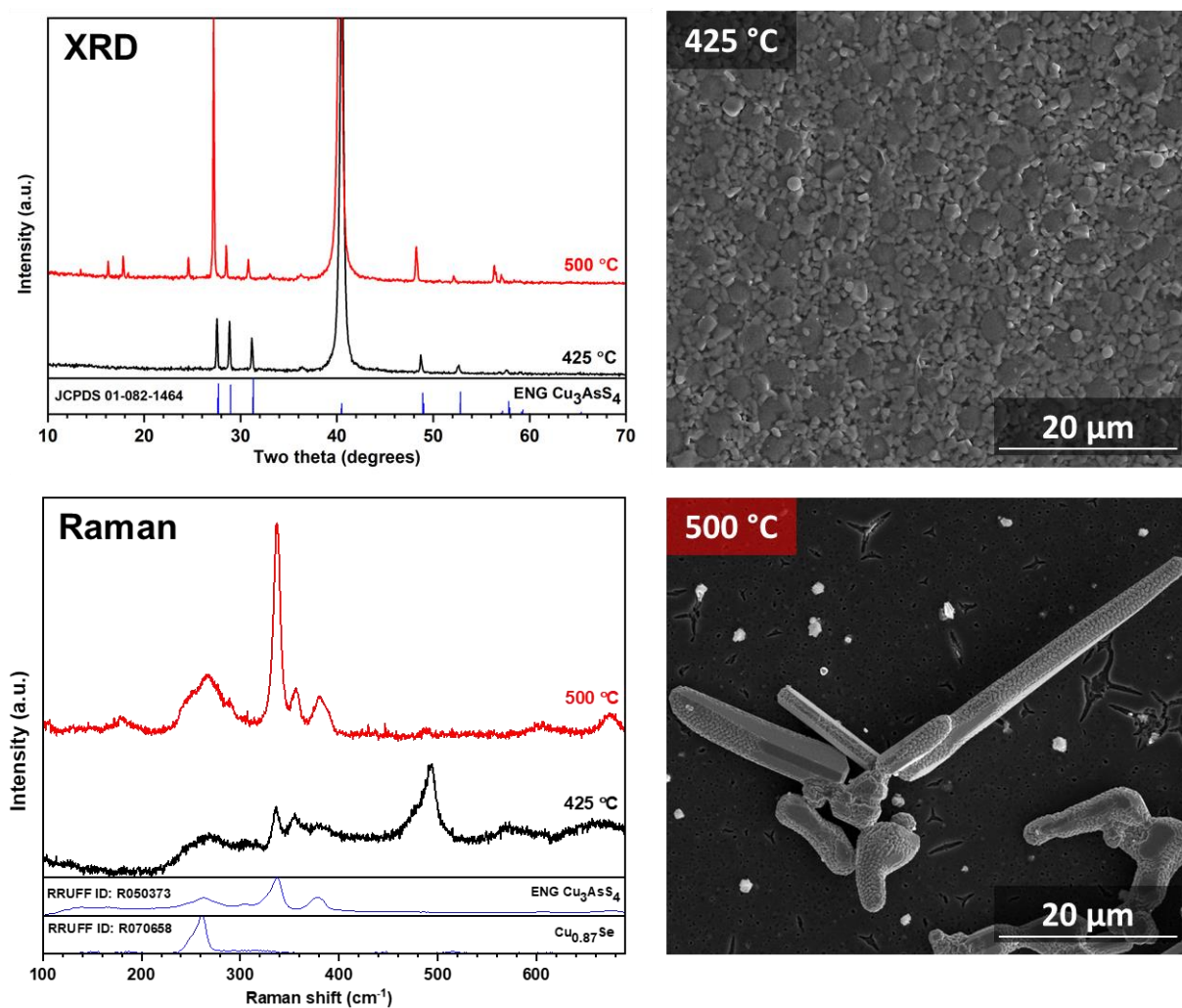


Figure B.2. XRD spectra, Raman spectra, and plan-view SEM images of LUZ NP films that were annealed in As₂S₅ and selenium in a glass ampoule for 1 h at the given temperature.

The preliminary annealing experiments with selenium indicate that sulfoselenide alloys may not be readily achieved by placing selenium in the annealing atmosphere. Alternative approaches, such as synthesizing alloyed NPs and heat treating them, performing ligand exchange to introduce arsenic- or selenium-containing species to the surface, or heat treating in an As_2Se_3 atmosphere, may be required.

B.3. Heat Treatments Towards Antimony Alloying

Substituting arsenic with antimony may result in a decrease of the bandgap and a potential shift to the tetragonal famatinite crystal structure with more than ~12% antimony substitution [7]; the toxicity of antimony is also lower than that of arsenic. The Cu-Sb-S system has a liquid phase that may be exploited for grain growth, though the processing temperatures required are higher [8]. The quaternary Cu-As-Sb-S system also has a liquid phase, though the mole fraction of antimony relative to arsenic remains relatively low [7].

To investigate the possibility of forming mixed As- and Sb- films, $\text{Cu}_3\text{As}_{0.75}\text{Sb}_{0.25}\text{S}_4$ NP films were coated and annealed in separate glass ampoules containing Sb_2S_3 and As_2S_5 . The XRD and Raman spectra (Figure B.3) do not indicate formation of a quaternary alloyed phase, with enargite Cu_3AsS_4 formed during As_2S_5 heat treatments and chalcostibite CuSbS_2 formed in the presence of Sb_2S_3 . Furthermore, EDX measurements on the micron-sized grains that were formed (Figure B.3) indicated no trace of the other element (i.e. Sb for As_2S_5 treatments and vice versa) in the film. It is likely that these elements evaporated from the film and were present in such low quantities that they did not saturate the vapor space in the ampoule.

To ensure the saturation of the vapor space with As and Sb, a heat treatment involving equimolar amounts of As_2S_5 and Sb_2S_3 was conducted on a LUZ NP film. In this case, the film gave no XRD signal that would suggest the formation of a crystalline ternary or quaternary phase. A cross-sectional SEM image (Figure B.4) of a solar cell (efficiency = 0%) from this material indicated the formation of a 3-4 μm thick layer, rather than the 1 μm typically seen from a treated NP film. EDX measurements revealed that this layer consisted of only As, Sb, and S, with small amounts of copper remaining near the Mo interface. There is one previous report of a “compound X” with composition AsSb_2S_2 , which may have formed here [7].

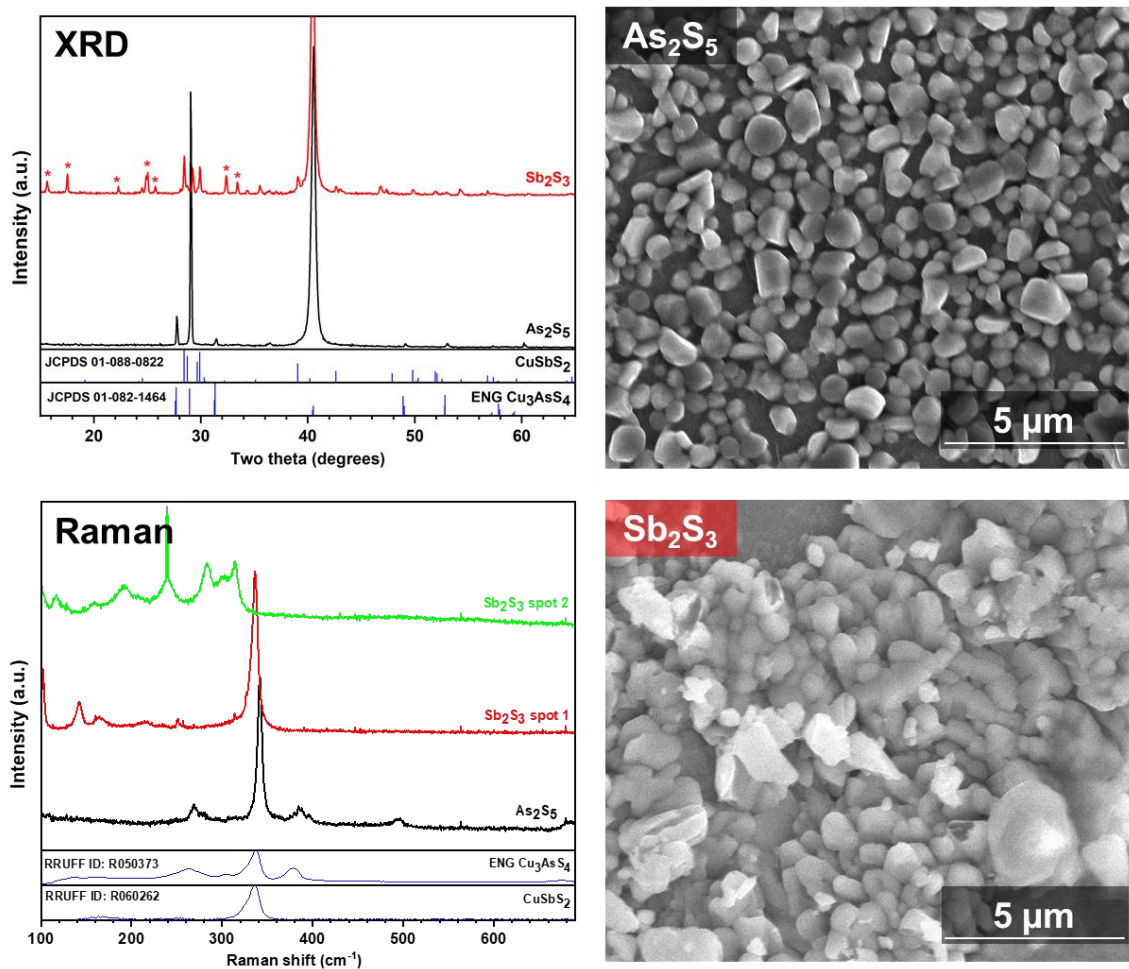


Figure B.3. XRD spectra, Raman spectra, and plan-view SEM images of $\text{Cu}_3\text{As}_{0.75}\text{Sb}_{0.25}\text{S}_4$ NP films that were annealed in As_2S_5 or Sb_2S_3 in a glass ampoule for 1 h at 425 °C. In the XRD spectrum, a * signifies a peak attributable to stibnite Sb_2S_3 , which agrees with the Raman spectrum labeled “ Sb_2S_3 spot 2.”

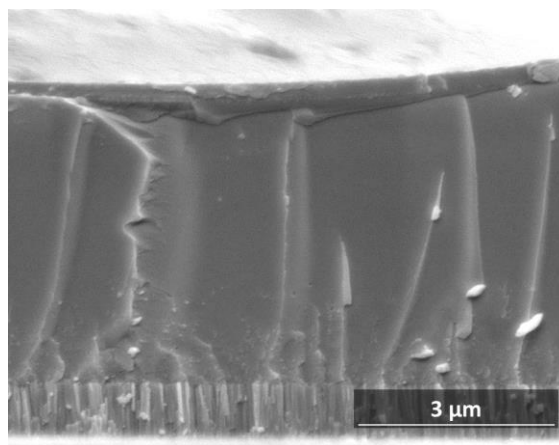


Figure B.4. Cross-sectional SEM image of a LUZ NP film that was annealed in an $\text{As}_2\text{S}_5/\text{Sb}_2\text{S}_3$ mixture in a glass ampoule for 1 h at 425 °C.

The heat treatments presented here suggest that using liquid-assisted grain growth to form $\text{Cu}_3(\text{Sb}_{1-x}\text{As}_x)_4$ thin films may not be feasible by simply mixing powders or starting from alloyed NPs. A quaternary liquid phase was not likely formed here due to limited control – the only true control knob is temperature, which controls the vapor pressures of both species (and hence the achievable As/Sb ratios). Alternative schemes may need to be devised to achieve alloyed films with micron-sized dense grains.

B.4. Conclusions

The experiments in this section involved modifying the annealing atmosphere to fabricate alloyed films of $\text{Cu}_3\text{As}_{1-y}\text{Sb}_y(\text{Se}_x\text{S}_{1-x})_4$ from NPs; such a scheme attempted to ensure a liquid phase in the film. The attempts were unsuccessful, likely due to the insolubility of arsenic in copper selenide phases and the differing nature of the liquid phase in Cu-As-S and Cu-Sb-S ternary systems. Successful formation of alloyed films may require significantly different design principles and experimental apparatuses.

B.5. Acknowledgements

S.A.M. thanks Joseph Andler for helpful discussions and experimental setup.

B.6. References

- [1] R. B. Balow, C. K. Miskin, M. M. Abu-Omar, and R. Agrawal, “Synthesis and Characterization of $\text{Cu}_3(\text{Sb}_{1-x}\text{As}_x)\text{S}_4$ Semiconducting Nanocrystal Alloys with Tunable Properties for Optoelectronic Device Applications,” *Chem. Mater.*, vol. 29, no. 2, pp. 573–578, Jan. 2017.
- [2] C. J. Hages, M. J. Koeper, C. K. Miskin, K. W. Brew, and R. Agrawal, “Controlled Grain Growth for High Performance Nanoparticle-Based Kesterite Solar Cells,” *Chem. Mater.*, vol. 28, no. 21, pp. 7703–7714, Nov. 2016.
- [3] S. McLeod, E. Alruqobah, and R. Agrawal, “Liquid assisted grain growth in solution processed $\text{Cu}(\text{In,Ga})(\text{S,Se})_2$,” *Sol. Energy Mater. Sol. Cells*, vol. 195, no. February, pp. 12–23, 2019.

- [4] K. Cohen, J. Rivet, and J. Dugue, "Description of the Cu-As-Se ternary system," *J. Alloys Compd.*, vol. 224, pp. 316–329, 1995.
- [5] L. Vegard, "Die Konstitution der Mischkristalle und die Raumfullung der Atome," *Zeitschrift fur Phys.*, vol. 5, no. 1, pp. 17–26, Jan. 1921.
- [6] A. R. Denton and N. W. Ashcroft, "Vegard's law," *Phys. Rev. A*, vol. 43, no. 6, pp. 3161–3164, Mar. 1991.
- [7] F. D. Luce, C. L. Tuttle, and B. J. Skinner, "Studies of sulfosalts of copper: V. Phases and phase relations in the system Cu-Sb-As-S between 350° and 500°C," *Econ. Geol.*, vol. 72, no. 2, pp. 271–289, Apr. 1977.
- [8] B. J. Skinner, F. D. Luce, and E. Makovicky, "Studies of the Sulfosalts of Copper III. Phases and Phase Relations in the System Cu-Sb-S," *Econ. Geol.*, vol. 67, no. 7, pp. 924–938, Nov. 1972.

APPENDIX C. EXPLORATION OF ALTERNATIVE SYNTHESIS METHODS FOR Cu_3AsS_4 NANOPARTICLES

C.1. Introduction

The original synthesis developed for luzonite (LUZ) Cu_3AsS_4 nanoparticles (NPs) used oleylamine (OLA) as the capping ligand [1]. While OLA has demonstrated success with CIGS and CZTS NP-based solar cell fabrication, it is not as advantageous for LUZ because OLA reacts with sulfur during heat treatments and is difficult to remove by thermal annealing or ligand exchange procedures. In this appendix, two preliminary experiments towards replacing OLA ligands are presented.

C.2. Use of 1-Dodecanethiol as a Ligand for Cu_3AsS_4 Nanoparticles

An alternative ligand such as 1-dodecanethiol (DDT) may be attractive for LUZ NP synthesis, as it has a lower boiling point than OLA and may alter LUZ surface chemistry due to its expected binding motif as an X-type ligand rather than an L-type ligand [2]. Graeser and Agrawal used DDT as a ligand to form phase pure Cu_3PS_4 NPs; an equivalent procedure for arsenic-based NPs was adapted here [3]. 2.5 mmol of copper(I) chloride, 0.625 mmol of arsenic(V) sulfide, and 10 mL DDT were mixed in a three-neck flask and heated. Aliquots were taken at 150 °C, 175 °C, 200 °C, and 225 °C after equilibration at each temperature for 1 h. The XRD and Raman spectra in Figure C.1 indicate the formation of copper sulfide Cu_{2-x}S phases at temperatures lower than 200 °C, with the formation of tennantite (TEN) $\text{Cu}_{12}\text{As}_4\text{S}_{13}$ at higher temperatures. The formation of TEN as opposed to LUZ, as well as the higher temperatures required for the formation of any Cu-As-S ternary phase, suggests that DDT may slow reaction kinetics significantly by forming a stable complex with Cu; such control over the reaction kinetics has been explored in the related Cu-Sb-S system [4], [5]. Tuning the reaction parameters to form LUZ was not attempted here.

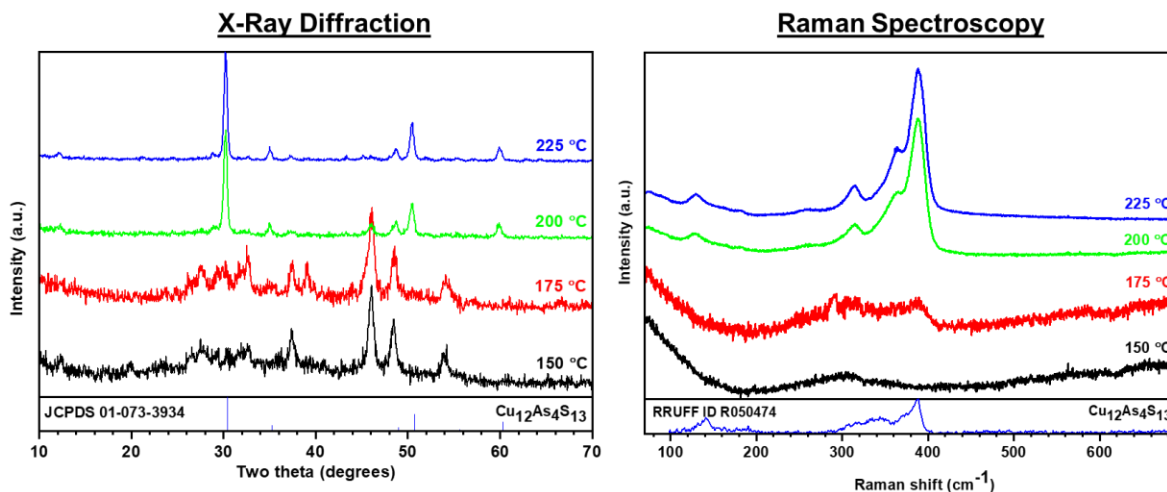


Figure C.1. XRD and Raman spectra of aliquots taken at the indicated temperature for a reaction mixture of CuCl and As₂S₅ in DDT.

C.3. Aqueous-Based Synthesis of Luzonite Nanoparticles

Chapter 5 discussed a carbon-free approach towards Cu-As-S thin films; OLA-capped LUZ NPs were synthesized and then subjected to a ligand exchange procedure which removed OLA and replaced it with a stabilizing conductive ligand such as AsS₃³⁻. To eliminate the initial processing and washing steps, it may be worthwhile to synthesize NPs directly capped with AsS₃³⁻ ligands. Such a concept was successfully used by Tang's group, who synthesized Cu- and Zn-based NPs stabilized by Sn-based ligands at room temperature; these NPs were then annealed and fabricated into solar cells [6]. Here, a similar setup was used to synthesize Cu₃AsS₄ NPs.

Precursor solutions of 1 M aqueous copper(II) nitrate, 1 M aqueous thiourea, and 0.4 M As₂S₃ in a 20-24 wt% (NH₄)₂S in water mixture were prepared in a glovebox. In a 4 mL vial, the desired amount of As₂S₃ ligand solution was added followed by thiourea solution, and then the Cu solution was added slowly. Precipitation occurred nearly instantly upon Cu addition, and the solid powder was resuspended in the solution and cast for characterization. Figure C.2 gives the XRD and Raman characterization of precipitates from solutions with and without added thiourea. The formation of arsenic(III) oxide and ammonium nitrate is noted in both cases, and the formation of copper(II) sulfide occurs in the absence of thiourea. From this initial experiment, it seems that the AsS₃³⁻ ligand may not be strong enough to stabilize NPs in solution; it also is particularly reactive with the oxygen in nitrate ion. Further experiments in this system were not pursued but revisiting

them may be interesting in the quest for carbon-free films of Cu-As-S materials. Controlling the reactivity of the various ligands through stoichiometry or the order of addition may be the key to a successful aqueous-based synthesis of LUZ NPs.

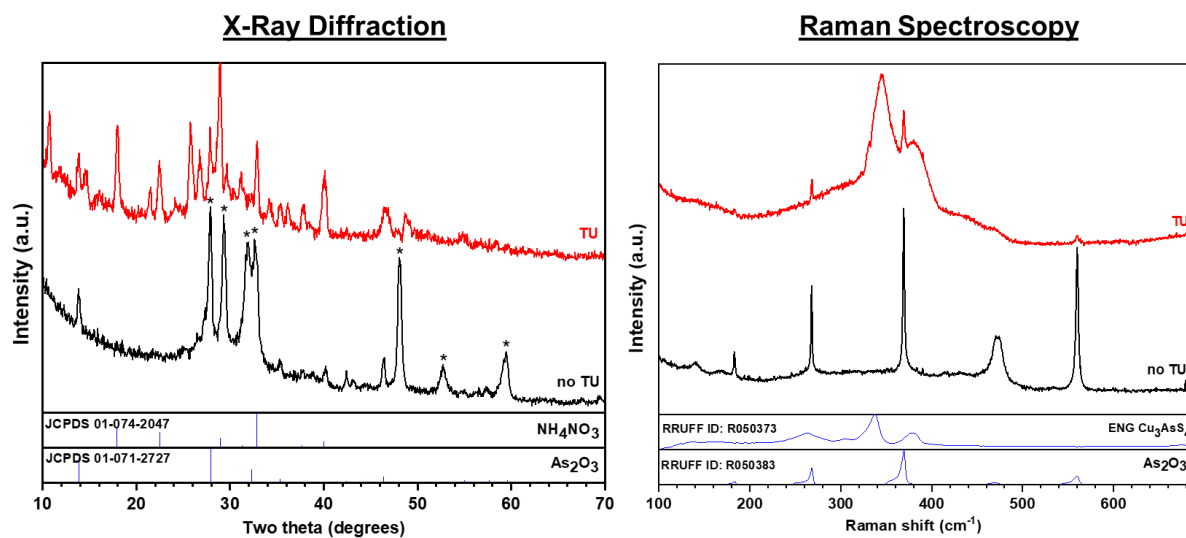


Figure C.2. XRD and Raman spectra of aqueous synthesis attempts for LUZ NPs. Aqueous copper(II) nitrate and arsenic(III) sulfide solutions were mixed with and without thiourea, and the resulting precipitate was characterized. The * in the XRD spectrum without thiourea signifies peaks that may also be assigned to covellite CuS.

C.4. Conclusions

The experiments presented in this appendix represent preliminary work towards the development of an alternative synthesis procedure for luzonite Cu_3AsS_4 nanoparticles; such a procedure would eliminate the disadvantages associated with bulky amines used in the established scheme. Using dodecanethiol as a ligand instead of oleylamine appears to favor the formation of tennantite $\text{Cu}_{12}\text{As}_4\text{S}_{13}$ rather than the desired luzonite. An aqueous-based synthesis was unsuccessful due to the oxidation of arsenic by nitrate ions in solutions. Both methods are relatively unexplored, however, and may be further researched with careful control exerted over the reactivity of various precursors used.

C.5. Acknowledgements

S.A.M. would like to thank Dr. Brian Graeser for advice on the aliquot experiments for the DDT-based synthesis.

C.6. References

- [1] R. B. Balow, E. J. Sheets, M. M. Abu-Omar, and R. Agrawal, "Synthesis and Characterization of Copper Arsenic Sulfide Nanocrystals from Earth Abundant Elements for Solar Energy Conversion," *Chem. Mater.*, vol. 27, no. 7, pp. 2290–2293, Apr. 2015.
- [2] R. Dierick *et al.*, "Surface Chemistry of CuInS₂ Colloidal Nanocrystals, Tight Binding of L-Type Ligands," *Chem. Mater.*, vol. 26, no. 20, pp. 5950–5957, Oct. 2014.
- [3] B. K. Graeser and R. Agrawal, "Pure phase synthesis of Cu₃PS₄ and Cu₆PS₅Cl for semiconductor applications," *RSC Adv.*, vol. 8, no. 59, pp. 34094–34101, 2018.
- [4] K. Ramasamy, H. Sims, W. H. Butler, and A. Gupta, "Selective Nanocrystal Synthesis and Calculated Electronic Structure of All Four Phases of Copper–Antimony–Sulfide," *Chem. Mater.*, vol. 26, no. 9, pp. 2891–2899, May 2014.
- [5] Q. Liang, K. Huang, X. Ren, W. Zhang, R. Xie, and S. Feng, "Synthesis of Cu–Sb–S nanocrystals: insight into the mechanism of composition and crystal phase selection," *CrystEngComm*, vol. 18, no. 20, pp. 3703–3710, 2016.
- [6] J. Zhong *et al.*, "One-Pot Synthesis of Self-Stabilized Aqueous Nanoinks for Cu₂ZnSn(S,Se)₄ Solar Cells," *Chem. Mater.*, vol. 26, no. 11, pp. 3573–3578, 2014.

APPENDIX D. PRELIMINARY SYNTHESIS OF ZINC SULFIDE THIN FILMS USING THE SILAR METHOD

D.1. Introduction

In Chapter 6, zinc sulfide (ZnS) was suggested as a candidate buffer layer for enargite Cu_3AsS_4 solar cells. ZnS has a bandgap of ~ 3.5 eV (so it will only absorb UV light), and single crystals have a conduction band edge near 3.5 eV [1]. Thin films of ZnS have been synthesized by several solution-based methods, including chemical bath deposition [2]–[4], spray pyrolysis [5], and successive ionic layer adsorption and reaction (SILAR) [6]. Here, SILAR is used to fabricate ZnS thin films.

D.2. SILAR-Based Synthesis of ZnS Thin Films

The SILAR method involves creation of precursor solutions of cations and anions and the immersion of the desired substrate sequentially in each solution. Here, a substrate was immersed in a 0.1 M solution of aqueous zinc acetate for 30 seconds, allowing Zn ions to adsorb to the surface. The substrate was then rinsed in a water bath, and then placed in a 0.1 M aqueous sodium sulfide solution for 30 seconds. After another rinse, the process was repeated to build up a thin film of ZnS.

Figure D.1 gives the XRD and Raman characterization of thin films deposited through the SILAR method. The XRD spectra show broad peaks characteristic of nanocrystalline domains. The peaks match well with the sphalerite ZnS phase, though the presence of wurtzite ZnS cannot be ruled out. The Raman spectrum matches relatively closely with that of ZnS quantum dots, with small shifts attributed to quantum confinement effects and a different laser source [7]. It should be noted that the films deposited here were on glass; deposition on a different substrate or Cu_3AsS_4 may change the crystal structure, orientation, and domain size of as-deposited ZnS thin films. Additionally, photographs indicate a somewhat non-uniform deposition of ZnS, so this must be addressed by ensuring a flat surface and thoroughly cleaned substrate.

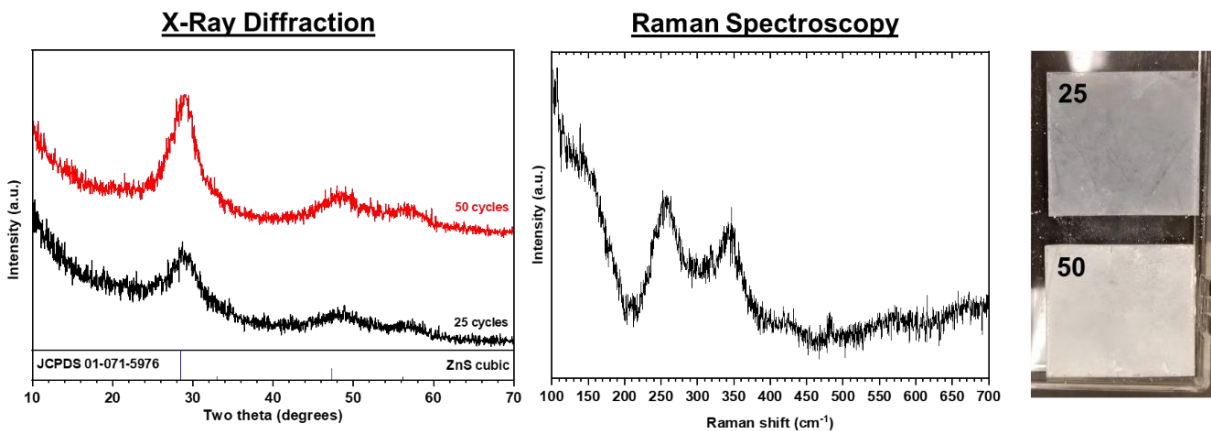


Figure D.1. XRD spectra, Raman spectrum (50 cycles), and photographs of ZnS thin films deposited by the SILAR method.

D.3. Conclusions

A preliminary route towards the deposition of cubic ZnS thin films through successive ionic layer adsorption and reaction has been presented. Future work must focus on measuring and tuning the properties of ZnS (such as thickness and carrier concentration), as well as determining the material's true band alignment with Cu_3AsS_4 solar cells for use in high-efficiency devices.

D.4. Acknowledgements

S.A.M. would like to thank Joseph Ander for assistance with the experimental setup.

D.5. References

- [1] M. Aven and C. A. Mead, "Electrical transport and contact properties of low resistivity n-type zinc sulfide crystals," *Appl. Phys. Lett.*, vol. 7, no. 1, pp. 8–10, 1965.
- [2] S. R. Kang, S. W. Shin, D. S. Choi, A. V. Moholkar, J.-H. Moon, and J. H. Kim, "Effect of pH on the characteristics of nanocrystalline ZnS thin films prepared by CBD method in acidic medium," *Curr. Appl. Phys.*, vol. 10, no. 3, pp. S473–S477, May 2010.
- [3] R. K. Choubey, S. Kumar, and C. W. Lan, "Shallow chemical bath deposition of ZnS buffer layer for environmentally benign solar cell devices," *Adv. Nat. Sci. Nanosci. Nanotechnol.*, vol. 5, no. 2, 2014.

- [4] D.-H. Jeon, D.-K. Hwang, D.-H. Kim, J.-K. Kang, and C.-S. Lee, "Optimization of the ZnS Buffer Layer by Chemical Bath Deposition for Cu(In,Ga)Se₂ Solar Cells," *J. Nanosci. Nanotechnol.*, vol. 16, no. 5, pp. 5398–5402, 2016.
- [5] C. Sabitha, I. H. Joe, K. D. A. Kumar, and S. Valanarasu, "Investigation of structural, optical and electrical properties of ZnS thin films prepared by nebulized spray pyrolysis for solar cell applications," *Opt. Quantum Electron.*, vol. 50, no. 3, pp. 1–18, 2018.
- [6] K. Priya, V. K. Ashith, G. K. Rao, and G. Sanjeev, "A comparative study of structural, optical and electrical properties of ZnS thin films obtained by thermal evaporation and SILAR techniques," *Ceram. Int.*, vol. 43, no. 13, pp. 10487–10493, 2017.
- [7] J. Trajić *et al.*, "Raman spectroscopy of ZnS quantum dots," *J. Alloys Compd.*, vol. 637, pp. 401–406, 2015.

APPENDIX E. SUPPLEMENTARY CHARACTERIZATION FOR TETRAHEDRITE-TENNANTITE AND COPPER ARSENIC ANTIMONY SELENIDE NANOPARTICLES

E.1. Introduction

In Chapter 7, the synthesis of tetrahedrite-tennantite (TET-TEN) $\text{Cu}_{12}\text{As}_{4-x}\text{Sb}_x\text{S}_{13}$ nanoparticles (NPs) was reported, and their properties before and after thermal annealing were investigated [1]. However, their optical properties, such as bandgap, were not explored. Additionally, the optical and thermal analysis for $\text{Cu}_3\text{As}_{1-x}\text{Sb}_x\text{Se}_4$ NPs previously synthesized by our lab has not been completed [2]. Here, diffuse reflectance spectroscopy was used to estimate the band gaps of both types of NPs [3], [4], and thermogravimetric analysis (TGA) was used to determine the thermal properties of Cu_3SbSe_4 NPs.

E.2. Characterization of Tetrahedrite-Tennantite Nanoparticle Band Gaps

Diffuse reflectance spectroscopy was acquired on alloy TET-TEN NPs that were mixed with potassium bromide, a zero-reflectance material. Figure D.1 shows the extrapolation of the squared Kubelka-Munk function to the x-axis, providing an estimate of the direct bandgap for each composition. Bandgaps in the range of 1.37 – 1.86 eV are extracted; each endmember deviates slightly from other reports in literature (TET ~1.5-1.6 eV, TEN ~ 1.75 eV), suggesting the possibility of impurity states or quantum confinement. A linear regression was performed on the extracted bandgaps; they vary somewhat linearly with the composition, but it may be necessary to introduce a bowing parameter to more accurately predict the bandgap of TET-TEN alloy NPs. The bandgaps of TET-TEN should be measured through some other means, such as UV-VIS transmission spectroscopy or photoluminescence, for comparison with the data here.

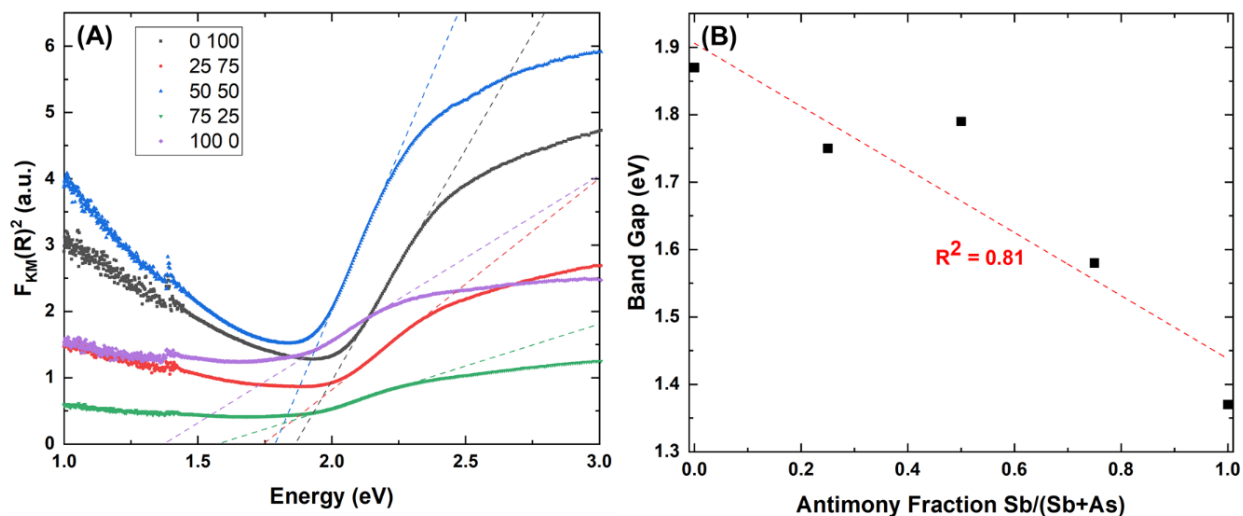


Figure E.1. Diffuse reflectance analysis for the band gaps of tetrahedrite-tennantite alloy nanoparticles. The key indicates the relative fraction of antimony, followed by the relative fraction of arsenic, i.e. “25 75” signifies a 25% Sb sample.

E.3. Characterization of Copper Arsenic Antimony Selenide Nanoparticles

Diffuse reflectance spectroscopy measurements were performed on Cu_3AsSe_4 and Cu_3SbSe_4 NPs; however, the data (Figure E.2) was too noisy to draw any definite conclusions regarding their bandgaps. The extrapolation of the Kubelka-Munk function extends below the data range of 0.5 eV, suggesting very low bandgaps in accordance with literature predictions and measurements [5], [6].

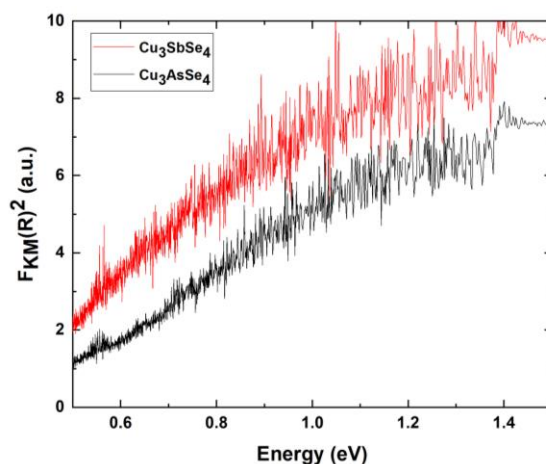


Figure E.2. Diffuse reflectance analysis for the band gaps of Cu_3AsSe_4 and Cu_3SbSe_4 nanoparticles. The y-axis is the squared Kubelka-Munk function.

The thermal properties of Cu_3SbSe_4 NPs were evaluated using thermogravimetric analysis (TGA) in a helium flow atmosphere. The ramp rate was $10\text{ }^\circ\text{C}/\text{min}$, and the sample was held at $340\text{ }^\circ\text{C}$ for 30 min in the middle of the run. Figure E.3 gives the TGA weight fraction and heat flow as a function of temperature. At $340\text{ }^\circ\text{C}$, a mass loss is noted over the course of 30 min, potentially attributable to the loss of oleylamine ligands or excess selenium. A major mass loss event begins at $\sim 460\text{ }^\circ\text{C}$, with a strong exotherm noted. It should be noted that previous heat treatments on Cu_3SbSe_4 were not conducted above $340\text{ }^\circ\text{C}$, so any treatments at higher temperatures must consider this potential decomposition event [2].

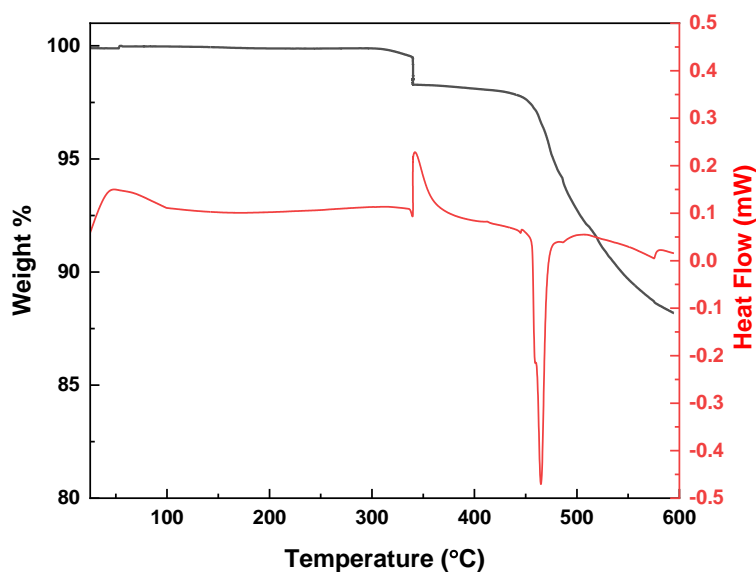


Figure E.3. Thermogravimetric analysis (TGA) of Cu_3SbSe_4 NPs in a helium flow atmosphere. The ramp rate was $10\text{ }^\circ\text{C}/\text{min}$ to $600\text{ }^\circ\text{C}$, with an isothermal hold at $340\text{ }^\circ\text{C}$ for 30 min.

E.4. Conclusions

The optical bandgaps and thermal analysis of several non- Cu_3AsS_4 nanoparticles was presented in this appendix. Some tetrahedrite-tennantite bandgaps are too large for single-junction solar cell applications, but they may find use in tandem cell applications. The bandgaps of Cu_3AsSe_4 and Cu_3SbSe_4 appear to be quite low, explaining their success in low-temperature thermoelectric applications. The decomposition of the selenide NPs appears to occur only at high temperatures that have not yet been explored for grain growth and densification.

E.5. Acknowledgements

S.A.M would like to thank Arthur Shih and Prof. Fabio Ribeiro for supplying the potassium bromide used in diffuse reflectance measurements, Alexei Lagoutchev for helpful discussions regarding diffuse reflectance measurements, and Juan Carlos Vega-Vila and Prof. Rajamani Gounder for access to and training on the TGA instrument.

E.6. References

- [1] S. A. McClary, R. B. Balow, and R. Agrawal, "Role of annealing atmosphere on the crystal structure and composition of tetrahedrite–tennantite alloy nanoparticles," *J. Mater. Chem. C*, vol. 6, no. 39, pp. 10538–10546, 2018.
- [2] R. B. Balow, E. P. Tomlinson, M. M. Abu-Omar, B. W. Boudouris, and R. Agrawal, "Solution-based synthesis and characterization of earth abundant $\text{Cu}_3(\text{As,Sb})\text{Se}_4$ nanocrystal alloys: towards scalable room-temperature thermoelectric devices," *J. Mater. Chem. A*, vol. 4, no. 6, pp. 2198–2204, 2016.
- [3] P. Kubelka and F. Munk, "Ein Beitrag zur Optik der Farbanstriche (Contribution to the optic of paint)," *Zeitschrift fur Tech. Phys.*, vol. 12, pp. 593–601, 1931.
- [4] V. Džimbeg-Malčić, Ž. Barbarić-Mikočević, and K. Itrić, "Kubelka-Munk Theory in Describing Optical Properties of Paper (I)," *Tech. Gaz.*, vol. 18, no. 1, pp. 117–124, 2011.
- [5] L. I. Berger and V. D. Prochukhan, *Ternary Diamond-Like Semiconductors*. New York: Consultants Bureau, 1969.
- [6] T. Shi, W.-J. Yin, M. Al-Jassim, and Y. Yan, "Structural, electronic, and optical properties of $\text{Cu}_3\text{-V-VI}_4$ compound semiconductors," *Appl. Phys. Lett.*, vol. 103, no. 15, p. 152105, Oct. 2013.

APPENDIX F. ON THE USE OF EDX TO DETERMINE NANOPARTICLE COMPOSITIONS

F.1. Introduction

Determining the composition of as-synthesized nanoparticles (NPs) is important to ensure reproducible production of high-efficiency solar cells. Energy-dispersive X-ray spectroscopy (EDX) was used to determine the composition of LUZ NPs used in the initial chapters of this thesis. Analysis was conducted using AZtec software.

EDX is a technique in which a sample is placed in a scanning electron microscope (SEM) and bombarded with an electron beam, typically at 20 kV. Some electrons will eject core electrons from various atoms in the sample. Electrons from outer shells may relax and fill these vacated states, releasing X-rays of a characteristic energy that can then be collected and analyzed. EDX analysis requires corrections for various spectral artifacts and reabsorption events that can take place, and it assumes that a flat, uniform sample is being analyzed. If this assumption is incorrect, it can confound data analysis, as demonstrated in this appendix.

F.2. Measurement of Luzonite Nanoparticle Compositions Using EDX

LUZ NPs were analyzed by drop-casting a suspension (typically in toluene) onto a conductive Si substrate. ~35 independent samples were synthesized by nominally the same method, with injection of 2.8:1 Cu:As chloride precursors into hot OLA and reaction at 175 °C for 10 min. Figure F.1 gives the calculated Cu/As ratio as a function of the Si substrate atomic percent. A wide variation in the Cu/As ratios is noted, and a statistically significant linear correlation between the Cu/As and Si wt% is established. This means that by making a thinner or thicker film of LUZ NPs, the apparent composition of the NPs is modified! The reason for this discrepancy lies in the assumption that a uniform thin film is being analyzed. If the electron beam penetrates to the Si substrate (i.e. if the film is < 1 μm thick), then Si X-rays are detected. The EDX analysis does not recognize that there are two layers in the material and hence incorrectly applies the corrections, leading to artificially low copper concentrations for higher silicon signal. Any future use of EDX must ensure that films are sufficiently thick so that the substrate is not detected.

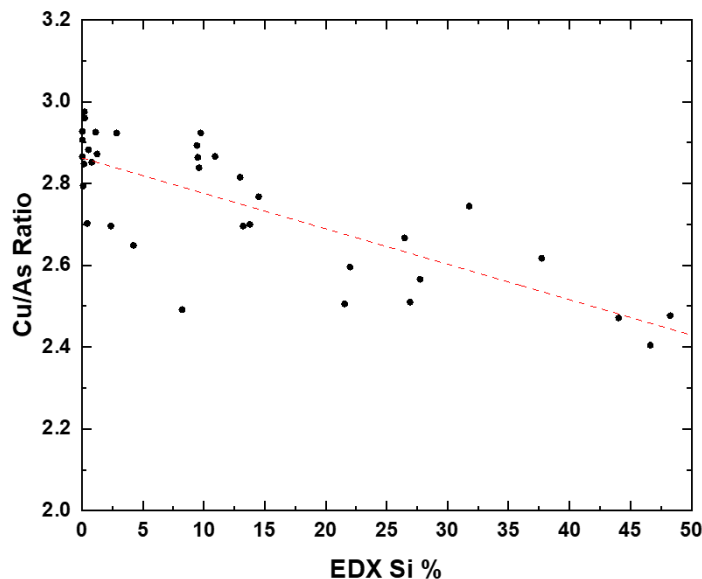


Figure F.1. Calculated Cu/As ratio as a function of the atomic percentage of silicon substrate measured through EDX. A linear trendline is plotted, and its slope is significantly different than zero at the 0.05 level.

F.3. Conclusions

EDX is relatively straightforward to implement and can be used to rapidly determine the composition of NP films. However, great care must be taken during sample preparation to ensure that signal from the substrate does not enter the EDX spectrum – otherwise, the compositional ratios will not be accurate. Alternative characterization techniques may also be used, such as X-ray fluorescence (XRF), which can be used to model multiple layers of a substrate/thin-film architecture, and ICP-MS, which is a very sensitive chemical technique that can detect atoms in parts-per-billion quantities.

F.4. Acknowledgements

S.A.M would like to thank Dr. Christopher Gilpin for training and insightful discussions regarding EDX data acquisition and analysis.

VITA

Scott Andrew McClary was born in Fort Morgan, Colorado to Kimberly and Andrew McClary on September 30, 1991. He has one younger brother, Michael. In school, he quickly developed an aptitude for math and science, always seeking to solve the most complicated problems he could find and spending endless hours preparing for national math contests. Scott spent much of his childhood and adolescent years in the Boy Scouts of America and achieved the rank of Eagle Scout in 2008; his time spent in the beautiful landscapes of Colorado inspired him to explore creative ways to protect the natural environment in whatever way he could. He was awarded the prestigious Boettcher Scholarship during his senior year and graduated from Fort Morgan High School in 2010.

Scott attended Colorado School of Mines beginning in Fall of 2010, unsure of his major but open to many options. After a year and a half taking the core courses and enjoying organic chemistry and thermodynamics, he decided to pursue his degree in chemical engineering with minors in mathematics and renewable energy. The renewable energy program, particularly courses on solar energy and fuel cells, helped Scott set his sights on a career in clean energy technologies for the benefit of humankind. Scott also worked as a tutor for three years and capped off his senior year by serving as a teaching assistant for thermodynamics and material and energy balances. The teaching and mentoring experiences, coupled with the opportunity to work at the forefront of the renewable energy field, motivated him to apply to graduate school to continue his education. Scott graduated from Colorado School of Mines in May of 2014 and earned the Outstanding Graduating Senior award for the Chemical Engineering Department.

Scott was admitted to the Ph.D. program in the Davidson School of Chemical Engineering at Purdue University in the Fall of 2014 and joined the research group of Dr. Rakesh Agrawal. At Purdue, he developed solution-based methods to thin films of emerging photovoltaic materials, most notably fabricating the world's first solar cells of copper arsenic sulfide. Scott finished his Ph.D. in August 2019 and joined Sandia National Laboratories as a postdoctoral researcher in the Joint Center for Energy Storage Research (JCESR). He hopes to spend his life teaching and researching critical problems that will preserve the planet for generations to come.

PUBLICATIONS

Scott A. McClary, Joseph Andler, Carol A. Handwerker, and Rakesh Agrawal. "Solution-processed copper arsenic sulfide thin films for photovoltaic applications." *J. Mat. Chem C.*, vol. 5, pp. 6913-6916, 2017.

Scott A. McClary, Joseph Andler, Carol A. Handwerker, and Rakesh Agrawal. "Fabrication of copper arsenic sulfide thin films from nanoparticles for application in solar cells." *Proceedings of the 44th IEEE Photovoltaics Specialists Conference*. Washington D.C., June 2017.

Scott A. McClary*, Robert B. Balow*, and Rakesh Agrawal. "Role of annealing atmosphere on the crystal structure and composition of tetrahedrite-tennantite alloy nanoparticles." *J. Mat. Chem. C.*, vol. 6, pp. 10538-10546, 2018.

Scott A. McClary, Weiwei Meng, Xinxing Yin, Joseph Andler, Siming Li, Louis R. Schroeder, Jason B. Baxter, Carol A. Handwerker, Yanfa Yan, and Rakesh Agrawal. "Evaluating novel semiconducting materials for photovoltaic applications: a case study of Cu₃AsS₄." *Conference Proceedings of the 2018 AIChE Annual Meeting*. Pittsburgh, PA. November 2018.

Xinxing Yin*, Scott A. McClary*, Zhaoning Song, Dewei Zhao, Brian Graeser, Changlei Wang, Niraj Shrestha, Xiaoming Wang, Cong Chen, Chongwen Li, Kamala K. Subedi, Randy J. Ellingson, Weihua Tang, Rakesh Agrawal, and Yanfa Yan. "A Cu₃PS₄ nanoparticle hole selective layer for efficient inverted perovskite solar cells." *J. Mat. Chem. A.*, vol. 7, pp. 4604-4610, 2019.

Scott A. McClary, Siming Li, Xinxing Yin, Patricia Dippo, Darius Kuciauskas, Yanfa Yan, Jason B. Baxter, and Rakesh Agrawal. "Optoelectronic characterization of emerging solar absorber Cu₃AsS₄." *Proceedings of the 46th IEEE Photovoltaics Specialists Conference*. Chicago, IL, June 2019.

Scott A. McClary and Rakesh Agrawal. "Synthesis and characterization of sinnerite $\text{Cu}_6\text{As}_4\text{S}_9$ for optoelectronic applications." *In preparation.*

Scott A. McClary, Canglang Yao, Siming Li, Mohammad Taheri, Daria Blach, Yining Feng, Darius Kuciauskas, Patricia Dippo, Luna Lu, Libai Huang, Jason B. Baxter, Yanfa Yan, and Rakesh Agrawal. "Optoelectronic and defect characterization of emerging solar absorber Cu_3AsS_4 ." *In preparation.*

Scott A. McClary and Rakesh Agrawal. "Ligand exchange of copper arsenic sulfide nanoparticles for thin-film photovoltaics." *In preparation.*

Canglang Yao, Scott A. McClary, Rakesh Agrawal, and Yanfa Yan. "Band alignments in the $\text{Cu}_3\text{-V-VI}_4$ material system: a combined theoretical and experimental study." *In preparation.*

A * signifies equal contribution to the work.